NATIONAL AERONAUTICS AND SPACE ADMINISTRATION
U.S.A.

VAPORIZATION OF HIGH-TEMPERATURE POTASSIUM IN FORCED CONVECTION AT SATURATION TEMPERATURES OF 1800° TO 2100° F

N67-391

by J. A. Bond and G. L. Converse

Prepared by
GENERAL ELECTRIC COMPANY
Cincinnati, Ohio
for Lewis Research Center

VAPORIZATION OF HIGH-TEMPERATURE POTASSIUM IN FORCED CONVECTION AT SATURATION TEMPERATURES OF $1800°$ TO $2100°$ F

By J. A. Bond and G. L. Converse

Distribution of this report is provided in the interest of information exchange. Responsibility for the contents resides in the author or organization that prepared it.

NATIONAL AERONAUTICS AND SPACE ADMINISTRATION

FOREWORD

The work described in this report is part of an alkali metal boiling and condensing heat transfer program conducted by the General Electric Company under NASA Contract NAS 3-2528. The work was done under the technical management of Ruth N. Weltmann, Space Power Systems Division, NASA Lewis Research Center.

ABSTRACT

The results of an experimental investigation of heat transfer and fluid flow during forced convection vaporization of high temperature potassium in vertical up-flow in single tubes are presented. The experiments were conducted in a Cb-1% Zr facility with radiant-heated test sections at saturation temperatures up to 2100° F. Two-phase heat transfer results are presented for nucleate boiling and the critical heat flux condition, along with exploratory measurements of transition boiling, film boiling and superheated vapor heat transfer coefficients. Measurements of pressure drop in adiabatic two-phase flow, liquid heat transfer coefficients measured at low Peclet numbers, and results from tests with net liquid superheat exploring some of the instabilities associated with boiling inception are also presented.

TABLE OF CONTENTS

LIST OF ILLUSTRATIONS

LIST OF ILLUSTRATIONS (CONT'D)

LIST OF TABLES

NOMENCLATURE

The symbols and units listed below are used in all derivations. The symbols listed below are occasionally used with other units in the figures, tables, or in the written text. Whenever this is done, the appropriate units are indicated.

Simple Latin Letter Symbols

Symbol	Quantity	Units
A	Area	ft^2
a	Radial acceleration	ft/sec^2 or ft/hr^2
b	Bubble height	ft
D	Diameter	ft
d	Diameter of wire for wire coil	ft
E	Mass fraction of liquid entrained in the vapor core	Dimensionless
f	Darcy-Weisbach friction factor	Dimensionless
$\mathcal{F}$	Gray-body configuration factor for thermal radiation	Dimensionless
G	Mass velocity (flow rate per unit flow area)	$lb_m/hr\text{-}ft^2$
g_c	Gravitational conversion coefficient	4.17×10^8 ft/hr^2
h	Heat transfer coefficient	$Btu/hr\text{-}ft^2\text{-}°R$
J	Conversion factor (mechanical equivalent of heat)	778 $ft\text{-}lb_f/Btu$
K	Slip ratio ($K = V_g/V_\ell$)	Dimensionless
k	Thermal conductivity	$Btu/hr\text{-}ft$ °R
K'	Orifice loss coefficient	Dimensionless
L, ℓ	Length	ft
n	Exponent in Equation (6)	Dimensionless
p	Pressure	lb_f/ft^2
	Helix pitch, length for one 360° turn	ft
	Rate of heat flow	Btu/hr
	Radius at tube wall	ft
	Radius, Bubble radius	ft

Simple Latin Letter Symbols (Cont'd)

Symbol	Quantity	Units
t	Time	seconds
T	Temperature	°R and °F
$\hat{T}$	Weighted-Average Temperature	°F
V	Velocity	ft/hr
$\bar{V}$	Velocity vector	ft/hr
W	Flow rate	lb_m/hr
X	Flowing quality ($X = W_g/W$)	Dimensionless
y	Distance from wall	ft
z	Distance along flow axis, coordinate	ft

Composite Latin Letter Symbols

Symbol	Quantity	Units
a_r	Radial acceleration relative to gravity at radius r	g's
a_R	Radial acceleration relative to gravity at tube wall	g's
C_p	Constant pressure specific heat	Btu/lb_m-°R
D_{CB}	Insert centerbody diameter	ft
D_{or}	Orifice diameter	ft
f_o	Smooth tube friction factor	Dimensionless
G_{HM}	Mass velocity in helical flow	lb_m/ft^2-sec
h_f	Liquid enthalpy	Btu/lb_m
h_g	Vapor enthalpy	Btu/lb_m
h_v	Superheated vapor heat transfer coefficient	Btu/hr-ft^2-°F
h_{fg}	Latent heat of vaporization	Btu/lb_m
N_{Nu}	Nusselt number ($N_{Nu} = h\,D/K$)	Dimensionless
N_{Pe}	Peclet number ($N_{Pe} = G\,D\,C_p/K$)	Dimensionless
N_{Pr}	Prandtl number ($N_{Pr} = \mu\,C_p/K$)	Dimensionless
N_{Re}	Reynolds number ($N_{Re} = \rho\,V\,D/\mu$)	Dimensionless
P/D	Insert twist ratio, tube diameters for 360° turn of helix or coil	Dimensionless

Composite Latin Letter Symbols (Cont'd)

Symbol	Quantity	Units
q''	Heat flux	$Btu/hr\text{-}ft^2$
q''_c	Critical heat flux	$Btu/hr\text{-}ft^2$
r_c	Critical cavity radius	ft
r_{max}	Maximum cavity radius	ft
R_g	Vapor volume fraction	Dimensionless
R_ℓ	Liquid volume fraction	Dimensionless
T_o	Initial temperature of semi-infinite plate	°F
v_{fg}	Specific volume change in going from liquid to vapor	ft^3/lb_m
X_c	Quality at the critical heat flux	Dimensionless
X_e	Quality at test section exit	Dimensionless
ΔT	Wall-to-fluid temperature difference	°F
ΔT_r	Radial difference in saturation temperature, Equation (23)	°F
$(dP/dZ)_{TPF}$	Two-Phase friction pressure gradient	lbs/ft^3, psi/ft
$(dP/dZ)_O$	Friction pressure gradient for all-liquid flow	lbs/ft^3, psi/ft

Greek Letter Symbols

Symbol	Quantity	Units
α	Angular coordinate	radians
β	Bubble contact angle	radians, degrees
Δ	Finite difference	Dimensionless
δ	Film thickness	ft
ϵ	Emissivity for thermal radiation	Dimensionless
θ	Angular displacement, cavity angle	radians, degrees
μ	Dynamic viscosity	$lb_m/hr\text{-}ft$
π	Dimensionless groups used in Equation (71)	Dimensionless
ρ	Mass density	lb_m/ft^3
σ	Surface tension	lb_f/ft
τ	Time interval	seconds
ϕ	Two-Phase friction pressure gradient, defined by Equation (56)	Dimensionless
δ_{SH}	Degrees of Vapor Superheat, $(T - T_{sat})$	°F

Subscripts

a	Acceleration in two-phase region
b	Bulk fluid temperature
cb	Value at the insert centerbody
c	Value at the critical hear flux condition
e	Equivalent value of a given quantity for application to helical flow
f	Indicates a liquid phase property
FB	Film boiling
FBE	Value at film boiling inception
FE	Film evaporation
g	Indicates a vapor phase property
i	Inside
I, i	Inlet
if	Value at the vapor-liquid film interface
ℓ	Refers to liquid phase
m	Measured value
NB	Nucleate boiling
o	Outlet or outside
or	Orifice
p	Calculated or predicted value
PB	Pool boiling
r	Component in radial direction
s, sat	Saturation
sc	Subcooled
SH	Superheat
T	Tangential
TB	Transition boiling
TP	Two-Phase
TPF	Two-Phase friction
w	Value at the tube wall
z	Component in axial direction

SUMMARY

The results of an experimental investigation of heat transfer and fluid flow during forced convection vaporization of high temperature potassium in single tubes are presented. This investigation was undertaken to obtain local boiling heat transfer data for potassium and to extend the range of available boiling data up to 2100°F, for use in development of potassium boilers applicable to Rankine cycle space power systems.

The experiments were conducted in a Cb-1%Zr facility consisting of a single loop system with radiant-heated test sections. Data was obtained in five different test sections, both with and without vortex generator inserts. The heated length of all test sections was 30 inches and two different tube diameters were used, 0.42-inch ID and about 0.75-inch ID. The insert geometries included two different helices, a wire coil, and both a smooth plug and a wire-wrapped plug in the inlet region of the test section. One of the helices and both of the plug inserts were instrumented with internal thermocouples for local fluid temperature measurement. Most of the data were taken at 2100°F saturation temperature, although some data were taken at lower temperatures down to 1800°F to investigate dependence on temperature.

A large body of nucleate boiling data was obtained in the five test geometries. The heat transfer coefficients for the plain tubes (no insert) were typically high, in the order of 10,000 Btu/hr-ft^2-°F for the range of heat fluxes tested. Two analytical models were developed to predict the nucleate boiling heat transfer performance for plain tubes and recommended procedure for design application is given. The nucleate boiling data for the test sections with helical inserts indicate that the insert tends to lower the heat transfer performance in nucleate boiling. An empirical correlation of the nucleate boiling data with inserts is also presented.

The critical heat flux data obtained from the radiant-heated test sections are in reasonably good agreement with an empirical correlation for potassium developed from lower temperature data obtained in a two-fluid boiler. Local measurements of the wall temperature at the onset of the critical heat flux condition give an insight into the critical heat flux phenomenon as it occurs both in plain tubes and in test sections containing inserts.

Local transition boiling heat transfer coefficients were calculated from the data using the time-average of the fluctuating wall temperature obtained from multiple printouts of a digital recorder. These data are in fair agreement with an empirical correlation developed for potassium from lower temperature data obtained in a two-fluid boiler.

Exploratory measurements of the film boiling and superheated vapor heat transfer coefficients are presented. The film boiling coefficients are typically high with respect to calculated values based on standard correlations for vapor heat transfer. The superheated vapor heat transfer measurements are correlated reasonably well after analytical corrections are made for the effect of the helical inserts and for the effect of radiation from the heated wall.

Pressure drop data for potassium in two-phase adiabatic flow were obtained for three different insert geometries. These data are correlated reasonably well by a homogeneous model prediction (equal liquid and vapor phase velocities).

Instabilities encountered during the course of testing are described, and the results from some specific experiments designed to study instabilities associated with boiling inception are presented. In addition to the boiling heat transfer results, some single-phase liquid potassium heat transfer data were obtained using a vortex generator insert in the entrance region of the test section. These data are in the range of Peclet numbers below 100, where other available data is sparse.

-2-

I INTRODUCTION

Under sponsorship of the National Aeronautics and Space Administration General Electric Company has been conducting experimental and analytical studies of boiling and condensing of high-temperature alkali metals since early 1961. This work was directed toward providing basic heat transfer information needed for development of Rankine cycle space power systems using potassium as the working fluid.

The experimental work was performed in three separate alkali metal heat transfer test facilities, two of which were used for boiling studies and the third was used for condensing experiments. Brooks (1)* has reported on the initial phase of this program, which included the design and fabrication of the three test facilities and some early test results. Results from the materials investigations done in support of the development of the two boiling facilities are reported by Semmel, et al.(2). One of the two boiling test facilities is a two-fluid test rig constructed of Haynes-25 alloy, which employed sodium at temperatures up to 1850°F to boil potassium in a single-tube, once-through boiling test section at temperatures up to about 1750°F, using test section geometries which approximate those anticipated for Rankine cycle space power boilers. The results from these two-fluid, once-through boiling experiments are reported by Peterson (3).

The second boiling facility, the experimental results from which are the subject of this report, is a single-loop test rig constructed from Cb-1%Zr, which is capable of operation at saturation temperatures up to 2100°F. The role of this test rig was to supplement and extend the results obtained in the two-fluid facility. Specifically, the objectives of the high temperature boiling potassium experiments done in the Cb-1%Zr Facility were:

---

*Underlined numbers in parentheses designate References listed at the end of the text.

(1) To obtain <u>local</u> heat transfer and pressure drop data for
      boiling potassium.

(2) To extend the results obtained in the two-fluid Haynes-25 alloy
      facility to higher temperatures up to 2100°F.

The ultimate application of the information presented in this report
will be in design of "once-through" boilers for Rankine cycle space power
systems which use potassium as the working fluid. Peterson (3) gives a
conceptual description of once-through boiling which will be briefly reviewed
in order to define some of the terms used in this report.

In the once-through boiling process, the fluid enters the boiler in
a subcooled liquid state and is converted, in a single pass through the
boiler, to superheated vapor at the exit. With subcooled liquid at the inlet,
the heat transfer mechanism is one of single-phase forced convection. Proceeding
along the boiler in the flow direction, the fluid temperature rises and
approaches the saturation temperature corresponding to the local pressure.
The point of boiling inception is determined by the heat flux, mass velocity,
tube geometry and tube surface condition. At relatively high heat flux levels,
for example, local surface boiling may occur while the bulk liquid is still in
the subcooled condition, with subsequent condensation of the vapor bubbles. At
lower heat flux levels, on the other hand, the bulk liquid may become super-
heated before boiling inception occurs. The point of boiling inception marks
the beginning of the nucleate boiling regime, which is characterized by
relatively high heat transfer performance. This regime persists, with increasing
quality, until the onset of the critical heat flux condition, at which point
the heat transfer performance begins to deteriorate due to breakdown of the
continuous liquid film believed to exist in the nucleate boiling regime. The
critical heat flux condition marks the beginning of the transition boiling
regime. In the transition boiling regime the wall temperature oscillates
within an envelope, the upper bound of which increases with increasing
quality and the lower bound of which is approximately constant at the value

corresponding to nucleate boiling. The range of quality over which the transition boiling regime exists depends primarily on the heat flux level. As the quality increases, the quantity of liquid available to wet the wall decreases and the mean wall temperature increases until the "spheroidal" state or Leidenfrost point is reached. This marks the beginning of the film boiling regime, in which the wall is believed to be blanketed with a continuous layer of locally superheated vapor and the wall-to-fluid temperature difference is in the same order as that associated with heat transfer to the single-phase vapor. The last stage of the once-through boiling process is the superheat regime, in which the heat transfer is by single-phase convection to the vapor.

The format of this report is closely related to the above conceptual view of the once-through boiling process. Local heat transfer results are presented for each individual stage of the process, together with associated analyses and empirical correlations of the data. In addition, the results of some two-phase pressure drop and stability studies are presented.

II   EXPERIMENTAL APPARATUS

The Cb-1%Zr Facility is a single loop system designed to study forced-convection vaporization of potassium at fluid temperatures up to 2100°F. The alkali metal containment piping is constructed from columbium-1% zirconium and is enclosed in a high-vacuum environmental chamber to avoid atmospheric contamination. Brooks (1) gives a detailed description of the facility as it was originally designed and built, including welding techniques for the Cb-1%Zr. Descriptions of the vacuum system and loop components are included in this report as Appendix A. During the summer of 1964, the loop was modified to include a preboiler upstream of the test section.

A.   General Loop Description

Figure 1 is a schematic of the Cb-1%Zr Facility after its modification in 1964. Liquid potassium is discharged from the electromagnetic pump and flows through an electromagnetic flowmeter to an 8 KW radiant preheater, which controls the preboiler inlet subcooling. Upon leaving the preheater, the liquid potassium flows through a throttling orifice into the preboiler.

The preboiler consists of a coil of pipe with a radiant heater in the core, all contained within a radiation shield assembly (Figure 2). The preboiler heater element is fabricated from coiled tungsten wire and has operated at gross electrical power levels up to 60 KW. The function of the preboiler is to control the enthalpy of the potassium in the test section independent of test section heat flux, thus permitting separation of the effects of quality and heat flux in the tests.

After leaving the preboiler, the potassium passes in vertical up-flow through an insulated entrance length of about 10 inches, and into the test section. A total of five test section geometries, described in the next section, were employed in the Cb-1%Zr Facility after its modification. Each

of these test sections had a heated length of 30-inches. The radiant heater for the test sections consisted of an array of 27 tungsten rods surrounding the test section and enclosed in a radiation shield assembly (Figure 3). The test section heater was operated at gross electrical power levels up to 32 KW.

Energy is rejected from the potassium as it flows through approximately 60 ft. of condenser piping radiating to the water-cooled walls of the environmental chamber. Some control of the heat rejection rate is accomplished with adjustable shutters which surround the condenser coil (Figure 4).

B. Test Sections

Table 1 lists the five test sections employed in the Cb-1%Zr Facility to obtain the data presented in this report.

Table 1
Cb-1%Zr Facility Test Sections

Test Section Number	Inside Diameter Inch	Insert
1	0.767	No Insert
2	0.740	Helical Insert, P/D = 6
3	0.423	No Insert
4	0.738	Combination annular plug and helix with P/D = 2 (instrumented)
5	0.742	Combination wire-wrapped annular plug (P/D = 2) and wire coil with P/D = 2 (instrumented)

TEST SECTION NO. 1

Figure 5 is a sketch showing the general arrangement and instrumentation of Test Section No. 1. This test section was a plain segment of 3/4-inch

Schedule 80, Cb-1%Zr pipe with no insert. Temperatures of the outside surface were measured at ten locations as indicated in the sketch and the fluid temperature at the test section outlet was measured with three thermocouples contained in an axial well which terminated 1-3/4-inches downstream of the end of the heated zone.

TEST SECTION NO. 2

This test section was a 3/4-inch Schedule 80 pipe containing a non-instrumented helical insert with a pitch-to-diameter ratio of six. Figure 6 is a sketch of Test Section No. 2 showing the thermocouple locations and Figure 7 is a photograph of the test section and insert.

TEST SECTION NO. 3

Test Section No. 3 was a 3/8-inch Schedule 80 pipe with no insert. Thermocouple locations are shown in Figure 8.

TEST SECTION NO. 4

This test section was a 3/4-inch Schedule 80 pipe containing an instrumented plug-helix insert. Figure 9a is an overall view of Test Section No. 4 with the insert installed. The insert, shown in Figure 9b, consisted of an inlet plug followed by a helix vortex generator. Figure 10a shows the inlet plug which, when installed, formed an annular flow passage extending over approximately half of the heated length. The helix section of the insert (Figure 10b) consisted of a spiral (P/D = 2) tape welded to a 1/4-inch center-body to form a helical flow path. Both the inlet plug and the helix center-body were hollow and contained a total of five Pt-Pt 10% Rh thermocouples distributed along the heated length as shown in Figure 11 for Test Section No. 4. After its removal from the loop, Test Section No. 4 was instrumented with pressure taps, and water tests were conducted to determine the single-phase friction factors for the annular region and the helix region. The locations of these pressure taps are shown in Figure 11.

TEST SECTION NO. 5

Figure 12a is an overall view of Test Section No. 5 with its insert installed. The components of the insert are shown in Figure 12b along with the test section pipe. The inlet section of the insert consisted of a plug extending over approximately half the heated length. A 3/32-inch diameter wire was fitted into a spiral groove (P/D = 2) machined on the plug surface. When installed in the test section pipe, the wire-wrapped inlet plug formed a helical flow passage between the plug outside diameter and the pipe inside diameter. Downstream of the plug, the wire was attached to the inside surface of the pipe by welding through holes. The hollow plug contained five Pt-Pt 10% Rh thermocouples distributed along its length as shown in Figure 12. Fluid temperatures at the test section outlet were measured with thermocouples installed in an axial well. Figure 13 shows locations of thermocouples in this test section. Also shown in Figure 13 are the locations of pressure taps which were used in water tests after the test section was removed from the loop.

An additional feature of Test Section No. 5 was a radiant heated artificial nucleator of the "hot-finger" type located upstream of the test section. The nucleator, shown in Figures 14 and 15 was used in boiling inception studies described in this report.

C. Instrumentation, Calibration Techniques and Estimate of Errors

The principal measurements obtained in the facility include the following:

1. Power
2. Temperatures
3. Flow
4. Pressures
5. Liquid Level In Dump Tank

The instruments used for these measurements, estimated measurement accuracies, and the procedures used in calibrations are as follows.

POWER MEASUREMENTS AND HEAT LOSS CALIBRATIONS

Electrical power to the preboiler heater and to the test section heater was measured with two General Electric type P-3 polyphase wattmeters, each having a rated accuracy of $\pm$ 1% of full scale. Current and voltage transformers were used to adjust the sensitivity such that the meters were always reading as nearly as possible to full scale. Although calibration data indicate that accuracies on the order of $\pm$ 0.5% of full scale can be obtained, the wattmeters were not always used with the current and voltage transformers in the same configuration as they were during the calibrations. Therefore, a value of $\pm$ 1% of full scale is judged to be the best estimate of the electrical power measurement error.

The preboiler and test section radiation shield assemblies consisted of sheets of tantalum enclosed in stainless steel cases. The temperatures of each of these cases were measured at six locations and these temperatures were used to determine heat losses using heat loss calibration data. The heat loss calibrations were performed with the preboiler and test section piping removed. Each shield assembly, enclosing its heater, was mounted in its normal position within the vacuum chamber. With the vacuum chamber evacuated, power was supplied to the heaters and the corresponding steady-state radiation shield case temperatures were measured. This procedure was repeated at several power levels and since all the power dissipated by the heaters was lost through the shields, a direct correlation of heat loss as a function of case temperature was obtained. The temperature used in the heat loss correlations is a weighted average, $\hat{T}$, of the six measured values:

$$\hat{T} \ (^\circ R) = \left[\frac{\sum_1^6 T_i^4}{6} \right]^{\frac{1}{4}}$$

where the T_i's are the six measured temperatures in degrees Rankine. The results of the preboiler heat loss test are presented in Figure 16a, and Figure 16b shows the results of the test section heat loss calibration.

TEMPERATURE MEASUREMENT

Thermocouples were used throughout the loop for temperature measurement. These measurements can be classified as either those used for general monitoring purposes or those used for data reduction. Temperatures not directly used for data reduction purposes include such items as the pump duct temperature and condenser pipe wall temperatures. None of these thermocouples were calibrated.

The temperature measurements used directly in the data reduction are:

1. Flowmeter magnet temperature

2. Pipe wall temperature at the flowmeter

3. Fluid temperature at the preboiler inlet

4. Preboiler radiation case temperatures

5. Fluid temperatures at the preboiler outlet

6. Test section outside wall temperatures

7. Test section radiation case temperatures

8. Fluid temperatures either at the test section outlet (Test Sections 1, 2 and 3) or in the test section insert (Test Sections 4 and 5)

Fluid temperatures at the preboiler inlet, preboiler outlet and test section outlet (for 1, 2 and 3) were measured with W3%Re - W25%Re thermocouples located in wells. Fluid temperature distributions along Test Sections 4 and 5 were measured with Pt-Pt-10%Rh thermocouples contained within the centerbody of the inserts.

Surface temperatures were measured with W3%Re-W25%Re thermocouples resistance welded to the surface. Figure 17 shows typical thermocouple junctions on the test section wall. A continuing problem was repeated failures of the wall thermocouples. One mode of failure was due to the relatively brittle W3%Re leg of the thermocouple lifting off the pipe surface. It was found that a small tab of 0.002-inch thick tantalum foil tacked over the junction reduced the frequency of this type of failure. However, due to the severe operating conditions imposed on the test section, wall thermocouple failures remained the chief cause of loop "downtime".

In-loop calibrations of test section thermocouples were performed as follows. With the test section mass velocity held constant at a relatively low value, the preboiler power was increased until the vapor quality of the potassium entering the test section was about 10%. Neglecting the small temperature changes due to pressure drop, the temperature of the two-phase fluid in the test section was assumed to be uniform. After the system had reached a steady-state condition, the test section heat loss was determined using the radiation case temperatures. The test section power was then increased until the electrical power input balanced the heat losses. Under these very nearly isothermal adiabatic conditions, the temperatures of all test section thermocouples closely approximately each other. Using one of the fluid temperature thermocouples as the standard, a thermocouple correction was obtained for each of the test section thermocouples by comparison with this standard.

Samples from the same spool of W3%Re and W25%Re wire were calibrated in a vacuum furnace. Initial calibrations of this kind indicated appreciable drift of about 20°F. However, after the thermocouples were "soaked" for a few hours at 2300°F, repeatability to within ± 3°F was obtained. As part of the procedure for in-loop calibrations, newly installed thermocouples were held at 2100°F for at least five hours before taking the first calibration reading, followed by two additional readings at one hour intervals to verify

absence of drift.

The most significant temperatures in the tests are those associated
with measuring the inside wall-to-fluid temperature differences for
determining the local heat transfer coefficients. Typically, for nucleate
boiling operation these temperature differences were small, in the order of
10°F. Consequently errors in the measurement of these temperature differences
are significant. A detailed analysis of the probable error in the measurements
of the wall-to-fluid temperature differences is given in Reference 41. The
results of this error analysis are given in Figure 18, which shows the
calculated probable error in the measured wall-to-fluid temperature difference
as a function of the heat flux and temperature difference.

FLOW MEASUREMENT

The flow rate was measured with a permanent magnet type electromagnetic
flowmeter. Calibration of this meter was performed by comparing the flow rate
calculated from the flowmeter output signal (using the equations in Reference 4)
with that indicated from an energy balance across the test section during all
liquid operation. The magnetic flux density of the permanent magnet, required
in the flowmeter calculation, was measured as a function of magnet temperature
and the results are presented in Figure 19. The flowmeter calibration data
are plotted in Figure 20, which shows that the flow rate obtained from an
energy balance was consistently higher than the flow rate calculated using the
equation of Reference 4. The accuracy of this calibration is dependent upon,
among other things, the accuracy of the liquid enthalpy of potassium which was
obtained from NRL data (Reference 5). Analysis of the errors indicates that
the probable error in the flow rate measurement is $\pm$ 10%.

PRESSURE MEASUREMENT

System pressures were monitored with two slack-diaphragm type pressure
transducers located upstream and downstream of the inlet throttling orifice.
The argon pressure in the dump tank was an additional indication of system

pressure, since the loop was normally operated with the dump valve open.

DUMP TANK LEVEL MEASUREMENT

The liquid level in the dump tank was measured with a resistance "J" type probe, described in Reference 1.

OSCILLOGRAPH RECORDER

During testing with Test Section No. 2 (.74" ID with helical insert P/D = 6) an eight channel Sanborn oscillograph recorder was installed to provide simultaneous readouts of pertinent system parameters. This instrument was useful in studying system stability and in the critical heat flux, transition boiling and superheat experiments.

ESTIMATE OF EXPERIMENTAL ERRORS

Based on the errors in measurement estimated for the test section and preboiler power, test section wall-to-fluid temperature differences and flow rate, the following estimated errors in the experimental data presented in Section III are believed to be representative.

Quantity	Estimated Error
Nucleate Boiling Heat Transfer Coefficients	$\pm$ 50%
Critical Heat Flux	$\pm$ 10%
Quality at Critical Heat Flux	$\pm$ 12%
Transition Boiling Coefficients	$\pm$ 20%
Film Boiling Coefficients	$\pm$ 10%
Superheated Vapor Coefficients	$\pm$ 10%
Two-Phase Friction Multipliers	$\pm$ 35%
Liquid Heat Transfer Coefficients	$\pm$ 25%

D. Operating Procedures and Limitations

The following discussion outlines the facility operating and data taking procedures and some of the limitations imposed by the system.

START-UP PROCEDURE

The procedure for getting the system back in operation after a shut-down period was as follows:

Pump-Down and Bake-Out. During shut-down periods, the potassium inventory was stored in the dump tank and the upper section of the vacuum chamber was usually in the raised position. Before starting the pump-down procedure, the surfaces were cleaned with a small portable vacuum cleaner followed by wiping with cheese-cloth soaked in acetone. The upper section of the chamber was then lowered into position and the mechanical and diffusion pumps started. The bake-out heaters, set to hold the chamber temperature at 450°F, were then turned on and the pump-down and bake-out continued for about 24 hours at which time the chamber pressure was usually down in the 10^{-7} to 10^{-6} torr range.

Loop Fill Operation. After the pump-down period, the loop was prepared for filling by first insuring that the dump valve (see Figure 1) was closed and then opening the loop vacuum line to evacuate the loop piping. The loop was filled with the bake-out heaters energized to avoid freezing of the potassium in the pipes before flow was established. Having evacuated the piping, the loop vacuum valve was closed and the dump tank was pressurized with argon. The dump valve was then opened and potassium at about 600°F was forced up to fill the loop piping. The E.M. pump was then energized to establish flow. Having established potassium flow in the loop, the bake-out heaters were turned off and the vacuum chamber pressure would decrease to the 10^{-8} to 10^{-7} torr range with a potassium temperature of about 600°F.

Initiation of Boiling. The usual procedure for initiation of boiling was to first set the flow rate and system pressure at the values required for the test. The system pressure was set by the pressure in the dump tank with the dump valve open. This valve had to be open during boiling initiation (to provide an expansion volume for the potassium) and was usually left open even during boiling operation. Boiling was then initiated by increasing the test section power until the fluid temperature at the test section outlet reached the saturation temperature corresponding to the pressure at that point. (More detailed descriptions of the system instability associated with boiling inception are given below in the "stability limitations" section and in the "Experimental Results" section). Increases in test section and/or preboiler power caused increases in surface temperatures which in turn increased the outgassing rate with a resultant increase in vacuum chamber pressure. The magnitude of the chamber pressure rise depended on how fast the temperatures were increased. The usual procedure was to increase loop temperatures such that the chamber pressure did not exceed about 5×10^{-6} torr.

After high temperature boiling conditions (say 1800°F) were reached and testing began, the chamber pressure would slowly come down to the 10^{-7} to 10^{-6} torr range over a period of two or three days. In going from 1800°F to 2100°F test conditions, the chamber pressure would again rise at a rate dependent upon how fast the temperature was raised. Again, the policy was to keep the chamber pressure below 5×10^{-6} torr during the temperature increase. Once the higher temperature condition was reached, the chamber pressure would come down to the 10^{-7} to 10^{-6} torr range. If testing continued at any one temperature for long periods (about one week), the chamber pressure would get down in the 10^{-8} to 10^{-7} torr range.

OPERATION WITH NET VAPOR GENERATION

The general procedure during operation with net vapor generation was to hold the saturation temperature, the flow rate and the test section heat flux

constant while a series of data points were obtained at various vapor
qualities by increasing or decreasing the preboiler power. The first
point of such a series was usually taken with the preboiler power
adjusted to give a test section outlet quality of about 10% to 30%. The
preboiler power was then increased in increments of test section exit quality
of about 5% to 10%. If the system remained stable, this procedure was
continued until onset of the critical heat flux condition, as manifested by
either an abrupt increase in the test section wall temperature or by
relatively large wall temperature oscillations.

The operating procedure beyond the critical heat flux condition varied,
depending on the behavior of the test section wall temperature. At
relatively high test section heat fluxes ($\geq$ 150,000 Btu/hr-ft^2), when the
critical heat flux conditions occurred the wall temperature would rise
rapidly toward excessively high levels. If this occurred, the test section
heat flux was quickly reduced (either manually or with an automatic power
trip) until the wall temperature dropped down to an acceptable value, in
order to protect the test section from damage. The test series was then
continued, as described above, at this lower heat flux. In this case (low
heat fluxes), it was sometimes possible to continue to increase the exit
quality and to obtain data in the transition boiling, film boiling and
superheated vapor regimes by increasing the preboiler power.

Whenever possible, the general data taking procedures outlined above
were followed. Deviations from these procedures were sometimes necessary
due to either facility or stability limitations.

FACILITY LIMITATIONS
The limitations of the facility can be visualized with the aid of
Figure 21. This is a plot of the net power input to the fluid vs. the fluid
temperature at the test section outlet.

Since the radiating surface area of the condenser was fixed, the maximum heat load is determined by the temperature of the piping which, for this discussion, is assumed equal to the fluid temperature in the piping. For a saturated two-phase mixture at a given temperature at the inlet, the condenser becomes limiting when the outlet reaches saturation (neglecting temperature changes due to pressure variations). When this condition occurs, the pump "vapor locks" and violent flow oscillations result. One point on the condenser limit curve of Figure 21 was determined experimentally at a saturation temperature of 1800°F and corresponding power of 50 KW. The curve itself is a T^4 line drawn through this experimental point.

The fluid temperature limit of 2100°F is determined by the maximum permissible test section wall temperature. The wall temperature depends on the fluid temperature, the test section heat flux and on the heat transfer "regime" (i.e., nucleate boiling, film boiling, etc.). For this discussion, the maximum fluid temperature is taken as 2100°F, although at very low heat fluxes it is possible to exceed this fluid temperature without exceeding the test section wall temperature limit.

The maximum combined heater limit is determined from the preheater, preboiler and test section heater limits. This has been determined to be about 80 KW net thermal power to the fluid (about 105 KW gross electrical power).

The cross hatched area of Figure 21 represents the region outside of which it was impossible to operate. Whether it is possible to operate at a point inside this area depends upon, among other things, the system stability.

STABILITY LIMITATIONS

Within the envelope of facility or equipment limits discussed above, the range of permissible operating variables was further limited by

instabilities which are common in two-phase flow loops. Although it was possible to obtain a considerable body of data under stable conditions, the problem of stability imposed rather severe limitations on the operation.

The general problem of instability in two-phase flow systems is extremely complex, as evidenced by the considerable time and effort consumed in attempts to predict the onset of an instability and the subsequent behavior of a system. It was beyond the scope of this investigation to study the general problem of stability in two-phase flow systems. What is included here is a qualitative description of some of the instabilities encountered. Also, the results of some experiments designed to study certain types of instability are included in the "Experimental Results" section.

Perhaps the best way to describe some of the instabilities which were encountered is by considering the sequence of events during a typical test run in which the system pressure and flow rate are held constant:

1. Initially, with no power applied to the system, the fluid is all liquid with a steady flow rate and pressure.

2. The usual procedure was to next bring the test section heat flux up to the required level. As the test section power was increased, the fluid temperature at the boiler exit approached the saturation temperature corresponding to the pressure at that point.

3. Further increases in test section power, above that required to increase the outlet fluid temperature to saturation, usually resulted in superheating of the liquid. During the superheating process, the flow and pressure remained essentially constant as the liquid temperature rose above the saturation temperature.

4. Finally, a "critical" liquid superheat was reached at which the liquid "flashed" and the fluid temperature dropped sharply to saturation. The amount of liquid superheating was found to be a function of the mass velocity, heat flux, test section geometry and a rather strong function of saturation temperature, with values ranging from about 50°F at T_{sat} = 2100°F to 350°F at T_{sat} = 1500°F. Simultaneous with the liquid flashing, a sudden decrease in flow was usually observed, accompanied by dump tank pressure and level oscillations. The flow would then oscillate a few times and the fluid would begin to resuperheat. If no further action were taken, this cyclic process would continue indefinitely. A more detailed discussion of this "boiling inception" instability is given in the "Experimental Results" section.

5. Following the instability associated with boiling inception, the behavior of the system with increasing power was dependent upon several variables, the most significant of which were the saturation temperature and the flow rate. In general, the system tended to become less stable as the saturation temperature was reduced. For example, at T_{sat} = 2100°F, instability problems were relatively minor, whereas at T_{sat} = 1500°F it was almost impossible in this system to obtain stable boiling conditions. A saturation temperature of 1800°F was the practical lower limit for reasonably stable boiling tests. Also, system instability became more of a problem as the flow rate was decreased. This effect was dependent on the amount of throttling in the orifice upstream of the preboiler. For the range of orifice sizes used, a test section mass velocity of about 16 lb/sec-ft^2 was the practical lower limit for stable boiling tests.

6. As the power was further increased, at a vapor quality of about 10% to 20% (typical for T_{sat} = 2100°F and $G \geq$ 16 lbs/sec-ft^2) stable boiling would begin, as indicated by the flow rate, loop

temperatures, loop pressure and dump tank level all becoming relatively steady.

7. Stable boiling continued as power was further increased. Usually at this time, the required test section heat flux had been set and the power was increased with the preboiler. With each power increase, the boiling boundary moved upstream toward the test section inlet.

8. As the boiling boundary approached the test section inlet, small disturbances in flow rate and pressure were usually observed, and when the boiling boundary moved from the test section inlet to the preboiler outlet, large fluctuations occurred. This was probably a result of flashing of the superheated liquid in the 10-inch unheated length between the preboiler and test section. Once the boiling inception point entered the preboiler the system again became stable.

9. When the preboiler power was increased further, the system usually remained stable (at T_{sat} = 2100°F) until the vapor at the test section outlet started to become superheated.

The above description is necessarily qualitative and is intended only to be typical. Different types of behavior have been observed depending on, for example, the rate at which the power is changed. Rapid power changes often resulted in system instability, whereas the same power change, when done slowly, resulted in a stable condition.
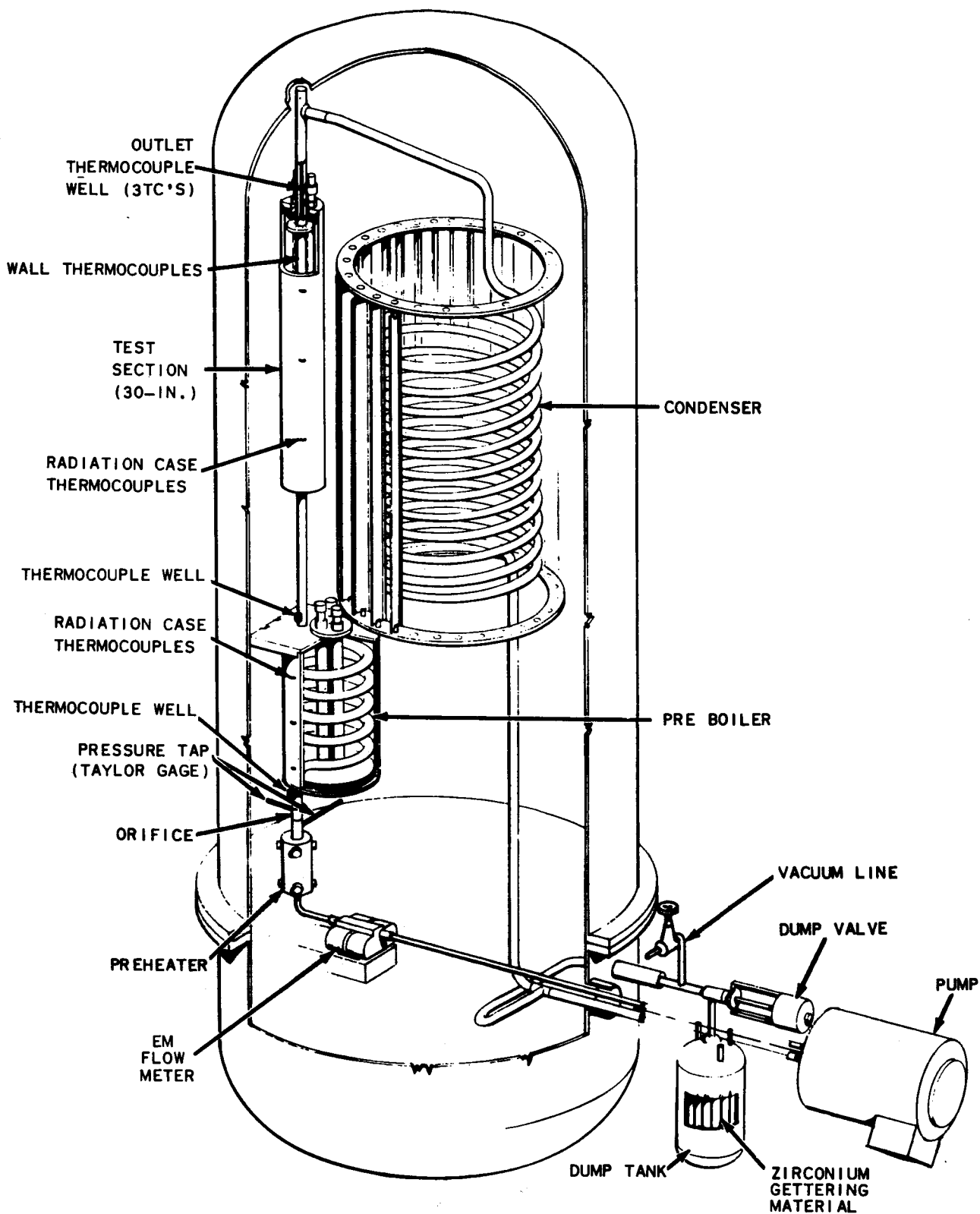
Figure 1. Cb-1%Zr HIGH-TEMPERATURE HEAT TRANSFER FACILITY
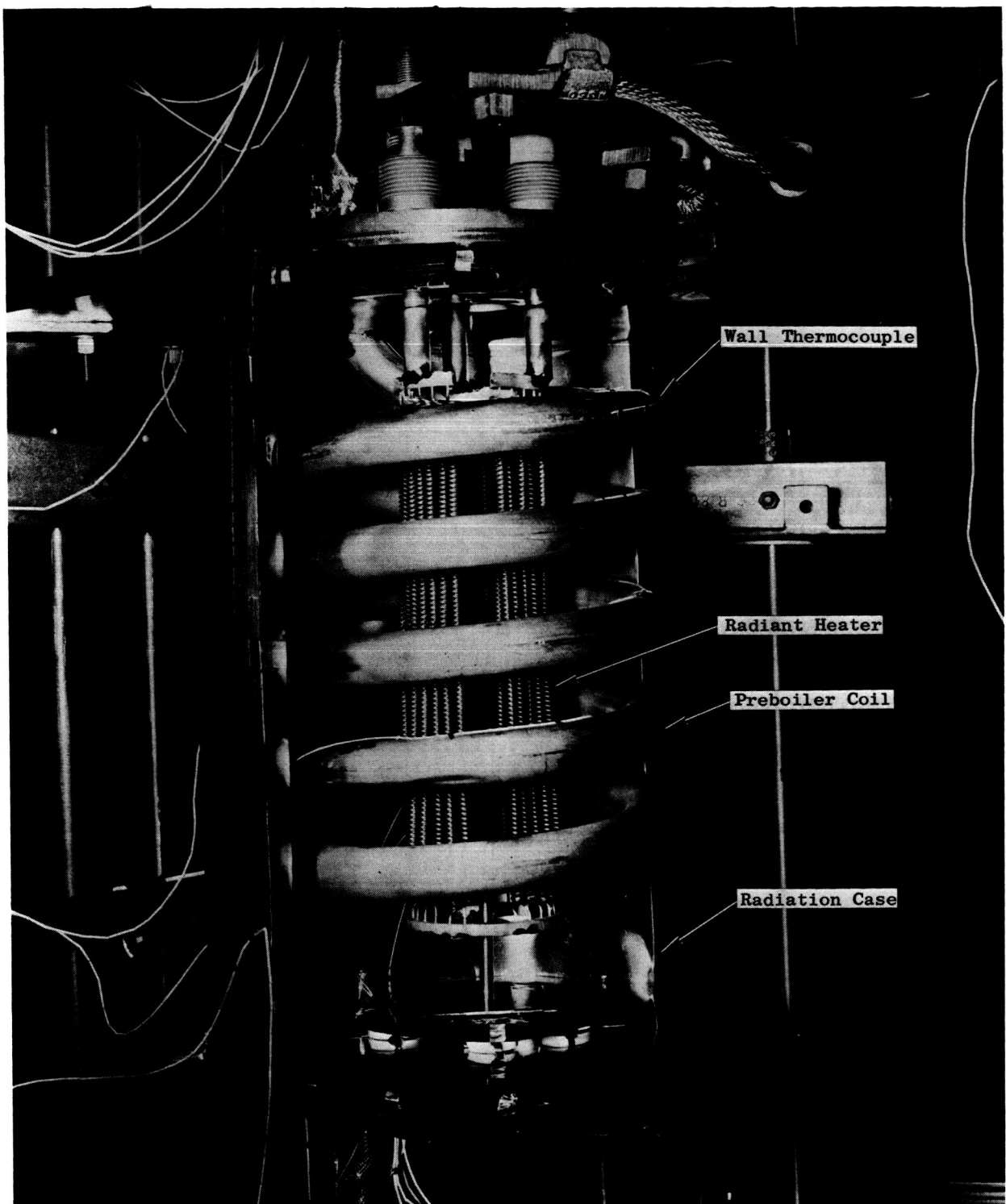
Figure 2   View of Preboiler with Half of Radiation Case Removed

Wall Thermocouples

Test Section

Radiant
Heater Rods

Radiation Case

Potassium Inlet

Radiant
Condenser Coils

Condenser
Control Shutters
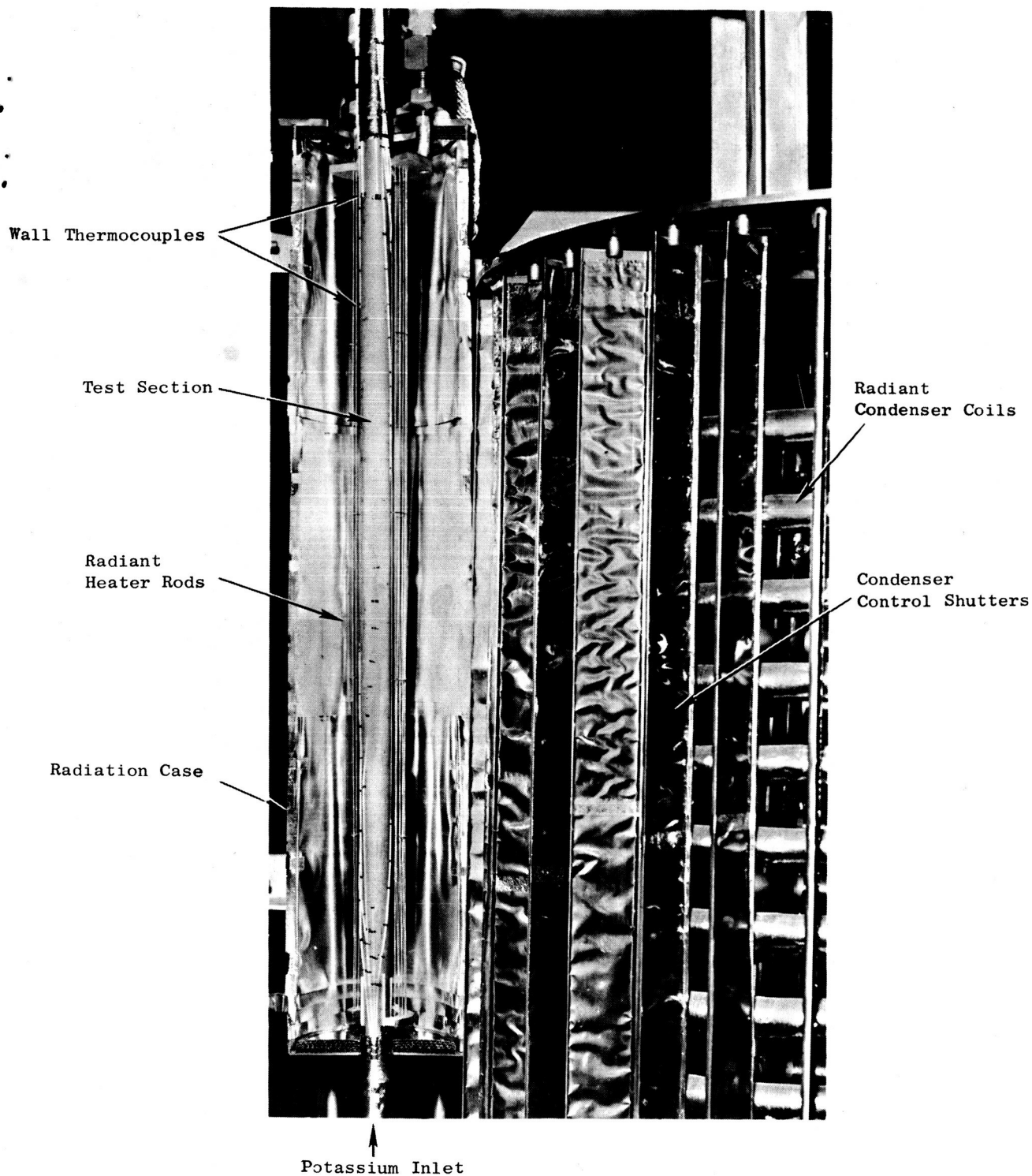
Figure 3   View of Test Section Arrangement with Half of Radiation
Case Removed
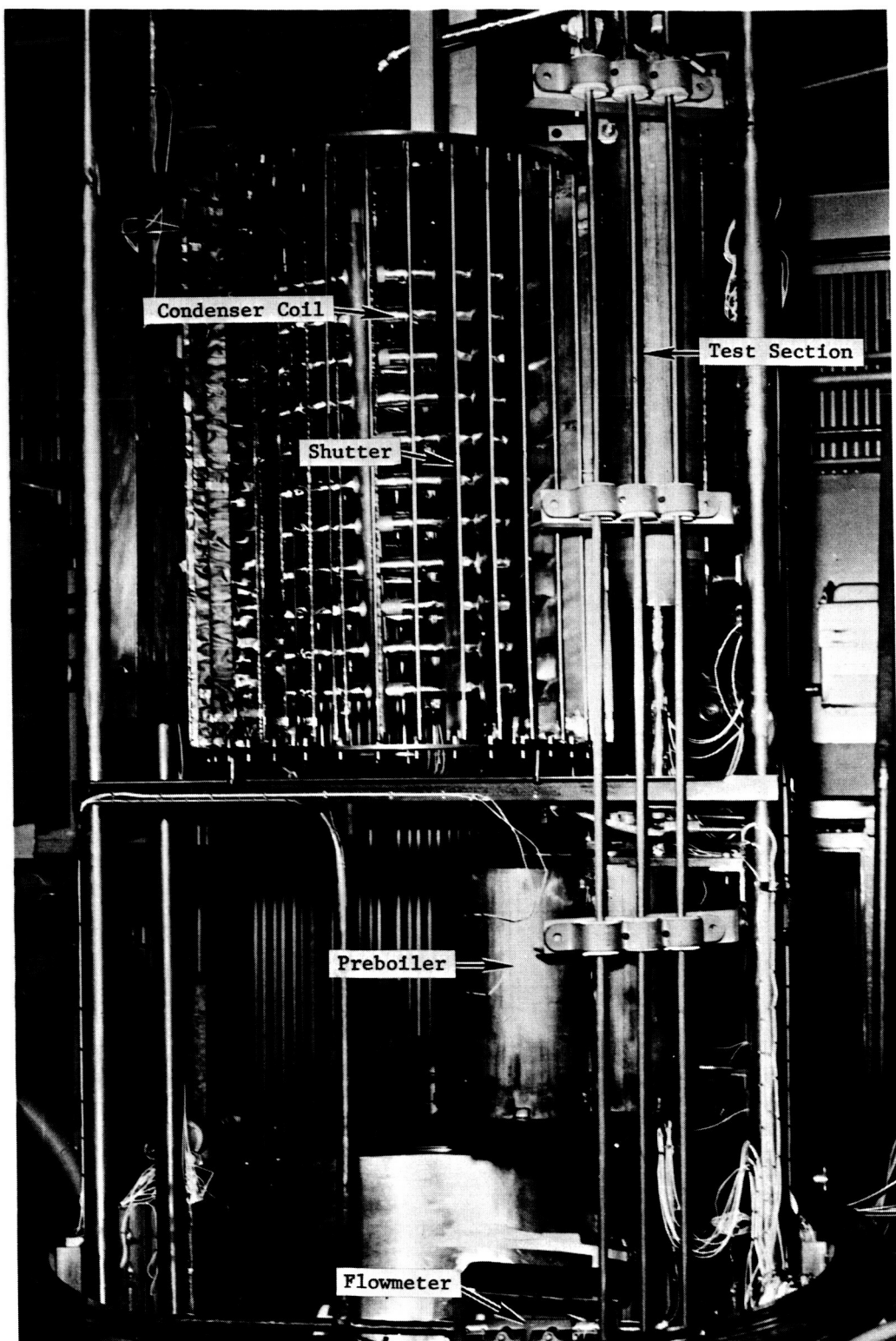
Figure 4   View of Loop Showing Condenser Coil and Shutters

T/C No.	Location	Distance, Z Inches
	Start of Heated Zone	15 1/4
20	Test Section Wall	19
21	Test Section Wall	22
22	Test Section Wall	25
23	Test Section Wall	28 1/8
24	Test Section Wall	31
25	Test Section Wall	33 7/8
26	Test Section Wall	36 7/8
27	Test Section Wall	39 13/16
31	Test Section Wall	43
32	Test Section Wall	43
	End of Heated Zone	45 1/4
33	Test Section Outlet Well	47
34	Test Section Outlet Well	47
35	Test Section Outlet Well	47

Test Section I.D. = 0.767-inch,
        No Insert
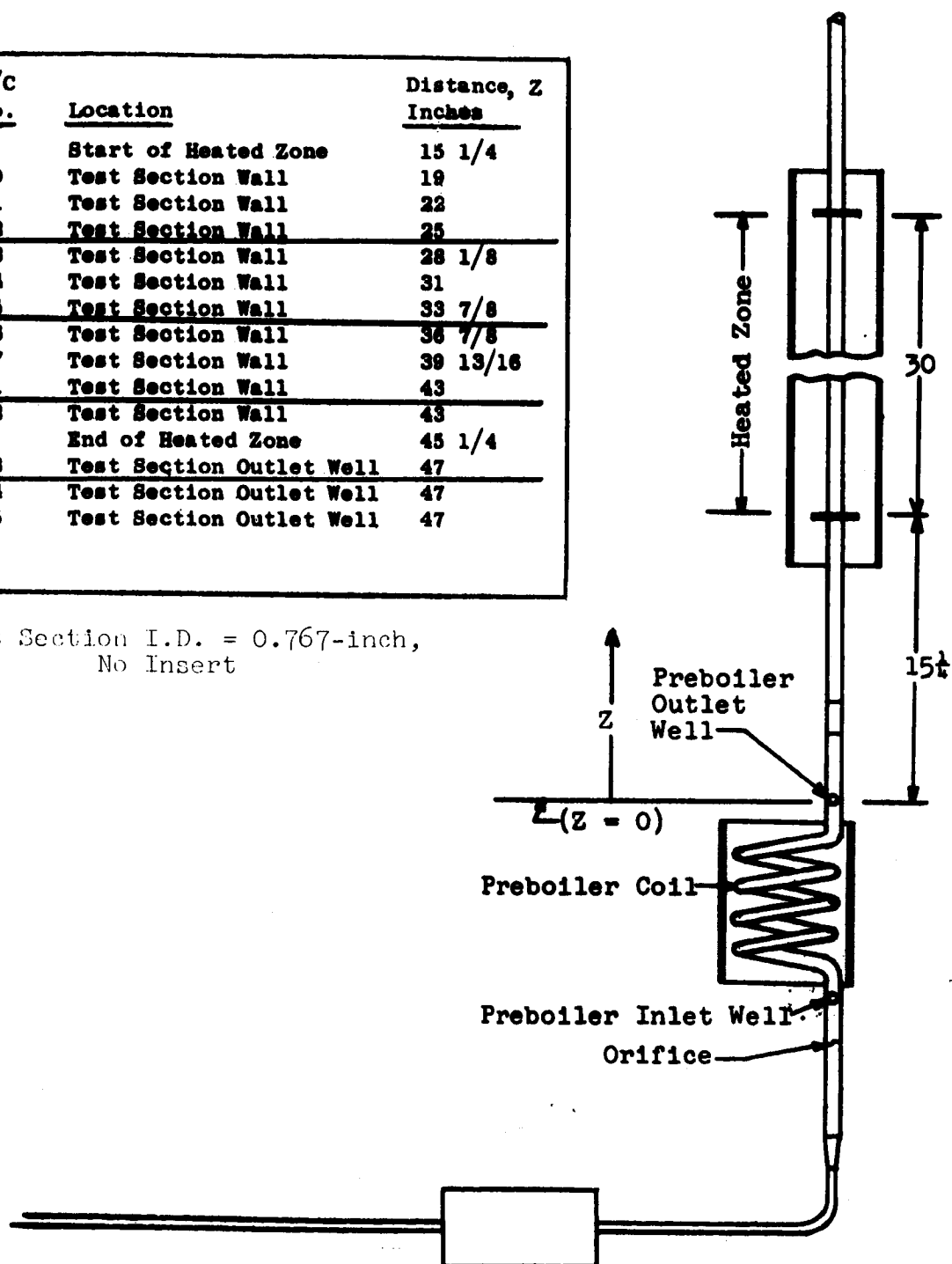
Figure 5. Sketch of Test Section No. 1 Showing Thermocouple
        Locations

T/C No.	Location	Distance, Z Inches
	Start of Heated Zone	15 1/4
20	Test Section Wall	19
21	Test Section Wall	22
22	Test Section Wall	25
23	Test Section Wall	28
24	Test Section Wall	31
25	Test Section Wall	33 7/8
26	Test Section Wall	37
27	Test Section Wall	40
31	Test Section Wall	43
32	Test Section Wall	43
	End of Heated Zone	45 1/4
33	Test Section Outlet Well	47
34	Test Section Outlet Well	47
35	Test Section Outlet Well	47

Test Section I.D. = 0.740-inch with Helical Insert (P/D = 6)
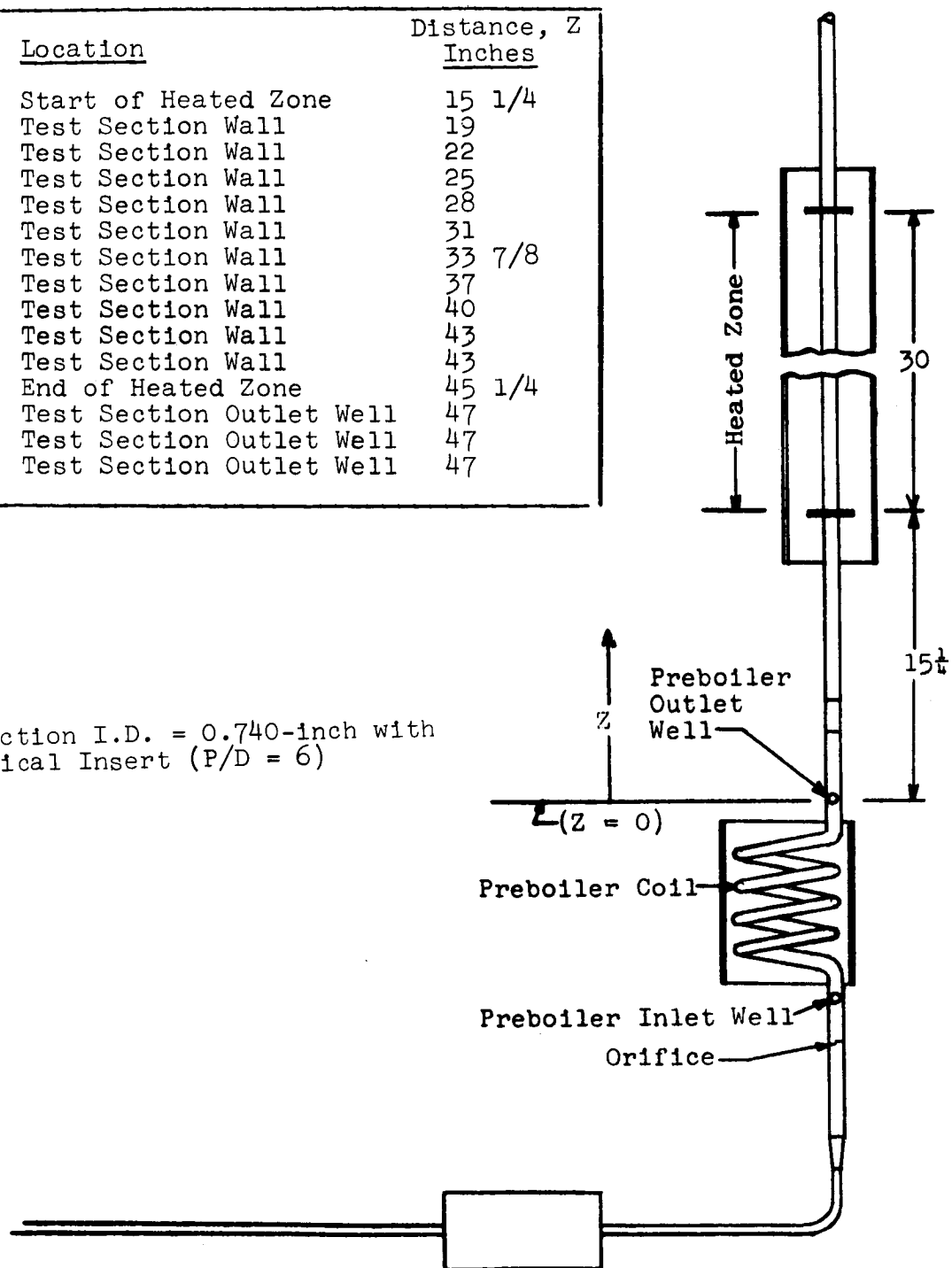
Figure 6. Sketch of Test Section No. 2 Showing Thermocouple Locations
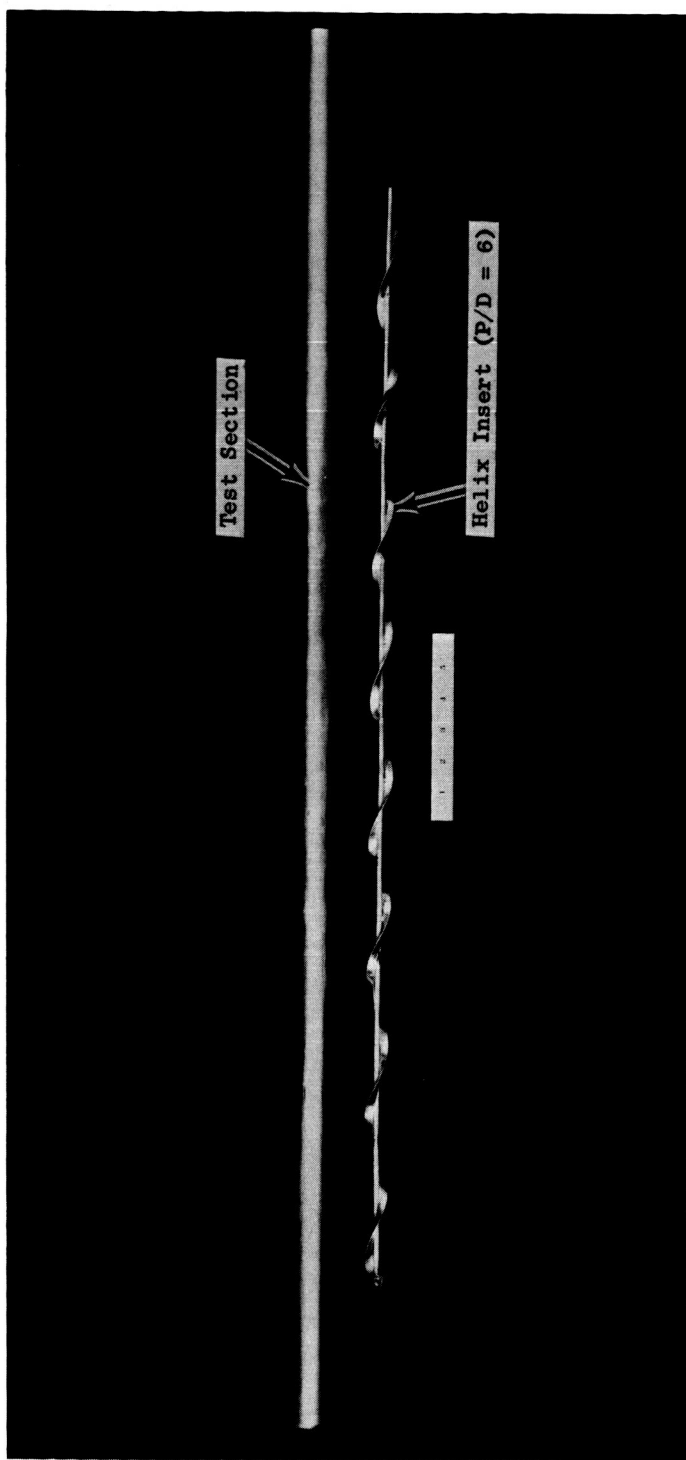
Figure 7 Test Section No. 2

T/C No.	Location	Distance, Z Inches
	Start of Heated Zone	15 1/4
20	Test Section Wall	20 7/16
21	Test Section Wall	20 1/2
22	Test Section Wall	30
23	Test Section Wall	30
24	Test Section Wall	41 5/8
25	Test Section Wall	41 5/8
26	Test Section Wall	43 3/4
27	Test Section Wall	43 5/8
31	Test Section Wall'	43 9/16
32	Test Section Wall	43 5/8
	End of Heated Zone	45 1/4
33	Test Section Outlet Well	47
34	Test Section Outlet Well	47
35	Test Section Outlet Well	47

Test Section I.D. = 0.423-inch
No Insert
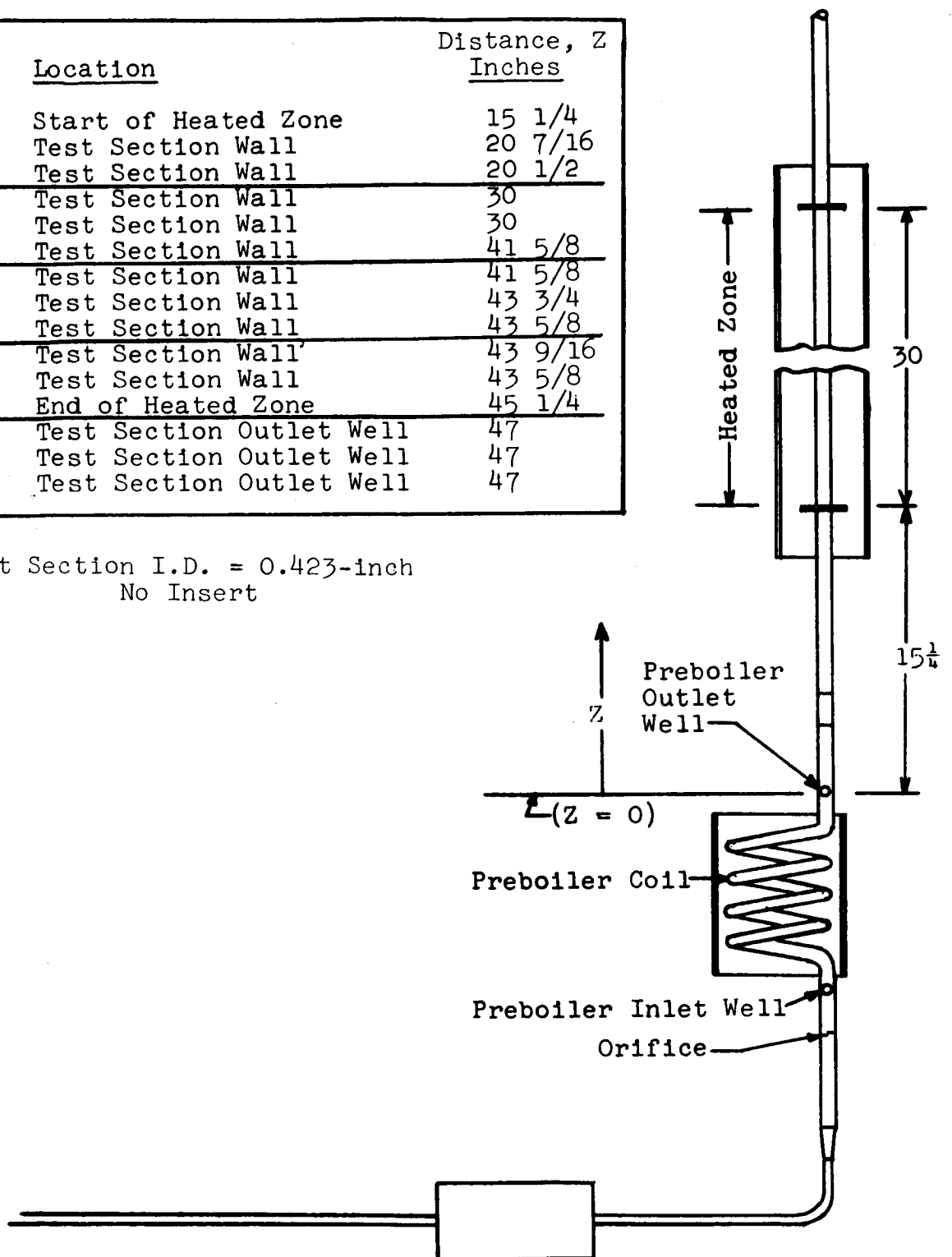
Figure 8. Sketch of Test Section No. 3 Showing Thermocouple Locations
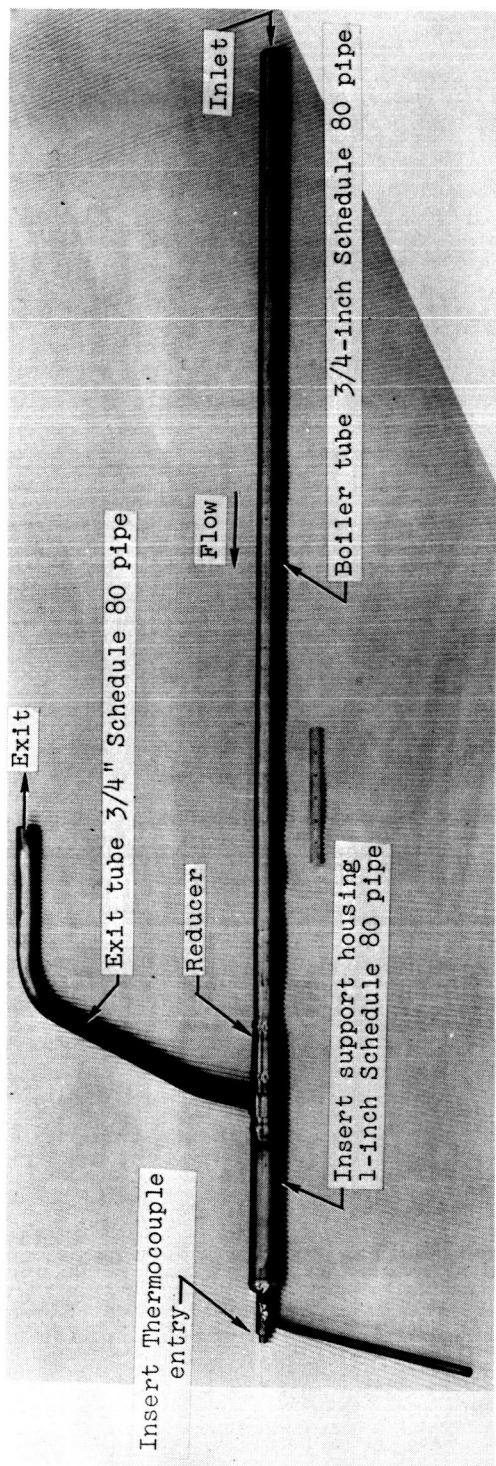
Figure 9a. Test Section No. 4 (.738 ID) with Insert Installed.
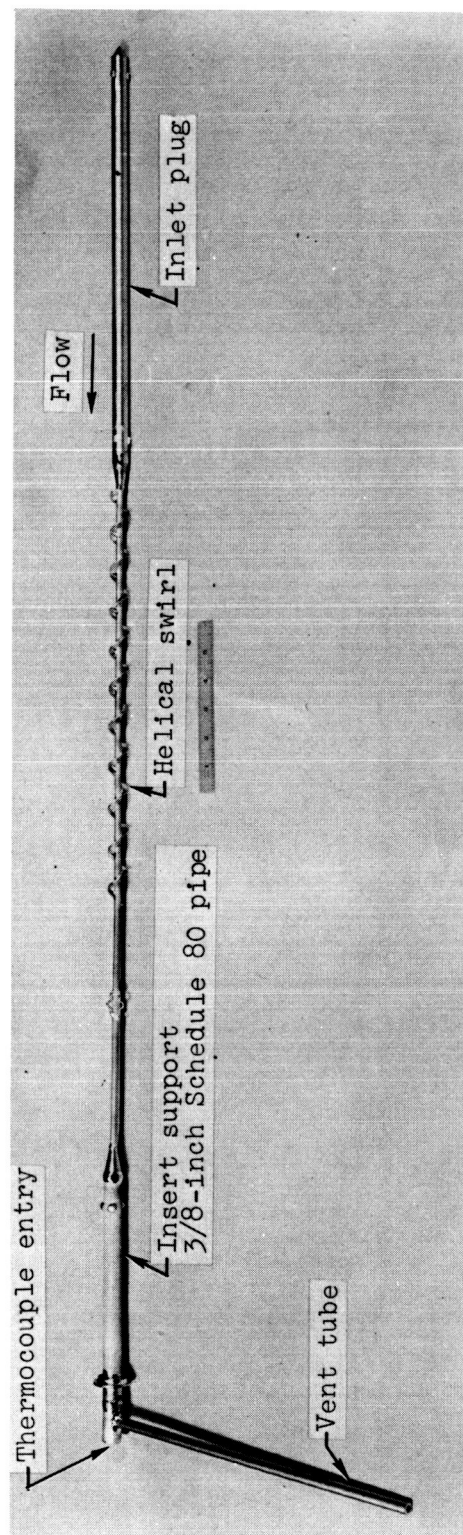
Figure 9b. Plug-Helical Insert for Test Section No. 4 (.738' ID).
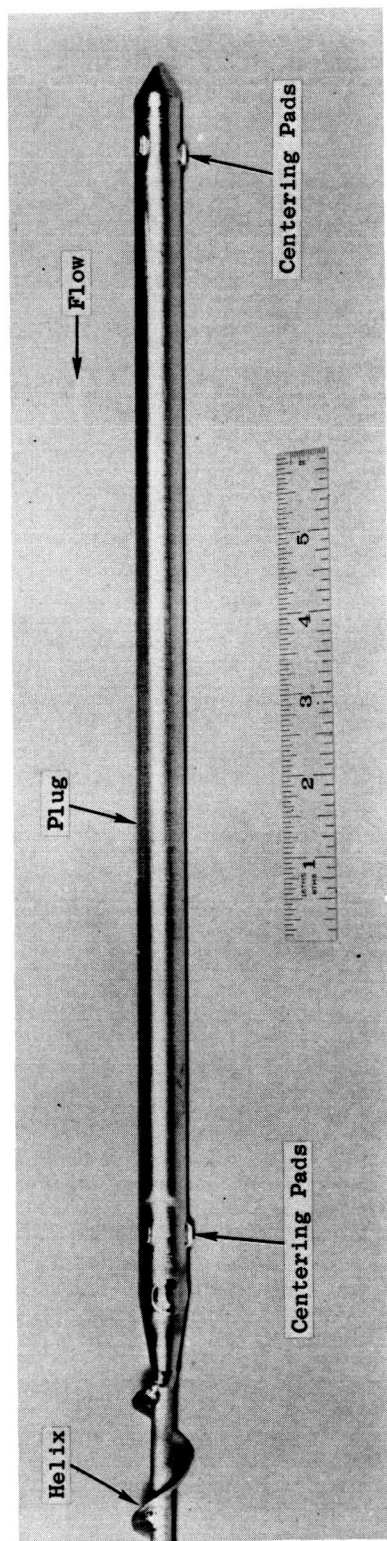
Figure 10a.   Insert Plug - - Test Section No. 4 (.738"ID).
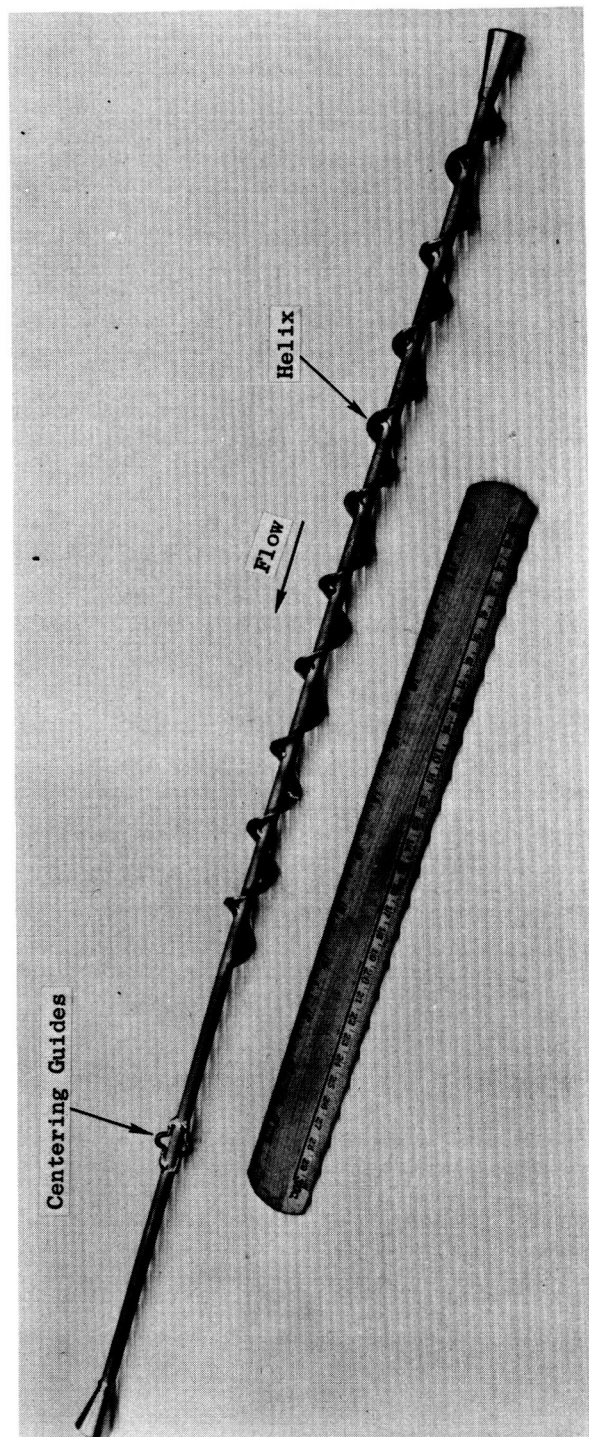
Figure 10b.   Helix Section of Insert - - Test Section No. 4 (.738"ID).
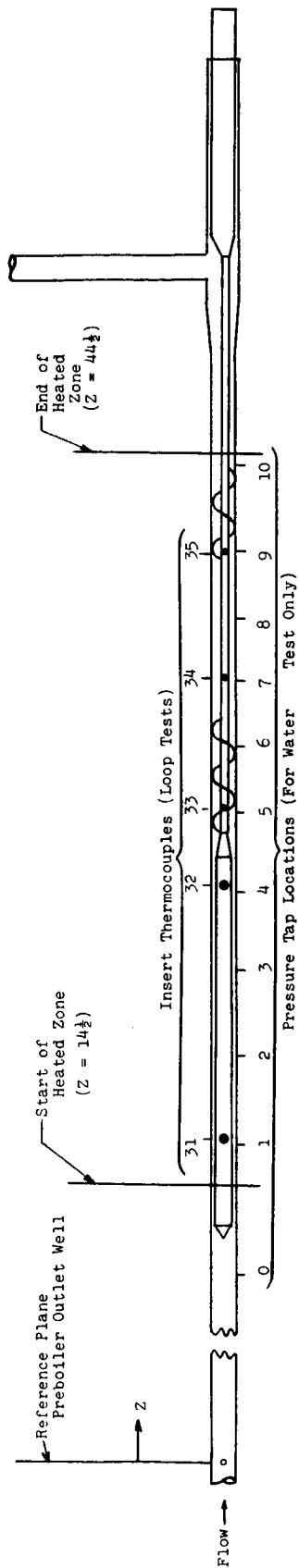
Description	Z (inches)
Preboiler Outlet Well	0
Pressure Tap 0	11 1/6
Tip of Plug	12 7/16
Start of Heated Zone	14 1/2
Pressure Tap 1	16 3/16
T/C 31	16 7/16
Pressure Tap 2	19 11/16
Pressure Tap 3	23 3/16
Pressure Tap 4	26 9/16
T/C 32	26 13/16
Pressure Tap 5	29 13/16
T/C 33	30 1/16
Pressure Tap 6	32 15/32
Pressure Tap 7	35 5/32
T/C 34	35 3/8
Pressure Tap 8	37 13/16
Pressure Tap 9	40 1/2
T/C 35	40 11/16
Pressure Tap 10	43 3/4
End of Heated Zone	44 1/2

Figure 11. Sketch of Test Section No. 4 Showing Thermocouple Locations Used For Potassium Tests And Pressure Taps Used During Single Phase Water Pressure Drop Test
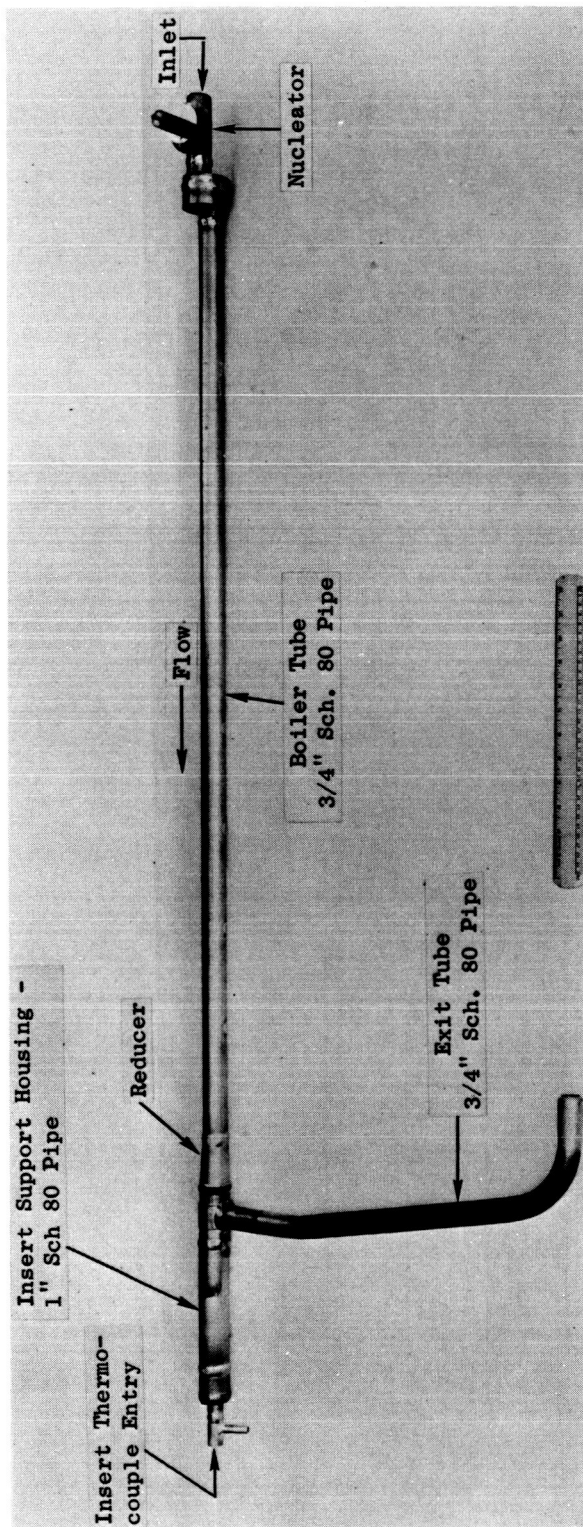
Figure 12a. Test Section No. 5 (.742"ID) with Insert Installed.
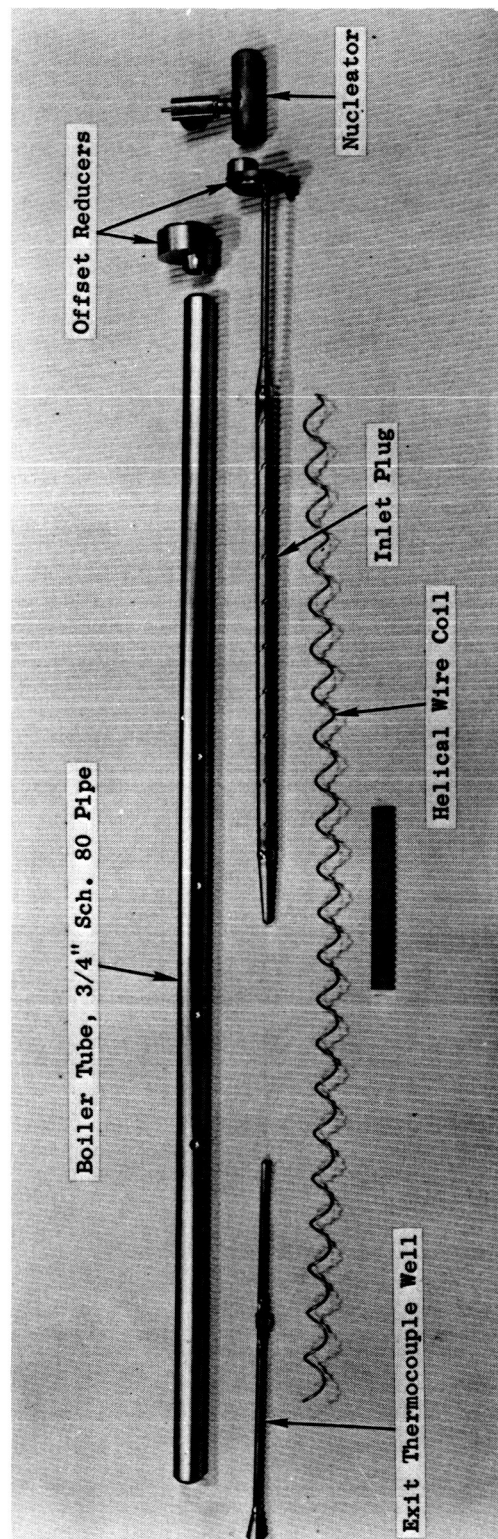
Figure 12b. Components of Test Section No. 5 (.742"ID). . . . .

-34-
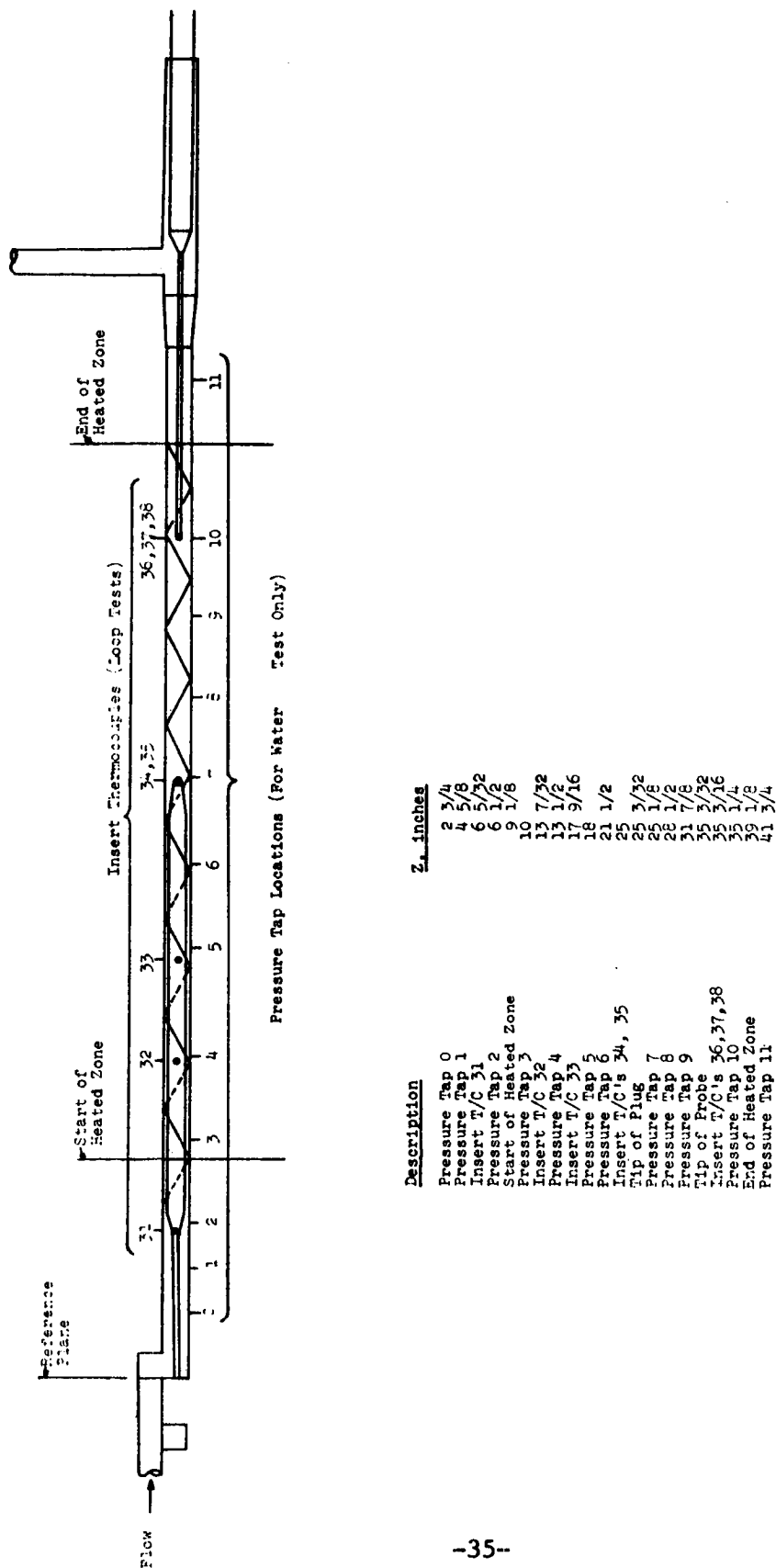
Figure 13. Sketch of Test Section No. 5 Showing Thermocouple Locations Used For Potassium Tests And Pressure Taps Used During Single-Phase Water Pressure Drop Test

-35-
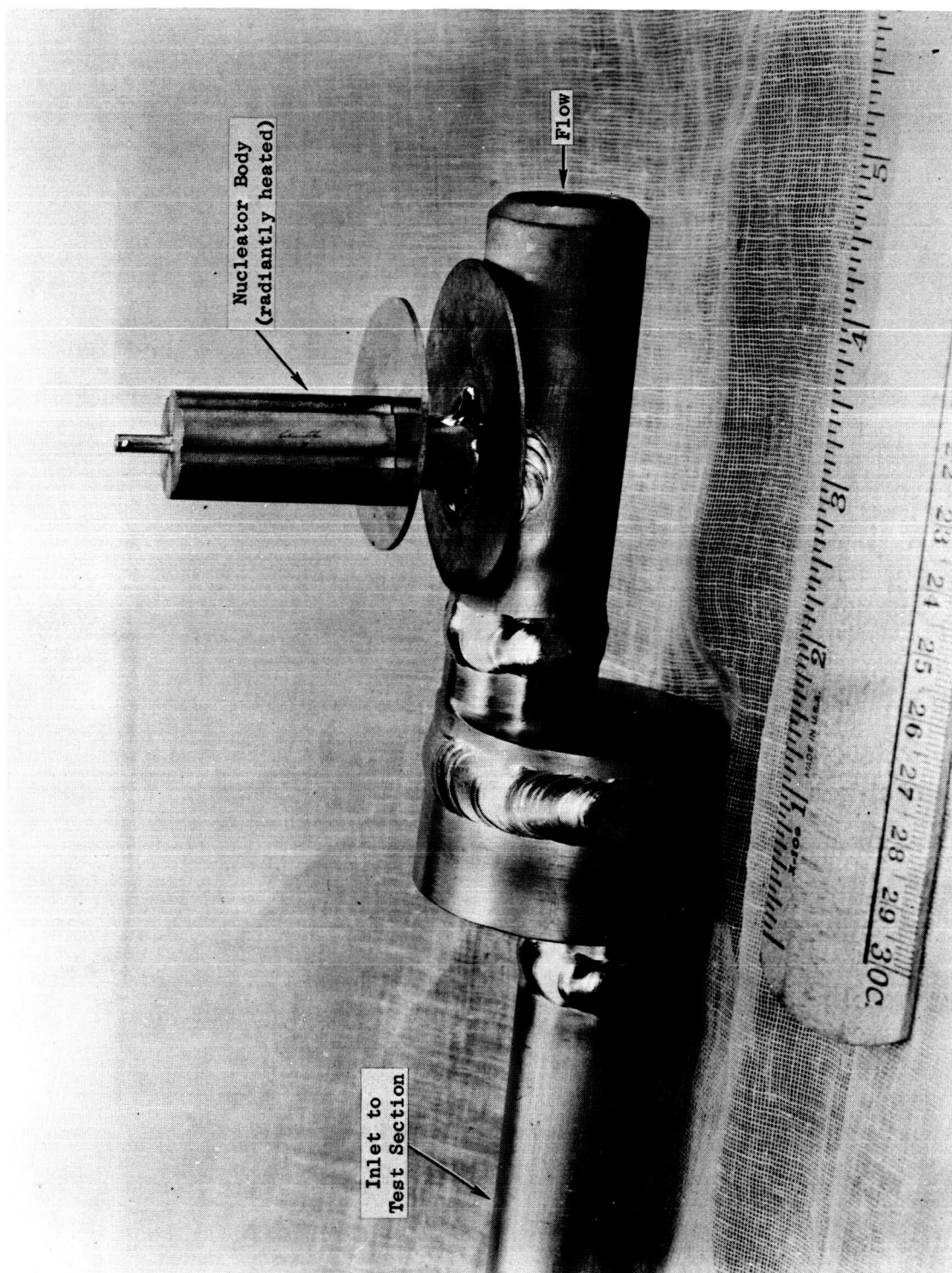
Figure 14 Boiling Nucleator without Heater Element - Test Section No. 5

Insert Thermocouple Leads

1.05" O.D. Pipe

Flow to Test Section Inlet

Heater Wire

Insulator

Radiation Shields
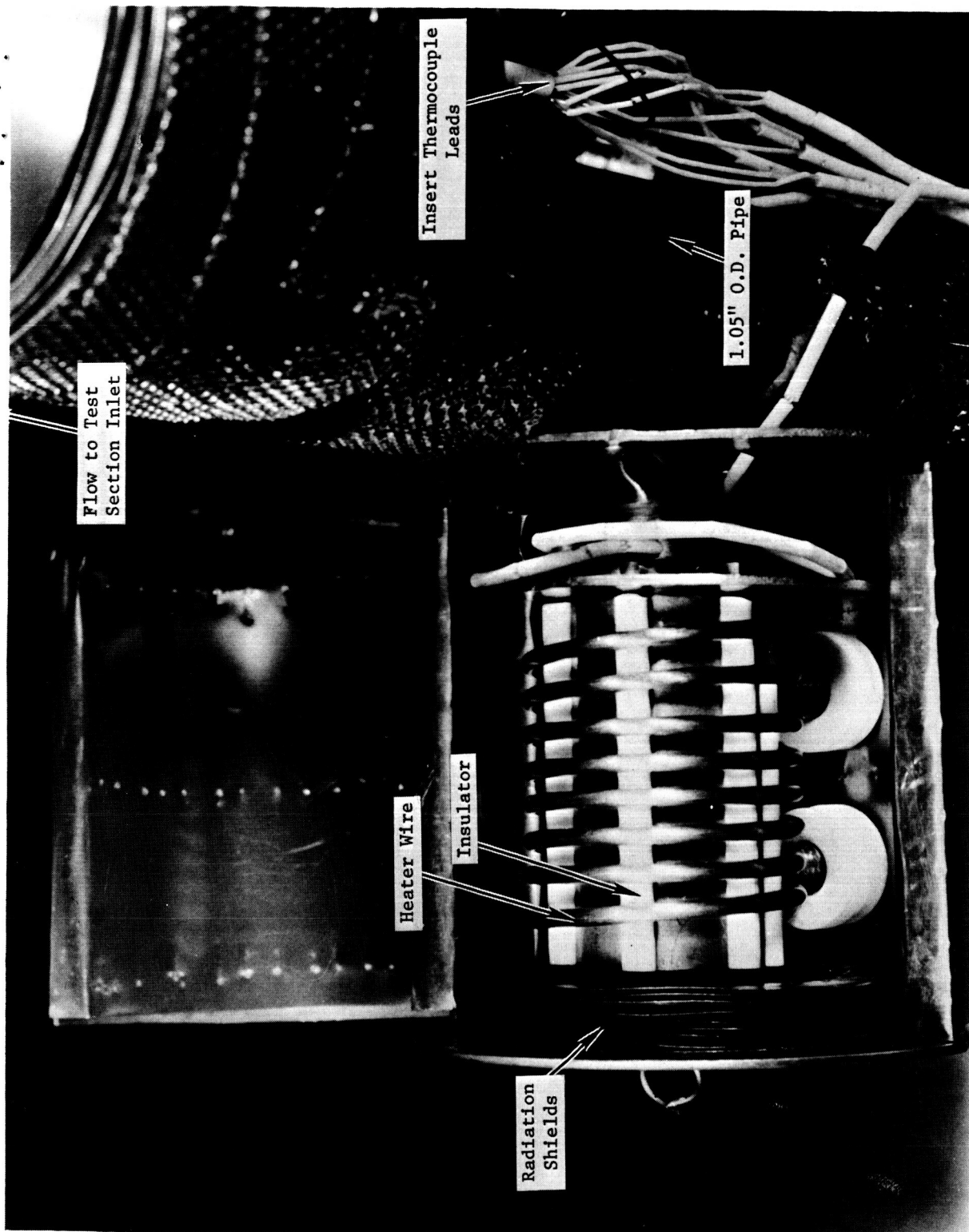
Figure 15   Boiling Nucleator with Heater Installed – Test Section No. 5

-37-
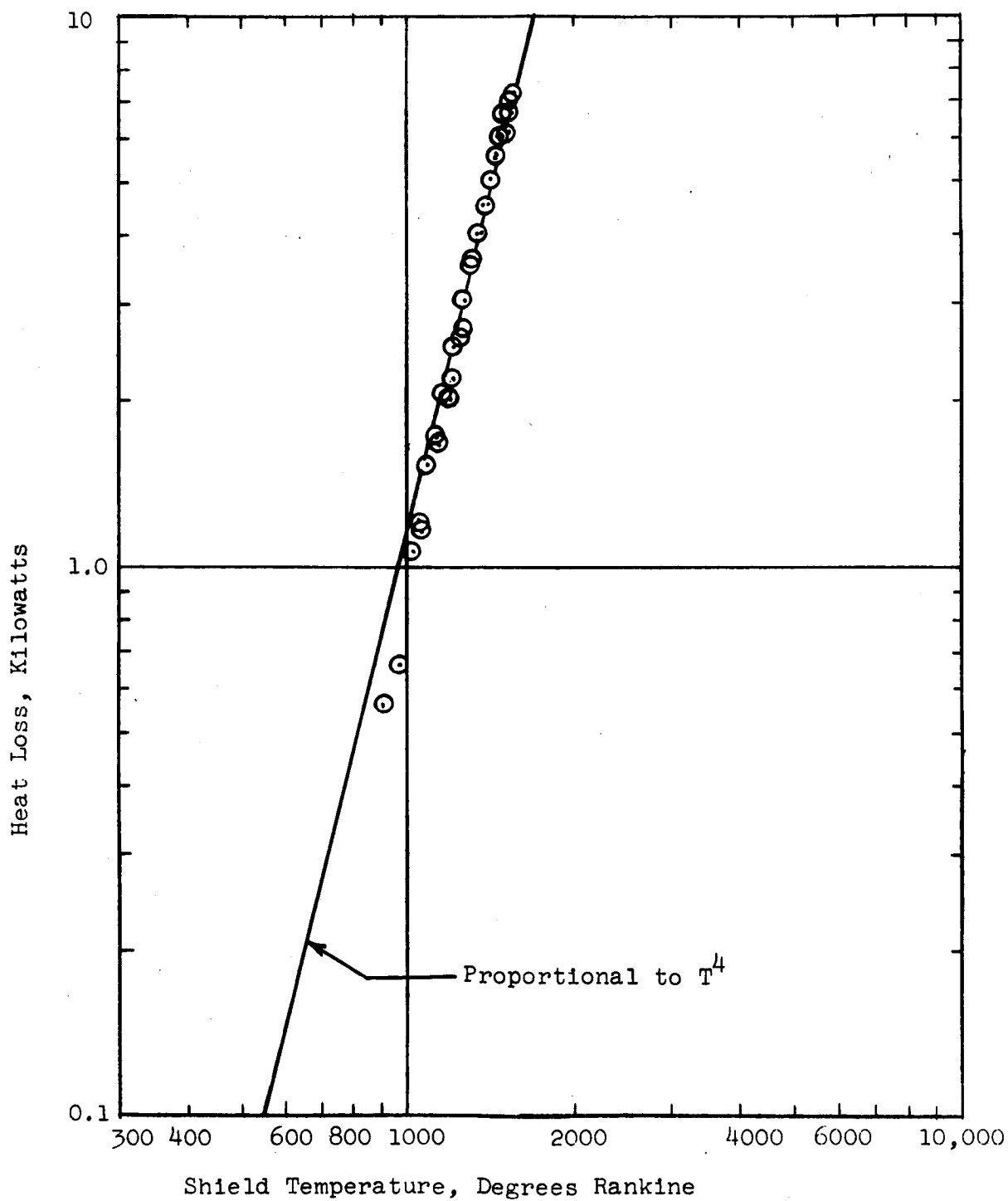
Figure 16a. Preboiler Heat Loss
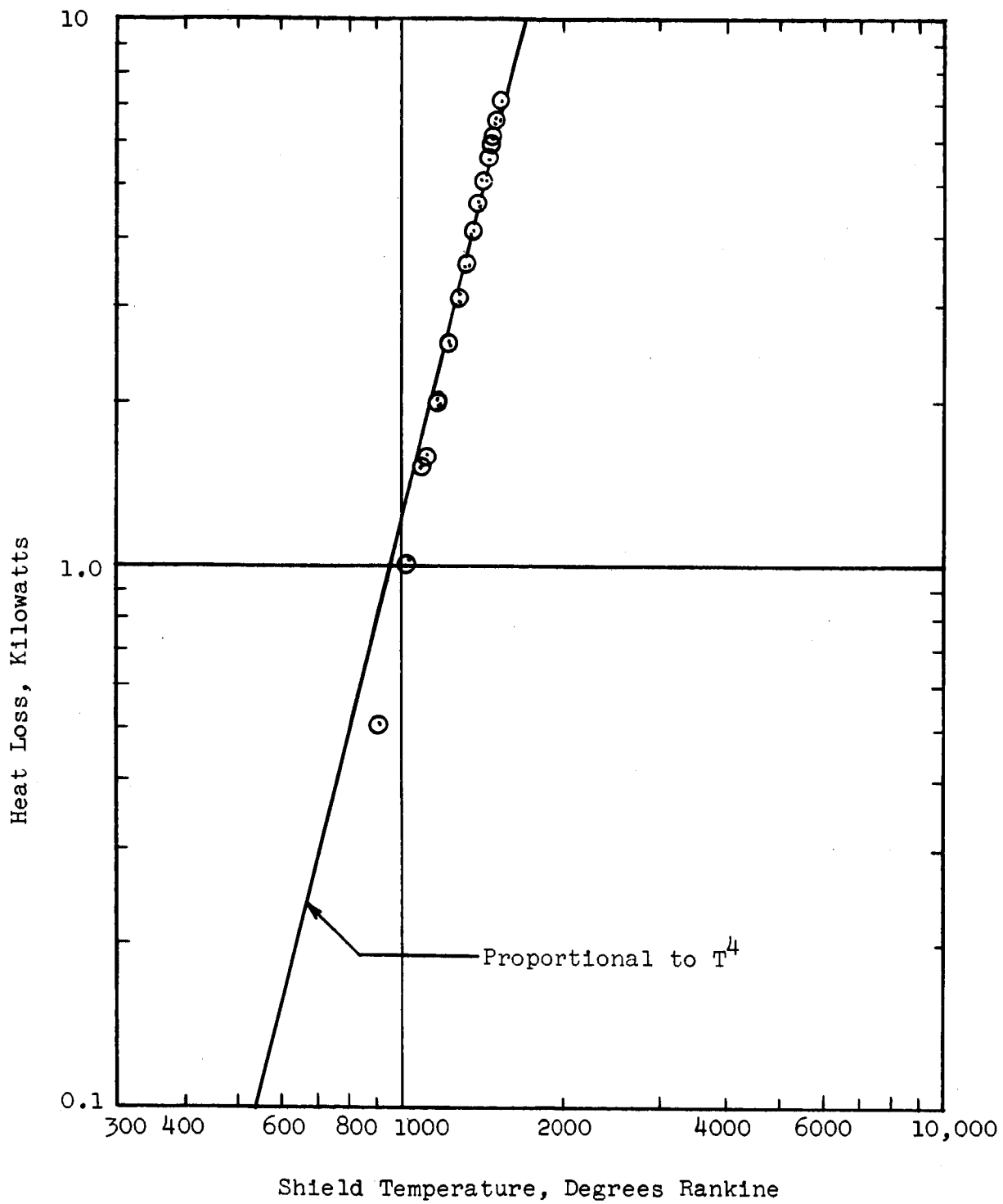
Figure 16b. Test Section Heat Loss

BeO Insulators
(1/32-in. OD)

Thermocouple Wire
(5-Mil OD)

2-Mil Thick
Tantalum Tab
Over Junction
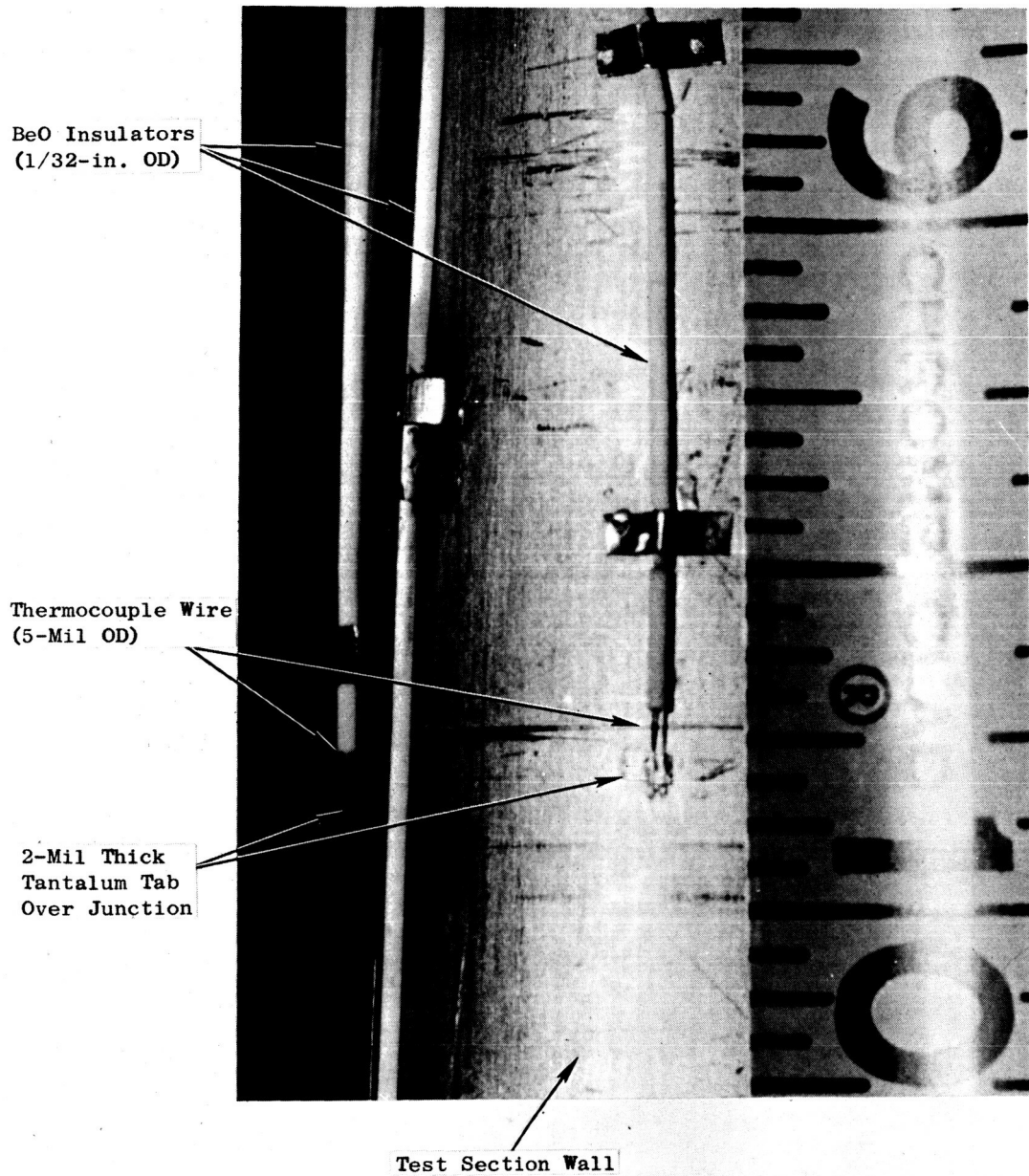
Test Section Wall

Figure 17. Wall Thermocouple Attachment on Test Section
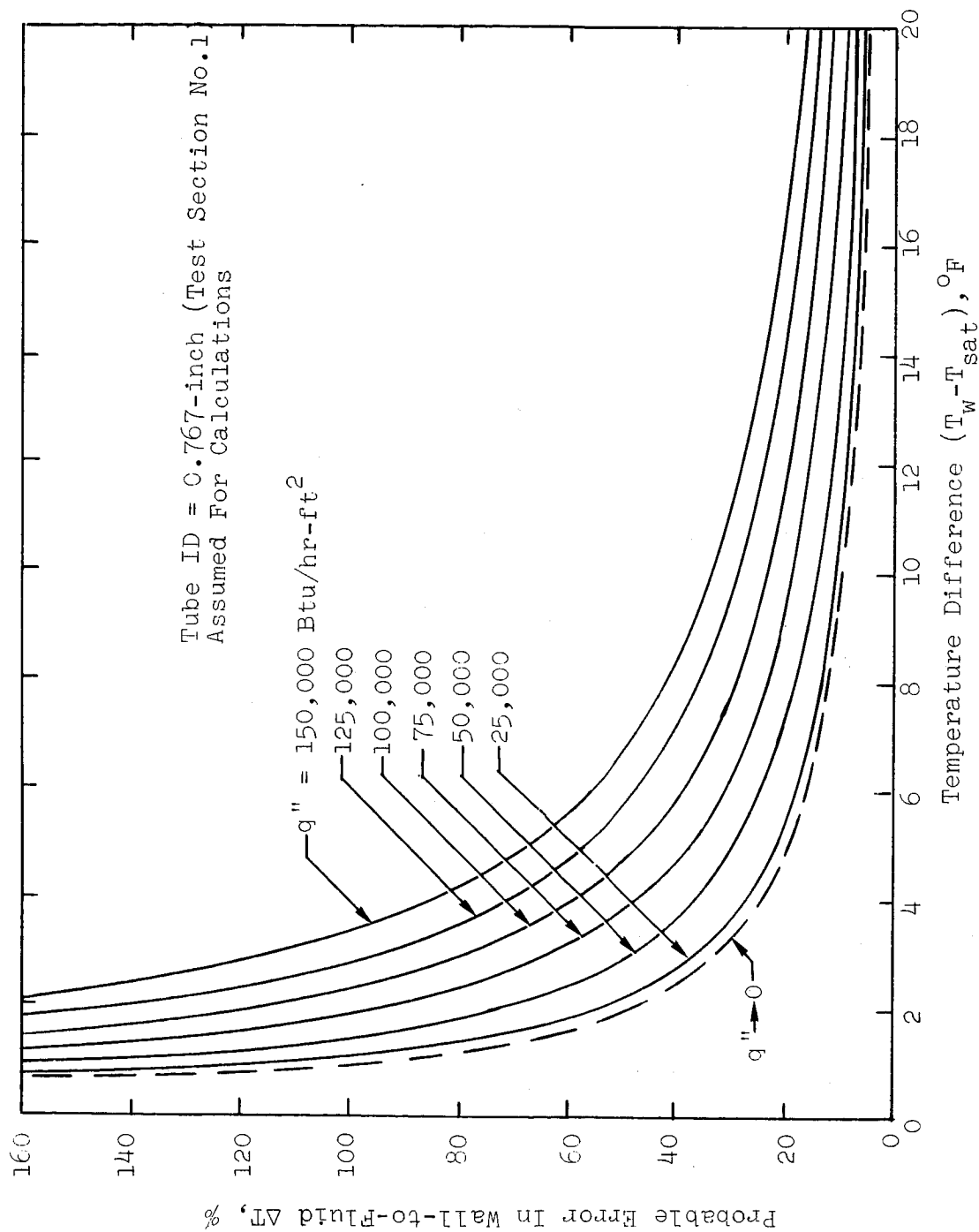
Figure 18. Estimated Probable Error In Wall-to-Fluid Temperature Difference For Boiling Heat Transfer Coefficient Tests As Function Of Heat Flux And Temperature Difference
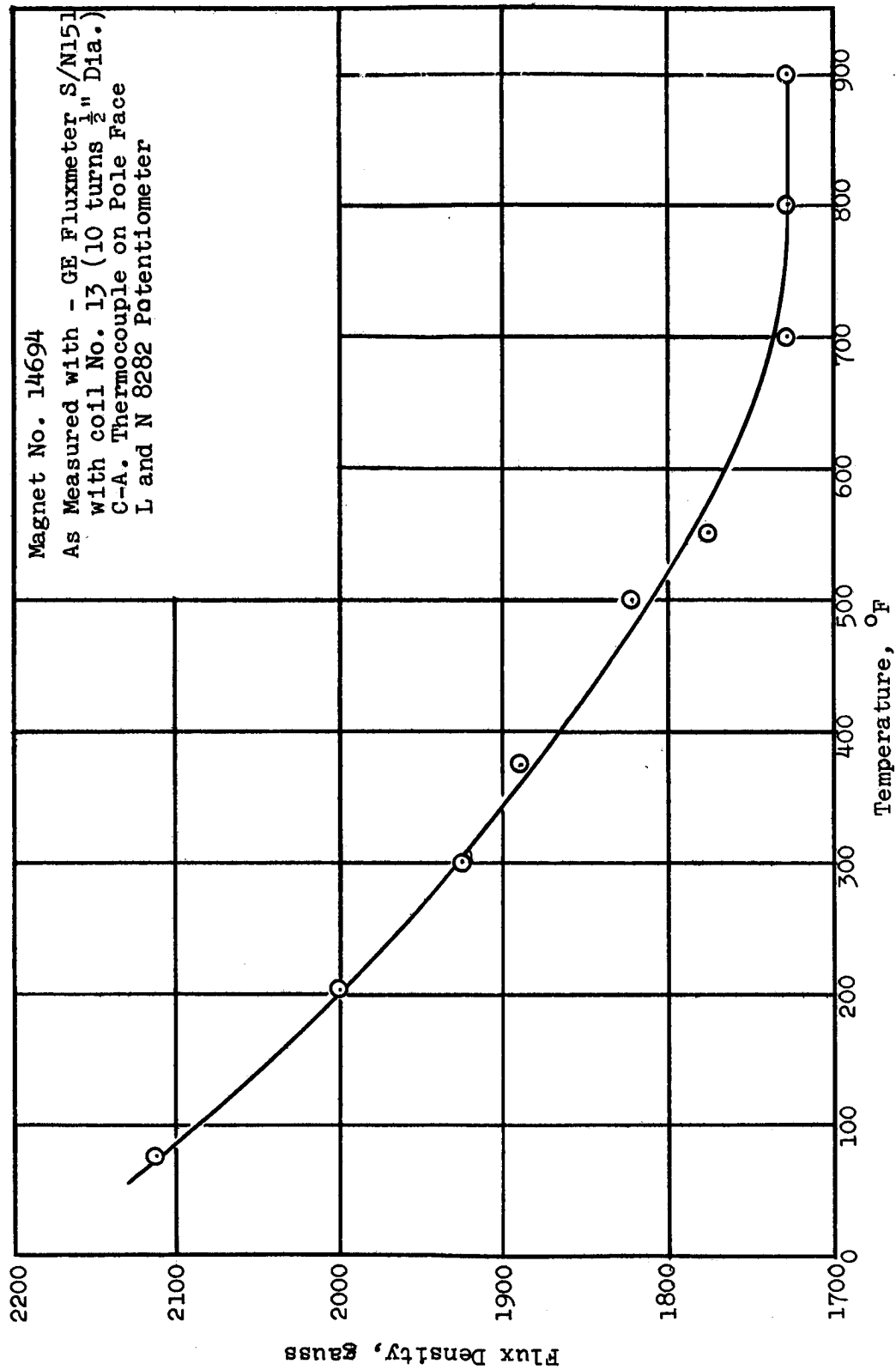
Figure 19. Flux Density vs. Temperature for the Flowmeter Magnet.

Magnet No. 14694

As Measured with - GE Fluxmeter S/N151
with coil No. 13 (10 turns $\frac{1}{2}$" Dia.)
C-A. Thermocouple on Pole Face
L and N 8282 Potentiometer
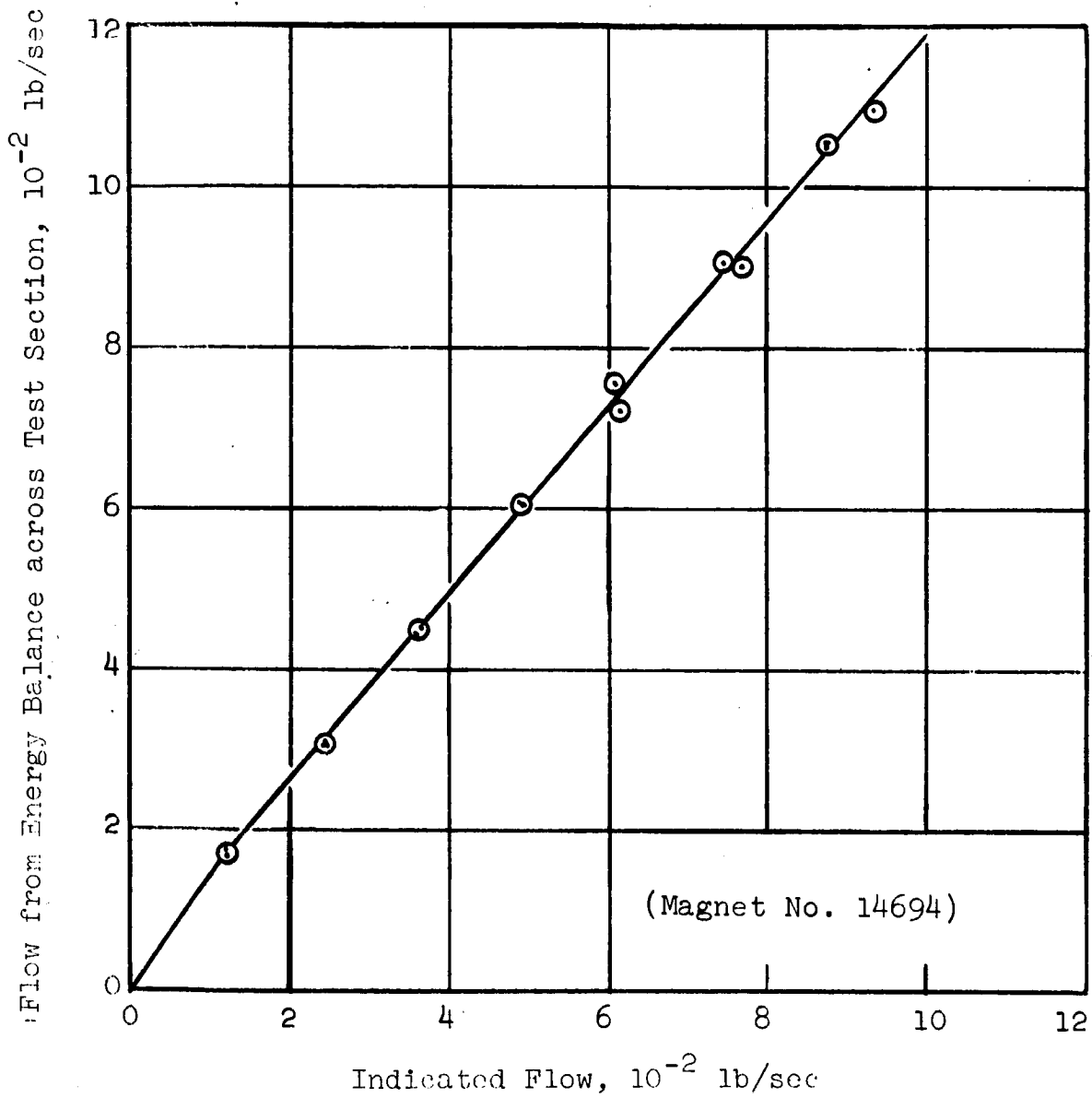
Figure 20. Flowmeter Calibration.
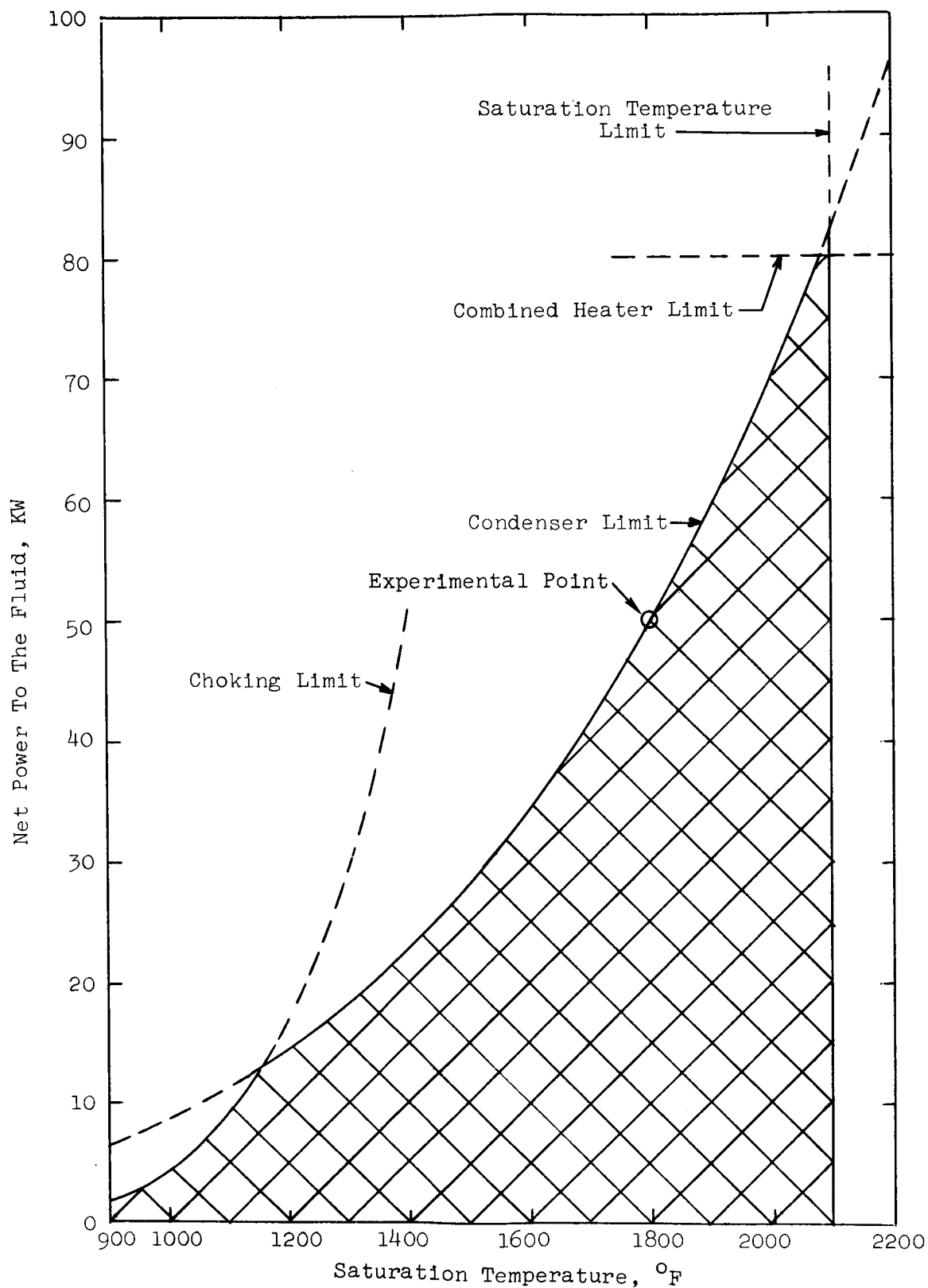
Figure 21   Overall Facility Limits

-44-

III EXPERIMENTAL TEST RESULTS AND ANALYSIS

A. Nucleate Boiling Results

Five different test sections were used in the Cb-1%Zr facility in order to obtain local heat transfer performance in a wide variety of geometries. Each of these test sections is described in Section II-B of this report. For all five test sections the results obtained in the nucleate boiling region will be presented and discussed. The data on nucleate boiling heat transfer are tabulated in Table 2.

For purposes of treating the nucleate boiling data, the tests are best considered in two separate groups. The first group consists of the plain tube (no insert) tests (Test Section Nos. 1 and 3); the second group is composed of test sections containing inserts (Test Section Nos. 2, 4 and 5).

In the plain tube tests, the measured wall to fluid temperature differences (ΔT) are quite small, in the order of 10°F, and the corresponding heat transfer coefficients are high (in the order of 10,000 Btu/hr-ft^2-°F) and exhibit considerable scatter (due to the difficulty in accurately measuring small values of ΔT). For this reason an empirical correlation of the data was not attempted, but rather an understanding of the behavior of the data was sought through the use of two relatively simple models. Using these two models, comparisons are made of measured and predicted relationships between heat flux and ΔT in an effort to gain some insight into the vaporization* process in the tubes without inserts.

---

* The terms vaporization or vapor generation are used to designate the production of vapor by either one or a combination of the following mechanisms:
  (a) Evaporation from the liquid-vapor interface
  (b) Vapor production by bubble formation at the heat transfer surface (boiling or ebullition)

The second group of data (for the test sections containing inserts) is quite different from the first. For this data the measured wall-to-fluid temperature differences are generally larger than for the plain tube data, and thus it was felt that an empirical correlation would be successful. Such a correlation is discussed subsequently in this Section.

From a design standpoint, correlation of the second group of data is more important than correlation of the first. The heat transfer coefficients for the first group (without inserts) are generally high relative to the single phase and transition boiling values and, thus will not exert an appreciable influence on boiler design. The heat transfer coefficients for the second group (with inserts) are sufficiently low that they are likely to be of significance in boiler design.

ANALYTICAL MODELS FOR TUBES WITHOUT INSERTS

In this section, the analytical models used to interpret the plain tube results will be presented and discussed. The specific area of interest is defined by the following conditions:

1. Vertical axially symmetric flow in a constant area tube with a uniform heat flux.

2. Steady flow

3. Two-phase single-component flow of potassium with net vapor generation.

4. Flow regime of the annular or annular-mist type

5. Heat fluxes less than the critical

Under the above conditions two mechanisms of vapor generation are possible, i.e., vapor generation by bubble formation and/or by evaporation

at the liquid vapor interface. In the present section, proposed methods for predicting the heat transfer coefficients for both mechanisms of vapor generation will be presented. Some of the factors which determine the mechanism of vapor generation will then be discussed.

Vapor Generation by Evaporation at Existing Liquid-Vapor Interfaces. For this case it is assumed that bubble formation is totally suppressed, and that vapor is generated by evaporation at existing liquid vapor interfaces.

The flow pattern is assumed to consist of a thin concentric layer of liquid on the wall with the remainder of the liquid entrained in the vapor core and traveling with the vapor velocity (see Sketch A below).

Sketch-A

-47-
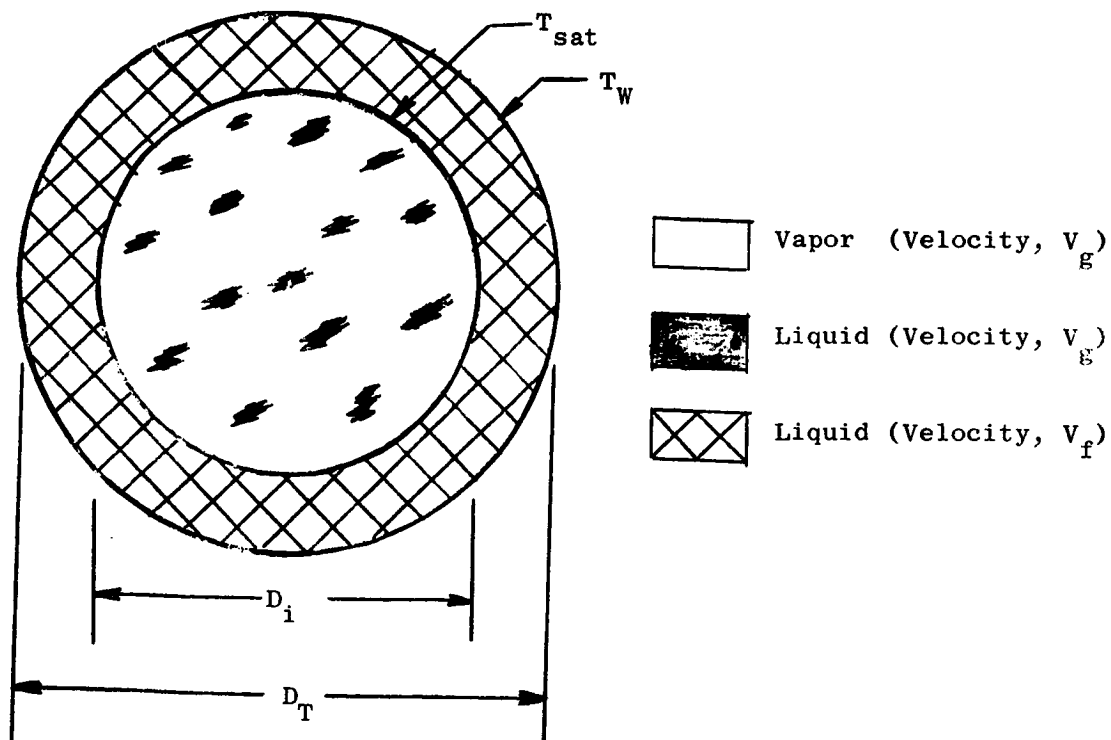
The mechanism of heat transfer is assumed to be conduction from the wall to the liquid vapor interface. Evaporation of the droplets is neglected and the interface is assumed to be at the local saturation temperature.

By utilizing the expression for conduction across an annulus with a uniform heat flux imposed on the boundary, the following equation is obtained:

$$N_{Nu} = \frac{h_{FE} D_T}{k_f} = \frac{2}{\ln D_T/D_i} \qquad (1)$$

Equation 1 may be rewritten in terms of the average void fraction and mass fraction of entrained liquid as follows (see Reference 6).

$$N_{Nu} = \frac{h_{FE} D_T}{k_f} = - \frac{4}{\ln\left[1 - (\frac{1-x}{x})(\frac{\rho_g}{\rho_f}) R_g (K-E)\right]} \qquad (2)$$

where

$$K = (\frac{\rho_f}{\rho_g})(\frac{x}{1-x})(\frac{1-R_g}{R_g}) \qquad (3)$$

and E is the entrainment (fraction of liquid flowing as droplets).

In an effort to assess the effect of entrained liquid, Equation 2 was evaluated for several values of the entrainment E with slip ratios K of one and $(\rho_f/\rho_g)^{\frac{1}{2}}$. The resulting Nusselt numbers are shown in Figure 22. From this figure it can be seen that, within the limitations of the model chosen, the effect of entrainment is significant only for small values of the slip ratio, i.e., for slip ratios of order one.

In order to obtain an estimate of the slip ratio, the momentum exchange model (Reference 7) was used. In this model the relationship between quality and void fraction is given by the equation:

$$\frac{(1-x)^2}{(1-R_g)} + \frac{x^2}{R_g}\,\frac{\rho_f}{\rho_g} - \frac{1}{2}\,\frac{(1-x)^2}{(1-R_g)^2} = \frac{1}{2}, \qquad (4)$$

if it is assumed that $R_g \longrightarrow 0$ when $x \longrightarrow 0$.

The void fraction-quality relationship calculated from equation (4) is shown in Figure 23. This void fraction-quality relationship was then used in Equation 3 in order to obtain an estimate of the slip ratio. The resulting values of the slip ratio are shown in Figure 24. From Figure 24 it can be seen that, except in the low quality region, the slip ratio is quite large for the range of saturation temperatures considered. In view of the above results, it was decided to use the momentum exchange model to predict the slip ratios and void fractions to be utilized in Equation 2, and to assume that the entrainment was zero. The Nusselt numbers calculated from Equation 2 utilizing the above assumptions are shown in Figure 25.

In the derivation of Equation 2 the heat was assumed to flow along a straight radial path from the tube wall to the liquid-vapor interface, i.e., the curvature of the interface in the axial direction was neglected.

$$\text{In general} \quad \frac{d\delta}{dL} = \frac{d(\delta/D)}{dx}\,\frac{dx}{d(L/D)} = \frac{4\,q''}{G\,h_{fg}}\,\frac{d\,(\delta/D)}{dx} \qquad (5)$$

Figure 26 is a plot of the ratio of film thickness to tube radius against quality obtained from the void fraction plot in Figure 23 by assuming that all the liquid is on the tube wall. From Equation 5 it can be seen that the assumption of small interfacial curvature in the axial direction is poor in regions where either $d\,(\delta/D)/dx$ or $\frac{4q''}{Gh_{fg}}$ is large. In particular, the assumption is very poor in the low quality region, i.e., beyond the knee of the void fraction or liquid film thickness curves. In this region, the Nusselt numbers shown in Figure 25 drop below the theoretical single-phase value and the solution is no longer valid. In order to obtain agreement

between the Nusselt number at zero quality and the fully developed single phase liquid value an interpolation formula of the form

$$\frac{h_{TP} D_T}{k_f} = \left[(\frac{h_\ell D_T}{k_f})^n + (\frac{h_{FE} D_T}{k_f})^n \right]^{1/n} \qquad (6)$$

can be used. The Nusselt numbers calculated from this formula approach the single phase liquid values at low qualities and approach the film evaporation values at high qualities. This procedure was used in the construction of Figure 27. A liquid phase Nusselt number of seven was employed together with n = 2 in Equation 6.

In addition to the possibility of liquid being entrained in the vapor core, there also exists the possibility that vapor may be entrained in the liquid film. Vapor entrained in the liquid film is probably either vaporizing or condensing depending upon the size of the particular vapor packet considered. If it is assumed that this change of phase takes place at a very slow rate (i.e., that a small heat transfer coefficient exists at the interface), then the presence of the vapor serves to reduce the effective thermal conductivity of the liquid film. The effect of vapor entrainment may then be estimated by assuming a small vapor film of thickness δ_g adjacent to the wall. Equation (2) then takes the form (E = 0):

$$\frac{hD_T}{k_f} = -\frac{4}{\ln\left[R_g - \frac{4\delta_g}{D_T}(1 - \frac{\delta_g}{D_T}) \right] + 2(\frac{k_f}{k_g} - 1)\ln\left[1 - \frac{2\delta_g}{D_T} \right]} \qquad (7)$$

For small values of δ_g/D_T Equation (7) takes the form

$$\frac{hD_T}{k_f} = -\frac{4}{(\ln R_g) - 4(\frac{k_f}{k_g} - 1)\frac{\delta_g}{D_T}} \qquad (8)$$

The effect of δ_g/D_T on the Nusselt number is shown in Figure 28. From this Figure it can be seen that the model is very sensitive to the quantity of vapor entrained in the film. For this reason the values of the Nusselt Number given in Figure 27 probably represent an overestimate in the intermediate to high quality region.

The following qualitative trends in the two-phase Nusselt number resulting from the assumption of an evaporative mechanism of vapor generation should be noted.

a) N_{Nu} increases with increasing quality for a given saturation temperature.

b) N_{Nu} increases with increasing liquid Peclet number (this follows from Equations 6 and 7).

c) N_{Nu} increases with increasing liquid entrainment in the vapor core.

d) N_{Nu} decreases with increasing vapor entrainment in the liquid film.

e) N_{Nu} decreases with increasing saturation temperature for a given quality (no vapor entrainment).

f) N_{Nu} is independent of heat flux for the particular analytical model chosen. However, the parameter $\dfrac{4q''}{G\,h_{fg}}$ would probably be important if a more sophisticated analytical approach were used. This would be particularly true in the low quality region (i.e., beyond the knee of the void fraction quality curve).

g) h_{FE} increases with decreasing tube diameter if the remaining variables are held constant.

Vapor Generation by Vigorous Nucleate Boiling. For this case it was
assumed that vapor generation by evaporation at the liquid vapor interfaces
was negligible. Vapor was assumed to be generated by the formation of
vapor bubbles at the wall of the tube, with the subsequent growth and
transport of these bubbles into the vapor core.

The heat transfer coefficient was assumed to consist of that obtained
by the superposition of the single-phase liquid forced convective heat
transfer coefficient and the nucleate pool boiling heat transfer coefficient
(Reference 8).

The single-phase forced convective heat transfer coefficient was
calculated from the following equation 9 (Reference 9).

$$N_{Nu} = 7 + 0.025 \ (N_{Pe})^{0.8} \tag{9}$$

The nucleate pool boiling heat transfer coefficient was obtained from
Equation 10 below as given by Bonilla in Reference 10.

$$T_W - T_{sat} = 49.8 \ (q'')^{0.0867} \ P^{-0.276} \tag{10}$$

Where T is in °F, q'' in Btu/hr-ft^2, and P in millimeters of mercury absolute
(torrs).

The heat transfer coefficients obtained from Equations 9 and 10 were
then combined using the interpolation formula suggested by Kutateladze
(Reference 8), i.e.,

$$\frac{h_{NB}}{h_\ell} = \sqrt{1 + \left(\frac{h_{PB}}{h_\ell}\right)^2} \tag{11}$$

-52-

The results of this calculation for a 3/4-inch ID tube are shown in Figure 29. It was assumed in the construction of Figure 29 that the single phase Nusselt number was equal to seven, i.e., that the mass velocity was small.

Equation 10 is based on the pool boiling data of Bonilla (Reference 11). The data was obtained by boiling potassium on a horizontal nickel plate. The approximate range of the data is given below.

P(psia)	T_{sat} (°F)	q''(Btu/Hr-Ft^2)
0.0387 to 0.2322	690 to 840	up to 10^5
13.55 to 29.1	1380 to 1540	up to 10^5

Since both the surface conditions and the range of operating pressures in the Cb-1%Zr Facility are different from those in the pool boiling test, precise agreement between the predicted forced convective boiling heat transfer coefficient using this data and those obtained from the Cb-1%Zr Facility cannot be expected.

The following qualitative trends in the two-phase heat transfer coefficients result from the assumption of a boiling mechanism of vapor generation.

a) h_{NB} is independent of quality (for all saturation temperatures)

b) h_{NB} increases with increasing heat flux at a given saturation temperature

c) h_{NB} increases with increased saturation temperature (increased pressure) at a given heat flux

d) h_{NB} increases with increasing values of the single phase liquid heat transfer coefficient

e) h_{NB} is independent of tube diameter

It should also be noted that while it is possible to have total suppression of nucleation (i.e., heat transfer by film evaporation only) it is not possible to have boiling without some evaporation taking place. To the extent that film evaporation takes place, the effects mentioned in the preceding section will also be present during boiling.

Suppression of Nucleation. The question as to which of the two preceding mechanisms of vapor generation will take place in a given situation will now be examined with the help of a model presented by Bergles and Rohsenow (Reference 12). In Reference 12 a graphical procedure was proposed which could be used to predict the conditions necessary for boiling inception.

The graphical procedure can best be understood by referring to Sketch B below:

Sketch-B

-54-
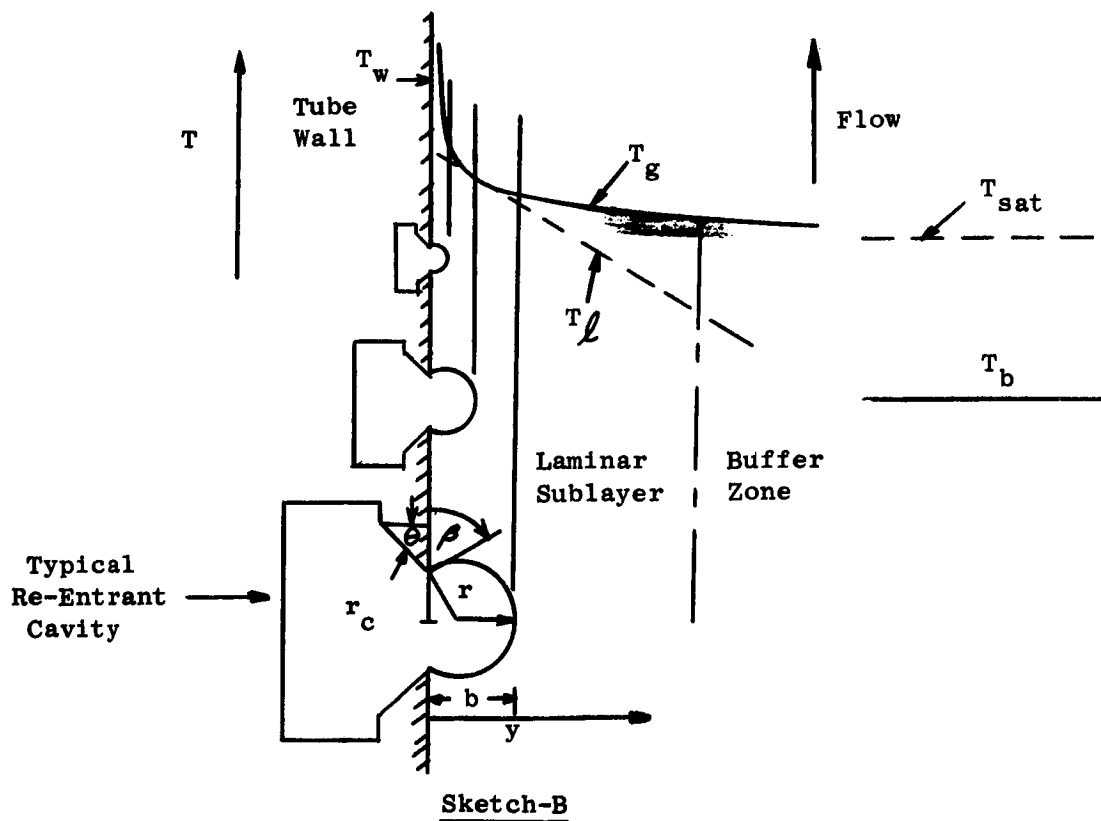
The condition for bubble growth given in Reference 12 is that $T_\ell \geq T_g$ for all values of $y \leq b$. For the limiting case of boiling inception, the following conditions apply:

(a) $T_\ell = T_g$ at $y = b$

(b) $\dfrac{dT_\ell}{dy} = \dfrac{dT_g}{db}$ at $y = b$

The liquid temperature near the wall is assumed to be linear and is determined from the equation:

$$T_\ell = T_w - q'' \frac{y}{k_f} \tag{12}$$

The temperature inside the vapor bubble is approximately the saturation temperature corresponding to the pressure inside the vapor bubble as given by the Helmholtz relations for the radius of curvature, i.e.,

$$P_g - P_\ell = \frac{2\sigma}{r} \tag{13}$$

The relationships between the height of the bubble (b), the bubble radius (r), and the cavity mouth radius (r_c) are given by the following equations (obtained from Sketch B).

$$b = (1 + \cos \beta) \, r \tag{14}$$

$$r \sin \beta = r_c \tag{15}$$

where

$$0° < \beta \leq 90°$$

It might have been well to omit the consideration of contact angle β in this derivation since in general the relationships between cavity mouth radius, bubble height, and bubble radius at boiling inception cannot be written down independently of the cavity shape. Since potassium is generally assumed to be a highly wetting fluid (i.e., small contact angle)*, it was assumed that all the non-re-entrant or conical type cavities would be "snuffed out" and that only those cavities which were not flooded by subcooled liquid (i.e., re-entrant cavities) would trap vapor**.

For the particular cavity shape shown in Sketch B, if it is assumed that $(\theta + \beta) > 90°$ then the conditions of equilibrium at the liquid vapor interface will require that the liquid be subcooled if the interface is within the cavity. Under these conditions the liquid vapor interface will retreat to the inside lip of the cavity as soon as some wall superheat is available. It will then, somehow, round the corner and hang on the outer lip of the cavity in the condition of equilibrium shown in Sketch B until boiling inception occurs. If it had been assumed that $(\theta + \beta) < 90°$ then the liquid would have been superheated within the cavity. The superheat required for boiling inception could then have been dependent on the cavity angle θ. Since it was desired to include (in at least an approximate fashion) the effect of contact angle β, but not the effect of cavity angle

---

*Some contact angle measurements for potassium obtained by General Electric Company - SPPS of the RSD by a sessile drop technique are given below (Reference 45)

Material	Temperature	Equilibrium Contact Angle (Receding)
Carboloy 907	~ 231°C	22°
Carboloy 907	~ 221°C	26°
Carboloy 907	~ 223°C	20°
Mo TZM	~ 230°C	0°

** Reference 13 contains a good discussion of re-entrant and conical type cavities

θ, the above cavity configuration was chosen. In reality, a complete solution to the boiling inception problem probably requires solution of the fluid flow and heat transfer problem associated with the expansion of the initial volume of trapped vapor to the final state of boiling inception.

In Reference 12, the bubbles were assumed to be hemispherical ($b = r = r_c$) and the above equations were solved graphically to obtain a boiling inception curve, i.e., the relationship between the heat flux and wall superheat at boiling inception. The actual point of boiling inception is then determined by obtaining the point of intersection of the boiling inception curve with the usual single phase forced-convection or natural-convection heat transfer relationship between q'' and T_w for a particular value of bulk fluid temperature.

Since the graphical procedure is somewhat tedious, an approximate solution to the above equations was obtained in the following manner. Assume that the vapor-temperature inside the bubble can be satisfactorily approximated for small superheats by Equation (16) (Reference 14), where T_{sat} is the saturation temperature corresponding to the external liquid pressure. Equations 12, 14

$$T_g = T_{sat} + \frac{2\sigma T_{sat} v_{fg}}{Jh_{fg} r} \tag{16}$$

15 and 16 are then solved simultaneously to determine the relationship between q'' and $T_w - T_{sat}$ which will satisfy conditions (a) and (b) listed according to Sketch-B. The resulting expression is

$$q''_i = \frac{Jh_{fg} k_f (T_w - T_{sat})^2}{8\sigma (1 + \cos\beta) T_{sat} v_{fg}} \tag{17}$$

The critical cavity radius (the radius of cavity that nucleates first) is given by the expression:

$$r_c = \frac{4\sigma v_{fg} T_{sat} \sin\beta}{Jh_{fg} (T_w - T_{sat})} \tag{18}$$

The accuracy of Equation 17 may be judged by referring to Figure 30, in which graphical solutions have been compared with calculated values from Equation 17 for different fluids. In each case it was assumed that $\beta = 90°$ (i.e., $b = r = r_c$). The graphical solution for water is given in Reference 12, while that for Freon 113 was obtained from Reference 15. The graphical solution for potassium shown in Figure 30 was made following the procedure given in Reference 12.

Equations 17 and 18 were used to generate the curves shown in Figure 31 for potassium. The wall superheat required for boiling inception at a given heat flux is shown as well as the critical cavity size.

Equation 17 applies strictly for the case of there being an infinite range of cavity sizes available on the heat transfer surface. If a finite maximum cavity size exists of radius r_{max}, then the wall superheat at boiling inception is given more correctly by Equation (19),

$$(T_w - T_{sat}) = \frac{2\sigma T_{sat} \ v_{fg} \ \sin \beta}{J h_{fg} \ r_{max}} + \frac{q_i''}{k_f} \ (\frac{1 + \cos \beta}{\sin \beta}) \ r_{max} \tag{19}$$

The existence of a limited range of cavity sizes acts to increase the superheat required for boiling inception at any heat flux. This behavior is shown in Figure 32. The nearly vertical lines represent the minimum wall superheat requirement as obtained from Equation 19 for the maximum cavity size shown on the curve. The asymptotic solid line was obtained from Equation 17. Also shown on Figure 32 are the usual single phase forced-convection lines obtained from Lyon's Equation (Reference 9),

$$N_{Nu} = 7 + 0.025 \ (N_{Pe})^{.8} \tag{20}$$

Figure 32 illustrates the manner in which the boiling inception point can be estimated. If, for example, the heat flux is set at 20,000 Btu/hr-ft^2

then about 1°F of wall superheat is required for boiling inception if an infinite range of cavity sizes are available. Boiling would then commence when the bulk fluid was about 10°F subcooled, as can be estimated from the forced convection liquid heat transfer plots on the Figure. If, on the other hand, a maximum cavity size of r_{max}^{v} = 0.05 mils existed on the heat transfer surface, then boiling would not begin until the bulk fluid was superheated about 30°F.

Equations 17 and 19 will now be used to investigate the question of total suppression of nucleation in the region of net vapor generation. Although many of the factors influencing nucleation are not clearly understood, it will be assumed as an idealization that nucleation from the tube wall will take place if the following conditions exist:

(a) Small cavities or pits are present on the tube wall

(b) These cavities contain entrapped vapor or gas

(c) The wall superheat is sufficient to activate the cavity, i.e., to cause the small vapor space present in the cavity to grow and produce bubbles.

Condition (a) is generally met by any commercial surface. Micrographs of the heat transfer surface in Test Section No. 1 used in the Cb-1%Zr Facility during the period 8/1/64 to 11/14/64, are shown in Figures 33 and 34. The particular test section shown in these figures was removed from the loop on 11/14/64 after approximately 671 hours of operation at temperatures above 800°F. The approximate size of some of the more obvious pits or scratches have been designated in the photographs.

Condition (b) is probably the most difficult of the three conditions to treat adequately for alkali metals. In the Cb-1%Zr Facility for example,

the potassium used as a working fluid is quite pure (less than 50 ppm O_2) and considerable care is taken to exclude any gases from the test section. With the potassium fill line closed, the loop piping is evacuated down to approximately 25 microns with an auxiliary vacuum pump. The vacuum line is then closed and the loop is filled by pressurizing the dump tank with argon. If it is assumed that inert gases are not present in the test section, then each time subcooled liquid flows over the heat transfer surface all of the cavities are "snuffed out" except those of the smaller re-entrant type. This is due to the fact that potassium wets the surface. The net result of the above effects is that relatively high degrees of wall superheat would be required at the beginning of two-phase operation. Some verification of the above hypothesis is found in the relatively high value of wall superheat (200°F at T_{sat} = 1800°F) observed at the beginning of two-phase operation (see Table 11).

Condition (c) can be treated by using Equations 17 and 19 in conjunction with the previously derived film evaporation theory as given in working chart form by Figure 27. It will be assumed that if the wall superheats calculated from the film evaporation model are sufficient to cause nucleation then nucleation will occur and the boiling mechanism will predominate. In view of the above discussion it is evident that this is a necessary but by no means sufficient condition for boiling. However, the use of this assumption will at least permit a preliminary estimation to be made of the regions in which nucleate boiling and film evaporation will take place.

The steps necessary to make such an estimate are illustrated by Figure 35. The wall superheats required are obtained from Equations 17 and 19. The maximum cavity size on the surface is taken as a parameter in the construction of these curves. The available wall superheat is then obtained from the film evaporation model using the Nusselt numbers from Figure 27. If the available superheat exceeds the required superheat it is assumed that nucleation will occur. The end results of this procedure for an approximately 3/4-inch diameter tube are

shown in Figure 36. The lines plotted in Figure 36 are calculated boundaries between conditions of boiling with nucleation (bubble formation) and conditions of evaporation from the liquid-film interface without nucleation.

In order to utilize Figure 36 some knowledge of the range of cavity sizes available on the heat transfer surface is required. For example, based on Figures 33 and 34, a maximum cavity radius of 0.1 to 0.2 mils may be estimated for the test section used in the Cb-1%Zr Facility. Based on this estimate Figure 36 indicates that the mechanism of vapor generation of $q'' = 10^5$ Btu/hr-ft^2 and $T_{sat} = 2100°F$ would be vigorous nucleate boiling for qualities less than 70%. For the same conditions at $T_{sat} = 1500°F$, Figure 36 indicates there would be no boiling and that the mechanism of vapor generation would be film evaporation. It should be pointed out that Figure 36 applies only to an approximately 3/4-inch ID tube. Since the film thickness increases when the tube size is increased (see Figure 26) the likelihood of boiling is greater for large diameter tubes and less for small diameter tubes if all other variables are the same.

The following qualitative trends can be deduced from Figure 36:

(a)   At a given heat flux, saturation temperature, and maximum cavity size, boiling with bubble formation tends to be suppressed by increasing quality.

(b)   At a given heat flux, saturation temperature and quality, boiling with bubble formation tends to be suppressed for smaller values of the maximum cavity sizes (i.e., for smoother heat transfer surfaces).

(c)   At a given quality, saturation temperature, and maximum cavity size, boiling with bubble formation tends to be suppressed by lowering the heat flux.

(d)   At a given quality, heat flux, and maximum cavity size,
      boiling with bubble formation tends to be suppressed by lowering
      the pressure.

The highly preliminary nature of the mapping shown in Figure 36 should
be stressed.   Some of the more important sources of error are the following:

1.   Inadequacies in the method used to calculate the film thickness.
     In this connection particular attention should be called to the
     fact that, in the method used, an assumption was made that the
     film thickness is independent of the heat flux.

2.   The assumption of a smooth interface .
     The assumption of a smooth interface (i.e., the assumed
     absence of waves on the liquid vapor interface) is known to be
     unrealistic.   In general the presence of waves on the interface
     will probably increase the film evaporation heat transfer
     coefficient.   Although there are many factors which influence
     the wave amplitude, the effect of heat flux should be particularly
     noted.   In Reference 16 Zuber suggested that the thrust exerted
     by the vapor on the liquid vapor interface would act to destabilize
     the interface.   Since the vapor thrust is proportional to the
     square of the heat flux, waves of larger amplitude might be expected
     at higher heat flux levels.   This would have the effect of extending
     the film evaporation region in Figure 36 at the higher heat fluxes,
     i.e., the boundary lines would become more vertical for the higher
     heat fluxes.

3.   The effect of vapor in the liquid film .
     The presence of vapor in the liquid film would lower the film
     evaporation heat transfer coefficient and thereby extend the
     boiling region in Figure 36.   The presence of vapor in the liquid

film could be due either to entrainment from the vapor core
or to latent (inactive) bubbles present on the heat transfer
surface.

4.   Errors in the estimate of the maximum cavity size

5.   The possible effect of contact angle on the wall superheat
      requirement

Any of the factors listed above could quantitatively alter Figure 36.
However, it is less probable that the qualitative trends evidenced by the
map would be radically altered. It should also be pointed out that Figure 36
was constructed by assuming that the mechanism of vapor generation was film
evaporation and then determining the conditions necessary for boiling to
begin. In general, the location of the boundary lines in Figure 36 would not
be expected to be independent of the direction in which they are traversed.
For this reason the map would be expected to be less reliable in predicting
the point of boiling suppression than the point of boiling inception.

In Figure 37 the boundary mapping has been presented in a generalized
dimensionless form. The effects of contact angle β and bubble radius r are
shown parametrically.

EXPERIMENTAL RESULTS FOR TUBES WITHOUT INSERTS
      In this section the process of forced-convection vaporization of potassium
inside a tube with a uniform heat flux imposed on the tube boundary will be
discussed with the aid of data from the Cb-1%Zr Facility. During the course
of the discussion frequent comparison will be made between the data and the
previously derived analytical results. In this way the areas of agreement
and disagreement can be assessed. Those weaknesses in the analyses which appear
to be the most likely cause of discrepancies will be noted.

Discussion of Results.   In Figure 38 measured axial wall temperature
distributions along the test section are shown.   Corresponding heat transfer
coefficients calculated from these measured temperatures in the two-phase
region are shown in Figure 39.   Some additional information on the runs
shown in Figures 38 and 39 which is pertinent to the discussion is tabulated
below:

Data Symbol In Figs. 38 and 39	$dT_b/d(L/D)$ To Peak	(L/D) To Sat'n	L/D To Peak	$T_b - T_{sat}$ At Peak (°F)	$T_w - T_{sat}$ At Peak (°F)	Est. Change In T_{sat} Due To ΔP_{TP}
◯	21.3°F	25.6	27.25	35.0	65	0.63°F
◆	19.9°F	27.9	30.00	41.8	62	0.61°F
▲	16.3°F	32.8	35.50	44.0	58	0.57°F

Focusing attention on the curves in Figure 38, two distinct regions
separated by a peak in wall temperature are observed.   Near the inlet
of the tube both the wall and liquid temperatures are rising at about the
same rate, since both temperatures are below the saturation temperature.   No
vaporization is taking place and the heat is transferred by ordinary single
phase liquid forced convection.   Further along the tube the wall temperature
increased above the saturation temperature so that surface boiling had become
a possibility.   However, the wall temperature continued to increase at about
the same rate, which indicates no significant change in heat transfer coefficient
and suggests that no surface boiling had taken place.   As shown by the wall
temperature peaks in Figure 38, boiling finally started at wall superheat
levels of about 60°F, depending on the heat flux.   The corresponding calculated
bulk liquid superheats at the points of boiling inception are about 40°F.

The point of boiling inception should be predictable using Figure 32.
If, based on Figure 34, a maximum cavity size of r_{max} = 0.1 mils is assumed,
boiling should occur, according to Figure 32, when the bulk fluid is about
50°F subcooled for the highest heat flux run in Figure 38.   The fact that

-64-

instead some bulk liquid superheat existed at the boiling inception point suggests the possibility that the larger cavities might have been "snuffed out", due to prior liquid phase operation, and that only the smaller cavities might have been operative.

If, for example, the maximum size of the cavities containing vapor is assumed to be r_{max} = 0.01 mils, then from Figure 32 the estimated bulk liquid superheat required to initiate boiling would be about 150°F for a heat flux of 100,000 Btu/hr-ft^2. When this high a liquid superheat is present, the position of the boiling boundary (boiling inception point) can fluctuate significantly. This in turn will cause corresponding fluctuations in the measured local wall temperatures in the vicinity of the boiling boundary, which were sometimes observed with the Cb-1%Zr Facility. The data plotted in Figure 40 are an example of this.

The data points in Figure 40 designated as T/C-A15, A16 and A17 are wall temperatures recorded in the vicinity of the boiling boundary. The numbers designate the particular thermocouples used to make the measurements. According to the Cb-1%Zr Facility Operating Log*, thermocouples number A16 and A17 had temperature fluctuations of approximately 100°F amplitude, and thermocouple A15 had slight fluctuations in temperature. These observed wall temperature fluctuations are believed to be due to fluctuations in position of the highly superheated boiling boundary. It should be noted that the temperatures shown in Figure 40 were read from inlet to exit of the tube with about a 10 second delay between each reading. Therefore, the resulting wall temperature profile shown in the figure is not an instantaneous picture.

The extent of the instability of position of the boiling boundary associated with the runs shown in Figures 38 and 39 is not known. However, it is felt that

---

*100 KW Facility Log, vol. II, page 149; 1445 hours, 2/14/64

some instability is always associated with the boiling boundary when the associated local bulk liquid is superheated (see Section III-G).

After vaporization had begun, the wall temperatures shown in Figure 38 decrease rapidly at first and then reach relatively constant values downstream of the peak. If the local instability of position of the boiling boundary is due to intermittent boiling, caused by periodic "snuffing out" of the larger cavities as discussed in Section III-G, then the mechanism of vapor generation in the low quality region downstream of the peak is probably one of film evaporation. For this case, in spite of the fact that the local wall superheat immediately downstream of this peak was sufficient to produce bubble nucleation from the larger cavities, boiling with bubble nucleation did not take place since these cavities had been snuffed out. For the runs shown in Figure 38 boiling with bubble nucleation may not have begun until sufficient vapor had been entrained in the liquid film to activate the larger cavities present on the surface of the tube. In order for this to occur the following sequence of events must take place:

1. Vapor must be entrained in the liquid film

2. The entrained vapor must displace the liquid from a nucleation site

3. The "captured site" must itself be capable of serving as a site for further nucleation or as a site from which nucleation can spread to adjacent cavities.

For the reasons given above, the heat transfer coefficients in the two-phase region downstream of the spike would be expected to increase with quality in accordance with the film evaporation theory until the larger cavities become active. At this point there should be a rather sudden increase in the heat transfer coefficient to about the pool boiling value, and very little change thereafter. There is some indication of these trends shown by the data in Figure 39.

Some further confirmation of the hypothesis that bubble nucleation is suppressed in the low vapor quality region immediately downstream of the boiling boundary is indicated by the data shown in Figures 41a through 41d. In these runs, some net quality was present at the inlet of the test section, and although the qualities were quite low, the heat transfer coefficients obtained were about the same as those calculated from the forced convection nucleate boiling model (Equation 11), and they showed little variation with quality as predicted by the model.

The Nusselt numbers obtained from the heat transfer coefficient data shown in Figure 39 were compared with the values calculated by the film evaporation model (Equation 6). This comparison is shown in Figure 42. The comparison at low qualities is a severe test of the film evaporation model, since it is in this region where the effects of both liquid entrainment and axial curvature of the interface are expected to be the greatest. As discussed earlier, the latter effect is related to the parameter $\frac{4q''}{Gh_{fg}}$. Values of this parameter for the data are shown in Figure 42. In general, the experimental Nusselt numbers apparently increase with increasing values of this parameter. It is felt that a film evaporation theory which included the two effects mentioned above could adequately predict the Nusselt numbers in the low quality region. From a design standpoint the present model may provide a conservative estimate of the heat transfer coefficients in this region, as shown in Figure 42 by the comparison between the experimental Nusselt numbers and the values calculated from the film evaporation model.

Forced convection nucleate boiling heat transfer data taken with Test Section No. 1, a 0.767-inch ID tube without inserts, are plotted in Figures 43 and 44, as local heat flux q'' versus wall-to-fluid temperature difference ΔT and as local heat transfer coefficient h versus local vapor quality. The data shown in Figures 43 and 44 all have wall-to-fluid temperature differences which are less than those calculated using the forced convection nucleate boiling model (Equation 11), except for one point in each of Figures 43a and 43c. The corresponding plots of local heat transfer coefficient h versus local

vapor quality in Figures 43b, d and 44b, d, respectively, show that the heat transfer coefficients are nearly independent of vapor quality, but have a definite trend of increased heat transfer coefficient with increasing heat flux.

These trends tend to confirm the hypothesis that there was boiling with bubble nucleation. For example, using Figure 36 it is estimated that all the 2100°F data in Figure 43a, except the single point to the right of the nucleate boiling line, should have been in boiling with bubble nucleation if maximum cavity sizes in the range 0.1 mil $<$ r_{max} $<$ 0.2 mil were present.

Local nucleate boiling data from Test Section No. 3, a 0.423-inch tube without insert, are shown in Figure 45. These data also show a trend of relative independence of the heat transfer coefficient with respect to vapor quality. The trend with respect to heat flux is not as clear as with the Test Section No. 1 data. The heat transfer coefficients for the Test Section No. 3 data are in about the same order of magnitude but are a little higher than those from Test Section No. 1 shown in Figure 43, for which a larger diameter tube was used. In both cases the order of magnitude of the coefficients is about 10,000 Btu/hr-ft^2-°F, with a few of the Test Section No. 1 data falling a little below this, especially at low heat flux, and most of the Test Section No. 3 data being above this value.

Further confirmation of the hypothesized mechanism of boiling with bubble nucleation at low heat fluxes and intermediate quality levels is obtained from Figures 46a and 46b. From these Figures it can be seen that there is little or no variation in heat transfer coefficient with quality along the tube length. This strongly suggests that there was boiling with bubble nucleation. The persistence of the boiling mechanism at these low heat fluxes may be due to the fact that once boiling begins in the tube the presence of the bubbles in the liquid film may increase the film thickness and thereby increase the liquid superheat at the wall. If this takes place, the process might "stay" in boiling with bubble nucleation somewhat longer than otherwise would be

expected at low heat fluxes.

Conclusions. Based on the preceding discussion of the data the following tentative conclusions may be drawn:

1. If boiling with bubble nucleation occurs in the tube, the heat transfer coefficients predicted by the forced convection nucleate boiling model, Equation (11), appear to be somewhat conservative (Figures 43a, b and 45a, b).

2. If vapor is generated by film evaporation without bubble nucleation, the heat transfer coefficients predicted by the film evaporation model, Equation (6), appear to be somewhat conservative in the low quality region (Figures 41 and 42), but may over-estimate the heat transfer coefficient in the intermediate and higher quality regions (Figures 43a, b, 45a, b and 46).

3. The map presented in Figure 37 is useful in making a preliminary judgement as to the predominant mechanism of vapor generation, if operation occurs entirely in a region of conditions well removed from the predicted boundary lines. Figure 37 should be used with caution, because the location of the boundary lines given by it may not be very accurate, due to such factors as the "history" of the surface, the distribution of cavity sizes and presence or absence of impurities in the fluids.

For the range of the tube diameters, heat fluxes, saturation pressures, and mass velocities considered for boiler design (Reference 3), the two-phase heat transfer coefficients at heat fluxes less than the critical heat flux are apparently quite high, in the order of 10,000 Btu/hr-ft^2-°F, regardless of the mechanism of vapor generation. For this reason an accurate method for

predicting the mechanism of vapor generation is not required for application to boiler design. It is important, however, to recognize that different mechanisms of vapor generation may occur in the tube, since this can aid in the correlation and understanding of the data. It is felt that the present treatment is probably adequate for design purposes and a recommended design procedure for calculating two-phase heat transfer coefficients based on this treatment is given below.

Suggested Design Procedure For Estimating Nucleate Boiling Coefficients In Tubes Without Inserts. A suggested design procedure for calculating two-phase heat transfer coefficients in tubes without inserts at heat fluxes less than the critical heat flux is the following:

1. Using Figure 25 together with Equation 6, calculate the film evaporation model heat transfer coefficient.

2. Using Equations 9, 10 and 11 calculate the forced convection nucleate boiling model heat transfer coefficient.

3. Utilizing a map like that shown in Figure 36 or 37 estimate the mechanism of vapor generation.

4. Use the heat transfer coefficient applicable to the particular mode of vaporization estimated. If additional conservatism is desired use the smaller of the two values calculated from step-1 and step-2 irrespective of the regime.

EXPERIMENTAL RESULTS FOR TUBES CONTAINING INSERTS

Test Sections 2, 4 and 5 contained swirl flow generator inserts, which are described in Section II-B. The data obtained from these test sections are shown in Figures 47, 48 and 49. Plots of both heat flux as a function of ΔT and heat transfer coefficient as a function of quality are shown in these figures. The data in these Figures are tabulated in Table 2. The data are

based on measured wall and centerline fluid temperatures and have not been corrected for effects of radial acceleration caused by swirl flow, as discussed below.

Since each of the inserts induces a swirling or helical motion in the flow, it effectively imposes a high radial acceleration on the fluid. If the flow pattern is visualized as a relatively thin layer of liquid adjacent to the wall with a vapor core, then there exists a radial pressure difference between the fluid at the wall and that at the center line. If it is assumed that the vapor is saturated at the center line, then the center line temperature must be corrected to obtain the saturation temperature at the wall, for use in the forced convection nucleate boiling model (Equation 11), or that at the liquid vapor interface for use in the film evaporation model (Equation 6).

If the annular flow pattern discussed above is utilized together with the assumption of a uniform axial velocity in the liquid and vapor phases, then the following equation is obtained for the radial acceleration a_R in g's (from Equation B-15 in Appendix B).

$$a_R = 2 \; (\frac{\pi}{P/D})^2 \; (\frac{1-x}{R_\ell})^2 \; (\frac{G^2}{g_c \; \rho_f^2 \; D_T}) \tag{21}$$

An approximate expression for the change in saturation temperature between the wall and center line is as follows, assuming $K = \sqrt{\rho_f/\rho_g}$ (Equation B-19, Appendix B).

$$\Delta T_r = (\frac{a_R}{2})(\frac{\rho_f \; D_T}{2}) \; (\frac{T \; v_{fg}}{J \; h_{fg}}) \; \left[1 - (\frac{D_{CB}}{D_T})^2 \right] \tag{22}$$

Since a_R at the wall can be varied by changing the slip ratio, a wide range of values for a_{Rf} and T_{sat} at the wall are possible. Values of a_R calculated using Equation (21) for an assumed slip ratio $K = \sqrt{\rho_f/\rho_g}$ are tabulated in Table 2 for each of the data points shown in Figures 47 through 49.

In an effort to ascertain if any detectable trend in the data as a function of radial acceleration existed, Figure 50 was constructed using the data from Test Sections No. 2, 4 and 5 at 2100°F. The corrected temperature difference appropriate to a slip ratio assumption of $K = (\rho_f/\rho_g)^{\frac{1}{2}}$ is plotted against a_R at the wall with heat flux as a parameter.

A line can be fitted through the data, but with considerable scatter. However, the data strongly suggest that $(T_w - T_{sat})$ may not be a single valued function of a_R for a given heat flux. A somewhat similar result was evidenced by the pool boiling data of Merte and Clark (Reference 17) showing the effect of gravity on nucleate boiling of water. This data showed a decrease in $(T_w - T_{sat})$ with increasing g's at low heat fluxes (possibly due to the enhanced natural convection effect), and an increasing $(T_w - T_{sat})$ with increasing g's at high heat fluxes. At intermediate heat fluxes $(T_w - T_{sat})$ was not a single valued function of the acceleration normal to the heated surface. A good discussion of these trends is given by Westwater (Reference 18).

It may be, for pool boiling, that at the low heat fluxes when the mechanism of heat transfer is predominately natural convection and bubble agitation the effect of gravity is to enhance the heat transfer process, while at the higher heat fluxes where the heat transfer mechanism may be by latent heat transfer process, as discussed in Reference 16, the effect of gravity is the reverse. However, whatever the reason may be for the case of pool boiling, there does not seem to be any clear cut dependence upon a_R for the forced convection boiling data shown in Figure 50.

An empirical correlation of the potassium nucleate boiling heat transfer coefficient data for flow in tubes with swirl generator inserts is given in Figure 51 for various saturation temperatures. Since the correlation is primarily empirical, extrapolation outside the range of the data should be made with caution. All of the nucleate boiling data taken with swirl generator inserts (Figures 47, 48 and 49) are included in Figure 51. It is seen from Figure 51 that the empirical equation

$$h_{NB} = 0.0016 \, (P/D)(1 + a_R)^{0.16}(q'')^{1.16}, \text{ Btu/hr-ft}^2\text{-°F} \tag{23}$$

correlates the data from the different insert test geometries reasonably well within the experimental uncertainties. Equation (23) includes the trends of: independence of the heat transfer coefficients with respect to vapor quality and saturation temperature; increasing heat transfer coefficient with increased heat flux; and increased coefficient with increasing insert twist ratio (P/D). These trends can be seen in the test data by examining Figures 47, 48 and 49. Comparison of Figures 47, 48 and 49 with Figures 43 and 44 shows that the heat transfer coefficients in the tubes with swirl generator inserts tend to be lower than those in tubes without inserts taken at comparable conditions.

B. Critical Heat Flux Results

The general procedure used for taking critical heat flux data was an extension of the procedure used to obtain nucleate boiling data; i.e., the saturation temperature, mass velocity and test section heat flux were held constant while the quality was increased by slowly increasing the preboiler power until the critical quality corresponding to the test conditions was reached. The onset of the critical heat flux condition was detected by observing the behavior of test section wall temperatures as they were recorded (along with other pertinent system parameters) on an 8-channel Sanborn oscillograph recorder. In the nucleate boiling regime, the test section wall temperature was relatively steady, with small random oscillations of less than about 5°F. The behavior of the test section wall temperature at the onset of the critical heat flux condition in tubes without inserts was found to be of two general types, depending on the magnitude of the heat flux.

When the critical heat flux condition was reached at relatively high heat fluxes, for tubes without inserts, the wall temperature would suddenly begin to rise on a rapid transient, sharply distinguishable from the small fluctuations typical of nucleate boiling conditions. Presumably, if no

corrective action were taken, the wall temperature would have continued to rise until stable film boiling was established, or until some limit to the process occurred such as test section failure or reduction of heat flux due to increased heat losses caused by the correspondingly higher wall and radiant heater temperatures. In order to protect the test section from damage, such runs were terminated by either automatic or manual reduction of the test section power after the wall temperature transient had begun.

At relatively low heat fluxes and correspondingly higher vapor qualities, onset of the critical heat flux condition was not so definite and the wall temperature behavior was similar to that illustrated in Figure 52. Under these conditions (low heat flux), when the vapor quality was raised beyond a certain critical value, which depended on the test conditions, there resulted an increase in amplitude of the wall temperature fluctuations above that characteristic of the nucleate boiling regime. Further increases in vapor quality resulted in corresponding increases in the amplitude of the wall temperature fluctuations and the time-average wall-to-fluid temperature difference until, at sufficiently high vapor qualities, stable film boiling was established. As illustrated in Figure 52, the wall temperature in the transition boiling regime oscillates within an envelope for which the upper temperature bound increases with increasing quality and the lower bound is approximately constant at the level corresponding to that for nucleate boiling.

The two general types of wall temperature behavior discussed above were observed in plain tubes without inserts. The rapid temperature transient, observed in plain tubes at relatively high heat fluxes was not observed (up to the maximum heat flux tested) in the test sections containing inserts. Rather, the temperature behavior in the test sections with inserts at relatively high heat fluxes, as well as low heat fluxes, was similar to that observed in the plain tubes at low heat fluxes. Also the inserts increased the critical quality corresponding to a given heat flux. Thus, the effect of the inserts was to:

-74-

1. Increase the critical heat flux corresponding to a given
    quality, or, equivalently, increase the critical quality
    corresponding to a given heat flux.

2. Prolong, to a higher quality, the transition boiling regime,
    prior to beginning of stable film boiling.

In what follows, specific examples of the wall temperature behavior
will be given and discussed. The critical heat flux data obtained and an
empirical correlation of the data will then be presented.

MEASURED TEMPERATURE AT POST-CRITICAL HEAT FLUX CONDITIONS

Figure 53 is a segment of a typical recorder chart, obtained during a
critical heat flux determination at a heat flux of 211,000 Btu/hr-ft^2. Prior
to the preboiler power increase (test section inlet quality increase), the
pressure downstream of the orifice, the flow rate and the fluid temperature
at the test section outlet were steady and the test section wall temperature
had small random oscillations, characteristic of nucleate boiling. Following
the power increase, the wall temperature began an abrupt, rapid transient
which actuated the automatic power reduction system. This run is typical of
the type of wall temperature behavior observed when the critical heat flux
condition was exceeded at heat fluxes above about 150,000 Btu/hr-ft^2, in tubes
without inserts.

Figure 54 shows segments of a continuous recorder chart obtained during
a run using a tube without insert at low heat flux ($\sim$ 50,000 Btu/hr-ft^2). The
time of day during the run when each segment was taken is marked on the recording
in hours. This run illustrates the general behavior of the test section wall
temperature as conditions are changed sequentially from the nucleate boiling
regime into transition boiling, stable film boiling and finally into superheated
vapor conditions. In segment-1, before the preboiler power increase, the test

section is apparently in nucleate boiling although there was an occasional small excursion in the wall temperature indicating that the critical heat flux condition was imminent. Immediately following the preboiler power increase (segment-1), the amplitude of the wall temperature oscillations momentarily reached values up to about 50°F and then became more steady. In segment-2, after the next preboiler power increase, the amplitude of the wall temperature oscillations increased markedly to values of about 75°F with a peak value of almost 150°F, indicating that the test section outlet region was in transition boiling. Following a further preboiler power increase, in segment-3, the wall temperature started to rise steadily and finally reached a maximum and leveled off in stable film boiling. In segment-4, the preboiler power was again increased, resulting in slightly superheated vapor at the test section outlet, as indicated by the rise in measured bulk fluid temperature. Further increases in power (segment-5) resulted in a measured outlet vapor superheat of about 200°F. In segments-6 and -7, the preboiler power was reduced in steps to repeat in reverse the sequence of events observed when going up in preboiler power. The wall temperature behavior during the power reductions is very similar to that observed when increasing power. Heat transfer coefficients calculated from the measured wall temperatures, using the procedures described earlier, are noted under segments-2, -3 and -4 of Figure 54 at the times for which they were calculated in the transition, film boiling and superheated vapor regimes, respectively.

Figure 55 compares the wall temperature behavior for a tube without insert with that obtained for a tube with a helical insert. The upper recorder chart in Figure 55 shows tne characteristic sharp temperature rise at onset of critical heat flux conditions for the tube without insert. The recorder chart segments in the lower part of Figure 55 were taken with a tube containing a helical insert (P/D = 6). For this run, the wall temperature began to oscillate slightly at a quality approximately equal to the critical quality in the run with no insert; but there was no sharp temperature excursion, even though the heat flux levels were the same. Further increases in quality,

approaching 100%, resulted in increases in amplitude and mean level of the wall temperature fluctuations, characteristic of the transition boiling regime, but did not result in onset of stable film boiling conditions. This suggests that a helical swirl-generator insert prolongs the transition boiling regime to higher quality levels than would be obtained in a tube without insert for the same heat flux.

CRITICAL HEAT FLUX DATA AND CORRELATION

As discussed above, onset of the critical heat flux condition was detected by observing the behavior of test section wall temperatures. In tubes without inserts at high heat fluxes, the critical quality corresponding to a given heat flux was rather definite, since, at that quality, the wall temperature would "jump" almost discontinuously from the value associated with nucleate boiling to the film boiling value. For tubes without inserts at low heat flux or in tubes containing helical inserts, the temperature fluctuated with a continuously increasing amplitude from nucleate boiling through transition boiling to film boiling as the vapor quality was raised. Thus, in these cases, the "critical quality" corresponding to the critical heat flux condition cannot be precisely determined. The criterion which was arbitrarily selected as a working definition for runs in which this type of behavior occurred is that for a given heat flux, the "critical quality" is that quality for which the time-average fluctuating wall-to-fluid temperature difference becomes approximately equal to twice the corresponding steady-state nucleate boiling temperature difference. For data taking purposes, the time-average fluctuating wall temperature at the critical heat flux condition was estimated directly from the recorder charts made for each of the test runs, and a constant value of 10,000 Btu/hr-ft^2-°F was taken as the nucleate boiling heat transfer coefficient over the range of variables covered in these tests.

The critical heat flux data obtained are tabulated in Table 3. Figure 56 is a plot of these data together with the critical heat flux data from

Reference 3, taken in the 300 KW two-fluid boiling test facility. The two groups of data are correlated reasonably well by the following empirical equation from Reference 3:

$$q_c'' = \frac{(1 + a_R)^{\frac{1}{4}} (10^6)}{1 + 2 \left(\frac{x_c}{1-x_c}\right)} \quad , \quad \frac{Btu}{hr-ft^2} \qquad (24)$$

The parameter a_R in equation (24) is the radial acceleration of the fluid at the tube wall, in g's, developed by the helical insert, and is calculated using the following equation:

$$a_R = \frac{2}{D_T g_c} \left[\frac{x_c G \pi}{(P/D) \rho_g \sqrt{\rho_f/\rho_g}} \right]^2 \qquad (25)$$

C. Transition Boiling Results

As described above, the critical heat flux condition marks the end of the "nucleate" boiling regime, which is characterized by relatively high heat transfer performance. After onset of the critical heat flux condition and before establishment of superheated vapor conditions, the test section was in either transition boiling or stable film boiling. The transition boiling regime was distinguished, in the constant heat flux test sections of the Cb-1%Zr Facility, by relatively large wall temperature oscillations which increased in amplitude when the quality was increased at constant heat flux. As pointed out by Peterson (3) these temperature oscillations are probably less in magnitude in a two-fluid heat exchanger where (in the transition boiling regime) the local heat flux decreases with increasing quality and the maximum possible wall temperature is limited by the local primary fluid temperature.

The transition boiling data obtained with Test Sections 3, 4 and 5 are presented in Table 4. The wall temperature used in calculating the effective heat transfer coefficient in the transition boiling regime is the time-average of the oscillating temperature which was recorded on a digital recorder at a rate of 3 printouts/second. The time period over which the average temperature was calculated was usually about one minute. Figure 57 is a plot of the transition boiling data obtained with Test Sections 3, 4 and 5. Also shown in Figure 57 is the following Equation (26), which was developed in Reference 3 as an empirical correlation of the transition boiling heat transfer coefficient data obtained with the 300 KW two-fluid boiling test rig.

$$\frac{(\frac{h_{TB}}{h_v} - 1)}{(1 + a_R)^{1/5}} = 2.25 \times 10^5 \left[\frac{(\frac{1 - x}{x})^{0.7}}{(\Delta T)^2} \right] \tag{26}$$

The vapor heat transfer coefficient, h_v, was calculated from the Colburn equation (22) for the data taken in tubes without inserts. Equation (27), which is based on the water data of Greene (19), was used to calculate h_v for the test sections containing inserts following the procedure given in Reference 3.

$$(N_{Nu})_e = 0.359 \ (N_{Re})_e^{0.563} \ (N_{Pr})^{1/3} \tag{27}$$

The Cb-1%Zr Facility data shown in Figure 57 are correlated reasonably well by Equation (26), except for the three data points taken at the lower range of the dimensional group $\left[(1-x)/x \right]^{0.7} (1/\Delta T)^2$. One possible explanation for this discrepancy is related to the method used in calculating the transition boiling heat transfer coefficient. The Cb-1%Zr Facility data are local values and the wall temperatures used are time-averages of the measured oscillating values. The data used in Reference 3 to develop Equation (26) are average values over the transition and film boiling region in the two-fluid boiler.

These regional average coefficients used in Reference 3 are probably lower than the corresponding local values since they include the relatively lower performance film boiling region. A second possible source of discrepancies between Equation (26) and the Cb-1%Zr Facility data is that the method used in calculating the vapor phase heat transfer coefficient h_v may not apply in the present case. The measured values of the superheated vapor heat transfer coefficient were considerably higher than those calculated by Equation (27). This is discussed in conjunction with the superheat results, presented in Section III-E.

D.   Film Boiling Results

The film boiling regime is the last stage of the "once-through" boiling process before the beginning of the superheat region. The range of quality over which this regime exists in a test section with uniform heat flux depends on the heat flux level and on whether or not the test section contains a vortex generator insert. In tubes without inserts at relatively high heat fluxes, the transition boiling region is relatively short or non-existent and the film boiling region extends from just after the critical heat flux point to the beginning of the superheat region. At low heat flux levels or in test sections containing inserts, the transition boiling region may extend from the critical heat flux point to nearly the superheat region with only a very short film boiling region.

The film boiling region is characterized by relatively steady and high wall-to-fluid temperature differences, which are in the same order as those for the superheat region. This would be expected, since in the film boiling region the wall is believed to be blanketed with a layer of locally superheated vapor. The liquid phase probably exists as droplets or mist entrained in the vapor core. If the wall is blanketed with superheated vapor, then the film boiling data might be expected to correlate in a manner similar to that for single phase vapor. The film boiling data obtained are tabulated in Table 5. Figure 58 is

a plot of this data compared with the Dittus-Boelter equation [22]:

$$\frac{h}{C_{pb}G} \left(\frac{C_p \mu}{k}\right)_b^{0.6} = 0.023 \left(\frac{GD}{\mu}\right)_b^{-0.2} \qquad (28)$$

In this plot, the flow parameters are the "axial" values defined by:

$$N_{Re} = \frac{GD_T}{\mu} \qquad (28a)$$

$$G = \frac{\text{Flow Rate}}{\text{Net Flow Area Normal To Pipe Centerline}} \qquad (28b)$$

$$D_T = \text{Test Section Inside Diameter} \qquad (28c)$$

The fluid properties for each of these data points were evaluated as follows:

1. All fluid properties were evaluated at the measured fluid temperatures.

2. The vapor specific heat, C_{pb}, was the saturation value from Reference 20.

3. The transport properties k_b and μ_b were the vapor values from Reference 21.

The film boiling measurements, reduced using the axial flow parameters, are considerably higher than the Dittus-Boelter single-phase prediction, particularly for the test sections containing inserts (Figure 58). In order to account for the effect of the helical inserts, the helical flow parameters derived in Reference 3 were introduced into the Dittus-Boelter equation, which results in the following equations.

$$\frac{h}{C_{pb}\, G_{HM}} \left(\frac{C_p \mu}{k}\right)_b^{0.6} = 0.023 \left(\frac{G_{HM}\, D_e}{\mu_b}\right)^{-0.2} \qquad (29)$$

where

$$G_{HM} = G \sqrt{1 + \left(\frac{\pi}{P/D}\right)^2} \qquad (30)$$

$$D_e = \frac{4\ (\text{Net Flow Area Normal to Pipe Centerline})}{\text{Wetted Perimeter in Plane Normal to Pipe Centerline}} \qquad (31)$$

Figure 59 is a plot of the film boiling data evaluated using the helical flow parameters. Although the data are still high relative to the Dittus-Boelter equation they do group together with less scatter around the values for the tube without insert. The apparent increase in performance in the film boiling region may be a result of entrained liquid droplets striking the wall, particularly for test sections 4 and 5, which contained vortex generator inserts.

E. Superheated Vapor Results

Superheated vapor conditions were obtained for the first time during the experiments with Test Section No. 3 (.423"ID, No Insert). Exploratory measurements of the superheated vapor heat transfer coefficient were made in Test Sections 3, (.423"ID, No Insert), 4 (.738"ID with annular plug and helix P/D = 2) and 5 (.742"ID with wire-wrapped plug and wire coil P/D = 2). These data are tabulated in Table 6.

The existence of a superheated vapor condition was inferred when a power increase at constant flow and pressure resulted in a corresponding increase in fluid temperature. Examination of the superheat data revealed a discrepancy between the measured enthalpy increase of the fluid and the calculated energy input based on the electrical power measurements (corrected for heat losses) together with the flow rate measurement. The discrepancy was that the calculated energy input was 8 to 17% greater than the measured enthalpy increase of the

fluid. This energy balance discrepancy was assumed to be due to an error in flow rate measurement. With this assumption, the question was asked: For a given superheated vapor temperature rise, what flow rate would be required to be consistent with the measured superheat? The required flow rate was calculated from an energy balance between the preboiler inlet and the point in the test section where the superheat was measured. This flow rate is given by:

$$W = \frac{q}{h_{g2} - h_{\ell 1} + \bar{C}_p (\Delta T)_{SH}}$$ (32)

where

q = Net power input up to the measuring station, Btu/sec

h_{g2} = Vapor enthalpy at the saturation temperature, Btu/hr

$h_{\ell 1}$ = Liquid enthalpy at the preboiler inlet, Btu/hr

$\bar{C}_p$ = Average superheated vapor specific heat, Btu/lb-°F

$(\Delta T)_{SH}$ = Degrees of superheat, °F

The flow rates calculated from Equation (32) were from 8% to 17% higher than the corresponding measured flow rates. The data presented in Table 6 have been corrected such that the flow rates are consistent with the measured superheat.

In order to investigate the validity of the assumption that the discrepancy in the energy balance was due to an error in flow rate, an independent check was made with the data from Test Section No. 4 (.738"ID with annular plug and helix P/D = 2). This was done by selecting runs in which superheated vapor conditions existed at two axial measuring stations in the test section (thermocouple numbers 34 and 35 in Figure 11). The power input to the vapor between these stations was calculated from:

$$q_{34-35} = W \bar{C}_p (\Delta T)_{34-35}$$ (33)

The corresponding net electrical power input between stations was
then calculated assuming uniform test section heat flux and correcting for
heat losses. It turned out that the ratio of the electrical power (corrected
for heat losses) to the power given by Equation (33) was within about 1% of the
corresponding ratio of calculated flow rate (Equation 32) to measured flow rate.
This means that if the flow rate used in Equation (33) were that calculated
from Equation (32), then the energy balance between the two superheated vapor
stations would check within about 1%. Although this agreement doesn't
constitute proof, it strongly suggests that the error in the energy balance is
due primarily to the flow rate. This is so because the flow rate calculated
from Equation (32) is a function of the preboiler power and the test section
power, whereas the power in Equation (33) is a function of the test section
power only. Since the preboiler power and the test section power are measured
independently, it seems unlikely that errors in power would combine in such a
way that the two energy balances described above would agree.

The flowmeter in the Cb-1%Zr Facility was calibrated from an energy
balance during single-phase liquid runs. During these runs the temperature
rise across the test section was on the order of 900°F. Any error in the values
of the liquid enthalpy used in this energy balance would appear as an error in
flow rate. The values of liquid enthalpy used in the flowmeter calibrations
were the preliminary NRL data from Reference 5. The final NRL data from
Reference 20 shows some discrepancy with the earlier data. Specifically, on
the basis of a liquid temperature rise from 1400°F to 2000°F, the liquid
enthalpy change calculated from the earlier data (Reference 5) would be 8%
higher than the corresponding change calculated from the final data (Reference 20).
Assuming that the final data are correct, this means that the flow rates should
be on the order of 8 to 17% low, which is in agreement with the discrepancy
observed during the superheated vapor runs.

Initial evaluation of the superheated vapor results consisted of comparing
the data with conventional single-phase predictions. Test data for heating

or cooling of fluids (flowing turbulently inside tubes) have been correlated by the following three widely-used equations given in McAdams (22).

The Dittus-Boelter Equation:

$$\frac{h}{C_{pb}\,G}\left(\frac{C_p\,\mu}{k}\right)_b^{0.6} = 0.023\left(\frac{GD}{\mu}\right)_b^{-0.2} \tag{34}$$

The Colburn Equation:

$$\frac{h}{C_{pb}\,G}\left(\frac{C_p\,\mu}{k}\right)_f^{2/3} = 0.023\left(\frac{GD}{\mu}\right)_f^{-0.2} \tag{35}$$

The Sieder-Tate Equation:

$$\frac{h}{C_{pb}\,G}\left(\frac{C_p\,\mu}{k}\right)_b^{2/3}\left(\frac{\mu_w}{\mu_b}\right)^{0.14} = 0.023\left(\frac{GD}{\mu}\right)_b^{-0.2} \tag{36}$$

In these equations, the subscript b, w or f indicates that the fluid property in question is to be evaluated at the bulk fluid temperature, the wall temperature, or the average "film" temperature, respectively. As pointed out by McAdams (22), the available data (at moderate ΔT) for tubes are correlated within a maximum deviation of $\pm$ 40% by the three equations.

Sutherland (23) measured heat transfer coefficients in high pressure superheated steam and correlated the data with the following equation:

$$\frac{h}{C_{pb}\,G}\left(\frac{C_p\,\mu}{k}\right)_b^{0.4}\left(\frac{T_w}{T_b}\right)^{0.575} = (0.021)\left(\frac{GD}{\mu}\right)_b^{-0.2} \tag{37}$$

Modifications of the Dittus-Boelter equation will be used as bases of reference for the superheated vapor results from this investigation.

Figure 60 is a plot of the measured superheat data from Test Sections No. 3 (0.423" ID, No Insert), No. 4 (0.738" ID with helix, P/D = 2) and No. 5 (0.742" ID with wire coil, P/D = 2). In this plot, no attempt is made to account for the

effect of the helical insert in Test Section 4 or the wire coil in Test Section 5. Rather, the flow parameters are the "axial" values defined by

$$N_{Re} = \frac{GD_T}{\mu}$$ (38)

$$G = \frac{\text{Flow Rate}}{\text{Net Flow Area Normal to Pipe Centerline}}$$ (39)

$$D_T = \text{Test Section Inside Diameter}$$ (40)

The fluid properties for each of these data points were evaluated as follows:

1. All fluid properties were evaluated at the measured vapor temperature.

2. The vapor specific heat, C_{pb}, was the <u>superheat</u> values from Reference 20.

3. The transport properties k_b and μ_b were the vapor values from Reference 21.

The data have been plotted in Figure 60 using "axial" flow parameters in order to compare the measurements with the corresponding prediction for a plain tube with no insert. As can be seen, the measurements are as much as three times the values predicted for plain tubes using Equation (34). Some possible reasons why the measured coefficients are higher than the corresponding plain tube predictions are as follows:

1. Direct thermal radiation from the pipe wall to the gas. The significance of this mechanism is difficult to predict since emissivity data for gaseous potassium are not available.

2. Thermal radiation from the pipe wall to the insert, followed by convection from the insert to the vapor. This effect will be discussed in more detail below.

3. The possible effect of entrained liquid droplets.

4. Uncertainties in the values of the thermodynamic and transport properties of potassium, particularly for the superheated vapor.

5. Fluid property variation effects in the vicinity of the wall. As pointed out by McAdams (Reference 22), Equations (34), (35) and (36) are applicable only for moderate ΔT. The wall-to-fluid temperature differences for the data in Figure 60 range from about 300°F to 725°F.

6. Experimental error.

7. The effect of the vortex generator inserts, for Test Sections No. 4 and 5.

In order to obtain an estimate of the effect of thermal radiation from the pipe wall to the insert centerbody, consider the physical situation depicted in Sketch C below.

Sketch-C
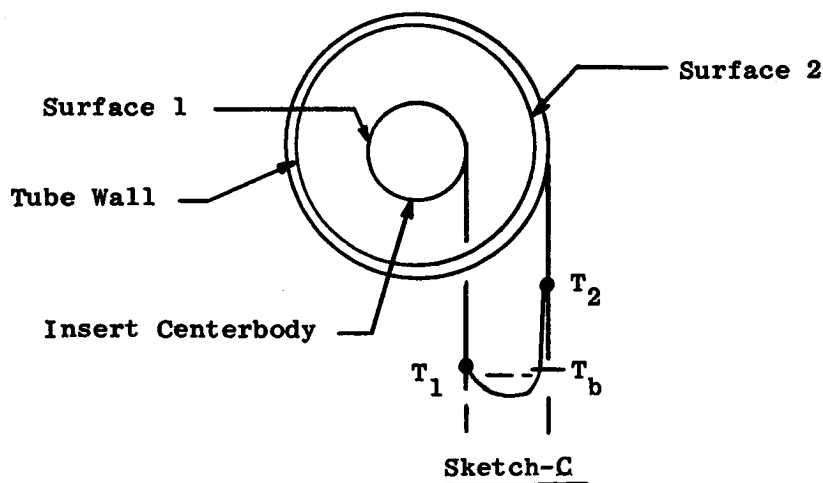
Here, it is assumed that fluid is flowing in the annulus between surfaces 1 and 2 and the fluid temperature distribution is as shown. The total rate of heat transfer at surface 2 is due to radiation and forced convection.

$$q = q_r + q_{c2} \tag{41}$$

where

q = total rate of heat transfer at surface 2

q_r = rate of heat transfer by radiation

q_{c2} = rate of heat transfer by forced convection

From the definition of the measured superheated vapor heat transfer coefficient h_m, the total rate of heat transfer is given by:

$$q = h_m A_2 (T_2 - T_1) \tag{42}$$

Assuming that the gas neither absorbs nor emits thermal radiation, then

$$q_r = \sigma A_1 \mathcal{F}_{12} (T_2^4 - T_1^4) \tag{43}$$

The forced convection heat transfer from surface 2 is given by:

$$q_{c2} = h_{c2} A_2 (T_2 - T_b) \tag{44}$$

Finally, assuming that the energy radiated from surface 2 to surface 1 is transferred to the fluid by convection, gives:

$$q_r = h_{c1} A_1 (T_1 - T_b) \tag{45}$$

Combining Equations 41, 42, 43, 44 and 45 results in:

$$\frac{h_m}{h_{c2}} = \left[\frac{A_1}{h_{c2} A_2} + \frac{1}{h_{c1}} \right] \frac{\sigma \mathcal{F}_{12} (T_2^4 - T_1^4)}{(T_2 - T_1)} + 1 \tag{46}$$

Assuming that $h_{c2} = h_{c1}$, then

$$\frac{h_m}{h_{c2}} = \frac{1}{h_{c2}} \left[\frac{A_1}{A_2} + 1 \right] \frac{\sigma \mathcal{F}_{12} (T_2^4 - T_1^4)}{(T_2 - T_1)} + 1 \qquad (47)$$

where $\mathcal{F}_{12}$ is the gray-body configuration factor between surfaces 1 and 2. For concentric cylinders,

$$\mathcal{F}_{12} = \frac{1}{\frac{1}{\epsilon_1} + \frac{A_1}{A_2} (\frac{1}{\epsilon_2} - 1)} \qquad (48)$$

Equation (47) predicts the ratio of the measured heat transfer coefficient h_m to the "true" convective heat transfer coefficient, h_{c2}, when there is direct thermal radiation between surfaces 1 and 2. Figure 61 is a plot of this ratio as a function of $T_2 - T_1$ with $T_1 = 2100°F$ and h_{c2} as a parameter. As can be seen, the radiation effect can be very significant, particularly at low values of h_{c2}. The thermal radiation has two effects, both of which tend to increase the underlined measured heat transfer coefficients. These effects are:

1. Due to radiation, the centerbody temperature T_1 (which is measured and used in calculating h_m) can be higher than the bulk fluid temperature, T_b.

2. The total rate of heat transfer at surface 2 (which is measured and used in calculating h_m) is greater than the rate of heat transfer due to forced convection alone.

In order to account for the radiation effect, a forced convection heat transfer coefficient was calculated from Equation (47) as follows:

$$h_{c2} = h_m - \left[\frac{A_1}{A_2} + 1\right] \frac{\sigma \mathcal{F}_{12} (T_2^4 - T_1^4)}{(T_2 - T_1)} \qquad (49)$$

The gray-body configuration factor, $\mathcal{F}_{12}$, was evaluated from Equation (48) using emissivity data for Cb-1%Zr from Reference 24, which is plotted in Figure 62. Figure 63 is a plot of the superheat data corrected for the radiation effect, again using the "axial" flow parameters. As can be seen, the experimental results are now in better agreement with the plain tube Dittus-Boelter prediction, Equation (34), although they are still higher than the equation gives.

The effect of the vortex generator inserts was accounted for by introducing the helix parameters, following the procedure given in Reference 3, for which:

$$G_{HM} = G \sqrt{1 + (\frac{\pi}{P/D})^2} \qquad (50)$$

$$D_e = \frac{4 \text{ (Net Flow Area Normal to Pipe)}}{\text{Wetted Perimeter in Plane Normal to Pipe}} \qquad (51)$$

For Test Section No. 4, containing a helical insert, the equivalent diameter is

$$D_e = \frac{D_2 \left[1 - (\frac{D_{CB}}{D_T})^2\right]}{1 + \frac{D_{CB}}{D_T} + \frac{1}{\pi}\left[1 - \frac{D_{CB}}{D_T}\right]} \qquad (52)$$

For Test Section No. 5, containing a wire coil, the equivalent diameter is

$$D_e = D_T - d \qquad (53)$$

Figure 64a is a plot of the superheat data corrected for radiation effects and using the helix parameters defined above. The data from Test Section No. 4 (.738"ID with annular plug and helix P/D = 2) are in better agreement with the Dittus-Boelter prediction, Equation (34), although the data are still higher

than values given by Equation (34).

It can be seen from Figure 64a that use of the helical flow parameters brings all of the data closer to the values calculated using Equation (34), but the wire coil data from Test Section No. 5 (.742"ID with wire-wrapped plug and wire coil P/D = 2) remain just as far from the other data as in the preceding graphs of Figures 60 and 63. The results of Sams (25) for air flowing in tubes with wire coils suggested that the reason the wire coil data have higher coefficients than the other data, as shown in the Figures, might be due to the effect of increased turbulence caused by the wire coil. This possibility was therefore examined, as follows.

The single-phase liquid pressure drop data obtained in Test Section No. 5 (.742"ID with wire-wrapped plug and wire coil P/D = 2) which are presented in Section III-F, show that even after the helical flow parameters are introduced, the friction factors in the wire coil region of Test Section No. 5 are in the order of twice those calculated for smooth tubes. The Reynolds analogy predicts that the Stanton number is directly proportional to the friction factor (22). Using this idea, a relationship between measured (m) and predicted (p) heat transfer results can be written as

$$\frac{(N_{St})_m}{(N_{St})_p} = \frac{f_m}{f_p} \tag{54}$$

where f_m is the single-phase friction factor measured for the test section and f_p is the corresponding value calculated for a smooth surface tube. Combining Equation (54) with the Dittus-Boelter equation, Equation (34), results in

$$\frac{(N_{St})_m \, N_{Pr}^{0.6}}{f_m/f_p} = .023 \, N_{Re}^{-0.2} \tag{55}$$

The liquid water pressure drop data obtained with Test Section No. 5

(Section III-F) indicate that for this test section the friction ratio in Equation (55) is approximately $f_m/f_p = 2$.

Figure 64b is a plot of the superheated vapor heat transfer data evaluated using the Reynolds analogy expressed by Equation (55). The data in Figure 64b are corrected for radiation effects using Equation (49) and they were calculated assuming helical flow for Test Sections No. 4 (.738"ID with annular plug and helix P/D = 2) and 5 (.742"ID with wire-wrapped plug and wire coil P/D = 2) using Equations (50) and (51). The friction factor ratio was assumed to be $f_m/f_p = 1.0$ for Test Sections No. 3 (.423"ID, No Insert) and No. 4 (.738"ID with annular plug and helix P/D = 2), and $f_m/f_p = 2.0$ for Test Section No. 5, based on the single-phase pressure drop results given in Section III-F for Test Sections No. 4 (.738"ID with Annular plug and helix P/D = 2) and No. 5 (.742"ID with wire-wrapped plug and wire coil). As shown by Figure 64b, this treatment using Equation (55) results in the best correlation of the data. The helical insert data from Test Section No. 4 and the wire coil data from Test Section No. 5 are brought into rather good agreement with each other. Apparently some additional effects remain to be accounted for, since all of the data still have coefficients which are higher than predicted using Equation (55).

F. Pressure Drop Results

In Test Sections No. 4 (.738"ID with annular plug and helix P/D = 2), and No. 5 (.742"ID with wire-wrapped plug and wire coil P/D = 2), axial fluid temperature distributions were measured with thermocouples contained within the centerbody of the inserts. During two-phase operation, these fluid temperature measurements were used to infer (assuming thermodynamic equilibrium) the axial pressure distributions from a knowledge of the vapor pressure-temperature relationship for saturated potassium. Part of the test plan for Test Sections 4 and 5 was to determine the friction pressure drop in adiabatic two-phase flow. These tests were conducted by holding the average system pressure and the flow rate constant while the test section quality was varied

by changing the preboiler power. Power to the test section heater was increased only enough to balance the heat losses, thus providing nearly adiabatic conditions in the test section. All of the adiabatic pressure drop tests were conducted at a saturation temperature of about 1800°F. Results were obtained for one mass velocity in Test Section No. 4 and for two mass velocities in No. 5.

Due largely to the work of R.C. Martinelli (26, 27, 28 and 29), it has become customary in the field to present two-phase frictional pressure drop data in the form of a pressure gradient ratio, $\emptyset$, defined by

$$\emptyset = \frac{(dP/dZ)_{TPF}}{(dP/dZ)_{o}} \qquad (56)$$

where

$(\frac{dP}{dZ})_{TPF}$ = The measured two-phase frictional pressure gradient

$(\frac{dP}{dZ})_{o}$ = The single-phase pressure gradient which would result if liquid had been flowing in the duct at a rate equal to the actual total mixture flow rate.

In order to calculate the single-phase pressure gradient, the friction factor - Reynolds number relationship for the particular geometry must be known. The inserts in Test Sections 4 (.738"ID with annular plug and helix P/D = 2) and 5 (.742"ID with wire-wrapped plug and wire coil P/D = 2) were such that four different flow geometries were involved, as listed below:

Test Section No. 4 -
    - Annular geometry over the inlet half of the test section
    - Helix geometry over the outlet half of the test section

Test Section No. 5 -

    - Annular-helix geometry over the inlet half of the test section

    - Helical wire coil over the outlet half of the test section

With the exception of the annular region of Test Section No. 4, there is not a great deal of single-phase pressure drop data available for these particular flow geometries. Consequently, after their removal from the loop, Test Sections 4 and 5 were instrumented with pressure taps and water tests were conducted to determine the single-phase friction factors. This data was used in evaluating the two-phase potassium results.

SINGLE-PHASE PRESSURE DROP

In 1913, Blasius (30) correlated a large body of single-phase pressure drop data for smooth, plain tubes (no inserts). The Blasius correlation, which is valid in the Reynolds number range from about 3000 to 100,000, is given by

$$f = \frac{0.316}{N_{Re}^{\frac{1}{4}}} \tag{57}$$

where f is the Darcy-Weisbach friction factor defined by

$$f = \frac{\Delta P}{(\frac{L}{D}) \frac{G^2}{2g_c \rho}} \tag{58}$$

In flow channels with non-circular cross-sections, the usual procedure is to introduce the concept of an "equivalent diameter" defined by

$$D_e = \frac{4(\text{cross-sectional Area Normal to Duct Centerline})}{\text{Wetted Perimeter in Plane Normal to Duct Centerline}} \tag{59}$$

If the flow channel does not deviate severely from a circular cross-section, introduction of the equivalent diameter reduces the channel to an "equivalent" circular channel and the pressure drop in turbulent flow can be calculated with

reasonable accuracy using Equation (57). With the exception of the annular region of Test Section No. 4, it has been found that the equivalent diameter concept alone does not correlate the pressure drop results in the rather complicated flow geometries encountered in Test Sections 4 and 5. For these geometries, additional concepts are introduced in order to correlate the single-phase data.

Single-Phase Pressure Drop in Test Section No. 4. Figure 11 shows the locations of the pressure taps during the water pressure drop test. The results of this test are presented in Table 7. For each flow rate, the incremental pressure drops (e.g., $P_1 - P_2$, $P_2 - P_3$,..) were measured. For the higher flow rates, $P_0 - P_1$ exceeded the limit of the manometer (due to the large change in flow cross-section) and was not measured. The overall pressure drop, $P_0 - P_{10}$, was measured independently as a check on the incremental pressure drops. In those runs for which $P_0 - P_1$ was measured, the sum of the incremental pressure drops was within 3% of the measured overall drop.

Figure 65 is a plot of the experimental single-phase friction factors for the annular region of Test Section No. 4 (.738"ID with annular plug and helix P/D = 2). The annular region friction factors were calculated from:

$$f = \frac{P_x - P_y}{(\dfrac{Z_y - Z_x}{D_e})(\dfrac{G^2}{2g_c \rho_f})} \tag{60}$$

where

$P_x - P_y$ = Pressure drop from station x to station y

$Z_y - Z_x$ = Axial distance between x and y

The Reynolds number in the annular region is defined by:

$$N_{Re} = \frac{G\ D_e}{\mu}$$

(61)

As can be seen from Figure 65, the friction factors show a significant entrance effect, as indicated by f decreasing with increased L/D_e. At the largest L/D, the data are in good agreement with the Blasius correlation, indicating that use of the hydraulic diameter concept reduces the annular results to an equivalent smooth tube in this case. The manner in which the entrance effect is taken into account in evaluating the two-phase potassium results will be discussed in a following section.

Figure 66 is a plot of the experimental single-phase friction factor for the helix region of Test Section No. 4. Here, the friction factor and Reynolds number are the "axial" values defined by:

$$f = \frac{P_x - P_y}{\left(\frac{Z_y - Z_x}{D_T}\right)\left(\frac{G^2}{2g_c \rho_f}\right)}$$

(62)

and

$$N_{Re} = \frac{GD_T}{\mu}$$

(63)

where

$$G = \frac{\text{Flow Rate}}{\text{Net Flow Area Normal to Pipe Centerline}}$$

(63a)

Also shown in Figure 66 is the Blasius correlation along with lines representing the water data of Peterson (3) and that of Greene (19). The data in the helix region of Test Section No. 4 again have a rather large entrance effect. Peterson's data are believed to be fully developed values since in all cases the L/D was greater than 90. Gambill, Bundy, and Wansbrough (31) investigated

pressure drop for water in tubes with internal twisted tapes and derived equivalent parameters to account for the effects of twist ratio and tube diameter. Peterson (3) derived the following helix parameters.

$$L_{HM} = (Z_y - Z_x) \sqrt{1 + (\frac{\pi}{P/D})^2} \qquad (64)$$

$$D_e = \frac{D_2 \left[1 - (\frac{D_{CB}}{D_T})^2\right]}{1 + (\frac{D_{CB}}{D_T}) + \frac{1}{\pi} \left[1 - \frac{D_{CB}}{D_T}\right]} \qquad (65)$$

$$G_{HM} = G \sqrt{1 + (\frac{\pi}{P/D})^2} \qquad (66)$$

Using these parameters, the following equivalent friction factor and Reynolds number can be defined for helical flow.

$$f_e = \frac{P_x - P_y}{(\frac{L_{HM}}{D_e}) \frac{G_{HM}^2}{2g_c \rho}} \qquad (67)$$

and

$$(N_{Re})_e = \frac{G_{HM} D_e}{\mu} \qquad (68)$$

Figure 67 is a plot of the "equivalent friction factor", defined by Equation (67), as a function of the "equivalent Reynolds Number", defined by Equation (68). The fully developed values are in fairly good agreement with the Blasius smooth tube correlation, Equation (57). These results, together with those from Reference 3 (shown in Figure 67), indicate that the method using Equations (67) and (68)

adequately correlates the data for test sections with helical inserts, for Reynolds numbers less than 10^5. For Reynolds numbers greater than 10^5 the Blasius correlation, Equation (57), may underpredict the friction factor, as it does for smooth tubes with no inserts at Reynolds numbers greater than 10^5 (32).

Single-Phase Pressure Drop In Test Section No. 5. Results of the single-phase water test for Test Section No. 5 (.742"ID with wire-wrapped plug and wire coil P/D = 2) are presented in Table 8. Figure 13 shows the locations of the pressure taps used for the test. The wire-wrapped plug region at the inlet of Test Section No. 5 was essentially the same as a helix insert with a large centerbody. Consequently, the single-phase friction factors in this region were calculated using the helix parameters discussed previously and the results are plotted in Figure 68. The rather large L/D effect is again apparent. The friction factors for the largest L/D are close to the Blasius smooth tube line.

The wire coil region of Test Section No. 5 forms a flow path which is neither helical nor like the straight tube, since the fluid could flow in a straight line down the central region as well as in a helical path adjacent to the wall. Figure 69 is a plot of the friction factors in the wire coil region, evaluated as if it were a straight pipe. This plot shows the large increase in friction factor caused by the wire coil. Sams (25) investigated the pressure drop in this type of geometry for various wire diameters and pitch-to-diameter ratios. Sams' results also show the large increase in friction factor, but no general correlation of the data was offered. In an attempt to correlate the effects of wire pitch-to-diameter ratio, an equivalent diameter was calculated from the usual definition, given by Equation (59). The length used was L_{HM}, given by Equation (64) and the mass velocity was G_{HM}, given by Equation (66). The results are plotted in Figure 70 for the wire coil region. The experimental friction factors are about twice the values predicted by the Blasius smooth tube correlation, given by Equation (57).

Summary of Single-Phase Pressure Drop Results. Figure 71 is a plot of the fully developed friction factors for the four geometries in Test Sections 4 (.738 ID with annular plug and helix P/D = 2) and 5 (.742"ID with wire wrapped plug and wire coil P/D = 2). In this plot, the flow parameters are the axial values and the friction factors are evaluated as if the test section were a plain tube with no insert. This type of plot shows the large increase in pressure drop due to the inserts, particularly in the wire-wrapped plug region of Test Section No. 5. Evaluation of the same data assuming helical flow, using Equations (59), (67) and (68) gives the results shown in Figure 72. Except for the wire coil region of Test Section No. 5, the method succeeds reasonably well in correlating results from the various geometries to values for an equivalent plain tube. The wire coil friction factors based on equivalent parameters are about twice the corresponding Blasius prediction (Equation 57). This is probably a result of the increased turbulence introduced by the wire coils in Test Section No. 5.

TWO-PHASE PRESSURE DROP

The two-phase friction pressure gradient multiplier data obtained in Test Sections 4 (.738 ID with annular plug and helix P/D = 2) and 5 (.742"ID with wire wrapped plug and wire coil P/D = 2) are compared with values from the Martinelli model (29) modified for potassium and values from a homogeneous flow model (K = 1). Two-phase multipliers from the modified Martinelli model are plotted in Figure 73 and those from the homogeneous model are plotted in Figure 74. Both of these models are derived in Reference 10. The homogeneous model, from which the curves in Figure 74 were calculated, is expressed by

$$\emptyset = \frac{1 + x\left(\dfrac{\rho_f}{\rho_g} - 1\right)}{\left[1 + x\left(\dfrac{\mu_f}{\mu_g} - 1\right)\right]^{\frac{1}{4}}} \qquad (69)$$

where $\emptyset$ is as defined by Equation (56)

Two-Phase Pressure Drop In Test Section No. 4. The results of the
adiabatic pressure drop test for Test Section No. 4 (.738" ID with annular
plug and helix P/D = 2) are presented in Table 9. The single-phase pressure
gradient, used in calculating the two-phase multipliers, was evaluated from
the results of the water tests. The entrance effect observed in the water
tests was taken into account by assuming that the same effect existed during
the two-phase tests. The two-phase potassium pressure drop data were obtained
using the thermocouples in the test section insert, the locations of which are
shown in Figure 11. The single-phase pressure drops used for the evaluations were
calculated for potassium using the friction factors determined by the water tests
for the region of the test section which coincided with the insert thermocouple
locations. Figure 11 shows the following correspondence between the single-
phase pressure measurement locations and the locations of the insert thermocouples
used to determine the two-phase pressure drop.

Locations for Single-Phase Tests	Locations for Two-Phase Tests
1 - 4	31 - 32
5 - 7	33 - 34
7 - 9	34 - 35

Single phase friction factors were calculated from the water data based on
pressure drop measurements obtained between locations 1 - 4, 5 - 7, and 7 - 9.
These values are plotted in Figures 75 and 76 for the annular region and the helix
region, respectively, and were used in calculating the two-phase multipliers
from Test Section No. 4 (.738" ID with annular plug and helix P/D = 2).

Figure 77 is a plot of the two-phase multipliers obtained in the annular
region of Test Section No. 4 (.738" ID with annular plug and helix P/D = 2).
Also shown are 1800°F predictions based on the modified Martinelli model
(Figure 73) and the homogeneous model (Figure 74). The data for the annular
region fall somewhat below the 1800°F homogeneous model prediction. This could

be partly due to a temperature effect since the actual data were obtained at average temperatures which increased from about 1790°F at the lowest quality to 1819°F at the highest quality.

Figure 78 is a plot of the data obtained in the helix region of Test Section No. 4 (.738" ID with annular plug and helix P/D = 2). These data generally fall between the homogeneous model and the Martinelli prediction. The apparent lesser dependence on vapor quality may again be due to temperature variations. For the helix data, the average temperature increased from 1787°F at the lowest quality to 1819°F at the highest quality.

Two-Phase Pressure Drop in Test Section No. 5. The results of the two-phase adiabatic pressure drop test in Test Section No. 5 (.742" ID with wire wrapped plug and wire coil P/D = 2) are presented in Table 10. Figure 79 is a plot of the two-phase results in the wire-wrapped plug region. Most of the data are correlated well by the homogeneous model prediction. The data which fall below the homogeneous line in Figure 79 were taken near the inlet where entrance effects may have been present. The location of the thermocouples by which the two-phase pressure drops were determined are shown in Figure 13. The procedure used for determining the two-phase friction multipliers was the same as that used for Test Section No. 4 (.738" ID with annular plug and helix P/D = 2).

It will be noted from Table 10 that the temperatures at the tip of the plug (T/C-34,35) and at the test section exit (T/C-36, 37, 38) indicate a slightly negative pressure drop in the wire coil region of Test Section No. 5. It is believed that this is because the temperature measured at the tip of the plug is the saturation temperature corresponding to the pressure in the plug region. There is probably a net pressure rise due to the area change from the plug region to the wire coil region, which is not indicated by the temperature measured at the tip of the plug. For this reason the two-phase pressure changes indicated for the wire coil region are not the actual friction pressure drop. Thus, these data were not treated further.

Summary of Two-Phase Pressure Drop Results. The two-phase adiabatic friction pressure drop data from Test Sections No. 4 (.738"ID with annular plug and helix P/D = 2) and 5 (.742"ID with wire-wrapped plug and wire coil P/D = 2) are plotted together in Figure 80. As can be seen, the data are in fair agreement with the homogeneous model prediction from Figure 74 and fall somewhat below the modified Martinelli model prediction from Figure 73.

G. Boiling Inception and Stability

Instabilities, as manifested by oscillations in loop flow rate, pressure and dump tank level, were sometimes observed during test operation of the Cb-1%Zr facility. These instabilities, at times, severely limited the range of loop operation. In an effort to gain further understanding of the cause and nature of the instabilities, careful observation of the loop behavior associated with some of the unstable operation was done, including recording of both the conditions leading up to the instability and the resulting loop oscillations or excursions in pressure and flow rate. In addition, an analytical effort to ascertain the mechanism which triggered the instability was made, and a qualitative understanding of the system behavior both in terms of the cause of the instability and the resulting loop behavior was sought. In those cases in which an operational method was found which would alleviate the instability, an understanding of the remedy was also sought. The results of this effort on two-phase flow stability, done in association with the boiling heat transfer tests in the Cb-1%Zr Facility, are presented in this section. Specifically, the Ledinegg stability criterion (33) is developed in detail and applied to the Cb-1%Zr Loop in an attempt to determine whether the type of instability described by Ledinegg's analysis likely occurred in the Cb-1%Zr Loop operation. Following this, the results from some specific tests aimed at investigating the effect on the system behavior of liquid superheat at boiling inception and at the boiling boundary in two-phase operation are presented.

LEDINEGG STABILITY CRITERION

In Figure 81, several curves of two-phase pressure drop (calculated using the homogeneous flow model given in Reference 10 and Figure 74) plotted against flow rate for forced convection boiling of potassium in Test Section No. 1 (.767"ID. No Insert) are shown. The distinguishing feature of these curves is that for a given value of subcooled liquid entering the test section, more than one flow rate is possible for a given pressure drop, depending on the available pressure-head characteristics. For example, in Figure 81, the available pressure-head characteristic given by line-1 intersects the pressure-loss characteristic given by curve-A at three different flow rates (points e, f and g). At lower values of the subcooling only a single flow rate is possible for a given pressure drop, with the same available pressure-head characteristic, e.g., curve-D. With an available pressure-head characteristic like that shown by line-1, operation along curves-A, B, C would tend to be unstable due to there being more than one flow rate possible for a given pressure drop. Operation along curve-D would tend to be stable.

This type of instability was first treated by Ledinegg (33) in 1938 in connection with flow in parallel-connected heated boiler-tubes lying between two headers. For this case, the available pressure drop between the headers was regarded as constant. The nature of the instability can be easily understood for this case by using Figure 81. Let line-1 represent the available pressure drop between headers, let curve-A represent the pressure-loss characteristic and assume initial operation is at point f. Then, if for any reason the flow is perturbed, say decreased, more liquid will be vaporized. The production of more vapor, (increase in vapor quality), however, raises the flow resistance although the flow rate is less. Thus, the flow rate continues to decrease until point e is reached. A similar argument starting with an increase in flow would shift the operating point from f to g. In the present example with multiple tubes in parallel, therefore, some of the tubes would be at higher flow and flooded with liquid (operation at point g) while some of the tubes would be at low flow and corresponding high vapor quality (operation at point e).

Somewhat similar considerations apply to a single tube, however, in this case the pressure drop across the boiler is not generally constant. For example, if the flow is provided by a positive displacement pump, which would give an available pressure-head characteristic like line-2 in Figure 81, the intersections with the pressure-loss characteristics are single-values and no instability would exist. For the EM pump used in the Cb-1%Zr Facility, the available pressure-head characteristic is similar to line-3 in Figure 81, for which, depending on the subcooling, more than one value of the flow rate is possible and thus instability is a possibility. A method for eliminating such instabilities is to introduce a flow restriction in the liquid-phase region between the pump and the boiler. This adds to the pressure-loss characteristic a component which increases with increasing mass velocity. This can eliminate the unstable region over a wide range of inlet subcooling, thus permitting stable operation over a considerably increased range of operating conditions.

The Ledinegg stability criterion will next be presented for several heat flux distributions. The effect of inlet orificing will then be discussed, and the criteria will be applied to the Cb-1%Zr loop.

Analytical Formulation of the Ledinegg Stability Criteria. Detailed derivations of the Ledinegg criterion are given in References 33, 34 and 35. The essential features of the derivation are given in Reference 36 which forms the basis of the present treatment. The basic assumptions are:

1. A homogeneous model (K = 1) is used for calculating the two-phase pressure drop (Reference 10 also Figure 74).

2. The variation of the single-phase friction factor with Reynolds number is neglected.

3. The rate and form of the heat input is regarded as independent of flow rate in the heated passage.

4. Vertical upflow is assumed.

5. It is assumed that pressure losses are small compared with the absolute pressure.

The geometry assumed for the analysis is shown in sketch D below.
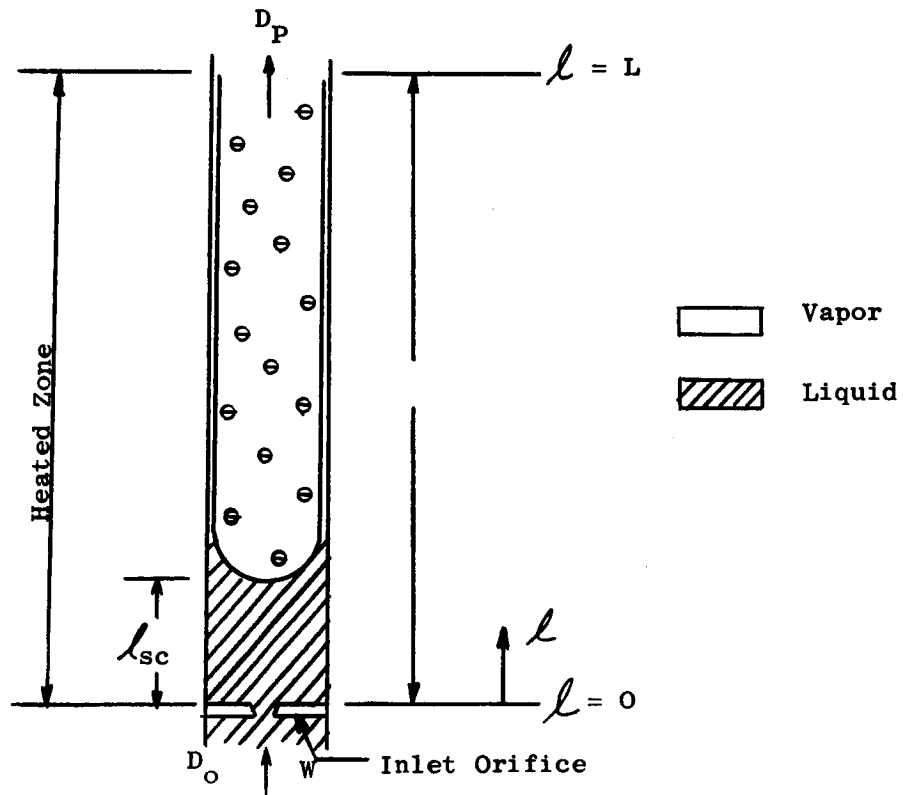
Sketch-D

Typical Test Section Geometry

The total pressure drop across the test section shown in sketch D above is the sum of the individual pressure drop components, i.e.,

$$\Delta P_{TP} = \Delta P_{or} + \Delta P_{sc} + \Delta P_a + \Delta P_{TPF} + \Delta P_{el} \tag{70}$$

where

ΔP_{TP} — total pressure drop across the test section

ΔP_{or} — single phase pressure drop across the orifice

ΔP_{sc} — single phase pressure drop in the subcooled region

ΔP_a — acceleration pressure drop in two-phase region

ΔP_{TPF} — two-phase friction pressure drop

ΔP_{el} — pressure drop due to the change in elevation

It was shown in Reference 36, that Equation (70) may be written in dimensionless form as follows:

$$\frac{\Delta P_{TP}}{\Delta P^*} = \pi_{sc}^2 \, \pi_G^2 \left\{ 1 + \frac{\pi_o}{\pi_f} + \frac{\pi_p}{\pi_G} \left[\int_{\frac{\ell_{sc}}{L}}^{1} \frac{Q'}{Q_T} \, d\left(\frac{\ell}{L}\right) + \frac{2}{\pi_f} \right] - \pi_p \pi_{sc} \left[1 - \frac{\ell_{sc}}{L} + \frac{2}{\pi_f} \right] \right\}$$

$$+ \frac{\rho_f \, L}{\Delta P^*} \left\{ \frac{\ell_{sc}}{L} + \int_{\frac{\ell_{sc}}{L}}^{1} \frac{d(\ell/L)}{\left[1 - \pi_p \pi_{sc} + \frac{\pi_p}{\pi_G} \frac{Q'}{QT} \right]} \right\} \tag{71}$$

where:

$$\pi_p = \left(\frac{\rho_f}{\rho_g} - 1\right) \qquad\qquad \pi_o = K' \left(\frac{D_T}{D_o}\right)^4$$

$$\pi_f = f \, L/D_T \qquad\qquad \pi_{sc} = \frac{c_p \, (T_{sat} - T_I)}{h_{fg}}$$

$$\pi_G = \frac{G h_{fg}}{Q_T/A_T} \qquad\qquad \Delta P^* = f \frac{L}{D_T} \left(\frac{G^*}{2g_c \rho_f}\right)^2$$

$$Q' = \text{Heat Transfer rate in region from inlet to point } \ell, \text{ Btu/hr}$$

$$G* = \frac{Q_T/A_T}{C_p (T_{sat} - T_1)}$$

$$Q_T = \text{Total heat transfer rate in boiling, Btu/hr}$$

$$K = \frac{\Delta P_{or}}{(\frac{D_T}{D_{or}})^4 \frac{G^2}{2 g_c \rho_f}}$$

$$A_T = \text{Total heat transfer area in boiler, ft}^2$$

The general procedure at this point is to substitute the particular form of heat flux distribution which is being investigated into Equation (71) and carry out the indicated integration. The resulting expression is then differentiated with respect to π_G holding all other parameters constant. The value of the subcooling at which the ΔP_{TP} vs. π_G curve becomes single valued is then obtained. In general, the inclusion of the elevation term leads to an expression which is difficult to solve for the stability condition. For this reason, the elevation component of the pressure drop will be neglected in subsequent calculations. The resulting expressions will be strictly applicable only when the friction and momentum pressure losses are large compared with the buoyancy effects. In Reference 36 three heat flux distributions were considered, as follows:

Case 1: <u>All the heat added at the inlet</u>
For this case $\ell_{sc}/L \longrightarrow 0$ and $Q'/Q_T \longrightarrow 1$

$$\frac{\Delta P_{TP}}{\Delta P*} = (1 + \frac{\pi_o}{\pi_f} - \pi_p \pi_{sc} - 2 \frac{\pi_p \pi_{sc}}{\pi_f}) \pi_{sc}^2 \pi_G^2$$

$$+ (\pi_p + \frac{2 \pi_p}{\pi_f}) \pi_{sc}^2 \pi_G \tag{72}$$

Following Ledinegg (33), the criterion for stability is:

$$\frac{\pi_p\,\pi_{sc}}{1 + \dfrac{\pi_o}{\pi_f}} \;\le\; \frac{1}{\frac{1}{2} + \dfrac{1}{\pi_f}} \tag{73}$$

Case 2: <u>All the heat added at the exit</u>

For this case $\ell_{sc}/L \longrightarrow 1$ and $Q'/Q_T \longrightarrow 0$

$$\frac{\Delta P_{TP}}{\Delta P^*} = (1 + \frac{\pi_o}{\pi_f} - \frac{2\,\pi_p\,\pi_{sc}}{\pi_f})\,\pi_{sc}{}^2\,\pi_o{}^2 + (\frac{2\pi_p}{\pi_f})(\pi_{sc}{}^2\,\pi_G) \tag{74}$$

The criterion for stability is:

$$\frac{\pi_{sc}\,\pi_P}{1 + \dfrac{\pi_o}{\pi_f}} \;\le\; \pi_f \tag{75}$$

Case 3: <u>Uniform heat flux</u>

For this case $\ell_{sc}/L \longrightarrow \pi_{sc}\,\pi_G$ and $Q'/Q_T \longrightarrow \ell/L$

$$\frac{\Delta P_{TP}}{\Delta P^*} = (\frac{1}{2}\,\pi_P\,\pi_{sc}{}^2)\,\pi_{sc}{}^2\,\pi_G{}^3 + (1 + \frac{\pi_o}{\pi_f} - \pi_P\,\pi_{sc} - \frac{2\pi_p}{\pi_f}\,\pi_{sc})\,\pi_{sc}{}^2\,\pi_G{}^2$$

$$+ (\frac{2\pi_P}{\pi_f} + \frac{\pi_P}{2})\,\pi_{sc}{}^2\,\pi_G \tag{76}$$

The criterion for stability is:

$$\frac{\pi_{sc}\,\pi_P}{1 + \dfrac{\pi_o}{\pi_f}} \;\le\; \frac{1}{1 + \dfrac{2}{\pi_f} - \sqrt{3/2}\,\sqrt{\frac{1}{2} + \dfrac{2}{\pi_f}}} \tag{77}$$

-108-

Equations (73), (75) and (77) are plotted in Figure 82. The curves are boundaries between regions of stable and unstable operation. Inspection of the curves in Figure 82 shows that peaking the heat flux toward the inlet results in a smaller region of stable operation than when the heat flux is uniform or is peaked toward the exit. Figure 82 also suggests that the effect of heat flux distribution is small for values of $\pi_f \leq 2$. Thus over most of the range of π_f Case I (all the heat added at the inlet) represents the least stable case.

Application of the Ledinegg Stability Criteria to the Cb-1%Zr Loop.
Figure 83 shows the stabilizing effect of inlet orificing at a value of $\pi_f = 1$ for Cases 1 and 3. The values of the orifice loss coefficient K' used for these calculations were obtained from Reference 37 and are shown for ease of reference in Figure 84. Also shown in Figure 83 is the range of operation used with Test Section No. 1 (.767"ID, no insert) in the Cb-1%Zr Loop for the different orifice size employed.

In general the subcooling in the Cb-1%Zr Loop was less than 1000°F at the preboiler inlet. This value was used in estimating the operating range of the loop. The value of π_f (i.e., f L/D = 1) corresponds to that obtained for the Cb-1%Zr test section at a G of 30 lb_m/sec-ft^2, f = 0.025 and an L/D ratio of about 40. This is somewhat conservative since the use of a larger L/D corresponding to the test section preboiler combination, or the use of a larger friction factor (which would be expected with inserts) result in larger values of π_f than that assumed, which, according to Figure 82, would result in a larger region of stable operation.

Examination of Figure 83 shows that with the orifice sizes and subcooling used the Ledinegg stability criterion predicts that the entire range of operation of the Loop used should be stable. Based on this it is therefore concluded that the instabilities which were observed in the Cb-1%Zr Loop tests were probably not caused by the mechanism assumed in the Ledinegg analysis.

EXPERIMENTAL STABILITY INVESTIGATIONS

Test Section No. 2 (0.740" ID, Helix Insert, P/D = 6) on February 11,
1965, the Cb-1%Zr Loop was operated for the specific purpose of obtaining
some quantitative data on previously observed loop instabilities. The
instability investigated was that associated with boiling initiation, i.e.,
the instability associated with the transition from a single-phase all
liquid system to a two-phase system. This instability was selected for two
reasons; first, it is fairly easy to reproduce in the tests and second it
involves the phenomenon of liquid superheat which might be important in
other modes of loop instability.

The tests were conducted in the following manner. The dump tank pressure
was set at about 75 psia, the argon pressure regulating valve was closed, and
the loop was operated in single phase, all liquid condition. The preheater
power was then increased until boiling began at the test section outlet. The
resulting surges in flow rate, pressure, dump tank level and temperature were
recorded on an eight channel Sanborn recorder. This test was conducted at two
values of the flow rate in order to ascertain the effect of flow rate on the
loop behavior.

The test conditions and the approximate frequency of the resulting
oscillations of the loop parameters are summarized in the table on the following
page.

The Sanborn trace for the test designated "High-Flow" in Table 11
($G = 29.7$ lb/sec-ft^2), done at a saturation temperature of about 1800°F, is
shown in Figure 85. The oscillations in pressure, temperature and dump-tank
level immediately after boiling inception have a frequency of about 0.24 cps
and rapidly disappear. The bulk liquid superheat at the boiling inception point
was about 160°F. The Sanborn trace for the test designated "Low-Flow" in
Table 11($G = 18$ lb/sec-ft^2), done at a saturation temperature of about 1820°F,
is shown in Figure 86. The bulk liquid superheat at the boiling inception

TABLE 11

RANGE OF VARIABLES FOR BOILING INCEPTION-STABILITY TESTS
WITH TEST SECTION NO. 2 (.74" I.D. with helical insert P/D = 6)

	High-Flow Test	Low-Flow Test
Flow Rate (lb_m/sec)	0.088	0.053
Test Section Mass Velocity (lb_m/sec-ft^2)	29.7	18
Initial Dump Tank Pressure (psia)	74.1	75.2
Test Section Heat Flux (Btu/hr-ft^2)	42,722	43,680
Test Section Exit Well Temperature After Boiling Inception (°F)	1797	1821
Approximate Bulk Liquid Superheat At Boiling Inception (°F)	160	200
Approximate Wall Superheat at Boiling Inception (°F)	175	211
Estimated Exit Quality After Boiling Inception (%)	4.9	5.8
Approximate Frequency of Oscillation in pressure, temperature, flow rate and dump-tank level After Boiling Inception (cycles/sec)	0.24(Disappeared)	0.24(Continued)

Test Section ID D_T, inch	0.740
Insert	Helix (P/D = 2)
Inlet Orifice Diameter D_{or}, inch	0.101

point in this case, was about 200°F. The frequency of the oscillations in pressure, temperature, flow rate and dump tank level after boiling inception were about the same as before (0.24 cps), but the oscillations continued. All of the parameters which were oscillating appear to have about the same oscillation frequency. Apparently the higher flow rate in the first test helped to stabilize the loop.

After the Low-Flow test was completed a period of about $6\frac{1}{2}$ minutes transpired before any further changes in operating conditions were made. No damping of the oscillations was apparent during this period of oscillation. The dump tank valve was then closed, with the result that the loop immediately became stable, as shown by Figure 87. When the valve was opened the loop parameters returned to the previous modes of oscillation (same frequency and amplitude). This test was subsequently repeated with results which were identical with those shown in Figure 87.

The following observations can be made regarding these tests:

1. The degree of liquid superheat prior to boiling initiation is appreciable (as indicated by Table 11). This may be understood at least qualitatively by referring to Figure 32, which is discussed in Section III-A. From Figure 32 it can be seen that a maximum cavity size of about $r_{max} = 0.01$ mils will yield a bulk superheat of the magnitude observed in the tests. Since cavities larger than this are expected to be present on the surface (see Figures 33 and 34), it may be postulated that the larger cavities have been "snuffed out" or flooded by highly subcooled liquid flowing over the surface when the loop was in a single-phase condition. The postulate seems reasonable in view of the highly wetting nature of potassium. Therefore, the initial vapors must be produced by activating the similar re-entrant cavities on the surface.

2. As a result of the high degree of bulk superheat obtained prior to boiling initiation, a substantial volume of liquid between the boiler exit and the condenser inlet is in a thermodynamically metastable condition. Therefore,

when the first vapors are produced this entire volume of liquid flashes and a considerable amount of vapor is produced. Note the almost simultaneous drop in boiler exit and condenser inlet temperatures when boiling is initiated, shown in Figures 85 and 86. It is this circumstance which results in the approximately 25 psi surge in pressure associated with boiling inception (Figures 85 and 86).

    3. Oscillations in pressure, temperature, flow rate and dump tank level occur after boiling initiation. It is not unreasonable to expect that the sudden surge of liquid into the dump-tank subsequent to boiling inception would cause the dump-tank level to oscillate about its new equilibrium position. It might be expected, however, that such oscillations in dump-tank level would be rather rapidly damped out. Such was the case for the High-Flow test, as indicated by Figure 85. However, for the Low-Flow test little damping of the oscillations in dump-tank level can be detected (Figure 86). This might be due to the fact that the single-phase liquid flow resistance is less at the lower flow rate (less orifice pressure drop). Closing the dump tank valve resulted in the loop becoming immediately stabilized. However, when the dump tank valve was again opened the loop parameters resumed the previously observed oscillations (Figure 87). This behavior was somewhat unexpected. It may be that the slight pressure difference between the dump tank and the loop was sufficient to re-excite this mode of oscillation at the lower flow rate, and that the compressible gas volume in the dump tank contributed to maintaining the steady oscillations of the loop parameters shown in Figure 87.

Test Section No. 3 (.423″ ID, no insert). If the qualitative picture of boiling initiation presented is correct, then the heat flux and flow rate would be expected to have a relatively small effect on the liquid wall superheat obtained prior to boiling initiation within the range of variation of these parameters possible in the Cb-1%Zr Facility. The significant parameter should be the loop pressure with wall superheat decreasing with increasing pressure. In order to test this hypothesis as well as to obtain data on the boiling initiation instability in a test section without an insert, three tests were conducted in Test Section No. 3 (0.42-inch ID, no insert). The range of variables for these tests are given in Table 12.

The Sanborn trace for the test designated "High-Pressure" in Table 12 (P = 201 psia, T_{sat} = 2100°F) is shown in Figure 88. As can be seen from this figure, oscillations in the wall temperature occur immediately after boiling initiation and persist for about 3 minutes. The wall temperature then became steady and the system proceeded into stable boiling. The wall superheat at boiling inception (about 125°F) is somewhat less than that obtained at the same mass velocity at P = 80 psia, T_{sat} = 1800°F in Test Section No. 2 (.74" ID with helical insert P/D = 6). (about 175°F).

TABLE 12

RANGE OF VARIABLES FOR BOILING INCEPTION-STABILITY TESTS WITH TEST SECTION NO. 3 (.423 I.D., no insert)

	High Pressure Test	Intermediate Pressure Test	Low Pressure Test
Date	3/19/65	4/2/65	4/2/65
Initial Dump Tank Pressure (psia)	201	80	27
Flow Rate (lb_m/sec)	0.03	0.043	0.045
Mass Velocity (lb_m/sec-ft^2)	30.7	44.0	45.0
Test Section Exit Well Temperature After Boiling Inception (°F)	2145	1812(min)	1580(min)
Approximate Wall Superheat At Boiling Inception (°F)	124	Unstable	Unstable
Test Section ID, D_T, inch		0.423	
Insert		None	
Inlet Orifice Diameter D_{or}, inch		0.0625	

The Sanborn trace for the test designated "Intermediate-Pressure" in Table 12 (P = 80 psia, T_{sat} = 1800°F) is shown in Figures 89a and 89b. Figures 89a and 89b are reproductions of segments of a continuous Sanborn oscillograph recorder trace made throughout the test.

The trace begins with boiling inception at the test section outlet after an increase of preboiler power (segment-1) followed by a period of boiling operation during which there were oscillations in pressure, temperature, flow rate and dump-tank level. Additional increases in preboiler power resulted in corresponding increases in the frequency of the oscillations of the loop parameters (segments-2 to -5 in Figures 89a, b). The test was terminated by reducing the test section power in steps until the system was brought back into non-boiling liquid flow conditions (segment-6 in Figure 89b).

In order to have a more quantitative record of the detailed nature of the fluid temperature oscillations than that provided by the Sanborn trace, a continuous digital recorder printout of the test section exit well thermocouple (TC-34) was obtained for a portion of the time period spanned by Figures 89a and 89b. The digital recorder was allowed to run for about 6 minutes at a rate of 3 printouts per second. In Figure 90 the first 160 seconds of the continuous printout have been plotted for temperature vs. time co-ordinates. A segment of the Sanborn recorder trace taken at the same time is also shown in Figure 90, for comparison with the plot of the digital recorder printout. It is apparent from Figure 90 that the large oscillations in temperature shown on the oscillograph recorder trace are accompanied by a number of smaller oscillations, which are shown on the plot of the digital recorder printout.

The Sanborn trace for the test designated "Low-Pressure" in Table 12 (P = 27 psia, T_{sat} - 1520°F) is shown in Figure 91. There were significant oscillations of the dump tank level and small oscillations of the condenser inlet wall temperature at the beginning of the recorder chart segment before boiling inception in the test section. During this interval before boiling had begun in the test section the flow was steady and the test section exit well and wall thermocouples indicate by their steadiness and level above the saturation temperature corresponding to 27 psia (1520°F) that the fluid was in a superheated liquid state at the test section exit. It is thought that the oscillations in the dump tank level and condenser inlet wall temperature during this period are indicative that flashing of the superheated liquid into

two-phase conditions was occurring in the crossover pipe which connects the test section outlet with the condenser inlet (see Figure 1). After boiling began at the test section exit, as indicated by an abrupt drop of the test section exit well and wall temperatures, the loop became highly unstable, as manifested by the oscillations in loop parameters shown in Figure 91.

In order to gain some further understanding of the large oscillations in temperature which sometimes occurred after boiling inception, as shown in Figures 89, 90 and 91, a mechanism for the temperature excursions will be postulated and analyzed briefly. The postulated mechanism is basically the same as that discussed in References 39, 40 and 41.

When the first bubbles are produced at boiling inception in the test section exit they grow very rapidly, due to the fact that the liquid is superheated across the entire flow area of the tube. This produces a local pressure pulse, which may result in an increase of the local wall temperature required for boiling to continue from the same size cavity which produced the first bubble. However, as the bulk liquid temperature drops toward saturation after the first bubble is produced there is a corresponding reduction in the local wall temperature. Therefore, after the first bubble is produced the system is faced with a situation where a higher wall temperature is required to continue boiling (due to the pressure pulse) but only a lower wall temperature is available due to the cooling of the wall. Under these conditions the boiling action may cease unless larger cavities have been activated by the first vapors. If larger cavities have not become active the boiling action will cease momentarily, the vapors produced will be swept away and the liquid will begin to superheat again and the cycle of boiling inception followed by the pressure pulse, corresponding reduction of wall temperature and cessation of boiling will be repeated. If no other changes were made this cyclic behavior would continue indefinitely.

The above hypothesis suggests that heat would be removed from the tube wall in short bursts (i.e., a period of very high heat flux during which the tube wall temperature drops, followed by a period of relatively low heat flux during which the tube wall temperature rises). In order to obtain some indication of the behavior of the wall temperature during these temperature excursions consider the test section tube wall to be a semi-infinite plate. Assume the plate has a uniform initial temperature T_o. Beginning at time t = 0 heat is removed from the face of the plate (located at $\mathcal{L}$ = 0) at a uniform flux q" for a time interval $\mathcal{T}$. The face of the plate is then insulated and the heat removal stops. A solution for the temperature distribution in the plate as a function of distance into the plate from the face $\mathcal{L}$ and time t after heat transfer starts is given in Reference 42. Using this model as a representation of the boiler tube wall of Test Section No. 3 (.423" I.D., no insert) ($\mathcal{L}$ = 0 corresponds to the inner surface of the tube and $\mathcal{L}$ = 0.124-inch corresponds to the outer surface of the tube), a calculation of the variation with time of the plate temperature at position $\mathcal{L}$ = 0 and $\mathcal{L}$ = 0.124-inch was made using the equations given in Reference 42. The results of this calculation are given in Figure 92, which shows the variation of the plate temperature at the positions $\mathcal{L}$ = 0 and $\mathcal{L}$ = 0.124-inch as a function of time after the beginning of heat removal.

The general similarity in the trend of the calculated behavior of the plate temperature in Figure 92 to that of the wall and fluid at the test section exit shown in Figure 90 suggest the plausibility of the proposed mechanism. The interaction between the thermal instability mechanism discussed above, and the thermal and hydraulic characteristics of the remainder of the loop alter the temperature oscillations somewhat. As can be seen from Figure 90 the fluid temperature does not appear to drop in one step from its initially super-heated value to the saturation temperature. Due to the pressure surges induced in the loop by the abrupt production of vapor several "bumps" are necessary before the wall temperature drops sufficiently to suppress further activity (Figure 90a). The flow pattern is probably highly irregular, but may be basically of the slug

flow type. As the inlet enthalpy is increased, the time required for the wall superheat necessary for nucleation to be reached at the boiler exit is evidently reduced. This probably accounts for the increase in frequency of the fluid temperature oscillation with increasing preboiler power as shown in Figure 89a and b.

The suggested thermal instability mechanism would predict that the instability at boiling initiation would become more violent as the pressure is lowered, due to the increasingly higher values of wall superheat required to initiate boiling from a cavity of a given size. A comparison of Figures 88, 89 and 91 tends to support this conclusion. At a pressure of 201 psi the oscillations pressure, temperature, flow rates and dump-tank level after boiling inception were relatively small and disappeared quickly (Figure 88). At 80 psia the oscillations of the loop parameters after boiling inception were of larger amplitude and were continuous (Figure 90). At 27 psia the oscillation amplitudes were continuous and were larger yet (Figure 91).

Surface conditions should also have a pronounced influence on the instability at boiling initiation. The helical insert present in Test Section No. 2 (.74" I.D. with helical insert, P/D = 6) apparently provides a sufficient number of large cavities (possibly in the crevices existing between the edge of the insert vane and the tube wall) so that once some vapor is present in the tube boiling may continue in a relatively stable manner from the larger cavities. This is indicated by the comparatively stable operation after boiling inception shown in Figures 85 and 86.

Experiments similar to the ones described above were conducted with Test Sections No. 4 (.738" I.D. with annular plug and helix, P/D = 2) and No. 5 (.742" I.D. with wire-wrapped plug and wire coil, P/D = 2) both of which contained inserts. In general the results were similar to those obtained with Test Section No. 2 (.74" I.D. with helical insert P/D = 6). These results tend to support the conclusions that surface conditions have a pronounced influence on this type of instability and that apparently the insert geometries have a

beneficial effect in reducing the temperature and pressure oscillations after boiling inception. This beneficial effect is probably due to the nucleation sites provided by the crevices between the insert and the tube wall.

One interesting method of alleviating the instability associated with large bulk liquid superheats at boiling initiation was reported by Hoffman (43). According to Reference 43 an artificial nucleation site of the "hot finger" type improved stability during operation of a potassium boiling loop. Basically, the "hot finger" was a 0.050-inch diameter hole drilled 0.256-inch deep in the boiler tube and was heated independently. A "hot finger" device similar to this was installed between the preboiler and test section and tested in the Cb-1%Zr loop with Test Section No. 5 (.742" I.D. with wire-wrapped plug and wire coil P/D = 2). The "hot finger" used is shown in Figures 14 and 15.

Since Test Section No. 5 (.742" I.D. with wire-wrapped plug and wire coil P/D = 2) contained an insert, there were no significant thermal instabilities with this test at boiling inception at pressures above 80 psia. The power capability of the "hot finger" used was not sufficient to provide the larger liquid superheat required for boiling inception at the test section exit at lower pressures than 80 psia. Thus, no tests were done which demonstrated the effect of the "hot finger" on the stability of boiling inception at the test section exit. However, when the boiling boundary was located in the plug region of the insert it was possible to virtually eliminate the small bulk liquid superheat (about 15°F) present at the boiling boundary during steady bulk boiling by using the "hot finger". Also, when boiling was initiated at the test section inlet (preboiler outlet) by raising both the preboiler power and the "hot finger" power with the test section maintained at approximately isothermal conditions, there was indication from the measured temperatures that the "hot finger" was effective in reducing the bulk liquid superheat at boiling inception under these conditions.

From a boiler design standpoint it is important to avoid or eliminate instabilities associated with boiling inception and fluctuations in position of the boiling boundary. Some possible methods of doing this are as follows:

1. For two-fluid boilers, force the point of boiling inception into the bulk subcooled liquid region by using a very high heat flux to achieve the degree of liquid superheat at the wall necessary to initiate boiling. This might be practical, for example, in a counter-flow boiler.

2. Use artificial nucleation sites formed as crevices, cavities or non-wetting inlays. The vortex generator inserts appear to be suitable to provide nucleation-promoting crevices and cavities. However, the inserts become effective only after the first vapors have been produced, and do not appear to significantly alter the liquid super-heat required for initial boiling inception.

3. It might also be possible to lower the single-phase heat transfer coefficient at the inlet region of boiler tubes so that the necessary wall superheat could be obtained without any significant degree of bulk superheat being present.

H. Liquid Heat Transfer Results

During testing with Test Section No. 5 (.742" I.D. with wire-wrapped plug and wire coil P/D = 2) experiments were conducted to determine the single-phase liquid heat transfer coefficient in the wire-wrapped plug region at the inlet. The data for this test are presented in Table 13 and include the following range of variables:

Reynolds Number N_{Re}	5,750 to	17,080
Peclet Number N_{Pe}	20 to	62
Fluid Temperature, °F	1,261 to	1,459
Wall-to-fluid ΔT, °F	16 to	44
Heat flux, Btu/hr-ft^2	40,200 to	168,000
Heat transfer coefficient Btu/hr-ft^2-°F	2,420 to	3,970

The Reynolds number and Peclet number used above are defined by

$$N_{Re} = \frac{G\,D_e}{\mu}$$

and

$$N_{Pe} = \frac{G\,D_e\,C_p}{k}$$

The mass velocity, G, is the "axial" value and does not include the effect of the helical flow path. The equivalent diameter, D_e, is defined in the usual manner as

$$D_e = \frac{4 \times (\text{Net Flow Area Normal To Pipe Centerline})}{\text{Wetted Perimeter In Plane Normal To Pipe Centerline}}$$

Figure 93 is a plot of the liquid data with the parameters defined as above. Also shown in Figure 93 is the Lyon (9) prediction for uniform wall heat flux and the empirical correlation of Lubarsky and Kaufman (44). Although the

Lubarsky-Kaufman correlation was based on data for Peclet numbers greater than 200, the data shown in Figure 93, which are in the low Peclet number range from 20 to 60, are in fair agreement with that correlation. In order to account for the helical flow effect in the plug region of Test Section No. 5 (.74-in I.D. with wire-wrapped plug and wire coil P/D = 2), the helix mass velocity G_{HM}, defined by Equation (50), was introduced. Figure 94 is a plot of the liquid data using this parameter. As can be seen, this increases the disagreement between the data and the Lubarsky and Kaufman correlation.

Measured values of liquid heat transfer coefficients for the liquid metals have historically fallen below predictions. This has been particularly true for Peclet numbers less than 100. An additional complication in the present data is that the flow channel deviates considerably from a circular duct. It is well known that use of the equivalent diameter concept in laminar flow through non-circular ducts can lead to gross errors. For the low Prandtl number fluids a similar error can result even in turbulent flow due to the predominance of molecular conduction over turbulent diffusion.

Table 2

NUCLEATE BOILING HEAT TRANSFER RESULTS

Test Section No. 1 (.76-in. I.D., no insert)

Date	Time	T_{sat},°F	G lb/sec-ft^2	q'' Btu/hr-ft^2	x %	avg. ΔT °F	h Btu/hr-ft^2-°F
9/12/64	1318	1749.2	15.6	30615	20.5	9.3	3292
	1448	1751.6	15.5	30043	21.9	7.4	4060
	1600	1752.6	15.5	30878	25.9	8.2	3766
	1800	1750.5	15.4	30990	27.8	8.3	3734
	1930	1751.6	15.4	30931	30.1	8.7	3555
	2330	1751.9	15.3	29828	31.5	8.0	3728
9/13/64	0240	1752.8	15.5	29892	33.0	8.0	3736
	0445	1753.2	15.3	30350	35.7	8.0	3794
9/12/64	0923	1748.2	15.6	54888	14.8	8.7	6309
	1106	1755.3	15.6	54938	16.6	4.9	11212
10/6/64	1306	1770.2	16.0	30244	39.0	7.4	4087
	1430	1773.6	15.7	29926	47.5	6.8	4401
	1830	1874.1	15.9	29011	50.1	7.1	4086
	2100	1878.0	16.1	29051	55.0	7.8	3724
	2300	1890.7	15.9	28437	53.8	7.7	3693
10/7/64	0240	1910.1	15.8	28297	58.2	7.4	3824
	0530	1923.4	15.9	29072	59.1	7.3	3982
	0950	1937.2	15.8	28785	61.3	9.6	2998
	1224	1954.6	15.8	27577	61.0	8.3	3323
	1350	1954.7	15.8	29186	66.2	6.8	4292
	1608	1975.9	15.8	29210	67.6	6.0	4868
	1800	1976.5	15.7	26717	69.5	7.5	3562
	2030	1990.8	15.9	27773	68.1	6.5	4273
	2320	2012.8	15.9	27245	71.9	7.1	3837
10/8/64	0135	2021.0	15.8	25618	72.9	7.2	3558
	0430	2037.9	15.9	28293	76.6	6.9	4100
	0620	2054.1	15.8	28181	81.1	6.5	4336
	0848	2061.0	15.9	27448	80.0	10.6	2589
8/27/64	1620	1788.7	16.5	33075	7.5	12.0	2756
	2152	1790.8	16.7	29277	8.1	11.8	2481

Test Section No. 1 (.76-in I.D., no insert)

Date	Time	T_{sat}, °F	G lb/sec-ft^2	q" Btu/hr-ft^2	x %	avg. ΔT °F	h Btu/hr-ft^2-°F
8/28/64	0240	1789.4	16.5	32601	10.5	10.5	3105
	0530	1794.2	16.3	29783	22.3	12.1	2461
	1005	1792.1	15.6	31068	25.4	10.5	2959
	1314	1793.6	15.3	30302	28.7	10.7	2832
	1430	1794.3	15.4	29775	30.5	10.2	2919
8/31/64	0455	1795.3	15.4	57108	17.9	7.4	7717
	1037	1824.6	15.6	54959	16.8	10.4	5285
	1219	1825.8	15.5	56661	20.0	9.1	6226
9/11/64	1815	1797.9	17.0	49788	5.5	10.8	4610
	2030	1796.7	15.8	55786	16.7	9.0	6198
	2230	1795.4	16.2	52837	17.7	9.9	5337
10/19/64	1403	1800.9	15.1	104820	28.9	-1.8	
	1721	1796.0	15.3	109720	31.6	-2.5	
	1725	1796.7	15.3	109950	30.4	-2.9	
10/13/64	1245	1901.2	15.2	97692	26.0	1.2	81410
	1428	1901.1	15.3	97890	26.7	2.0	48945
	1610	1902.2	15.3	97304	32.4	0.96	101358
10/14/64	1150	1905.0	15.3	96003	34.0	1.6	60002
	1255	1899.6	15.2	96242	35.1	0.80	120302
	1745	1902.1	15.4	85779	31.4	1.5	57186
10/8/64	1320	1982.0	15.5	58034	18.4	7.0	8291
	1450	1985.4	15.5	60056	23.8	4.8	12512
	1630	1985.7	15.4	58205	28.8	4.2	13858
	1750	1985.5	15.4	58503	34.6	5.1	11471
	1945	1985.0	15.3	56909	38.7	5.5	10347
	2145	1986.9	15.2	57470	43.9	4.4	13061
	2330	1984.9	15.2	56401	60.7	4.4	12818
10/9/64	0130	1985.4	15.3	56717	54.6	4.9	11575
	0325	1985.9	15.4	56434	58.9	4.1	13764
	0500	1986.7	15.5	59949	73.0	2.6	23057
	0630	1987.4	15.4	55573	68.9	4.8	11578
	0920	1986.2	15.7	55957	74.4	4.2	13323
	1233	1987.8	15.7	55739	81.8	4.7	11859
	1328	1987.6	15.3	67919	90.7	12.3	5522
	1510	1988.0	16.0	68174	81.6	4.0	17044

Table 2 (Continued)

Test Section No. 1 (.76-in. I.D., no insert)

Date	Time	T_{sat}, °F	G lb/sec-ft^2	q" Btu/hr-ft^2	x %	avg. ΔT °F	h Btu/hr-ft^2-°F
10/9/64	1725	1989.7	15.7	81501	86.3	3.2	25469
	1832	1987.6	16.0	80952	80.0	3.6	22487
	1930	1988.5	16.0	81313	78.0	3.4	23916
	2045	1989.2	15.9	81627	74.8	2.4	34011
	2200	1987.5	15.8	81986	72.7	3.1	26447
	2320	1990.5	15.7	82334	69.6	4.3	19147
10/10/64	0045	1986.8	15.7	82525	67.4	3.9	21160
	0230	1986.7	15.6	82654	64.9	2.8	29519
	0400	1985.9	15.6	82889	62.1	3.3	25118
	0530	1987.2	15.5	82690	59.5	4.0	20672
	0630	1986.2	15.5	83168	56.9	4.0	20792
	0810	1987.8	15.5	83320	54.6	3.6	23144
	1135	1989.4	15.3	84264	52.9	3.6	23407
	1425	1988.1	15.4	84694	49.5	3.7	22890
	1530	1989.4	15.4	84343	47.4	4.3	19615
	1703	1986.9	15.2	84400	46.0	3.3	25576
10/13/64	2130	2100.4	15.5	58693	21.9	7.3	8040
	2305	2100.2	15.5	58944	26.1	4.6	12814
10/14/64	0105	2097.2	15.5	57510	28.4	6.0	9585
	0300	2100.0	15.4	57682	31.4	5.8	9945
	0455	2100.7	15.5	57468	33.2	5.4	10642
	0625	2097.8	15.6	57994	35.8	4.7	12339
	0918	2096.5	15.3	57271	38.1	4.8	11931
10/21/64	0300	2097.2	15.5	81146	25.3	8.7	9327
	0425	2097.6	15.4	80759	27.6	8.1	9970
	0550	2098.8	15.4	80565	29.6	7.5	10742
10/20/64	0400	2097.6	15.4	105490	19.5	6.8	15513
	0520	2099.0	15.4	104270	23.6	7.1	14686
	0535	2100.6	15.3	102130	27.7	7.0	14590
	0755	2101.2	15.3	101310	32.0	6.5	15586
	1002	2099.5	15.3	101210	36.4	5.6	18073
	1214	2100.3	15.4	100930	36.8	5.5	18351
10/21/64	1325	2094.9	15.4	148950	36.1	7.7	19344
	1555	2092.3	15.5	153740	40.7	5.2	29565
	1725	2092.9	15.2	150410	44.3	5.5	27347
	1900	2094.5	15.5	150580	45.2	6.8	22144
	2030	2095.0	15.4	152170	48.6	6.4	23777
	2215	2097.8	15.4	154470	51.1	7.9	19553

Test Section No. 1 (.76-in I.D., no insert)

Date	Time	T_{sat}, °F	G lb/sec-ft^2	q" Btu/hr-ft^2	x %	avg. ΔT °F	h Btu/hr-ft^2-°F
10/22/64	0030	2097.6	15.2	150960	52.5	7.4	20400
	0200	2098.9	15.5	147930	52.1	6.5	22758
	0620	2096.2	15.4	151020	56.2	23.8	6345
	1325	2096.8	15.4	150840	54.8	5.2	29008
	1645	2095.0	21.4	65432	11.4	9.4	6961
	1815	2099.1	21.4	66507	13.0	7.8	8527
	2000	2097.2	21.5	65060	14.0	7.8	8341
	2130	2099.2	21.5	66950	15.9	6.3	10627
	2250	2096.5	21.5	67637	17.6	5.8	11662
10/23/64	0100	2099.3	22.1	65395	17.8	5.3	12339
	0245	2098.3	22.1	65013	19.7	5.9	11019
	0415	2097.8	22.1	64753	22.0	5.8	11164
	0535	2097.8	21.9	64901	24.0	7.0	9272
	0745	2098.9	22.2	65956	25.9	6.8	9699
	0925	2096.7	22.1	64130	28.0	6.6	9717
	1045	2097.1	21.6	63426	31.1	6.4	9910
	1330	2098.0	22.2	63268	32.8	7.0	9038
	1520	2099.6	22.2	64446	37.4	5.2	12393
	1940	2099.8	20.9	67071	62.1	-254	

Test Section No. 2 (.74-in I.D., with helical insert P/D = 6)

Date	Time	T_{sat}, °F	G lb/sec-ft^2	q" Btu/hr-ft^2	x %	avg. ΔT °F	h Btu/hr-ft^2-°F	a_R g's
11/30/64	0600	2101.7	18.6	102880	17.8	14.2	7245	0.45
	0625	2092.9	18.6	103070	18.5	18.6	5541	0.47
	0855	2095.0	18.6	102000	21.7	14.1	7234	0.58
	1155	2095.1	18.4	102230	26.2	16.6	6158	0.74
	1826	2097.2	18.5	101800	27.2	13.8	7377	0.78
	2147	2097.7	18.5	102700	31.3	15.1	6801	0.97
12/1/64	0045	2098.5	17.9	100280	34.4	14.8	6776	1.04
	0315	2096.3	18.4	99944	33.9	16.4	6094	1.08
	0500	2096.1	18.5	101500	34.9	13.5	7519	1.13
	1135	2097.7	18.7	102400	42.0	18.4	5565	1.55
	1345	2093.6	19.6	102830	42.9	16.8	6121	1.77
	1520	2095.4	18.5	102620	47.0	10.7	9591	1.83
	1928	2099.1	18.6	101690	52.7	14.2	7161	2.19
	2140	2095.2	18.5	101290	59.3	11.1	9125	2.67

Table 2, Continued

Test Section No. 2 (.74-in I.D. with helical insert P/D = 6)

Date	Time	T_{sat}, °F	G lb/sec-ft^2	q'' Btu/hr-ft^2	x %	avg. ΔT °F	h Btu/hr-ft^2-°F	a_R g's
12/2/64	0050	2094.5	18.9	102500	64.9	15.8	6487	3.26
	0320	2095.7	18.6	102190	74.2	14.4	7096	3.96
	0600	2097.9	18.8	100970	80.2	27.7	3645	4.61
	0825	2096.4	18.7	102490	82.1	22.5	4555	4.76
12/17/64	0115	2100.5	24.5	106640	11.4	9.02	11823	0.47
	0335	2100.5	24.6	104780	16.4	8.36	12533	0.71
	0550	2105.6	24.6	102100	20.7	7.93	12875	0.95
	0900	2097.7	24.4	102350	26.1	7.04	14538	1.29
	1115	2095.6	24.4	101450	31.6	9.16	11075	1.70
2/8/65	1320	2108.0	24.4	102820	32.3	12.0	8568	1.72
	1610	2108.0	24.6	99539	39.3	12.6	7900	2.36
	1951	2108.6	24.5	100720	51.8	12.3	8189	3.64
	2244	2112.0	24.6	98313	57.7	12.7	7741	4.38
2/9/65	0135	2109.0	24.7	101310	63.5	-5.96		5.22
	0400	2104.8	24.7	100710	65.1	19.3	5218	5.49
	0600	2109.2	24.8	100210	70.3	29.5	3397	6.26
	0832	2105.6	24.7	100620	77.6	13.9	7239	7.43
2/7/65	0600	2106.0	31.9	105890	5.3	18.9	5603	0.42
	0830	2110.6	33.3	104750	8.3	16.2	6466	0.64
	1030	2109.0	33.3	102950	11.8	15.6	6599	0.89
	1230	2110.6	33.4	101550	15.4	15.7	6468	1.20
	1450	2108.4	33.4	101620	25.6	13.8	7364	2.31
	1716	2107.2	33.4	100600	29.2	13.0	7738	2.79
	1951	2107.7	33.6	100490	33.7	11.3	8893	3.49
	2215	2107.3	34.0	99707	37.4	12.7	7851	4.16
2/8/65	0115	2104.1	33.4	100190	42.1	13.4	7477	4.90
	0430	2109.4	33.4	99873	49.2	11.8	8464	6.19
	0725	2107.2	33.9	99561	55.1	12.0	8297	7.73
1/28/65	1825	2107.2	18.0	152840	42.7	0.57	268140	1.44
	2118	2104.7	18.3	150270	48.2	3.76	39965	1.82
1/29/65	0045	2103.4	17.9	143030	49.3	5.95	24039	1.80
	0345	2107.2	18.2	147220	53.4	4.84	30417	2.11
	1325	2106.8	17.9	149180	80.3	10.3	14483	4.11
1/29/65	2113	2104.2	23.5	155840	29.9	2.59	60170	1.44

Table 2, Continued

Test Section No. 2, (.74-in I.D. with helical insert P/D = 6)

Date	Time	T_{sat}, °F	G lb/sec-ft²	q" Btu/hr-ft²	x %	avg. ΔT °F	h Btu/hr-ft²-°F	a_R g's
1/30/65	0	2104.4	23.6	148000	33.0	6.35	23307	1.68
	0235	2101.8	23.7	151990	38.9	4.08	37252	2.19
	0530	2104.6	23.8	149720	42.9	8.93	16766	2.56
	0845	2105.7	24.6	150100	47.2	7.19	20876	3.16
	1147	2106.8	24.8	151760	52.8	6.69	22685	3.87
	1353	2105.4	24.8	151340	58.0	6.29	24060	4.54
	1630	2106.0	24.6	150390	96.7	10.5	14323	10.85
1/30/65	2044	2106.0	33.5	151980	15.3	9.99	15213	1.20
	2258	2106.6	33.4	146360	18.3	10.7	13678	1.49
1/31/65	0200	2106.9	33.5	151430	23.8	9.36	16178	2.10
	0445	2106.3	33.6	151810	27.5	7.95	19096	2.60
	0705	2107.0	33.9	151580	31.6	8.60	17626	3.22
2/6/65	1148	2106.9	34.4	145280	28.5	19.8	7337	2.85
	1415	2106.4	34.5	143240	33.1	21.7	6601	3.56
	1606	2108.4	34.2	144530	36.8	20.2	7155	4.10
	1911	2109.4	33.9	139850	41.2	17.9	7813	4.81
	2202	2106.7	33.6	143000	48.2	18.6	7688	6.11
2/7/65	0130	2110.6	34.0	138270	51.1	18.5	7474	6.79
12/21/64	1335	1801.4	16.8	63200	15.1	8.47	7462	0.48
	1626	1803.3	17.0	59004	26.8	8.01	7366	1.15
1/22/64	0105	1806.2	17.0	70612	34.5	5.56	12700	1.73
	0310	1805.9	17.2	60671	31.0	8.20	7399	1.50
	0505	1805.9	17.2	60498	31.8	9.10	6648	1.56
	0900	1804.9	16.7	59403	39.3	8.96	6630	2.08
	1048	1802.6	17.1	58783	42.4	9.35	6287	2.51
	1320	1802.1	16.9	58663	48.3	8.55	6861	3.08
12/18/64	2100	1806.6	17.1	106210	19.1	7.01	15151	0.69
12/19/64	0405	1811.9	16.9	104760	50.2	8.96	11692	3.22
	0630	1809.6	17.2	104110	54.6	6.43	16191	3.92
	0812	1802.7	17.2	101980	56.9	5.93	17197	4.30
	0908	1801.0	17.2	104870	56.8	6.07	17277	4.31
	1000	1803.6	17.3	102630	56.9	7.43	13813	4.30
	1036	1800.2	17.1	102590	57.4	5.84	17567	4.33

Test Section No. 2 (.74-in I.D. with helical insert P/D = 6)

Date	Time	T_{sat}, °F	G lb/sec-ft^2	q'' Btu/hr-ft^2	x %	avg. ΔT °F	h Btu/hr-ft^2-°F	a_R g's
2/9/65	2202	1817.2	24.4	103060	41.7	17.0	6062	4.81
2/10/65	0200	1813.2	24.6	105480	46.2	16.5	6393	5.87
2/10/65	1504	1802.6	34.1	104000	26.5	4.1	25366	4.58
	1712	1810.3	33.4	104430	29.2	4.8	21756	5.08
	2026	1817.0	31.4	106220	41.1	6.4	16597	7.76
2/9/65	1255	1815.4	24.0	144590	52.5	25.0	5784	6.98
2/11/65	2158	1902.0	24.8	102430	45.6	9.9	10346	4.7
2/12/65	0045	1907.8	25.0	102060	55.4	9.8	10414	6.6
	0400	1912.4	25.9	101590	64.6	9.2	11042	9.1
	0725	1903.9	24.7	103820	38.5	9.5	10928	3.5

Test Section No. 3 (.42-in I.D., no insert)

Date	Time	T_{sat}, °F	G lb/sec-ft^2	q'' Btu/hr-ft^2	x %	avg. ΔT °F	h Btu/hr-ft^2-°F
3/12/65	1430	2105.2	31.3	96741	32.2	5.6	17275
	1625	2105.2	31.5	98805	41.5	7.3	13535
	1932	2103.4	31.3	94391	48.3	7.4	12756
	2204	2104.2	31.7	94836	55.2	7.5	12645
3/13/65	0217	2107.0	31.1	100300	66.6	8.5	11800
3/16/65	1330	2112.6	31.8	149510	49.4	13.2	11326
	1616	2064.9	32.0	153630	51.4	10.1	15211
3/18/65	0430	2105.2	31.0	151120	15.7	16.8	8995
	0650	2096.6	31.1	148800	22.5	14.7	10122
	1030	2102.4	31.6	147880	26.9	14.3	10341

Table 2, Continued

Test Section No. 3 (.42-in I.D., no insert)

Date	Time	T_{sat}, °F	G lb/sec-ft^2	q" Btu/hr-ft^2	x %	avg. $\triangle T$ °F	h Btu/hr-ft^2-°F
3/30/65	2200	2099.2	45.9	99845	31.2	9.4	10622
3/31/65	0140	2101.9	45.6	99294	40.7	1.7	58408
	0330	2103.6	45.2	97610	48.5	1.5	65073
	0510	2103.1	44.4	98236	58.5	1.8	54576
	0745	2102.6	44.1	98553	68.3	2.2	44797
3/30/65	1941	2100.3	45.9	118630	29.9	4.1	28934
4/1/65	0545	2096.9	46.1	219440	50.3	10.4	21100
2/25/65	1724	2105.7	61.6	100020	21.4	0.28	357214
	1955	2105.3	62.1	97175	25.4	2.8	34705
	2158	2103.3	62.3	95571	31.1	3.1	30829
2/26/65	0050	2101.0	60.9	95000	38.2	4.2	22619
	0250	2101.6	61.1	97911	45.1	3.0	32637
	0505	2101.0	61.3	99105	52.8	3.1	31969
	0830	2099.2	63.0	100960	57.4	3.5	28846
	1230	2096.0	63.0	103580	63.4	4.5	23018
2/26/65	2037	2107.6	61.6	143570	23.6	5.0	28714
	2307	2095.8	61.3	141410	28.7	19.4	7289
2/27/65	0152	2104.8	59.9	147530	35.9	3.2	46103
	0430	2103.6	60.9	147670	40.2	3.8	38861
	0632	2103.6	60.4	148120	47.3	3.9	37979
	0930	2106.0	61.4	152730	51.6	3.7	41278
	1215	2101.6	61.6	154710	60.1	5.2	29752
2/27/65	1838	2104.1	60.7	215690	36.3	11.7	18435
	2057	2106.0	60.6	220270	43.1	10.4	21180
	2329	2106.4	61.9	232540	48.7	6.4	36334
2/28/65	0223	2105.2	60.3	222860	55.9	4.1	54356
	0430	2114.9	60.3	223370	62.4	7.7	29009
	0625	2103.6	60.0	222870	69.4	6.0	37145
	0900	2102.2	61.7	224070	71.8	4.1	54651

Test Section No. 3 (.42 in.I.D., no insert)

Date	Time	T_{sat}, °F	G lb/sec-ft²	q" Btu/hr-ft²	x %	avg. ΔT °F	h Btu/hr-ft²-°F
3/25/65	0730	1804.6	30.5	99295	48.7	2.4	41373
	1330	1862.2	31.3	97820	48.9	3.0	32607
3/26/65	0308	1805.4	29.8	98678	78.3	5.2	18977
	0350	1804.8	30.6	98265	75.8	3.4	28901
	0430	1808.8	32.4	97346	77.4	1.9	51235

Test Section No. 4 (.73-in I.D. with annular plug and helix P/D = 2)

Date	Time	T_{sat}, °F	G lb/sec-ft²	q" Btu/hr-ft²	x %	avg. ΔT °F	h Btu/hr-ft²-°F	$^a R$ g's
5/10/65	0542	2098.5	29.5	111810	10.4	34.0	3288	7.8
	0845	2102.1	29.3	110610	14.7	33.1	3342	11.3
	1210	2099.3	29.5	110460	18.8	32.4	3409	15.7
	1813	2095.5	30.3	109870	22.0	31.0	3544	20.4
	2220	2102.7	29.3	109790	30.8	28.6	3839	29.4
5/11/65	0043	2098.1	29.5	111070	38.6	26.2	4239	41.2
	0320	2099.1	29.8	110800	43.2	26.2	4229	49.5
	0624	2097.1	29.6	110540	53.5	27.0	4094	68.2
	1430	2096.8	29.7	110630	69.1	26.3	4206	103.2
5/11/65	0215	2097.2	29.4	141940	18.1	28.3	5016	14.7
	0920	2101.4	29.7	145090	70.1	16.0	9068	107.4
5/12/65	0512	2095.6	29.4	141460	22.2	25.6	5526	19.4
	0800	2094.8	29.5	141880	26.2	23.0	6169	25.0
	1045	2098.8	29.5	140720	30.1	19.6	7180	30.2
	1400	2090.7	29.7	140700	34.5	25.8	5454	37.3
5/13/65	0120	2093.7	29.2	142010	41.9	22.0	6455	47.5
	0420	2101.8	29.4	140130	44.3	18.6	7534	51.3
	0640	2097.8	29.1	139920	48.9	17.8	7861	58.8
	1810	2106.6	29.3	141400	52.0	30.2	4682	64.5
	2025	2101.7	29.5	142010	58.8	21.8	6514	80.0
	2215	2103.3	29.9	144800	62.6	22.1	6552	90.2

Test Section No. 4 (.73-in. I.D. with annular plug and helix P/D = 2)

Date	Time	T_{sat}, °F	G lb/sec-ft^2	q" Btu/hr-ft^2	x %	avg. $\triangle T$ °F	h Btu/hr-ft^2-°F	a_R g's
5/14/65	0150	2101.4	29.7	139880	71.6	38.0	3681	111.2
	0445	2095.8	29.8	139090	76.0	18.7	7438	123.9
	0915	2102.2	30.3	139180	84.1	17.8	7819	150.5
5/21/65	0547	2095.6	29.1	151330	20.8	25.2	6005	17.5
	0830	2098.7	29.3	150010	23.3	23.4	6411	20.6
	1300	2100.1	29.6	151140	25.9	23.5	6432	24.3
	1830	2097.0	29.4	152140	29.7	22.4	6792	29.4
	2038	2101.6	28.9	154030	36.2	20.8	7405	34.1
	2133	2102.1	29.7	152430	35.0	20.6	7400	37.8
5/22/65	0130	2101.9	29.4	150280	38.1	19.8	7590	41.7
	0400	2100.4	29.2	150900	42.1	19.1	7900	47.7
	0630	2099.1	29.2	150890	45.7	21.2	7117	54.0
	0900	2101.4	29.1	151220	49.5	19.8	7637	60.3
	1215	2098.7	29.3	151520	53.2	20.4	7427	68.3
	1630	2098.6	29.3	152200	56.8	17.8	8551	75.9
	1830	2101.5	29.4	155320	61.8	20.8	7467	86.7
	2030	2101.6	29.0	152280	65.2	18.6	8187	92.2
	2230	2101.2	29.4	152220	68.6	20.0	7611	102.4
5/23/65	0120	2103.3	29.4	153700	74.5	20.3	7571	116.8
	0405	2100.3	29.1	151790	77.4	20.4	7441	123.0
	0620	2099.5	29.3	150690	80.4	19.9	7572	132.4
	0915	2101.1	29.5	152340	85.0	19.2	7934	147.5
5/23/65	2315	2100.3	29.0	178450	29.1	24.8	7196	27.2
5/26/65	0455	2094.7	29.3	179760	28.1	28.9	6220	27.0
	0630	2095.4	29.0	177740	30.8	28.2	6303	30.3
	0915	2094.5	29.2	167690	31.1	26.6	6304	31.2
	1235	2094.3	29.3	159100	33.3	25.8	6167	34.9
	1625	2094.9	29.3	166820	39.9	20.4	8177	45.7
5/27/65	0140	2096.5	29.3	168200	49.2	21.8	7716	61.7
	0510	2098.9	29.2	170750	58.4	23.6	7235	79.8
	1030	2097.3	29.8	161970	63.3	22.2	7296	93.8
	1330	2098.1	29.6	158160	72.7	24.7	6403	115.5

Test Section No. 4 (.73-in I.D. with annular plug and helix P/D = 2)

Date	Time	T_{sat}, °F	G lb/sec-ft^2	q" Btu/hr-ft^2	x %	avg. ΔT °F	h Btu/hr-ft^2-°F	a_R g's
6/8/65	0919	1808.7	18.4	150600	51.2	26.9	5598	54.0
	1302	1808.6	18.2	150190	64.6	29.7	5057	76.7
	1545	1809.5	18.8	149200	75.0	30.8	4844	104.3
6/3/65	0450	1806.7	29.2	99949	32.9	10.2	9799	58.5
	0915	1806.7	29.4	99659	42.6	13.3	7493	89.0
	1240	1809.3	29.4	98673	50.9	16.7	5909	119.2
	1345	1813.9	31.1	97569	46.6	12.2	7997	112.9
6/10/65	0330	1810.6	29.3	147030	38.9	27.0	5446	80.2
	0625	1808.5	29.2	146060	46.3	28.1	5198	106.1
	1015	1801.6	28.9	148620	56.1	31.0	4794	144.9
	1300	1803.6	29.2	149260	66.2	35.4	4216	194,7

Test Section No. 5 (.74-in I.D. with wire-wrapped plug and wire coil P/D = 2)

Date	Time	T_{sat}, °F	G lb/sec-ft^2	q" Btu/hr-ft^2	x %	avg. ΔT °F	h Btu/hr-ft^2-°F	a_R g's
7/7/65	1010	2091.6	25.1	97245	16.5	30.0	3242	9.4
	1420	2095.9	25.2	100060	23.1	30.4	3291	14.8
	1925	2093.8	25.3	98749	31.7	30.4	3248	22.7
7/8/65	0015	2097.8	25.4	96517	39.0	29.4	3283	30.5
	0530	2094.4	25.0	103240	52.7	31.1	3320	47.5
	1120	2098.4	24.8	102440	64.0	30.8	3326	63.1
	1403	2097.3	23.9	102490	75.7	30.1	3405	78.1
7/26/65	1325	2100.1	24.7	148650	24.7	41.4	3591	15.6
	1800	2102.2	25.3	148640	32.6	42.3	3514	24.7
	2150	2107.3	25.3	149940	44.3	30.4	4932	38.0
7/27/65	0135	2101.2	25.3	144020	55.4	31.6	4558	53.7
	0540	2103.1	24.8	143000	72.7	30.8	4643	79.8
7/27/65	1650	2100.6	15.6	156130	35.8	27.8	5616	10.9
	2005	2099.9	15.8	153540	43.4	28.4	5406	15.3
	2305	2102.6	16.0	147600	49.2	29.6	4986	18.9
7/28/65	0305	2098.8	15.6	148490	60.2	35.8	4148	25.2
	0605	2097.3	15.7	147700	69.5	31.7	4659	31.9
8/2/65	1626	1801.4	15.6	147980	34.2	16.8	8808	19.7
	1940	1798.9	15.6	147040	42.5	20.6	7138	28.7
	2220	1805.0	15.6	146230	50.5	17.4	8404	38.3

TABLE 3

CRITICAL HEAT FLUX DATA

Test Section No. 1 (.76-in I.D., no insert)

Date	Time	Tube I.D.	Insert P/D	T_{sat} °F	G_K lbs/sec-ft^2	x_c	q''_c Btu/hr-ft^2	a_R g's
10/22/64	0900	0.767"	None	2100	15.5	.67	152,000	0
10/22/64	0923			2100	16.0	.65	151,000	
10/22/64	1405	↓	↓	2100	15.5	.66	152,000	↓
10/23/64	1735			2100	22.0	.91	129,000	

Test Section No. 2 (.74-in I.D., with helical insert P/D = 6)

Date	Time	Tube I.D.	Insert P/D	T_{sat} °F	G_K lbs/sec-ft^2	x_c	q''_c Btu/hr-ft^2	a_R g's
1/30/65	1613	0.740"	6	2100	22.0	.93	150,000	9.5
1/29/65	1643	↓	↓	2100	16.0	.84	150,000	4.1

Test Section No. 3 (.42-in I.D., no insert)

Date	Time	Tube I.D.	Insert P/D	T_{sat} °F	G_K lbs/sec-ft^2	x_c	q''_c Btu/hr-ft^2	a_R g's
2/27/65	1350	0.423"	None	2105	61.6	.81	157,000	0
2/28/65	0945			2102	61.7	.74	224,000	
3/17/65	0440			2100	31.0	.66	101,000	
3/27/65	2120			1838	41.2	.57	171,000	
3/31/65	1155			2104	47.6	.88	95,000	
3/31/65	1214			2104	47.6	.85	94,000	
3/31/65	1328			2105	47.6	.89	50,000	
3/31/65	1345			2105	47.6	.90	50,000	
3/31/65	1438			2105	47.6	.89	53,000	
3/31/65	1455			2105	47.6	.87	50,000	
4/ 1/65	1332			2105	46.7	.59	211,000	
4/ 1/65	1440	↓	↓	2106	46.5	.61	214,000	↓

CRITICAL HEAT FLUX DATA

Test Section No. 4 (.73-in.I.D., with annular plug and helix P/D = 2)

Date	Time	Tube I.D.	Insert P/D	T_{sat} °F	G_K lbs/sec-ft^2	x_c	q_c'' Btu/hr-ft^2	a_R g's
5/23/65	1353	0.738"	2	2100	32.0	.79	148,000	130.4
5/28/65	1400			2100	20.4	.87	153,000	64.2
6/ 8/65	1723			1823	21.7	.83	149,620	132.1
6/ 8/65	1804			1813	21.9	.89	106,380	159.2
6/10/65	1602			1804	25.3	.88	148,400	213.0
6/10/65	1613			1809	24.6	.89	148,260	203.0
6/10/65	1652			1807	24.1	.91	100,800	205.0
5/28/65	1624	D_e	Smooth	2104	43.9	.90	77,270	0
5/28/65	1651	=.158"	Annulus	2100	43.0	.95	56,300	0
6/ 8/65	1824		(Plug)	1825	45.6	.87	104,470	0

Test Section No. 5 (.74-in.I.D., with wire-wrapped plug and wire coil P/D = 2)

Date	Time	Tube I.D.	Insert P/D	T_{sat} °F	G_K lbs/sec-ft^2	x_c	q_c'' Btu/hr-ft^2	a_R g's
7/ 8/65	1509	0.742"		2100	24.4	.907	103,120	99.9
7/ 8/65	1617			2105	23.4	.901	102,100	89.7
7/27/65	1110			2110	23.7	.923	142,870	95.5
7/27/65	1116		Wire Coil P/D = 2	2110	23.7	.886	142,870	88.0
7/28/65	1032			2106	18.4	.853	147,550	49.6
8/ 3/65	1348			1805	17.4	.866	137,900	97.4
8/ 3/65	1615			1805	19.1	.796	175,530	99.1
8/ 3/65	1650			1800	18.4	.801	176,930	94.4

Table 4

TRANSITION BOILING DATA

Test Section No. 3 (.42-in I.D., no insert)

Date	Time	T_{sat}, °F	G lb /sec-ft^2	q'' Btu/hr-ft^2	x_{TB} %	h_{TB} Btu/hr-ft^2-°F
3/31/65	1208	2105	47.6	94,000	92	3481
	1212	2105	47.6	94,000	93	2848
	1336	2105	47.6	49,900	91	1663

Test Section No. 4 (.73-in I.D., with annular plug and helix P/D = 2)

Date	Time	T_{sat}, °F	G lb /sec-ft^2	q'' Btu/hr-ft^2	x_{TB} %	h_{TB} Btu/hr-ft^2-°F	a_R g's
5/28/65	1418	2100	19.8	155,240	95	1106	72.6
	1450	2100	19.9	122,720	94	2360	71.8
6/8/65	1729	1827	20.4	150,905	91	1796	139.4
6/10/65	1620	1802	24.0	147,840	96	410	230.9
6/10/65	1625	1813	24.0	146,520	91	1368	200.9

Test Section No. 5 (.74-in I.D., with wire-wrapped plug and wire coil P/D = 2)

Date	Time	T_{sat}, °F	G lb/sec-ft^2	q'' Btu/hr-ft^2	x_{TB} %	h_{TB} Btu/hr-ft^2-°F	a_R g's
7/8/65	1545	2100	23.3	102,420	93.8	1874	97.6
8/3/65	1720	1802	16.4	171,510	95.2	1124	104.8

Table 5

FILM BOILING DATA

Test Section No. 3 (.42-in I.D., no insert)

Date	Time	T_{sat}, °F	G lb/sec-ft^2	q'' Btu/hr-ft^2	x_{FBE} %	x_{FB} %	h_{FB} Btu/hr-ft^2-°F
2/27/65	2105	61.6	157,000	87			
3/27/65	1838	41.2	171,000	57			
3/31/65	2104	47.6	94,000		96	258	
3/31/65	2105	47.6	49,900		96	228	
	2105	47.6	49,900	95-99			
	2105	47.6	52,000	98-96			
	2105	47.6	53,000	95			
4/1/65	2105	46.7	211,000	59			
4/1/65	2106	46.5	214,000	61			

Test Section No. 4 (.73-in I.D. with annular plug and helix P/D = 2)

Date	Time	T_{sat}, °F	G lb/sec-ft^2	q'' Btu/hr-ft^2	x_{FBE} %	x_{FB} %	h_{FB} Btu/hr-ft^2-°F	a_R g's
5/23/65	1414	2100	32.0	148,000	87			159.0
5/27/65	1610	2100	28.6	159,000			260	
5/28/65	1430	2106	19.8	155,800	98	98	335	76.2
	1527	2100	19.9	121,950	95	95	214	73.3
	1529	2100	19.9	121,950		96	196	74.9
	1608	2105	19.9	76,830	96	96	249	74.1
	1618	2104	19.9	78,140		99	172	78.9
	1634	2103	19.5	55,200	99	99	188	75.9
	1714	2100	19.6	56,500	99	99	176	77.2
6/8/65	1733	1824	20.4	150,340	93	93	222	146.8
	1809	1819	21.9	105,900	90	90	217	160.7
	1816	1824	21.3	105,520		97	148	174.1
	1843	1825	21.3	103,630	91			152.9
6/10/65	1625	1813	24.0	146,520	98	98	196	233.0
	1652	1807	24.1	100,800	96	96	185	199.9

Test Section No. 5 (.74-in I.D. with wire-wrapped plug and helix P/D = 2)

Date	Time	T_{sat}, °F	G lb/sec-ft^2	q'' Btu/hr-ft^2	x_{FBE} %	x_{FB} %	h_{FB} Btu/hr-ft^2-°F	a_R g's
7/8/65	1617	2105	23.4	102,100		99	208	108.3
7/28/65	1108	2105	17.9	145,480		95.1	256	58.5
8/3/65	1730	1811	16.0	174,880		99	201	105.1

Table 6

SUPERHEATED VAPOR DATA

Test Section No. 3 (.42-in I.D., no insert)

Date	Time	T_{sat}, °F	G lb/sec-ft^2	q'' Btu/hr-ft^2	δ_{SH} °F	h_{SH} Btu/hr-ft^2-°F
3/31/65		2105	47.6	49,900	25	194

Test Section No. 4 (.73-in I.D. with annular plug and helix P/D = 2)

Date	Time	T_{sat}, °F	G lb/sec-ft^2	q'' Btu/hr-ft^2	δ_{SH} °F	h_{SH} Btu/hr-ft^2-°F
5/28/65	1624	2104	19.6	77,270	15	162
	1645	2103	19.6	56,750	5	152
	1651	2100	19.2	56,300	144	183
	1659	2100	19.5	55,700	40	172
	1707	2100	19.6	56,030	5	152
6/8/65	1824	1825	20.4	104,470	85	145
	1832	1825	21.0	104,140	15	143
6/10/65	1705	1807	23.4	105,000	287	187

Test Section No. 5 (.74-in I.D. with wire-wrapped plug and helix P/D = 2)

Date	Time	T_{sat}, °F	G lb/sec-ft^2	q'' Btu/hr-ft^2	δ_{SH} °F	h_{SH} Btu/hr-ft^2-°F
7/8/65	1629	2100	23.5	100,980	45	213
	1640	2100	23.0	100,420	105	231
7/27/65	1125	2102	23.1	143,170	29	256
7/28/65	1120	2105	17.3	144,350	75	217
8/ 3/65	1738	1800	15.8	178,890	34	201
	1753	1805	15.4	179,230	202	233

Table 7

SINGLE-PHASE WATER PRESSURE DROP DATA

FROM TEST SECTION NO. 4 (.73 in I.D. with annular plug and helix P/D = 2)

Flow lb$_m$/sec	$P_0 - P_{10}$	$P_0 - P_1$	$P_1 - P_2$	$P_2 - P_3$	$P_3 - P_4$	$P_4 - P_5$	$P_5 - P_6$	$P_6 - P_7$	$P_7 - P_8$	$P_8 - P_9$	$P_9 - P_{10}$
.417	205	76.6	27.3	26.0	22.8	5.15	10.3	10.8	9.53	6.71	10.4
.556	348	135	48.6	44.8	39.4	6.91	16.9	18.6	16.0	15.1	17.2
.696	505	193	69.3	63.0	55.6	9.04	23.5	26.0	21.8	20.9	23.6
.835	716	279	100	89.3	77.4	11.0	33.3	36.7	30.1	29.5	33.0
.974	960	379	134	119	104	12.7	44.5	49.1	39.5	38.6	43.3
1.113	1230	490	171	151	131	13.9	56.6	62.9	50.0	48.7	54.4
1.252	1530		213	187	163	14.5	71.0	78.3	61.7	59.8	66.8
1.391	1741		243	213	185	15.1	81.3	89.2	69.8	67.8	75.8
1.530	2106		293	256	223	15.6	98.8	108	84.2	81.0	90.9
1.669	2568	ΔP exceeded	356	311	271	15.6	121	132	103	97.7	110
1.808	2988	Manometer limit	414	361	315	16.2	141	154	119	113	127
1.948	3457		478	417	364	17.8	163	179	137	131	146
2.087	3916		539	471	412	18.8	185	203	154	149	164
1.878	3180		440	384	336	14.7	151	164	126	121	135
1.739	2698		373	327	286	13.1	128	139	107	103	115
1.600	2285		317	277	243	14.3	108	117	91	88.2	98.3
1.461	1930		268	236	206	14.9	91.0	99.1	77.2	75.4	83.7
1.322	1605		223	207	171	14.5	75.3	82.4	64.6	63.7	70.3
1.182	1299	521	181	161	140	14.1	61.1	66.8	52.9	52.4	57.9
1.043	1022	404	142	158	111	13.1	47.6	52.4	42.2	41.7	46.4
.904	801	313	111	100	88.0	11.8	37.9	41.3	33.6	33.4	37.1
.765	631	245	87	79.7	69.8	10.4	30.0	32.6	27.0	26.6	28.7
.626	400	151	53.6	50.8	44.5	7.29	19.6	20.9	17.9	17.0	19.5
.487	273	103	36.4	34.6	30.8	5.54	13.8	14.7	12.6	11.8	12.9

Pressure Differences, lb/ft^2

Water Temperature = 25°C

Pressure Tap Locations Shown in Figure 11.

-139-

Table 8

SINGLE-PHASE WATER PRESSURE DROP DATA

FROM TEST SECTION NO. 5 (.74 in I.D. with wire-wrapped plug and wire coil P/D = 2)

Pressure Differences, lb/ft^2 →

Flow lb$_m$/sec	$P_0 - P_{11}$	$P_0 - P_1$	$P_1 - P_2$	$P_2 - P_3$	$P_3 - P_4$	$P_4 - P_5$	$P_5 - P_6$	$P_6 - P_7$	$P_7 - P_8$	$P_8 - P_9$	$P_9 - P_{10}$	$P_{10} - P_{11}$
0.4173	1198	1.01	4.56	366	241	241	197	83.5	19.1	9.75	12.9	22.3
0.4869	1534	1.52	6.08	475	308	305		103	25.2	12.5	17.0	28.4
0.5564	1964	2.03	8.62		399	389		128	33.2	16.0	22.4	36.8
0.6260	2421	2.54	9.63		490	475		152	42.1	19.5	28.1	44.6
0.6956	2957	3.55	11.7		600	578		181	51.9	23.4	34.9	54.1
0.6260	2317	2.54	9.13		470	456		147	41.0	17.6	26.7	42.8
0.5564	1974	2.03	8.11		400	390		128	34.7	15.2	22.6	36.8
0.4869	1534	1.52	6.08	479	310	306		104	26.1	12.1	17.0	28.6
0.4173	1168	1.01	4.56	357	234	233	195	80.7	19.1	9.17	12.7	21.9
0.4173	1167	1.01	4.06	354	234	234	192	81.5	18.6	9.75	12.9	21.5
0.4869	1539	1.52	6.08	478	310	306		103	25.2	13.1	17.6	28.5
0.5564	1950	2.03	7.10		392	383		126	32.7	16.2	22.6	35.9
0.6260	2459	3.04	9.63		498	482		154	42.4	20.1	29.3	45.0
0.6956	2929	3.55	11.7		593	572		179	51.0	23.4	35.1	53.0
0.6260	2439	3.04	9.63		494	479		153	42.4	19.5	29.1	44.7
0.5564	1911	2.03	7.61		385	377		125	33.1	15.0	22.2	35.1
0.4869	1552	2.03	6.08	483	314	310		105	26.6	12.3	17.9	28.9
0.4173	1160	1.01	4.06	356	233	235	192	81.5	19.0	9.6	13.1	21.6

Water Temperature = 10.5°C

Pressure top locations shown in Figure 13

Table 9

TWO-PHASE ADIABATIC POTASSIUM PRESSURE DROP DATA
FROM TEST SECTION NO. 4 (.73 in I.D. with annular plug and helix P/D = 2)

Date	Time	T_{31} °F	T_{32} °F	T_{33} °F	T_{34} °F	T_{35} °F	Flow lbs/sec	ϕ_{31-32}	x_{31-32}	ϕ_{34-35}	x_{34-35}
6-7-65	1128	1828.5	1820.0	1821.1	1816.4	1814.6	.0614	117.4	.907	125.9	.900
6-7-65	1444	1822.2	1814.3	1815.7	1811.4	1809.6	.0602	111.2	.805	129.0	.799
6-7-65	1845	1811.2	1803.6	1805.3	1801.2	1799.3	.0604	103.8	.668	132.3	.665
6-7-65	2230	1813.3	1806.4	1809.4	1805.1	1803.3	.0589	99.3	.580	132.0	.579
6-8-65	0130	1794.3	1788.4	1792.0	1787.6	1785.7	.0588	81.3	.478	133.8	.478

Thermocouple Locations Shown in Figure 11.

Table 10

TWO-PHASE ADIABATIC POTASSIUM PRESSURE DROP DATA
FROM TEST SECTION NO. 5 (.74 in I.D. with Wire-wrapped plug and wire coil P/D = 2)

Date	Time	T_{31} °F	T_{32} °F	T_{33} °F	T_{34} °F	T_{35} °F	T_{36} °F	T_{37} °F	Flow lbs/sec	ϕ_{31-32}	ϕ_{32-33}	$\phi_{33-34,35}$	x avg.
7/9/65	0615	1867.7	1839.1	1822.4	1799.3	1800.3	1800.5	1800.5	0.0580	67.1	111.7	113.6	.543
7/13/65	0315	1863.6	1838.1	1822.4	1801.4	1802.5	1802.8	1802.6	0.0609	61.3	96.2	94.7	.448
	0620	1869.6	1841.1	1824.0	1800.5	1801.5	1802.2	1801.7	0.0592	72.7	110.7	111.7	.534
	1219	1817.8	1807.6	1800.8	1792.3	1793.2	1793.9	1794.0	0.0467	35.8	62.7	57.1	.364
	1513	1836.4	1819.8	1810.1	1797.8	1798.7	1798.6	1798.8	0.0448	64.8	98.2	93.0	.504
	1940	1859.5	1834.3	1820.8	1802.7	1803.7	1804.4	1803.8	0.0479	91.5	125.7	124.5	.659
	2240	1865.1	1835.0	1819.2	1797.0	1798.0	1798.9	1798.8	0.0471	113.0	150.8	156.7	.848

Thermocouple locations shown in Figure 13

Table 13

SINGLE PHASE LIQUID HEAT TRANSFER DATA

PLUG REGION OF TEST SECTION NO. 5 (.74 in I.D. with wire-wrapped plug and wire coil P/D = 2)

Date	Time	T_{sat}, °F @ T/C 33	q'' Test Section Btu/hr-ft²	Flow lb$_m$/sec	G lb$_m$/sec-ft²	N_{Re} @ T/C 33	$(N_{Re})_e$ @ T/C 33	N_{Pe} @ T/C 33	$(N_{Pe})_e$ @ T/C 33	T T/C 19 °F	h T/C 19 Btu/hr-ft²-°F	N_{NU} @ T/C 19
7/14/65	1920	1459	163,500	0.127	116	17,080	31,800	61.7	115.0	41.2	3968	3.13
	2140	1410	167,860	0.112	102	14,750	27,460	52.4	97.6	43.8	3829	2.93
7/15/65	0045	1349	158,660	0.0945	86.0	12,030	22,410	42.3	78.7	43.6	3636	2.68
	0335	1261	133,260	0.0727	66.1	8,820	16,420	30.6	57.0	44.3	3006	2.10
	0600	1121	85,520	0.0393	35.8	4,360	8,120	15.2	28.3	45.9	1862	1.20
	2105	1462	60,090	0.0449	40.9	6,050	11,260	21.9	40.7	24.8	2422	1.91
	2250	1389	60,450	0.0584	53.1	7,610	14,170	26.9	50.1	23.0	2630	1.98
7/16/65	0145	1358	60,090	0.0732	66.6	9,370	17,450	33.0	61.4	20.0	3003	2.22
	0415	1340	59,710	0.0893	81.2	11,320	21,070	39.7	74.0	18.0	3316	2.43
	0910	1294	59,460	0.104	94.9	12,890	24,010	45.0	83.7	17.8	3349	2.38
	1310	1370	40,210	0.0446	40.6	5,750	10,710	20.3	37.7	15.6	2579	1.92
	1503	1361	53,700	0.0593	54.0	7,610	14,170	26.8	49.9	20.0	2680	1.99
	1755	1352	65,870	0.0739	67.2	9,420	17,550	33.1	61.7	22.0	2989	2.20
	2005	1369	80,360	0.0894	81.4	11,530	21,470	40.6	75.7	26.1	3082	2.30
	2105	1360	36,010	0.105	95.1	13,410	24,960	47.2	87.9	25.2	3415	2.53

Thermocouple Locations Shown in Figure 13
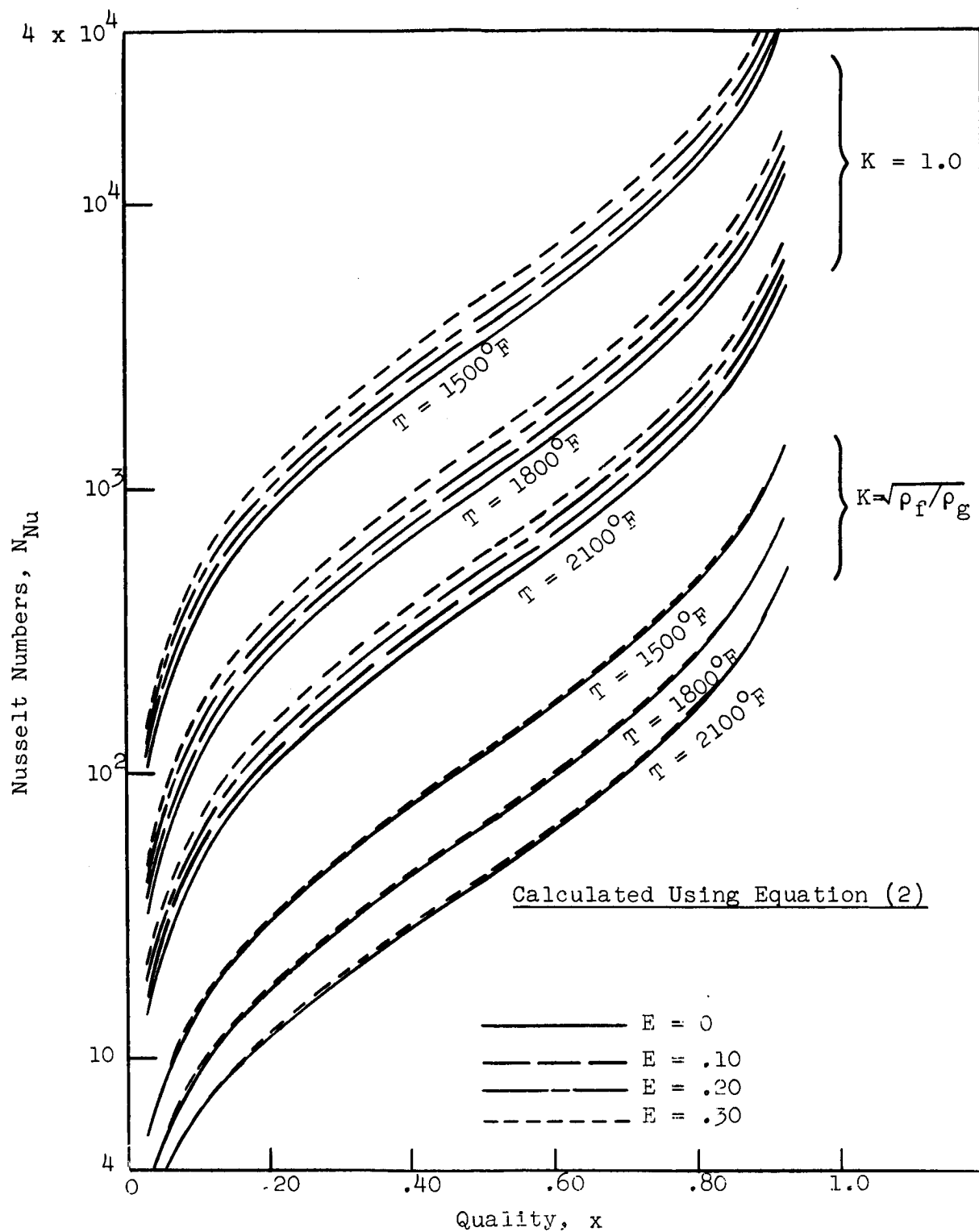
Figure 22. Effect of Liquid Entrainment E on the Nusselt Numbers
Calculated from the Film Evaporation Model

Calculated Using Momentum
Exchange Model of Reference 7,
Equation (4)
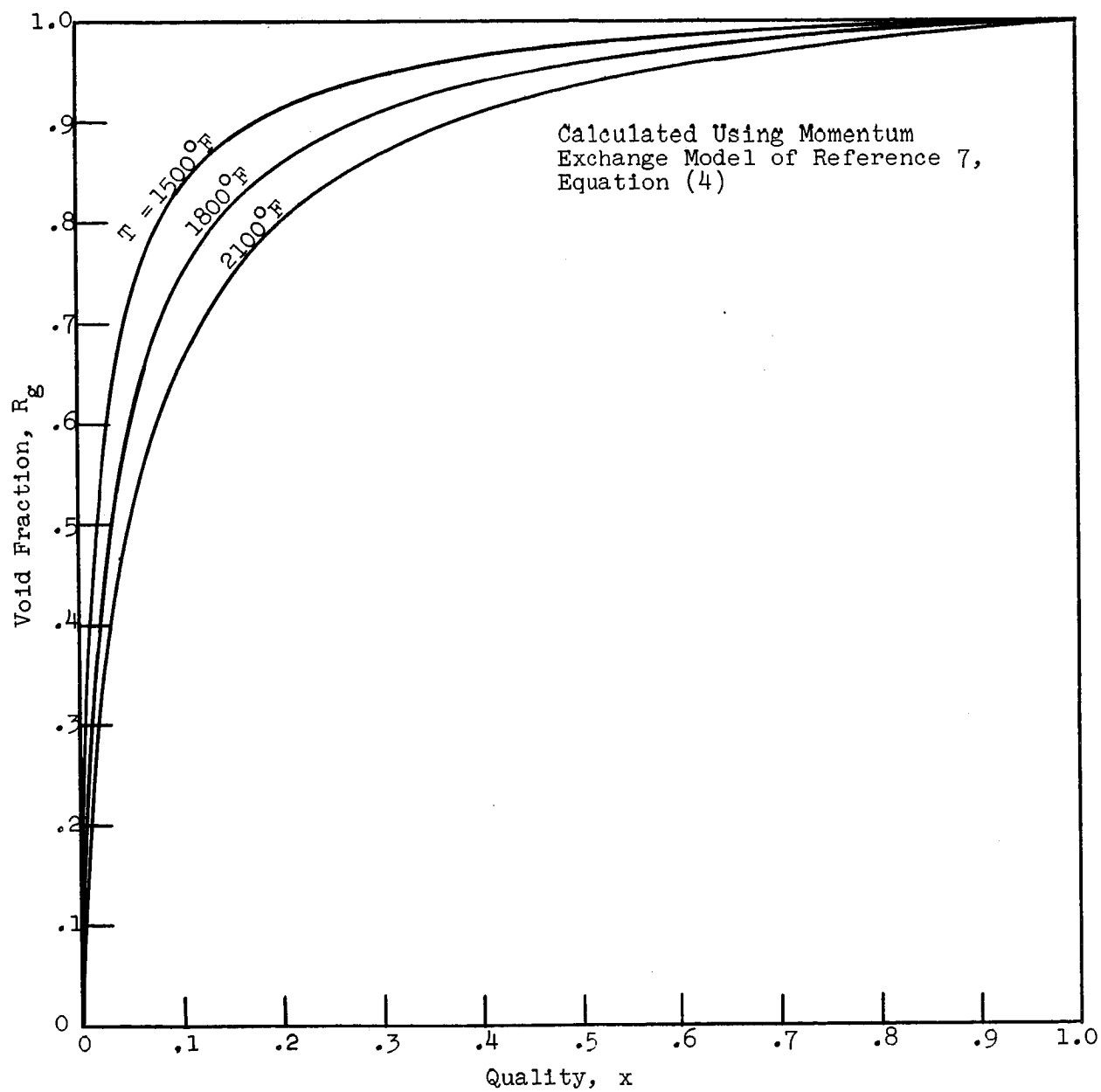
Figure 23. Void Fraction as a Function of Quality for Potassium
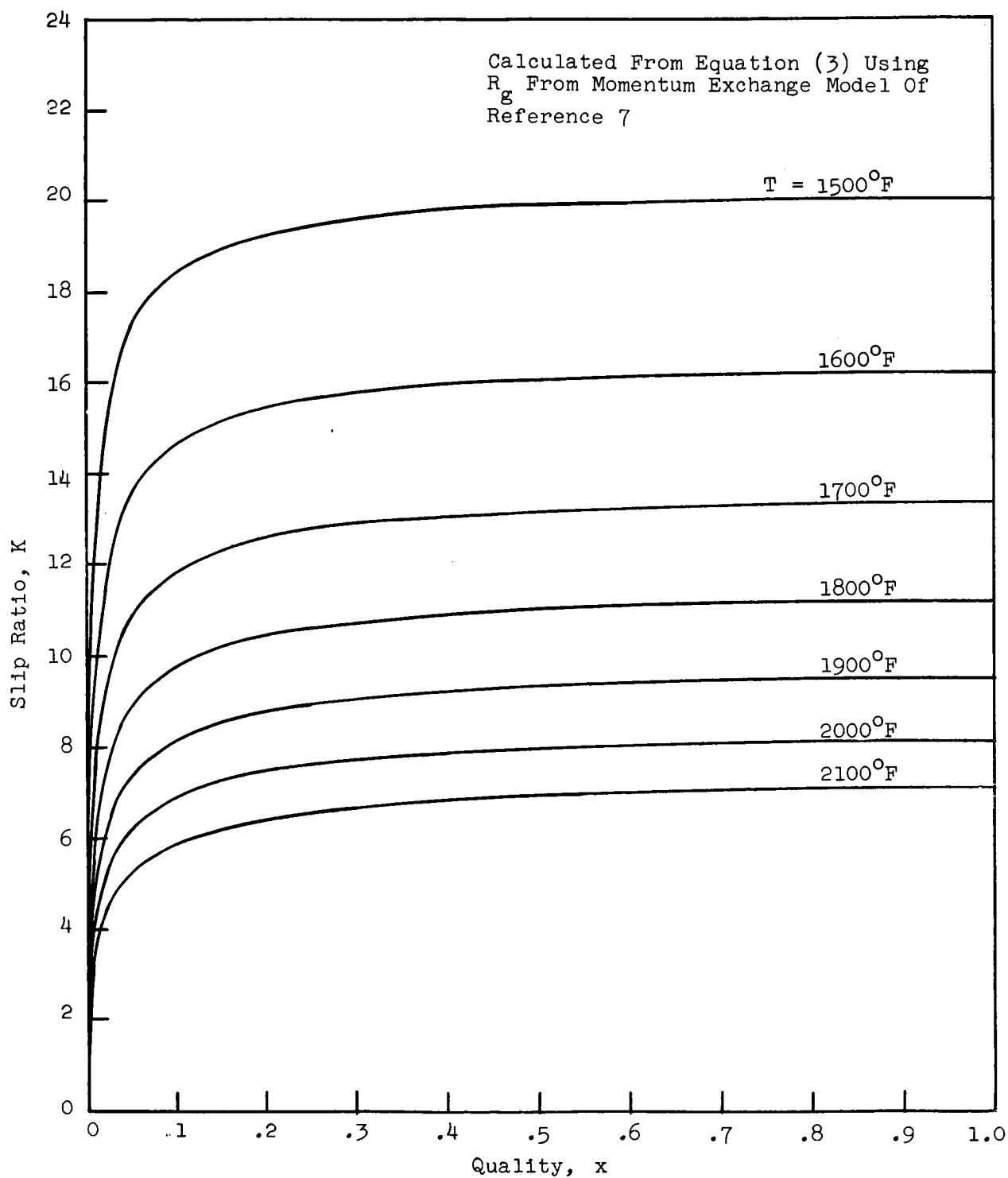
Figure 24.   Slip Ratio as a Function of Quality for Potassium
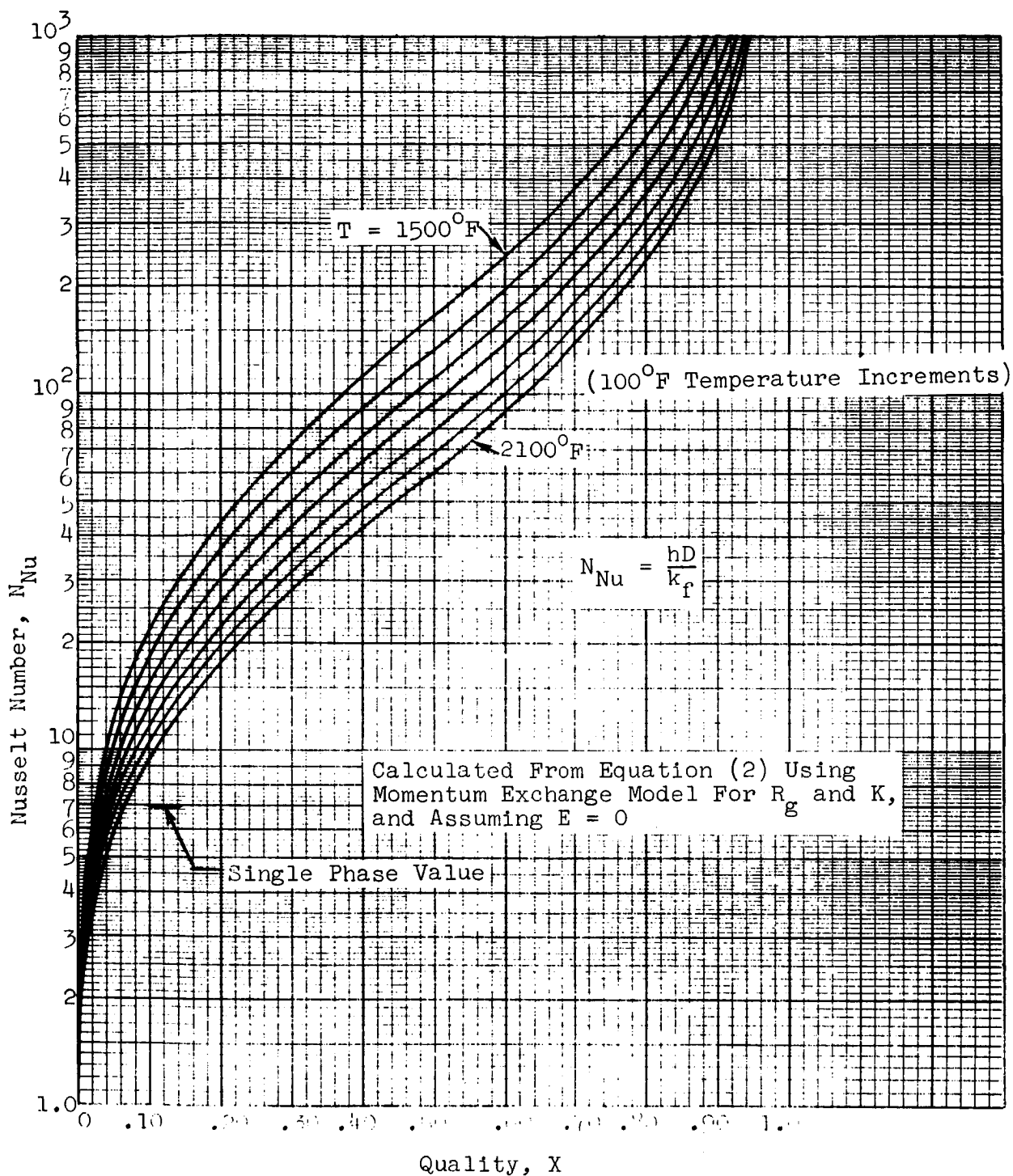
Figure 25. Nusselt Numbers Calculated From The Film
Evaporation Model

Film Thickness/Tube Radius, $2\delta/D_T$

Calculated From Momentum Exchange
Model Results Given In Figure 23

$T = 2100°F$
$1800°F$
$1500°F$
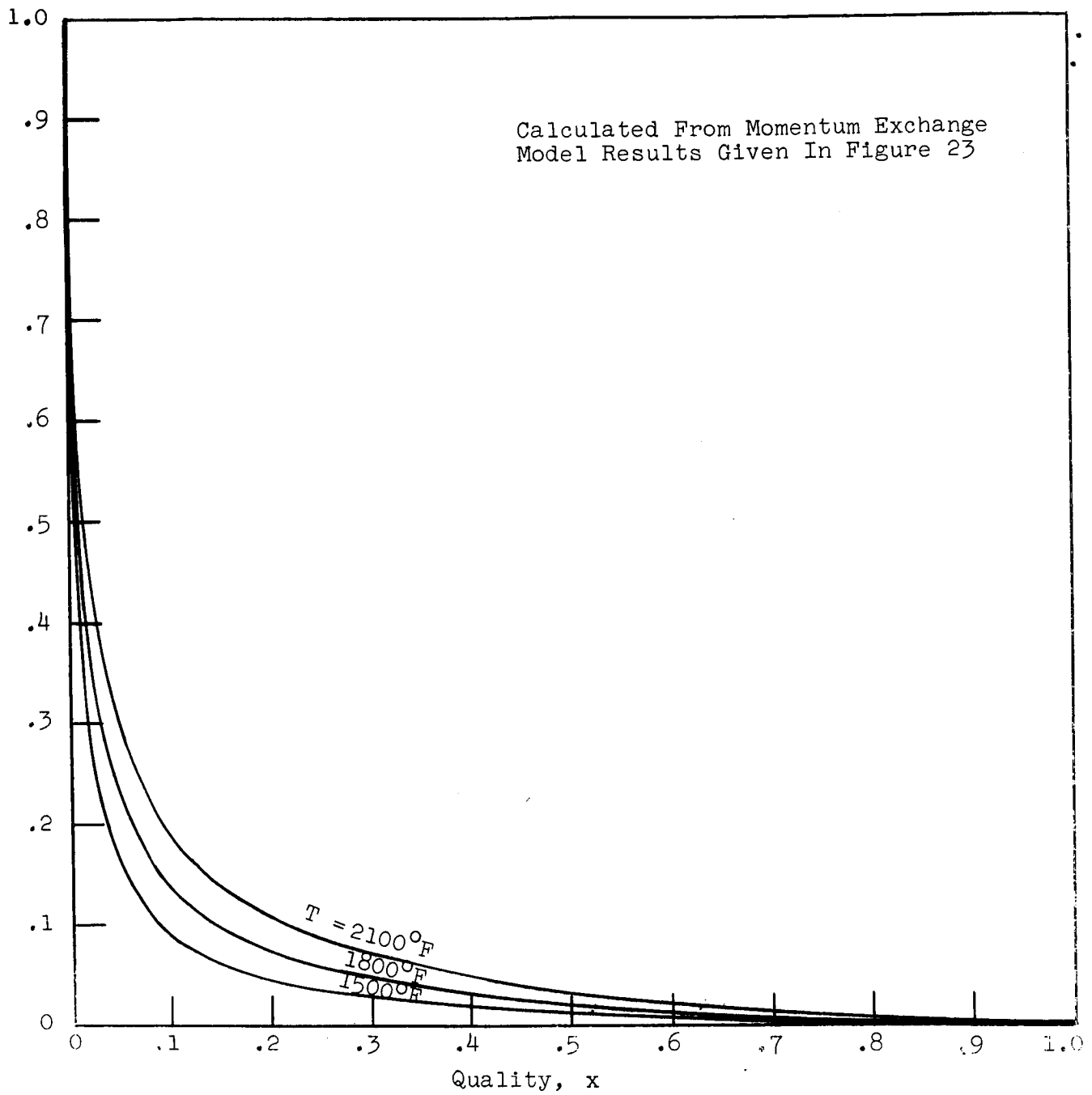
Quality, x

Figure 26   Film Thickness to Tube Radius Ratio as a Function
of Quality

-148-

$$N_{Nu} = \frac{hD_T}{k_f}$$

Calculated Using Equation (6), n = 2

T = 1500°F

2100°F

(100°F Temperature Increments)

Nusselt Numbers, N_{Nu}

Quality, X
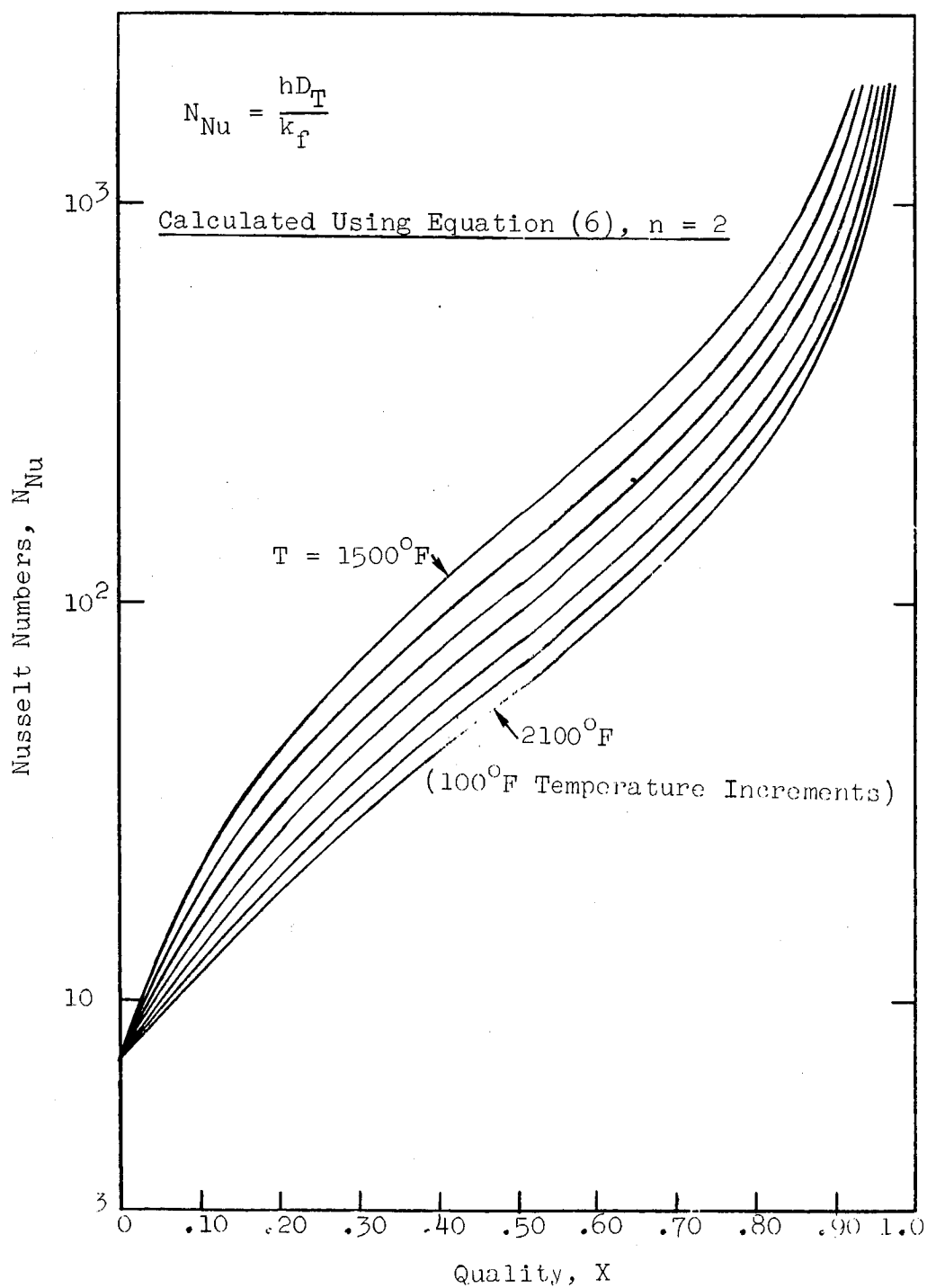
Figure 27. Modified Film Evaporation Model Nusselt Numbers

$$N_{Nu} = \frac{hD_T}{k_f}$$

Calculated Using Equation (8)

$T_{sat} = 1500°F, \delta_g/D_T = 0$

$T_{sat} = 2100°F, \delta_g/D_T = 0$

(1)

(3)

(2)

(4)

Nusselt Number, N_{Nu}

Curve	T_{sat}	δ_g/D_T
(1)	2100°F	1.03×10^{-5}
(2)	2100°F	2.236×10^{-5}
(3)	1500°F	1.03×10^{-5}
(4)	1500°F	2.236×10^{-5}

Quality, X, %
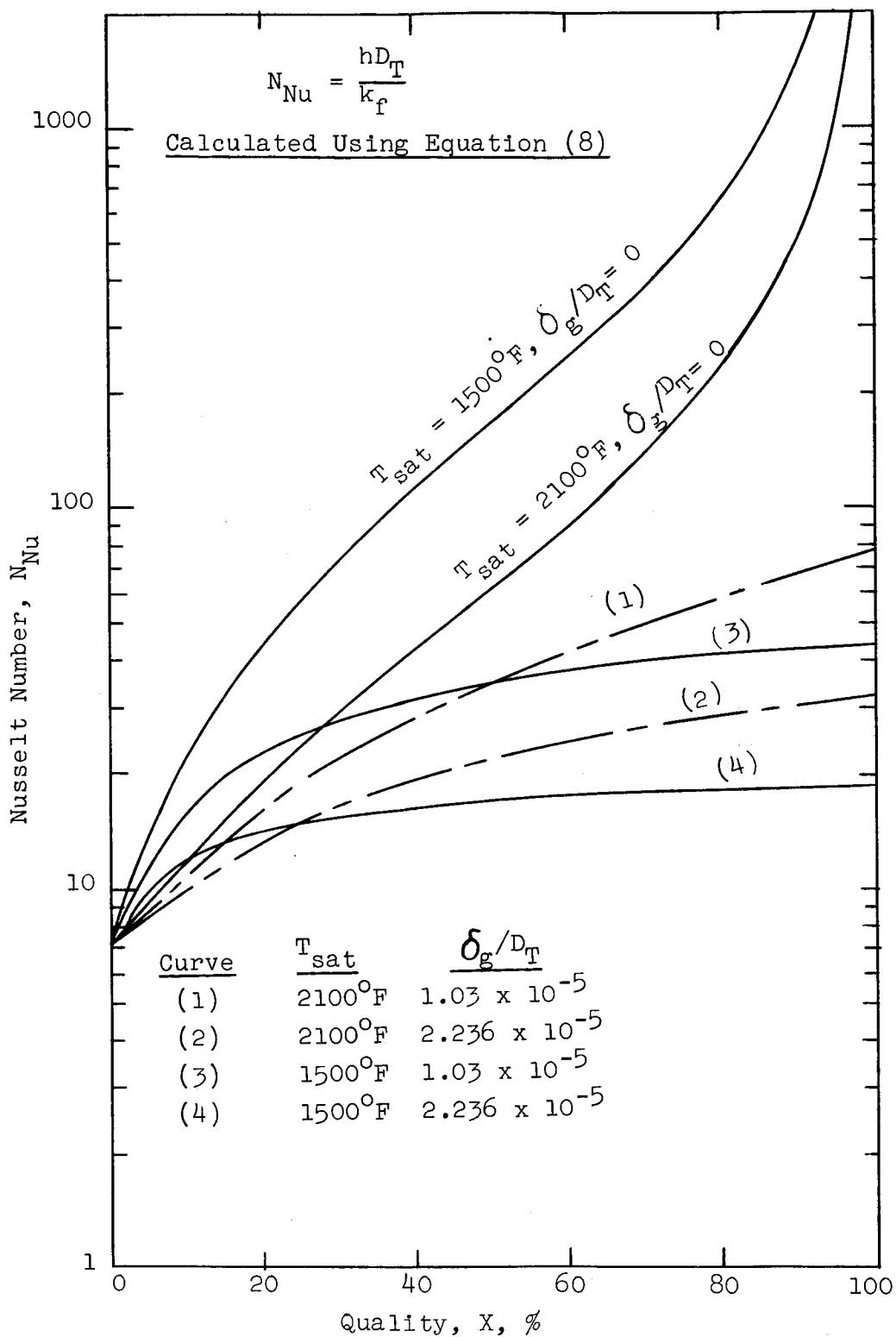
Figure 28   Effect of Vapor Film Resistance On
Two-Phase Nusselt Numbers
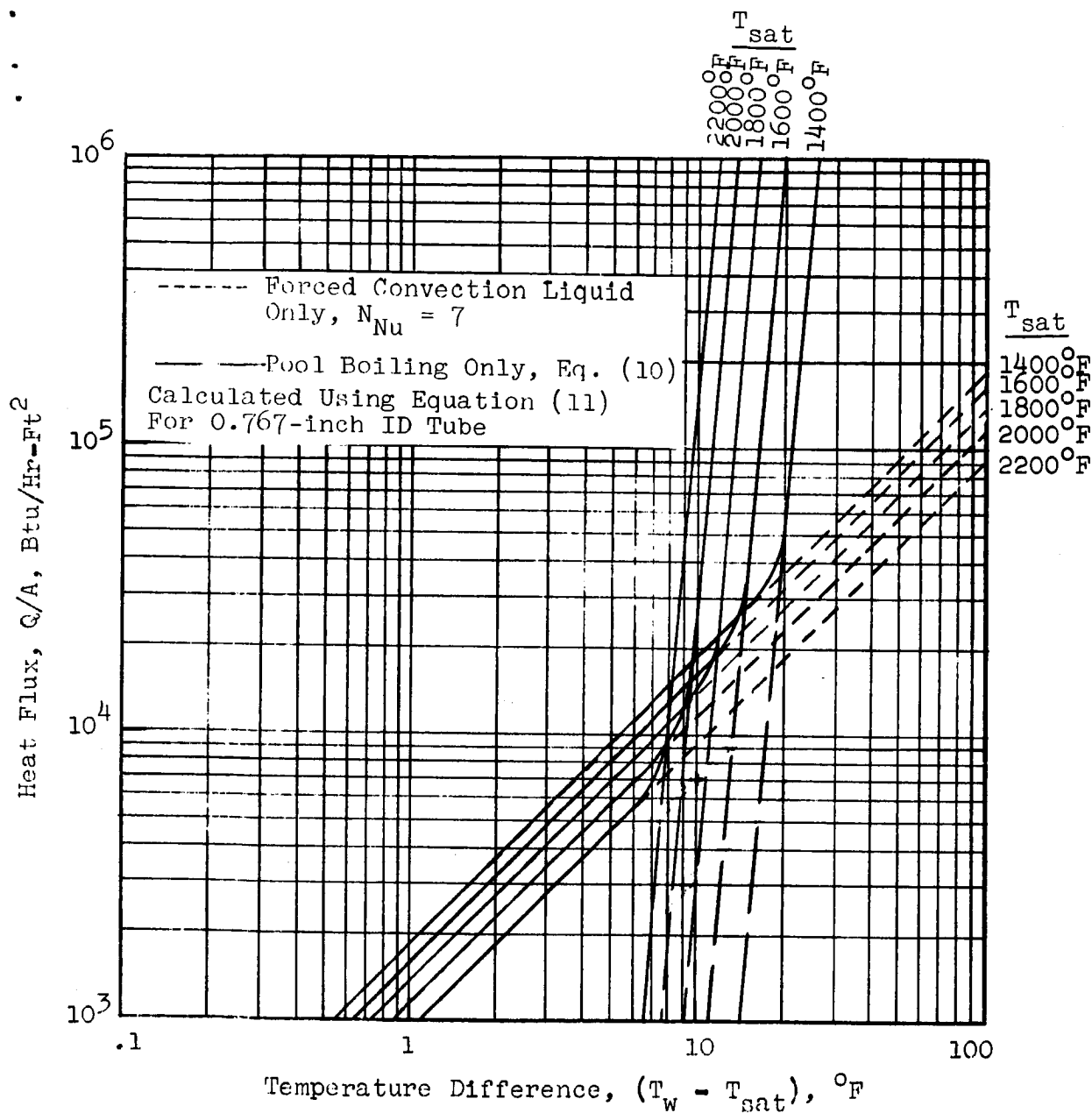
Figure 29. Heat Flux as a Function of Temperature Difference for the Forced Convection Nucleate Boiling Model
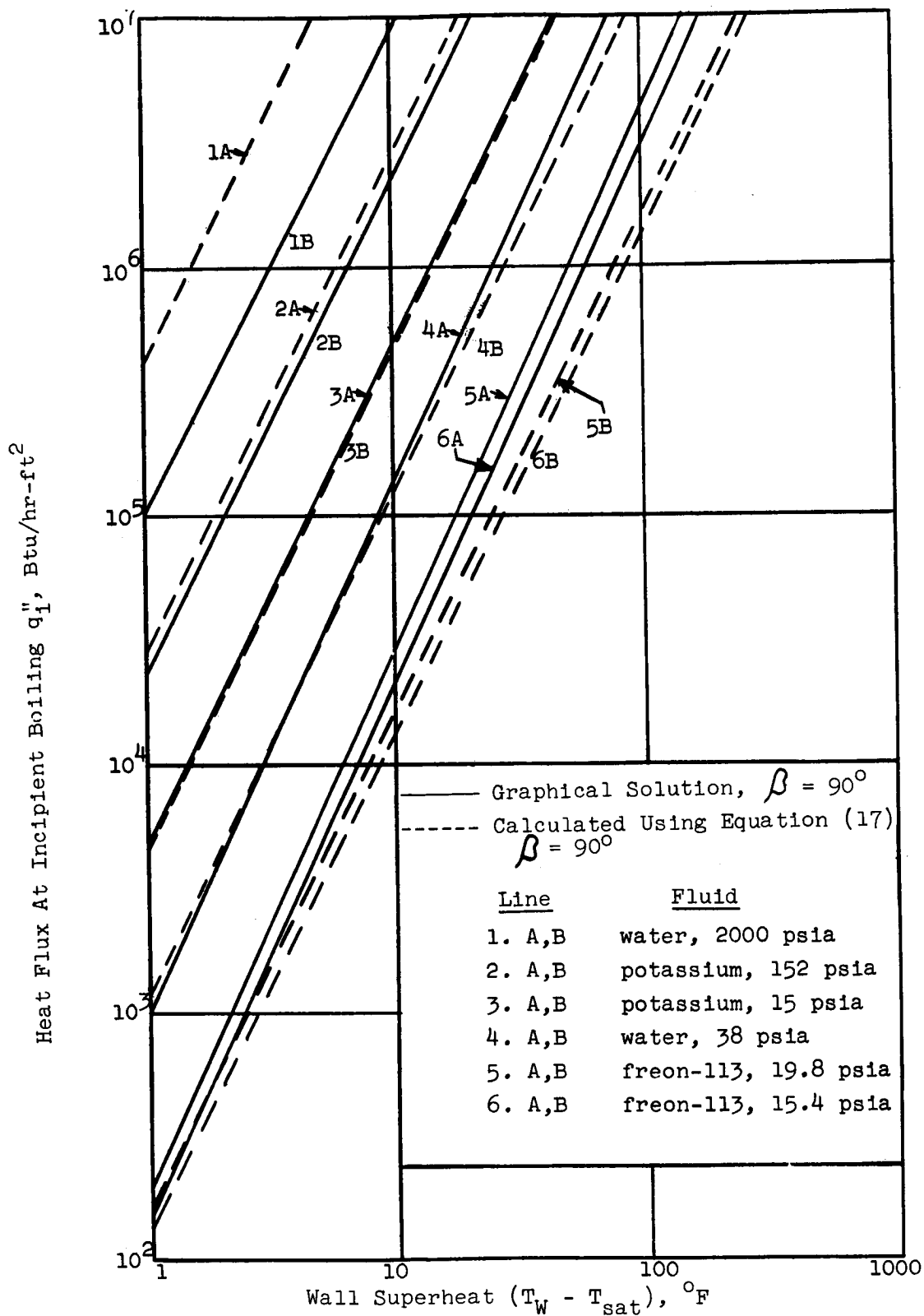
Figure 30.   Calculated Relationship Between Heat Flux and Wall
Superheat For Incipient Boiling Of Different Fluids
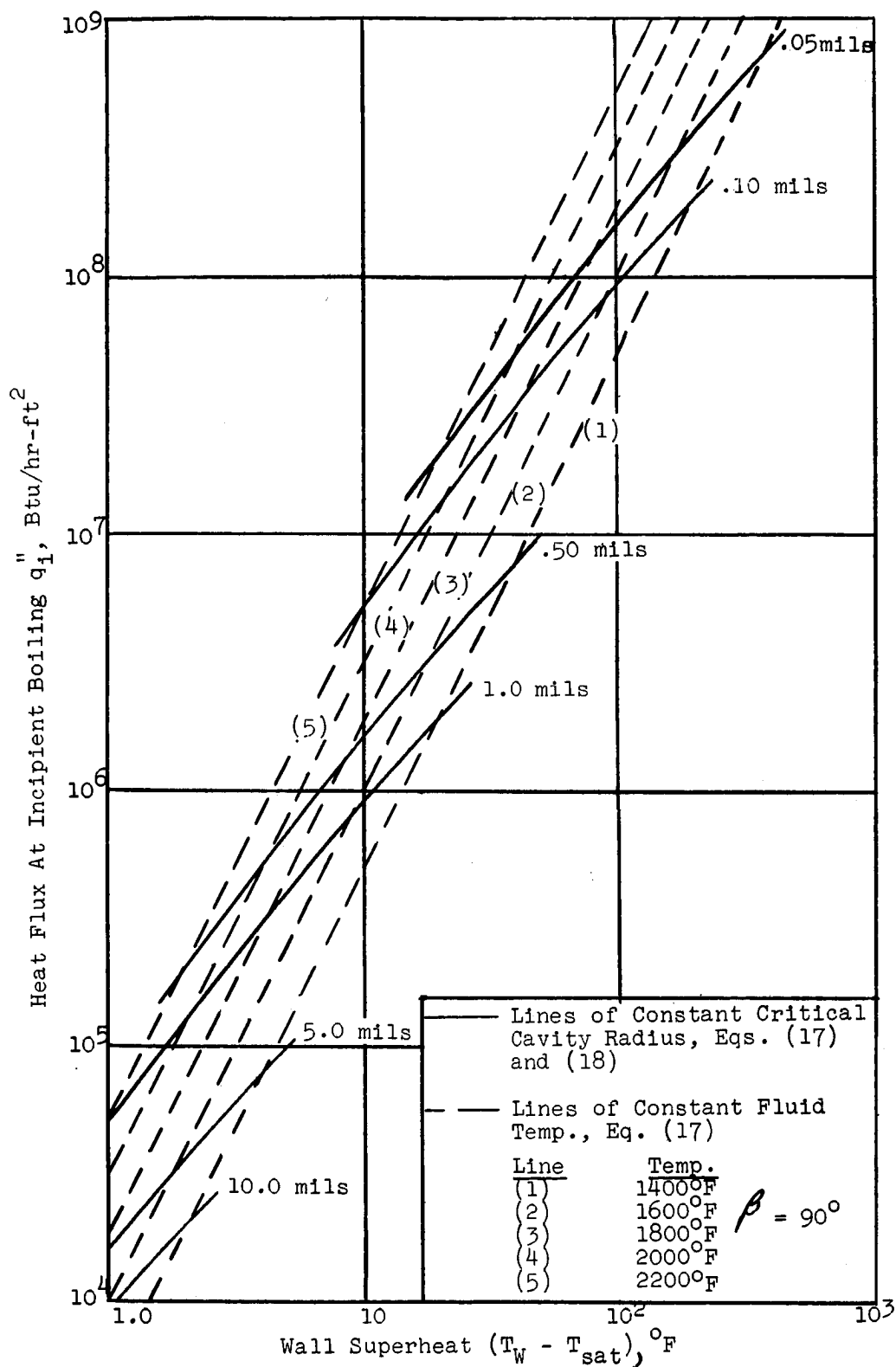
Figure 31. Calculated Relationship Between Heat Flux and
Wall Superheat For Incipient Boiling of Potassium
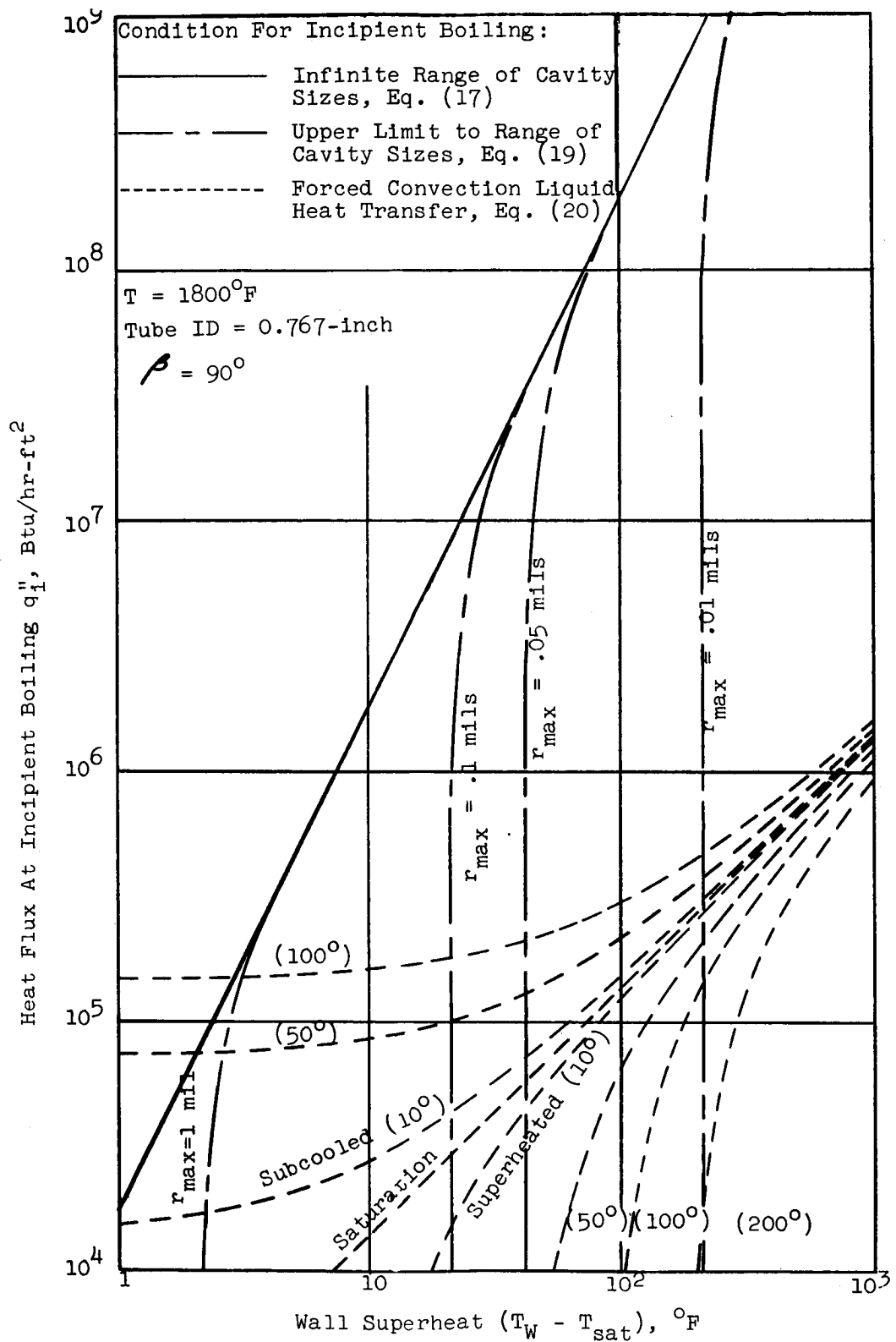
Figure 32. Calculated Effect of Cavity Size On The Relationship Between Heat Flux and Wall Superheat For Incipient Boiling Of Potassium At 1800°F
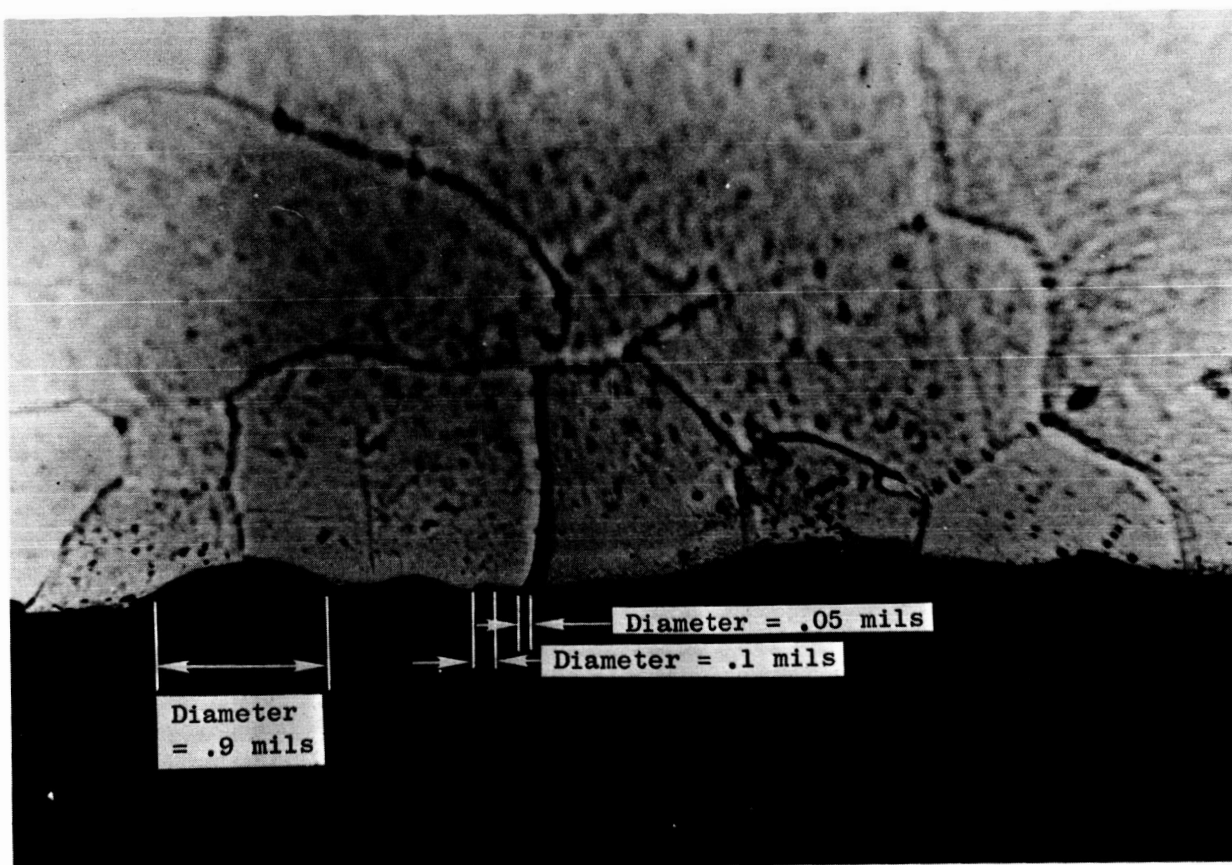
Figure 33. Micrograph of Test Section No. 1 (.767"ID, no insert) Inside Surface (ID Transverse Magnified 1000 X - Polished But Not Etched)
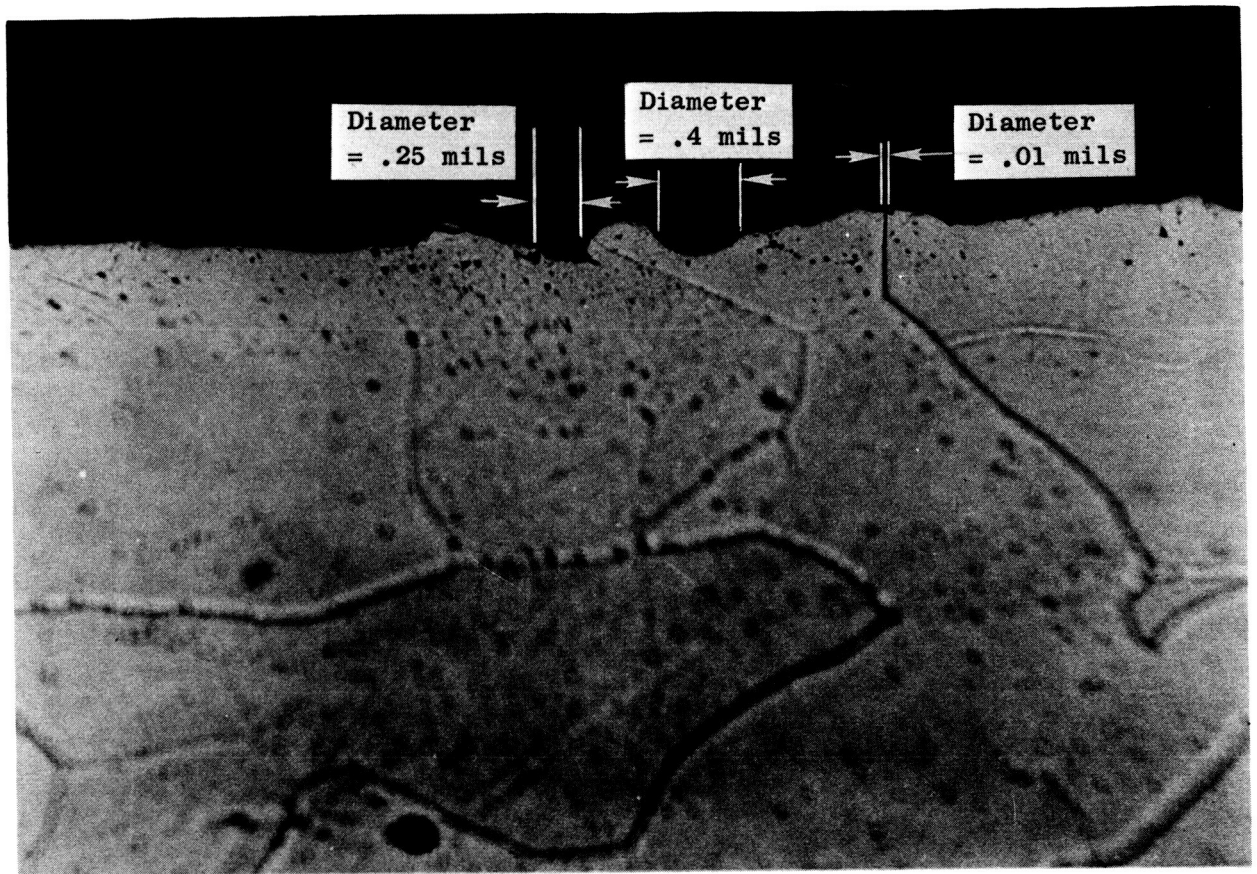
Figure 34. Micrograph of Test Section No. 1 (.767"ID, no insert) Inside Surface (ID Longitudinal Magnified 1000 X - Polished But Not Etched)
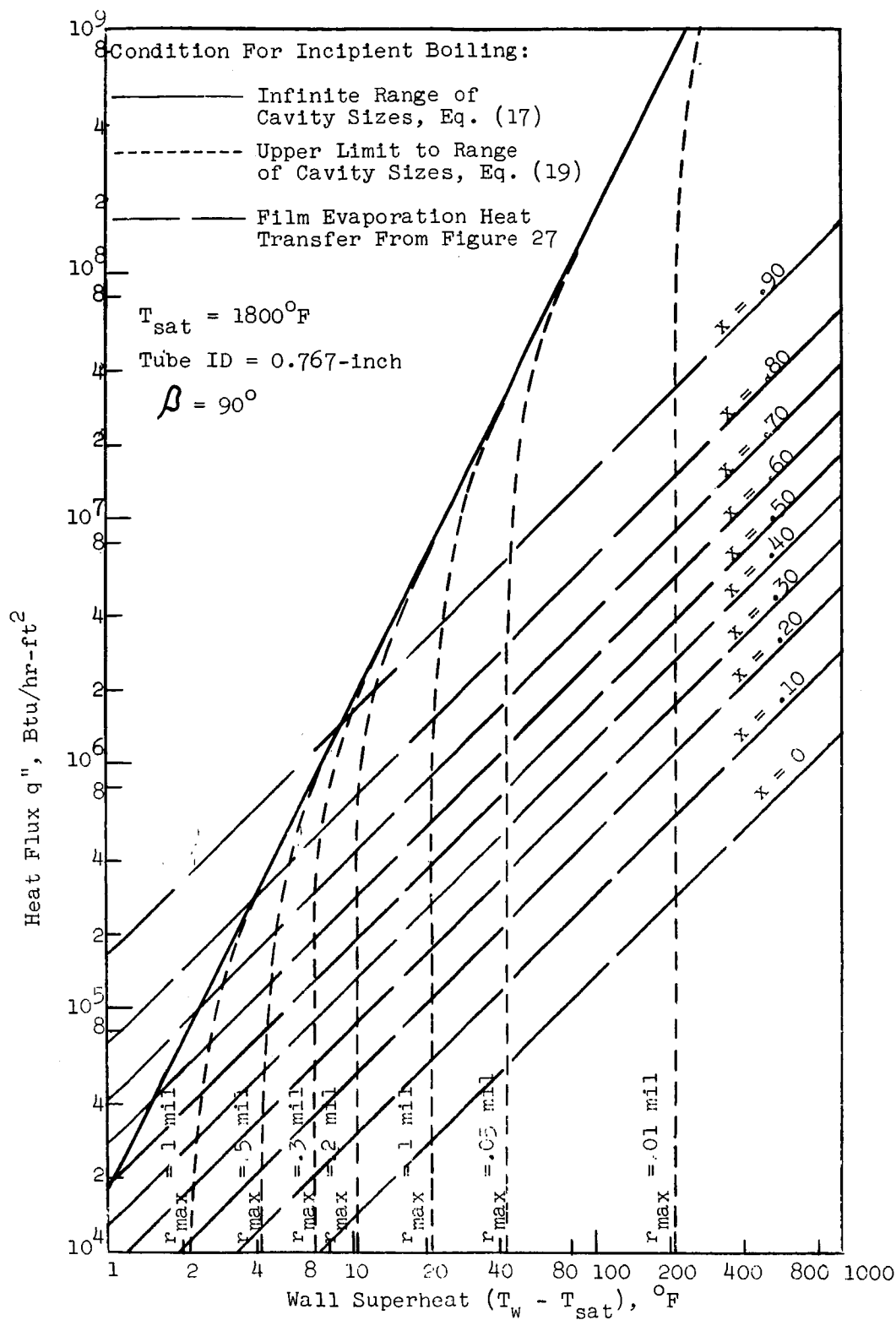
Figure 35 Calculated Wall Superheats Required To Initiate
Boiling For Potassium Compared With Available
Wall Superheats As Calculated From Film Evapora-
tion Model For Various Vapor Qualities
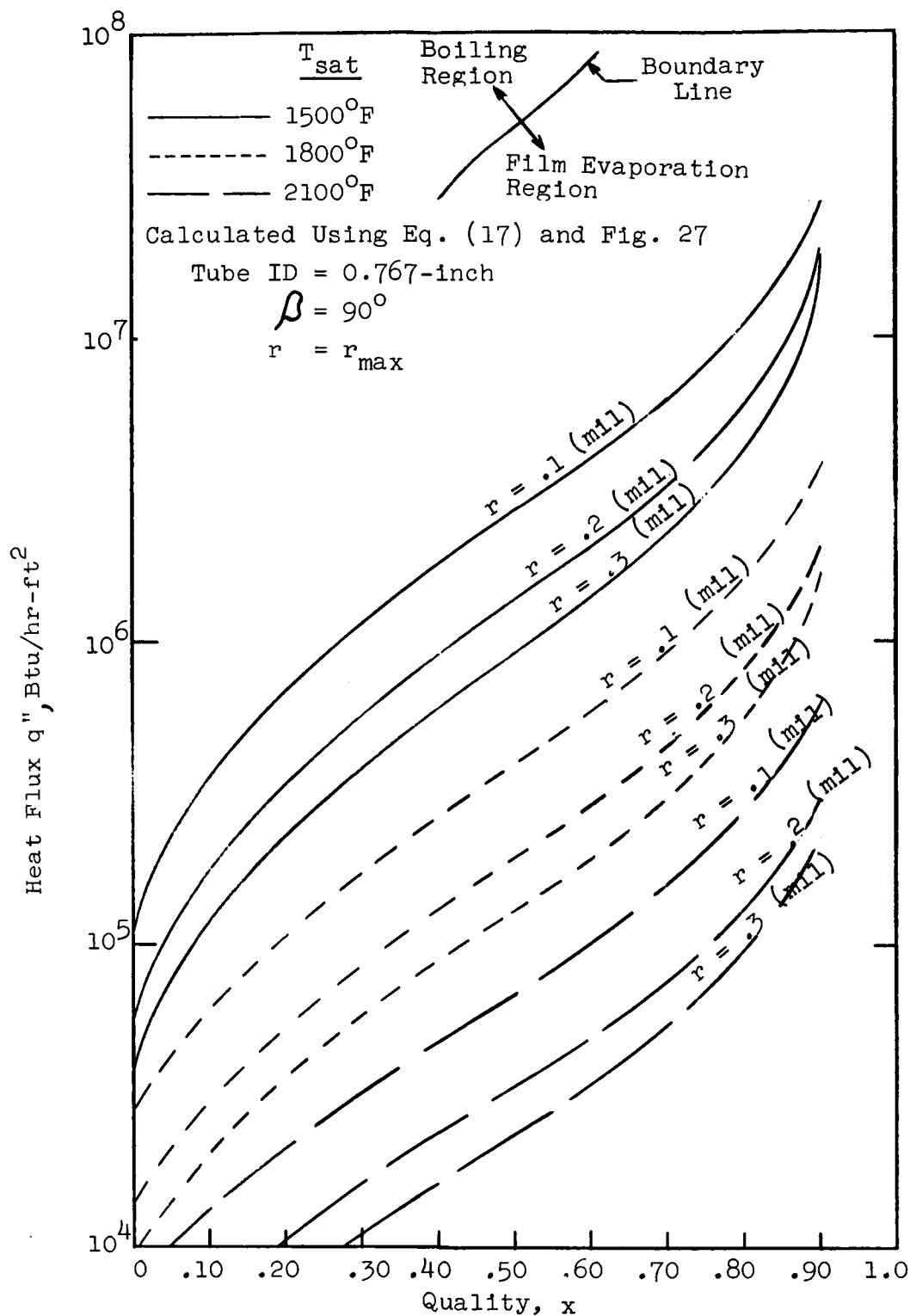
Figure 36. Map Showing Calculated Boundaries Between Boiling
With Bubble Formation And Evaporation Without
Bubble Formation For Potassium
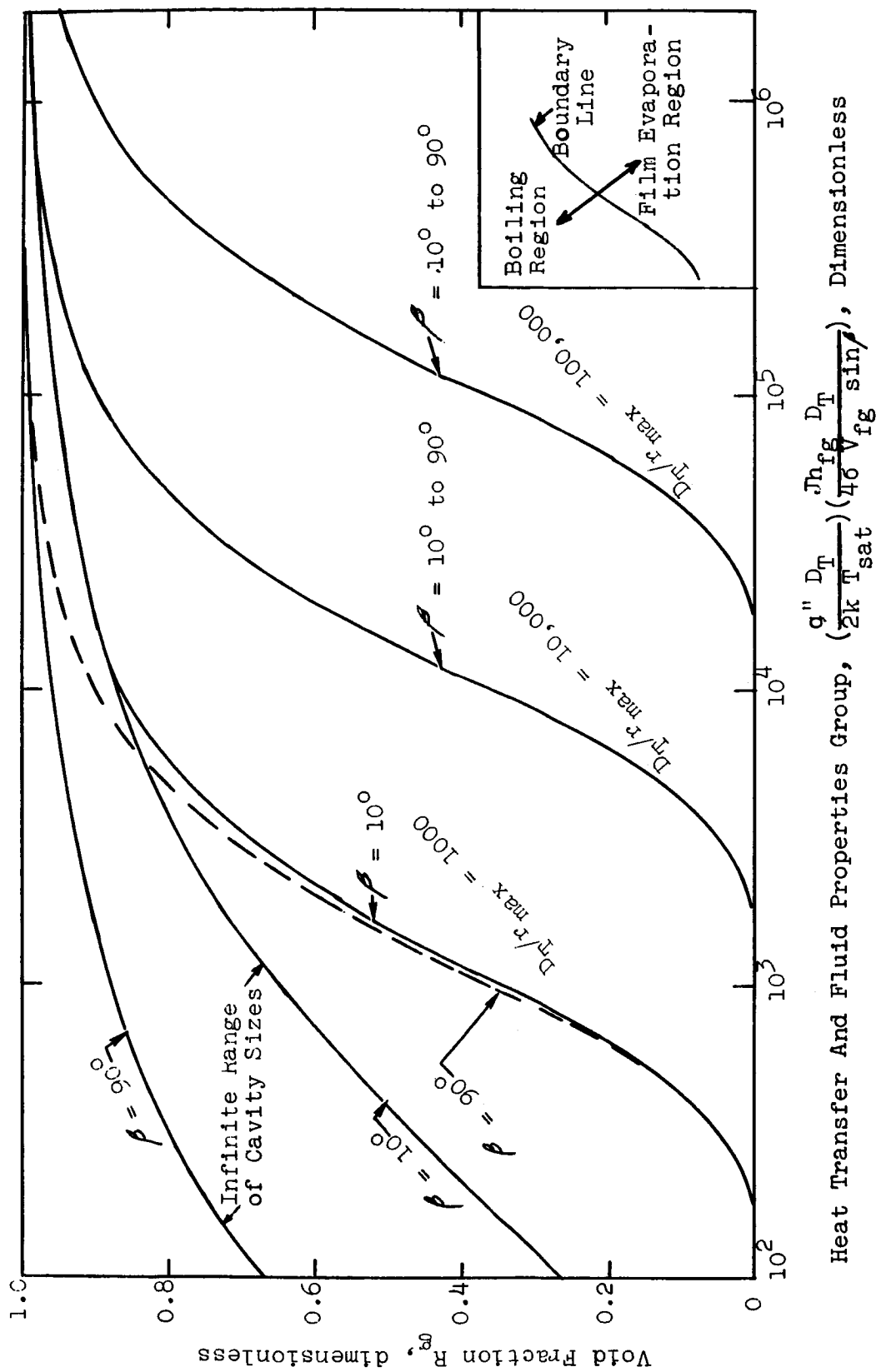
Figure 37. Generalized Map Showing Calculated Boundaries Between Boiling With Bubble Formation And Evaporation Without Bubble Formation
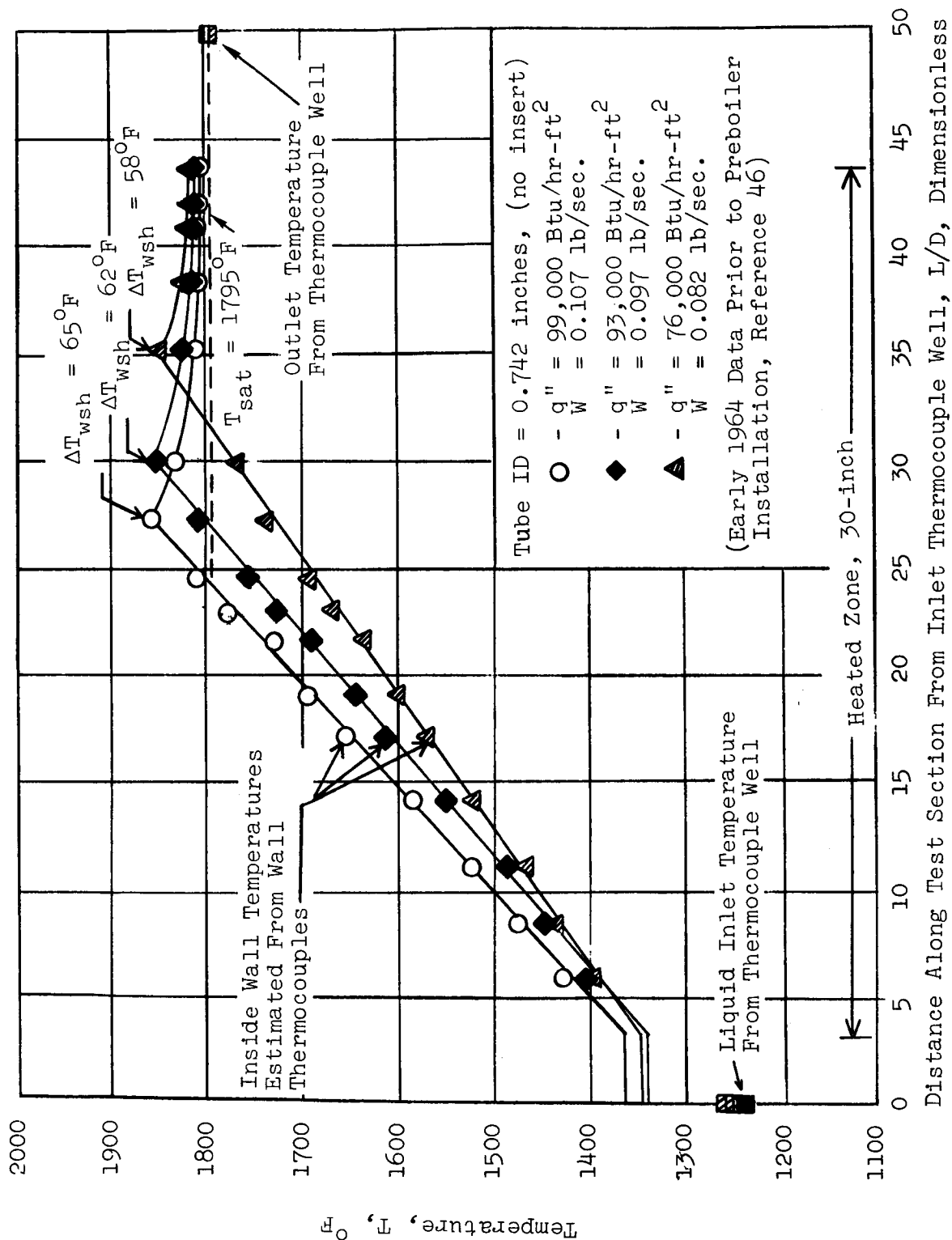
Figure 38. Inside Wall Temperature As a Function of L/D Along Test Section

Coefficients Calculated
From Wall Temperature
Measurements

Pool Boiling
Coefficient,
Eq. (10)

○ $q'' = 99,000$ Btu/hr-ft^2
$W = 0.107$ lb/sec.

◆ $q'' = 93,000$ Btu/hr-ft^2
$W = 0.097$ lb/sec.

◁ $q'' = 76,000$ Btu/hr-ft^2
$W = 0.082$ lb/sec.

$T_{sat} = 1795^{\circ}F$

Tube ID = 0.742-inch (no insert)

(Early 1964 Data Prior to Preboiler In-
stallation, Reference 46)

$X_e = .111$

$X_e = .089$

$X_e = .052$

Estimated Liquid-Phase Coefficient (Eq. 20)

Heated Zone, 30-inch

Heat Transfer Coefficient, h, Btu/hr-ft^2-$^{\circ}$F
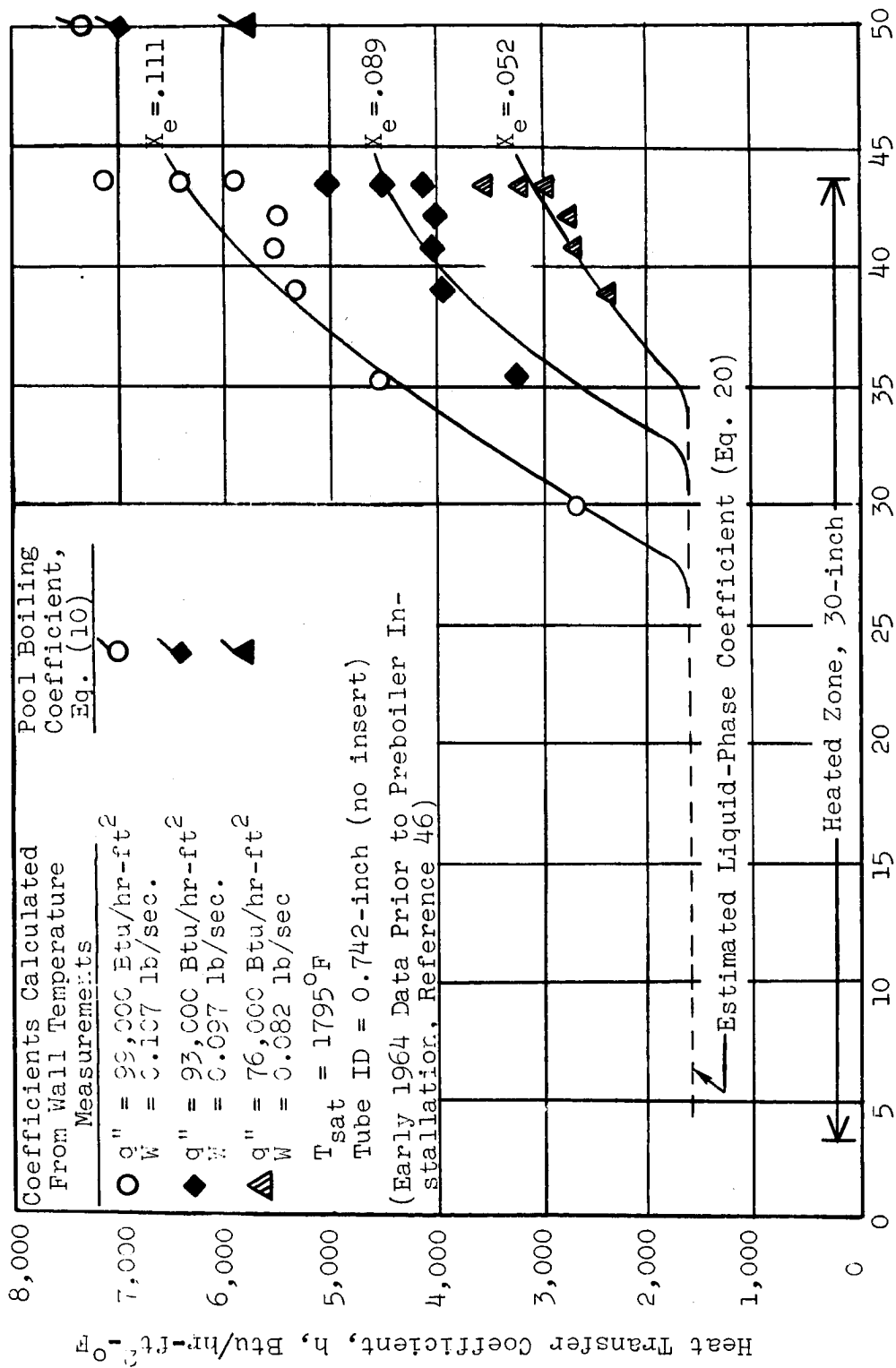
Distance Along Test Section From Inlet Thermocouple Well, L/D, Dimensionless

Figure 39. Boiling Heat Transfer Coefficient At Low Vapor Qualities As A Function
of L/D Along Test Section
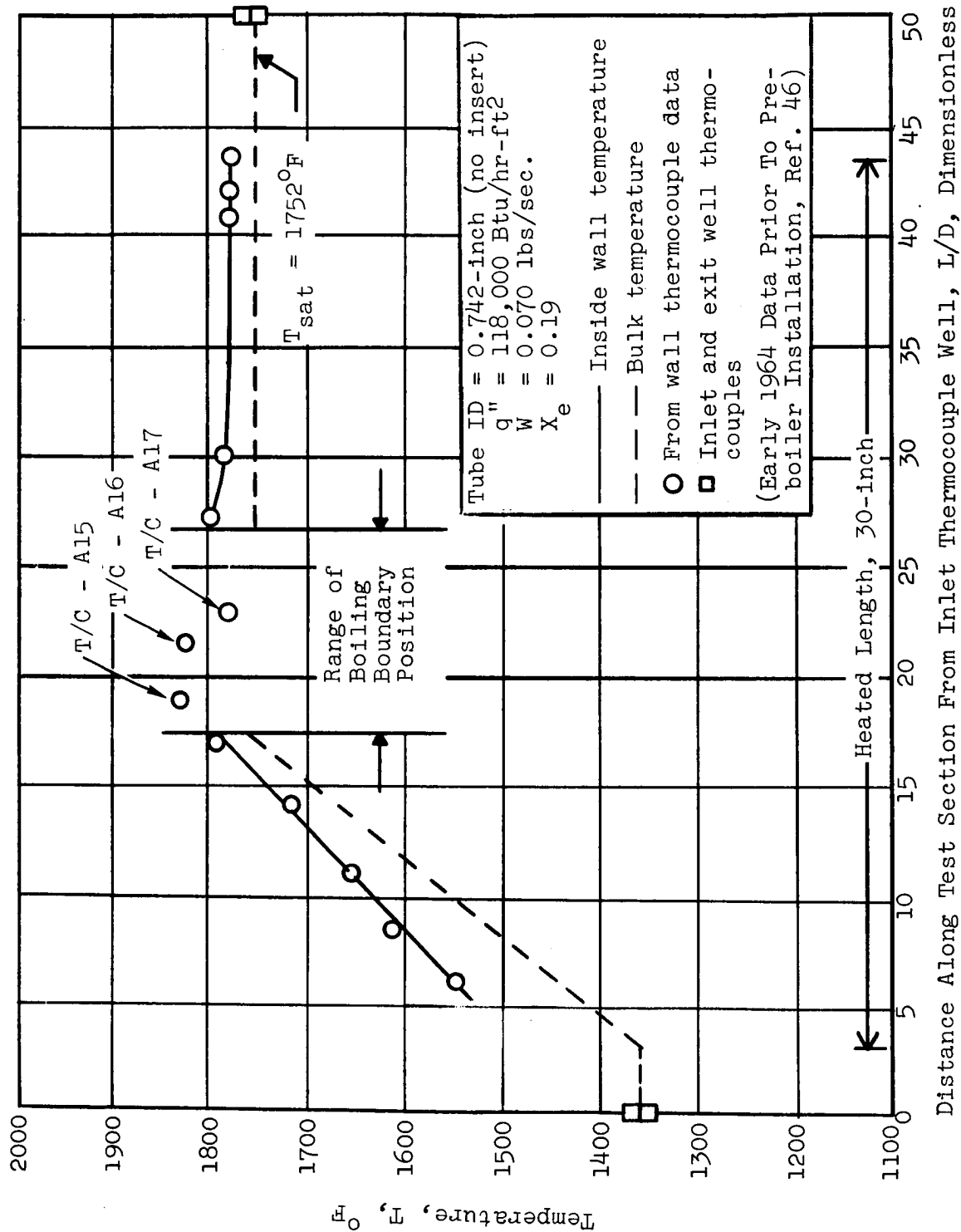
Figure 40. Inside Wall Temperature as a Function of L/D Showing Range of Movement of Boiling Boundary
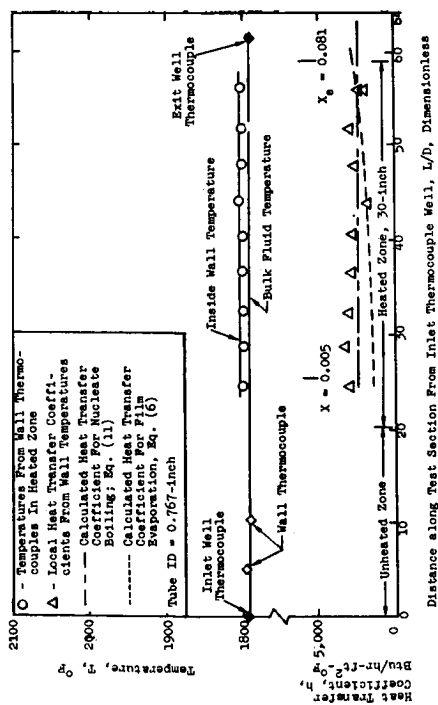
(a) q" = 29,300 Btu/hr-ft^2 and T$_{sat}$ = 1787°F
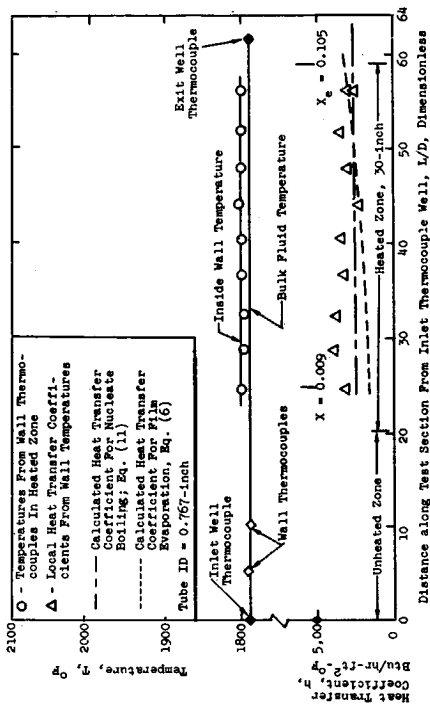
(b) q" = 32,500 Btu/hr-ft^2 and T$_{sat}$ = 1790°F
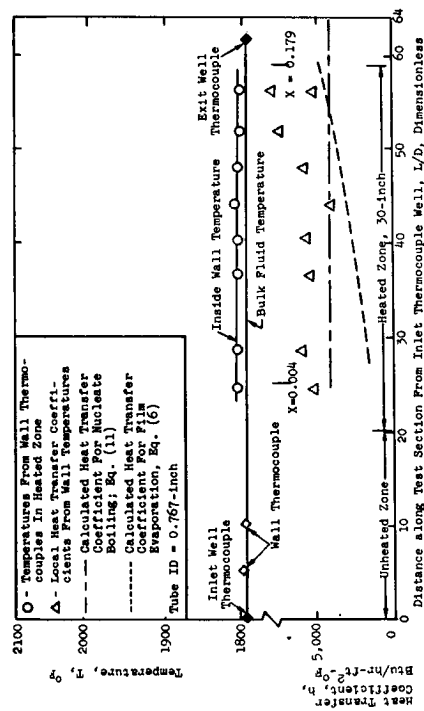
(c) q" = 57,100 Btu/hr-ft^2 and T$_{sat}$ = 1795°F
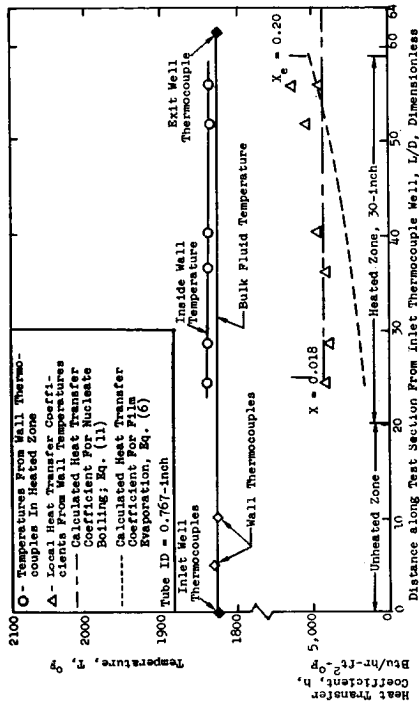
(d) q" = 56,700 Btu/hr-ft^2 and T$_{sat}$ = 1820°F

Figure 41. Wall Temperature and Heat Transfer Coefficients During
Forced Convection Vaporization of Potassium at Low Vapor
Qualities in Test Section No. 1 (.767" ID, no insert)
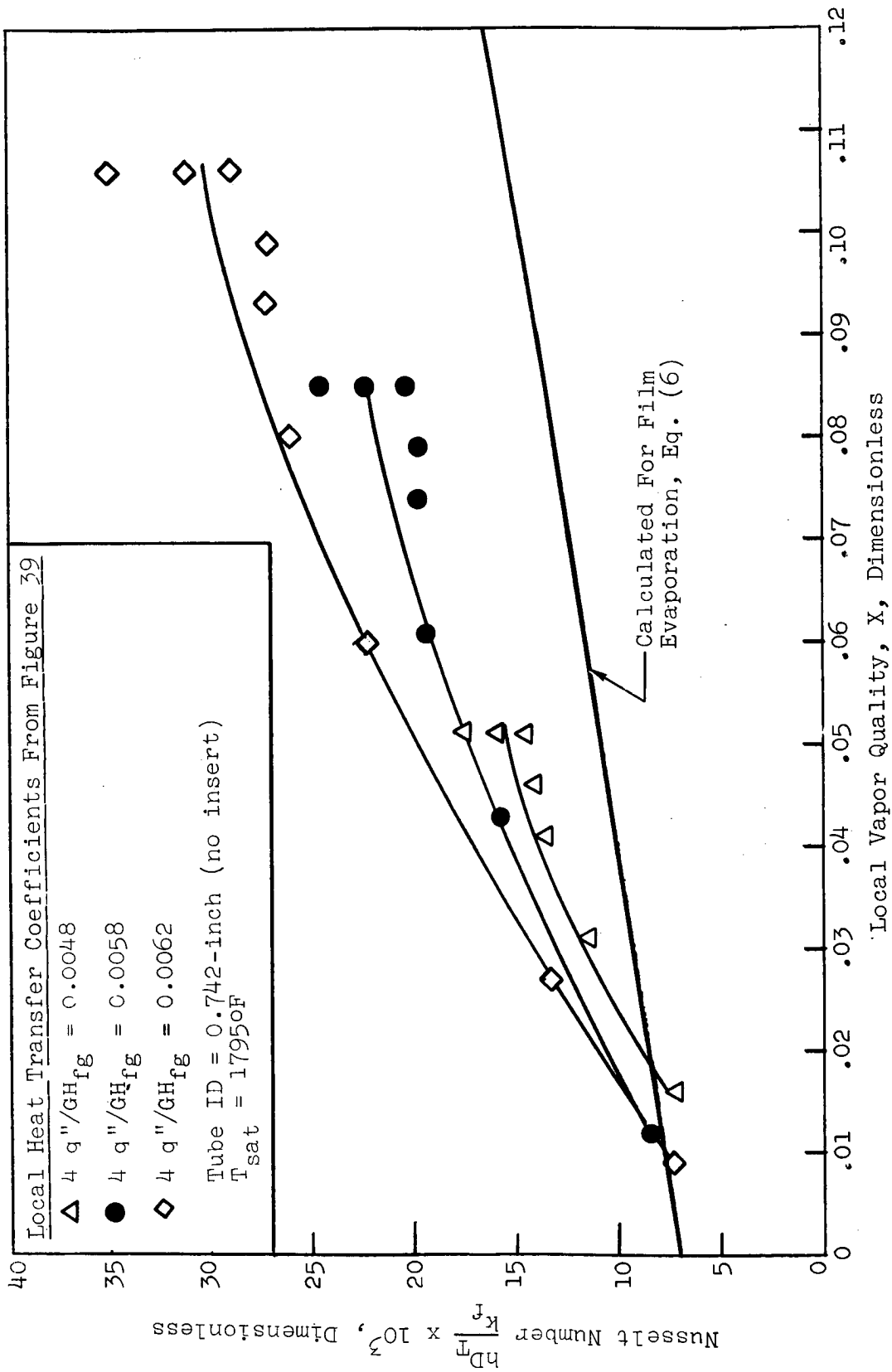
Figure 42. Local Nusselt Numbers as a Function of Local Vapor Quality Along Test Section
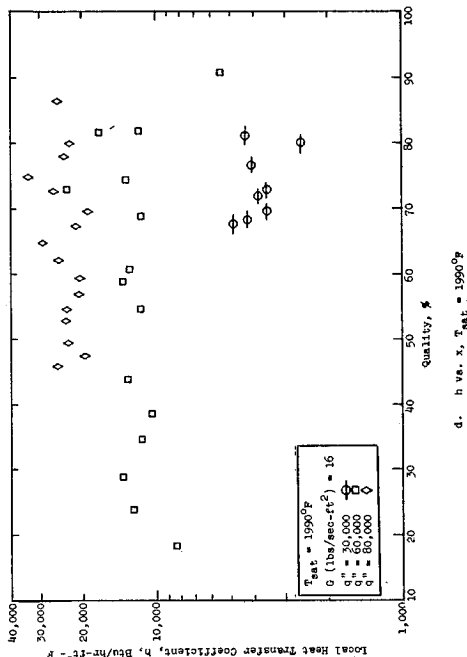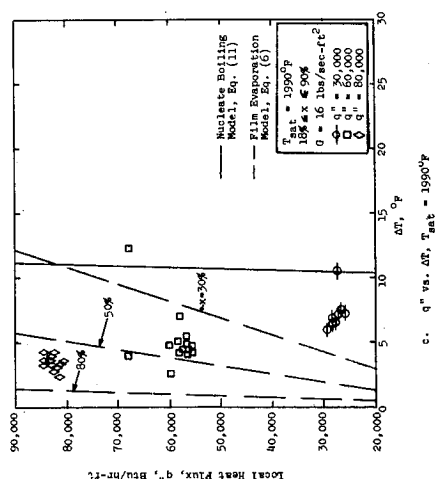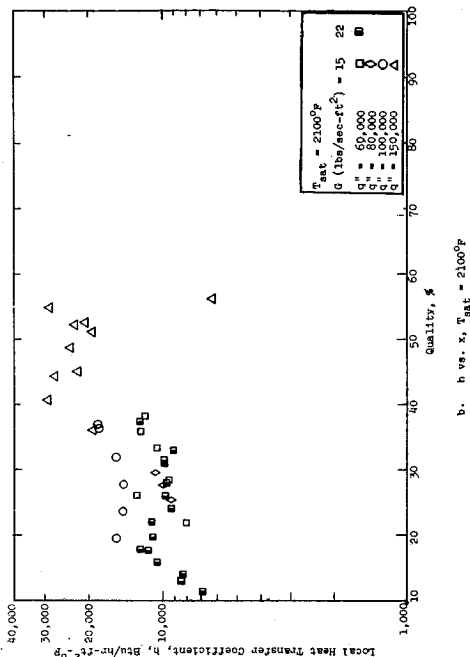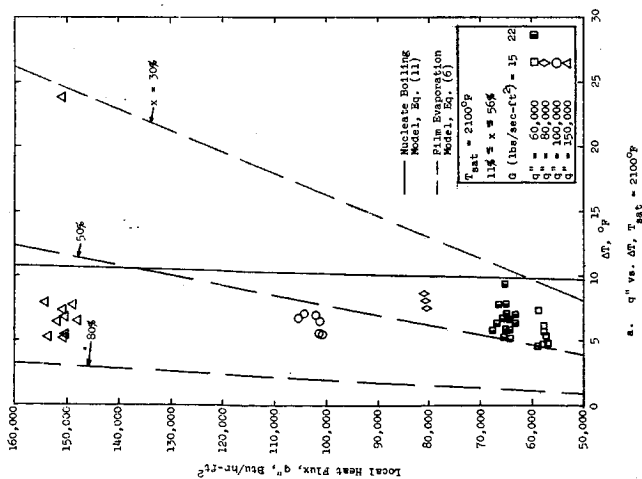
Figure 43. Nucleate Boiling Data from Test Section No. 1, 0.767-inch ID Tube, No Insert
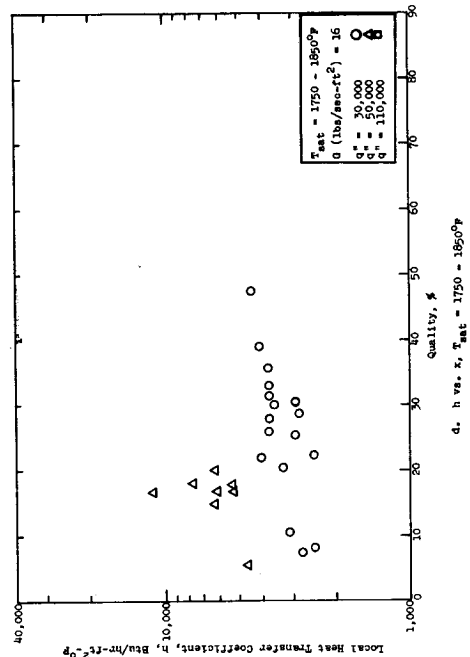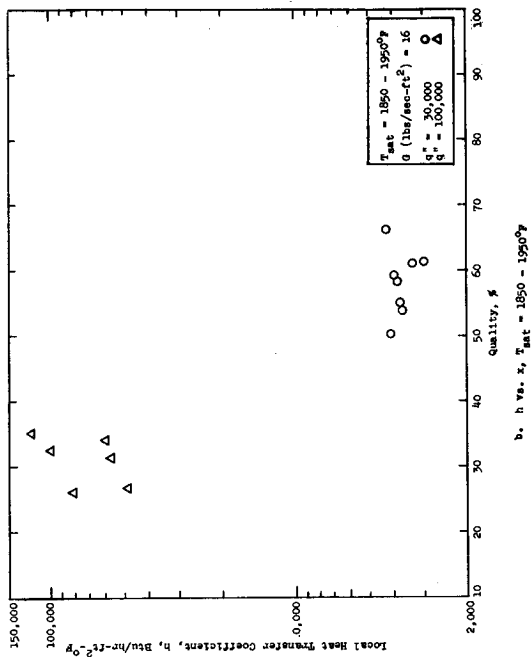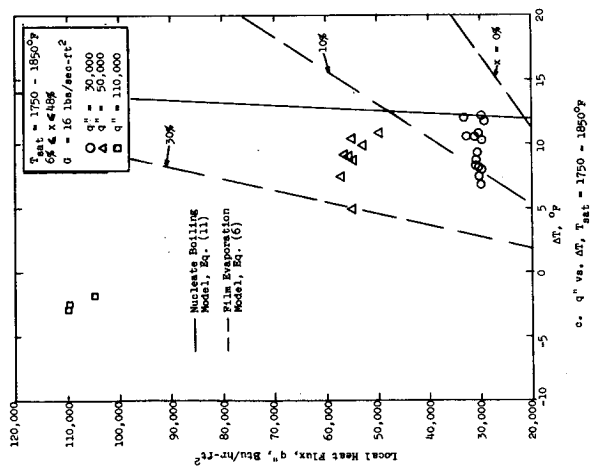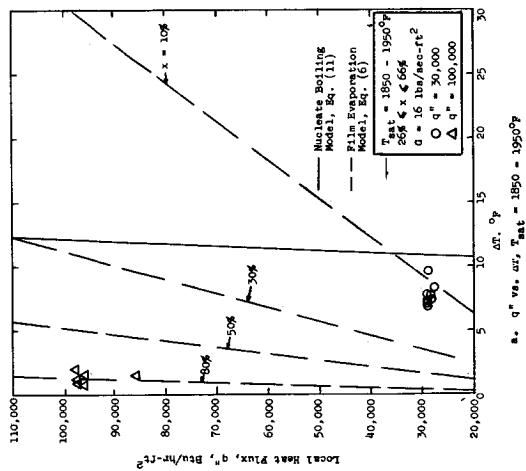
Figure 44. Nucleate Boiling Data from Test Section No. 1 Continued, 0.767-inch ID Tube, No Insert
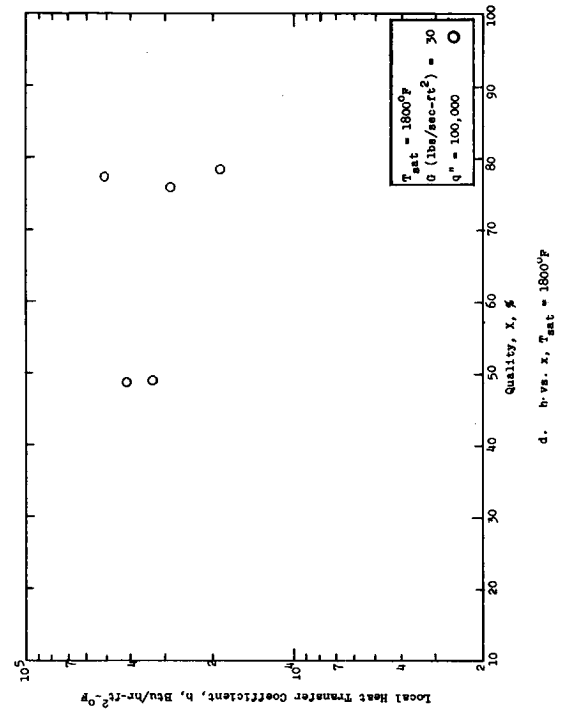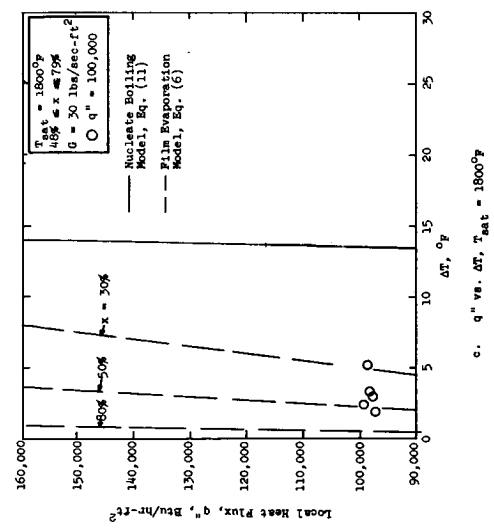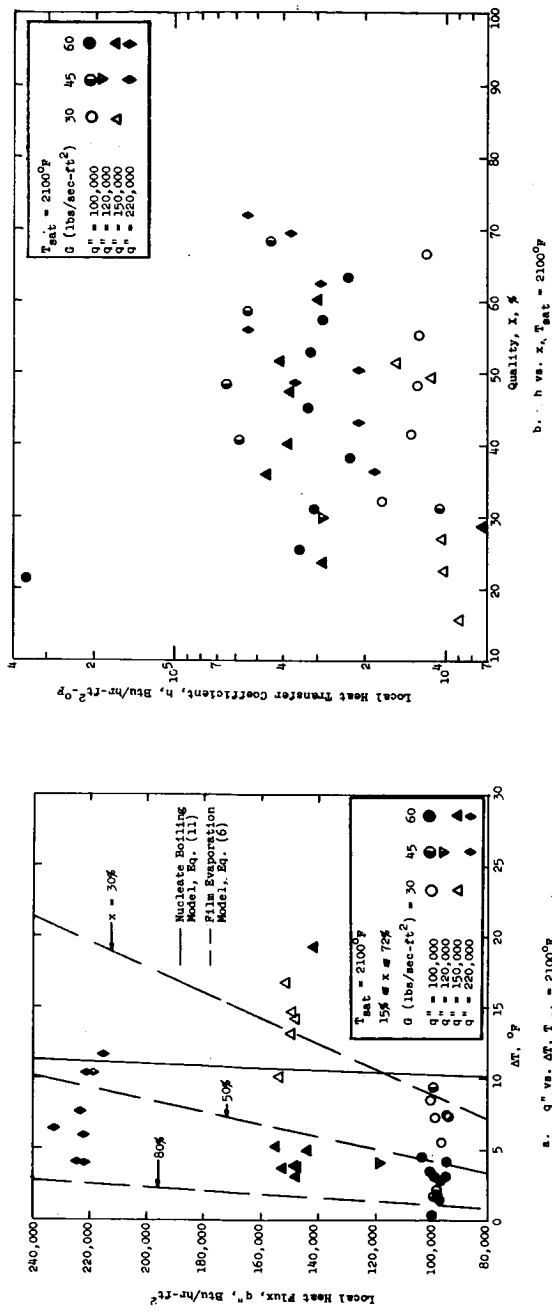
Figure 45. Nucleate Boiling Data from Test Section No. 3, 0.423-Inch ID Tube, No Insert
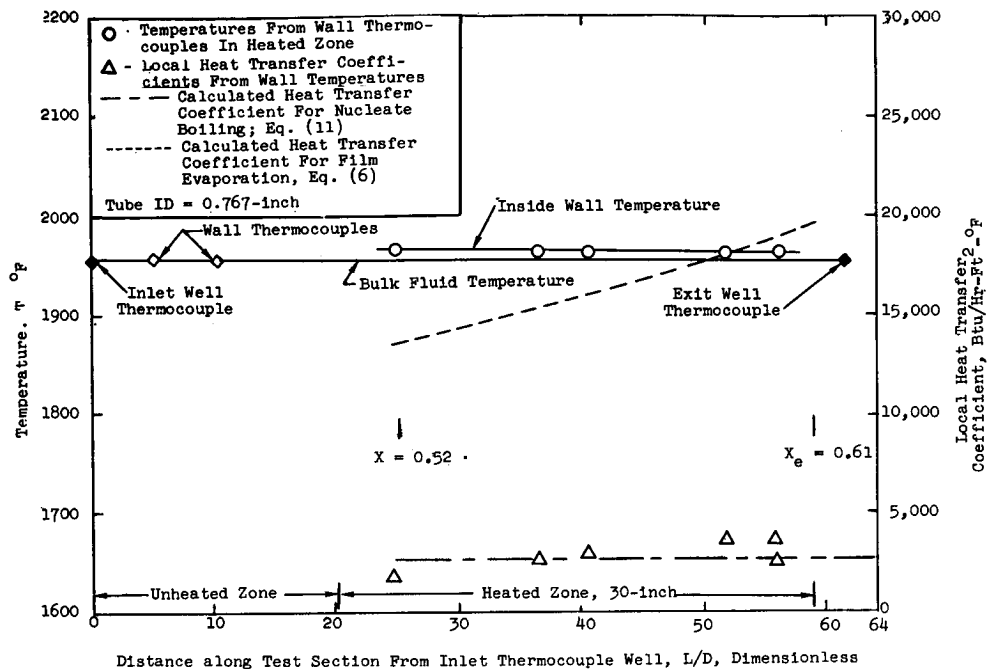
(a) $T_{sat} = 1955°F$
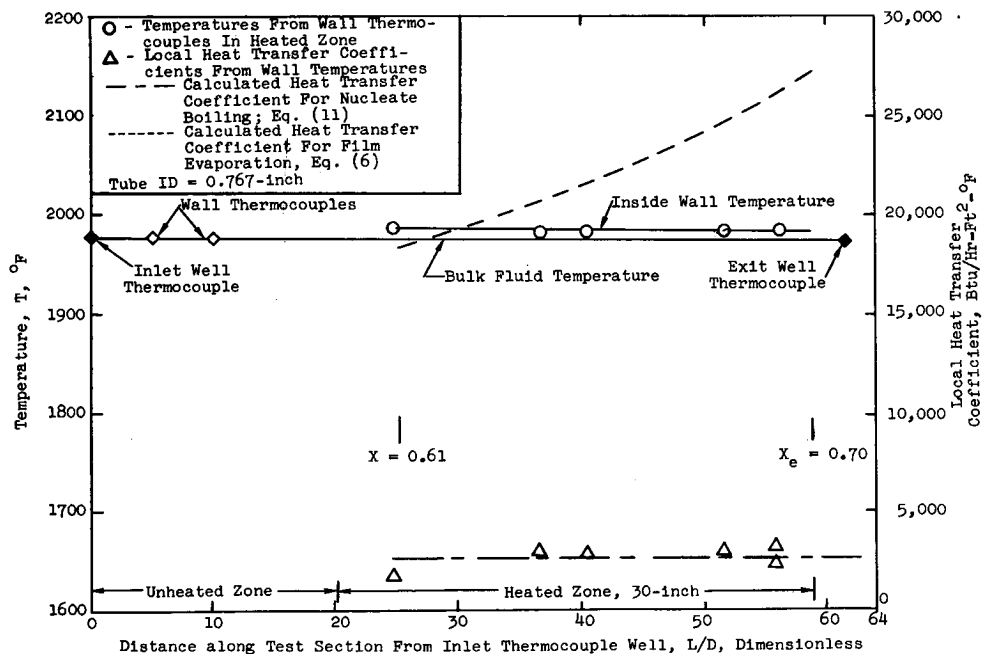
(b) $T_{sat} = 1975°F$

Figure 46. Wall Temperatures and Heat Transfer Coefficients During Forced Convection Vaporization of Potassium at Intermediate Vapor Qualities in Test Section No. 1 (.767″ ID, no insert) for $q'' = 27,700$ Btu/hr-ft^2
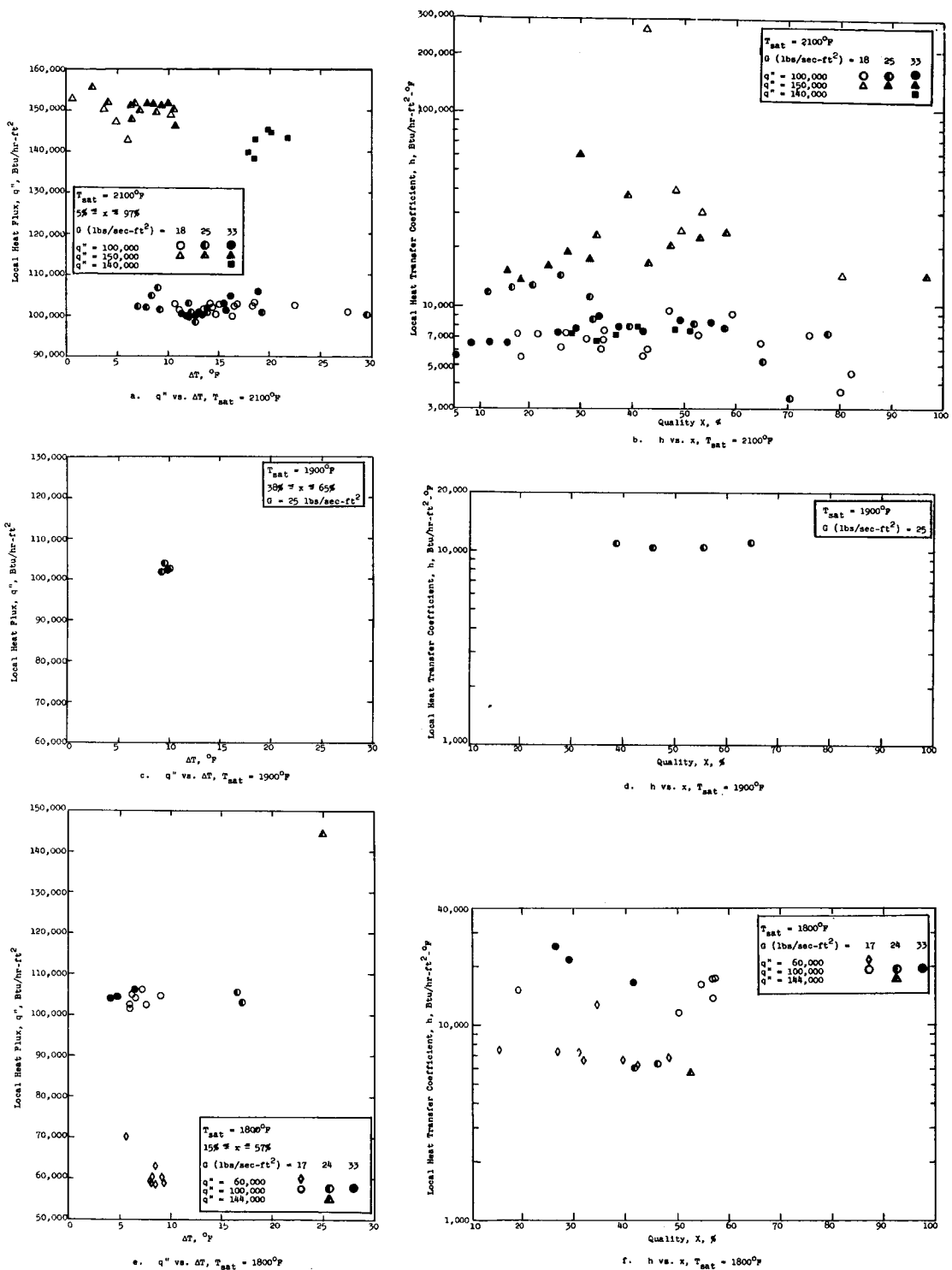
Figure 47   Nucleate Boiling Data from Test Section No. 2, 0.74-inch I.D.
Tube with Helical Insert (P/D = 6)
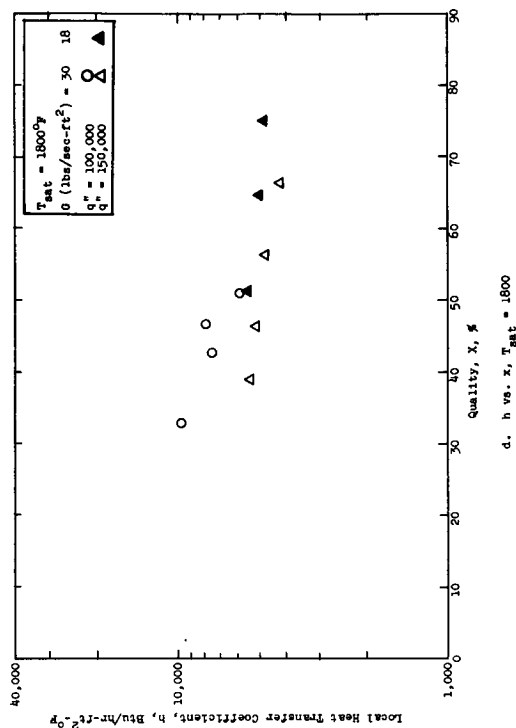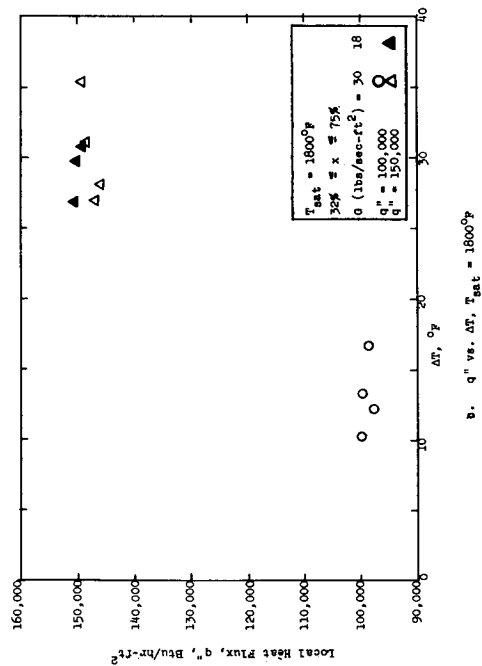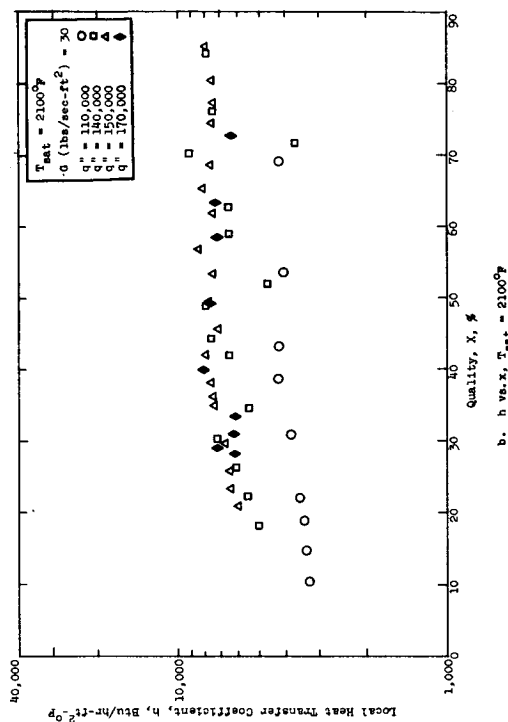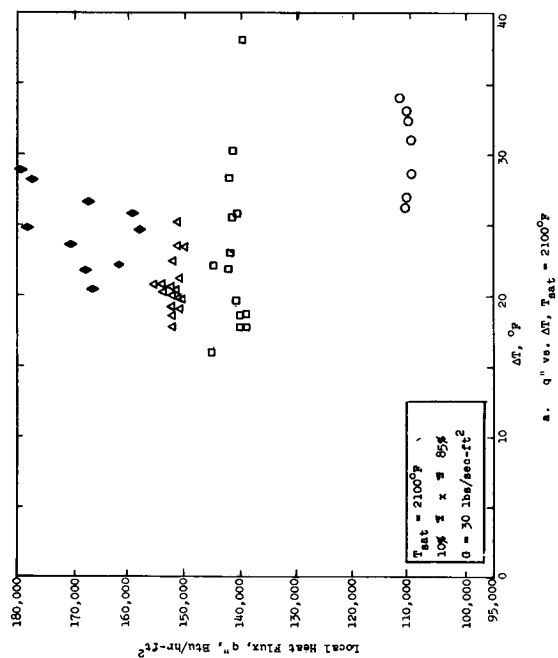
Figure 48 Nucleate Boiling Data from Test Section No. 4, 0.74-inch I.D. Tube with Helical Insert (P/D = 2)
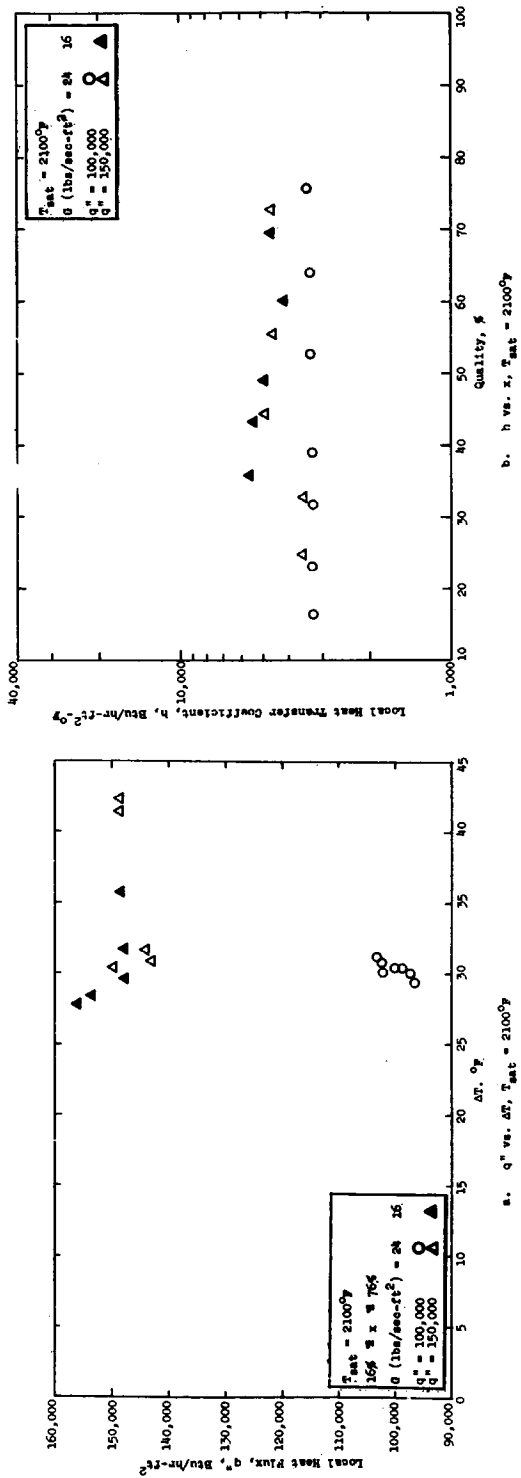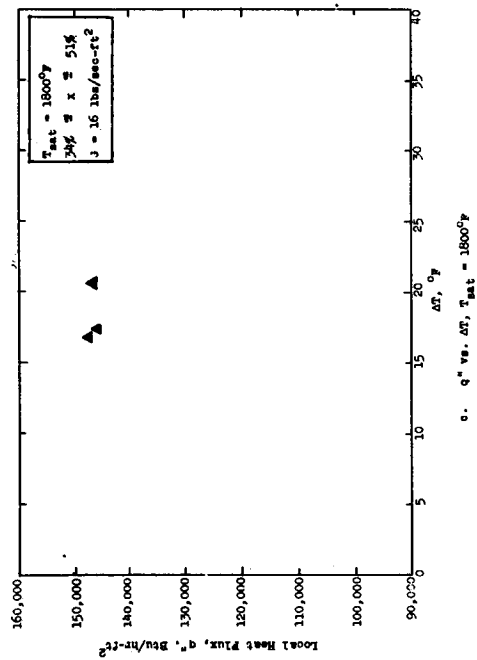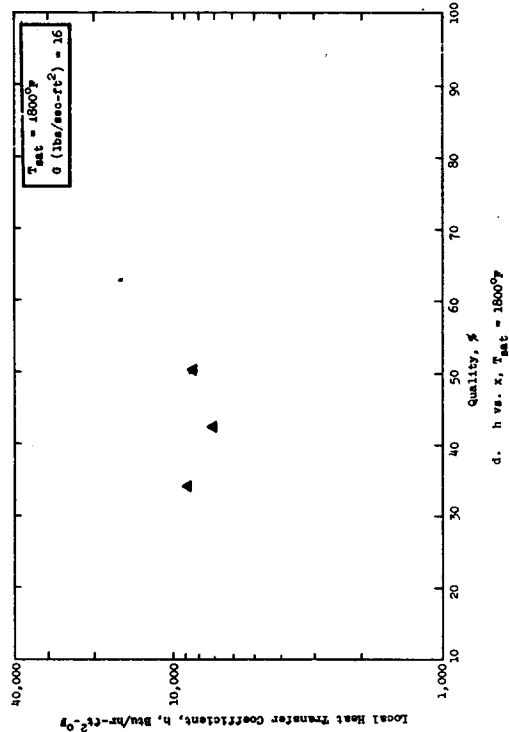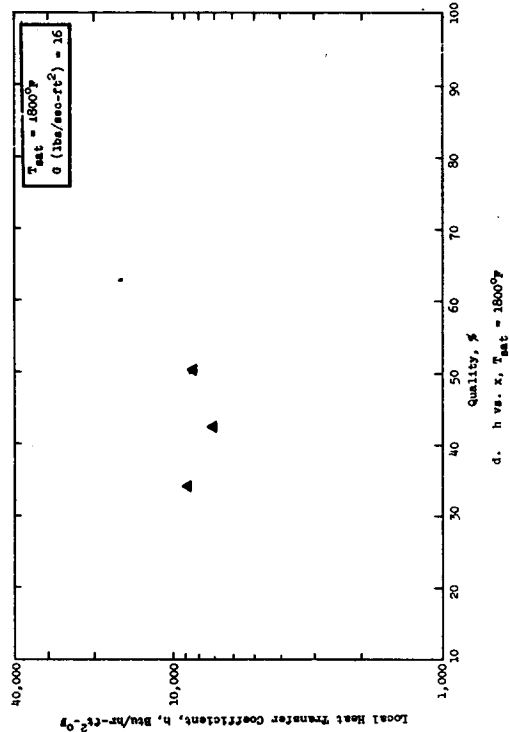
Figure 49. Nucleate Boiling Data from Test Section No. 5, 0.74-inch I.D. Tube with Wire Coil Insert (3/32-inch Wire, P/D = 2)
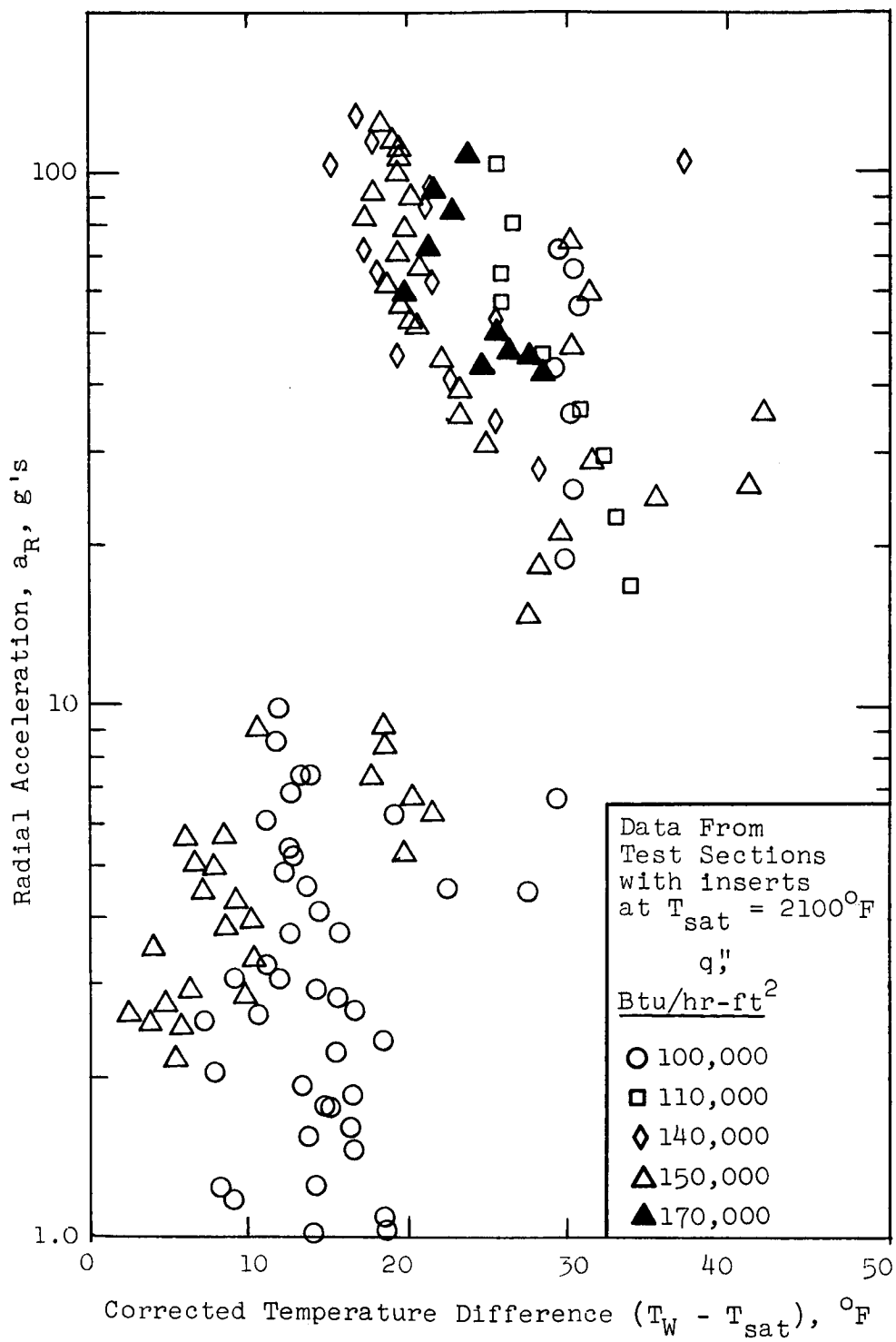
Figure 50. Radial Acceleration At The Tube Wall As A Function Of Corrected Wall ΔT For A Slip Ratio $K = \sqrt{\rho_f / \rho_g}$
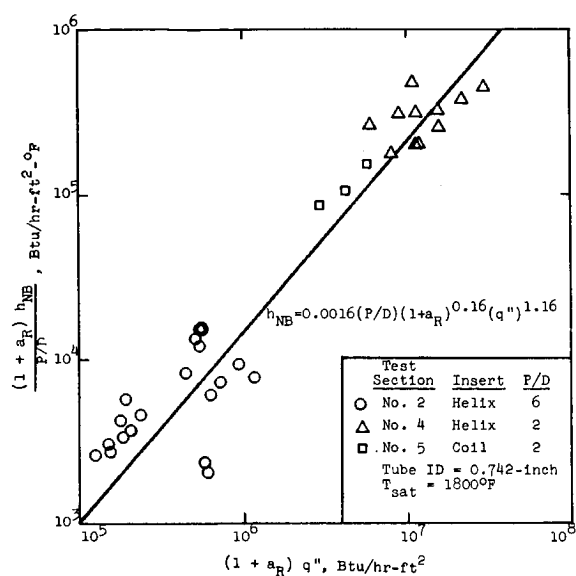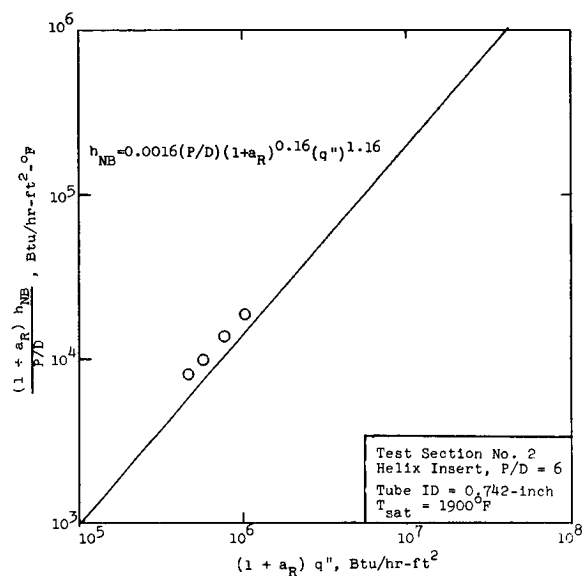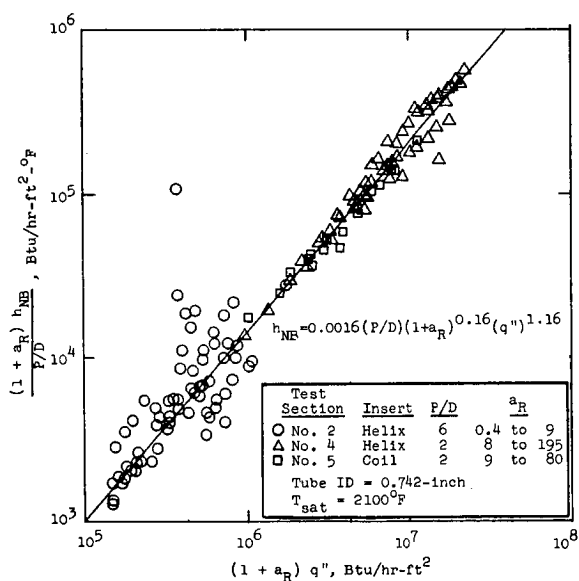
Figure 51. Empirical Correlation of Potassium Nucleate Boiling Heat Transfer Coefficient Data for Tubes Containing Helical and Wire Coil Inserts
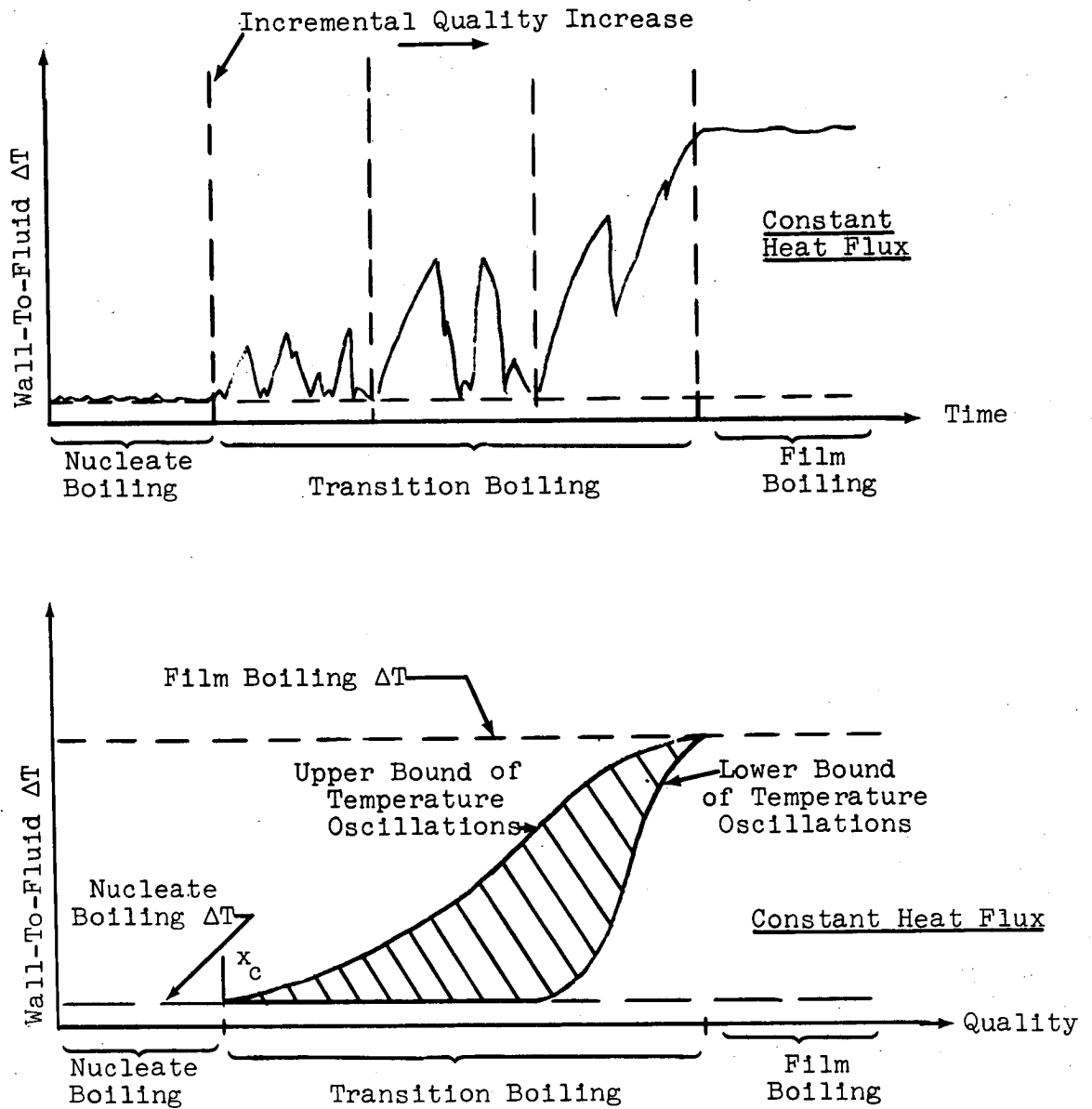
Figure 52   Sketch of Wall Temperature Behavior in Nucleate,
Transition and Film Boiling Regimes

-174-

Figure 53. Critical Heat Flux Determination At Relatively
High Heat Flux In Cb-1%Zr Facility
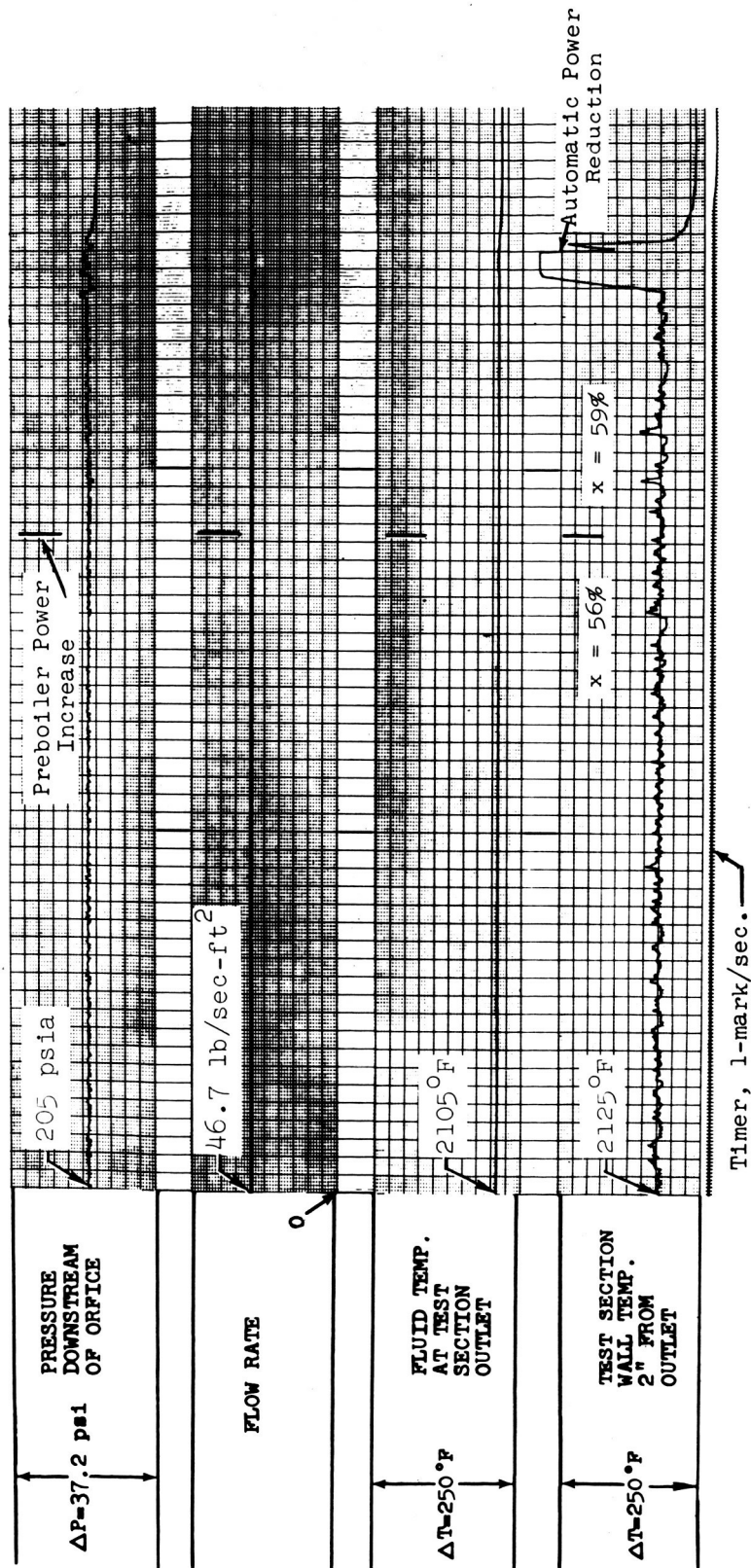
Data taken 4/1/65

$T_{sat} = 2105°F$
$G = 46.7$ lb/sec-ft^2
$q''_c = 211,000$ Btu/hr-ft^2

Test Section ID = 0.423-in. (no insert)

Timer, 1-mark/sec.

Automatic Power
Reduction

x = 59%

x = 56%

2125°F

TEST SECTION
WALL TEMP.
2" FROM
OUTLET

ΔT=250°F

2105°F

FLUID TEMP.
AT TEST
SECTION
OUTLET

ΔT=250°F

0

46.7 lb/sec-ft^2

FLOW RATE

Preboiler Power
Increase

205 psia

PRESSURE
DOWNSTREAM
OF ORFICE

ΔP=37.2 psi
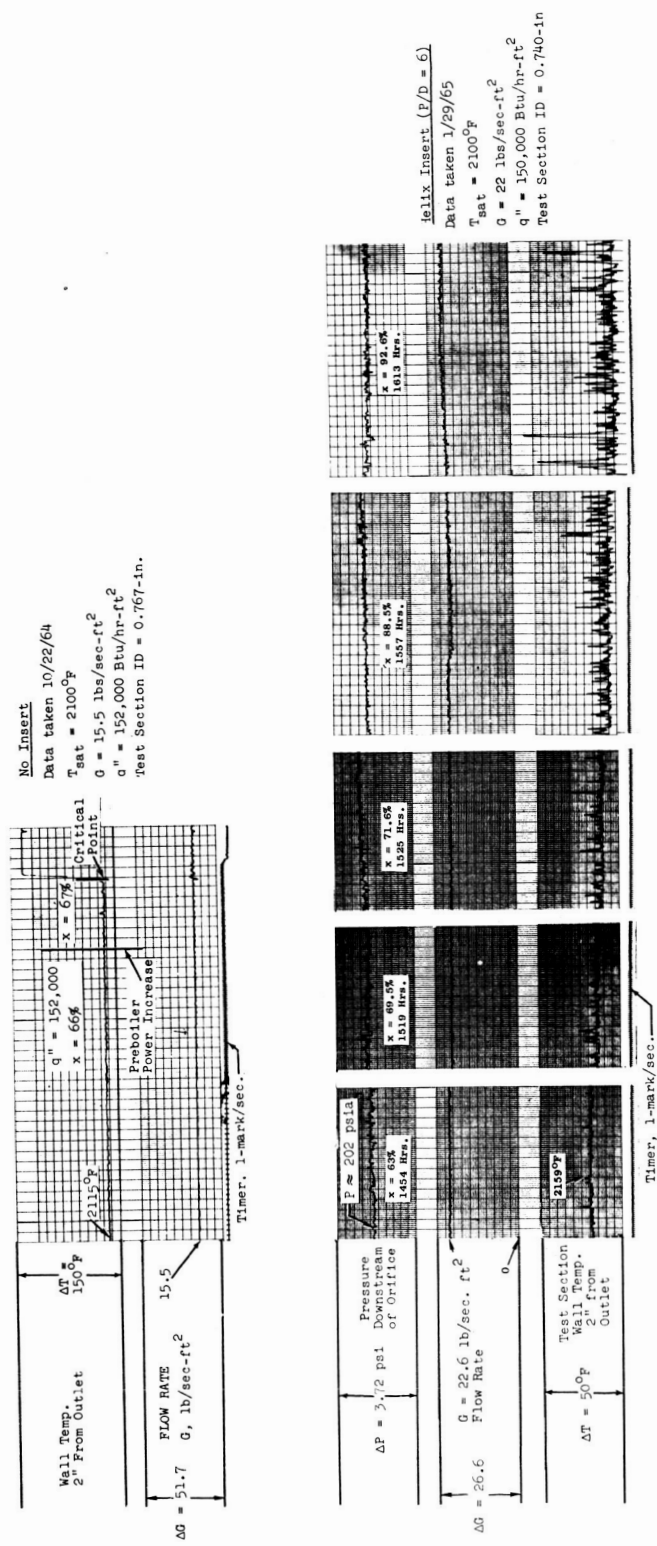
Figure 54. Wall Temperature Behavior During Operation From Nucleate Boiling to Superheated Vapor Conditions At Low Heat Flux In Cb-1%Zr Facility

-176-

Figure 55. Comparison of Wall Temperature Behavior At Critical Heat Flux and Transition Boiling Conditions With and Without Helix Insert - In Cb-1%Zr Facility
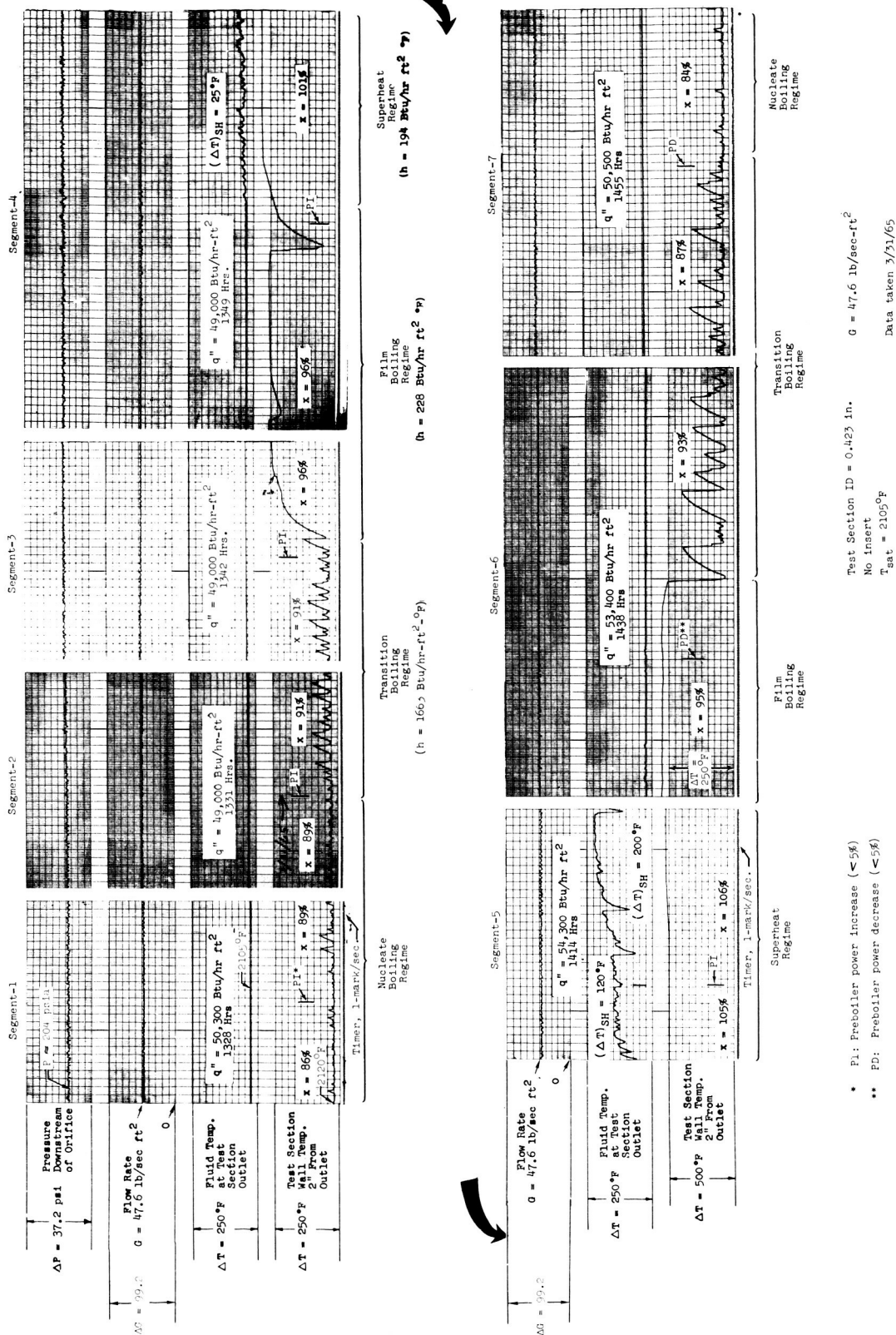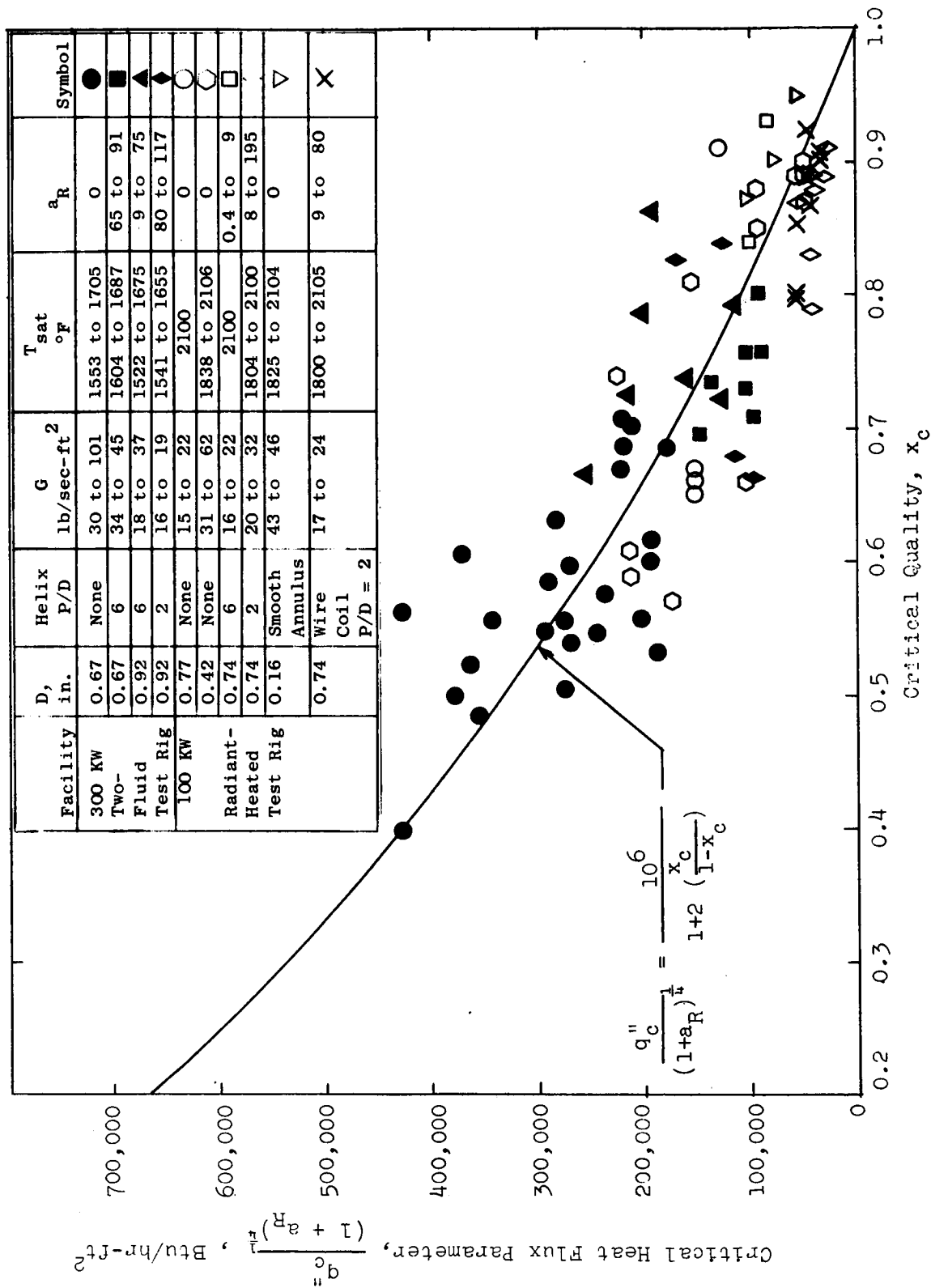
Figure 56. Potassium Critical Heat Flux Data and Empirical Correlation
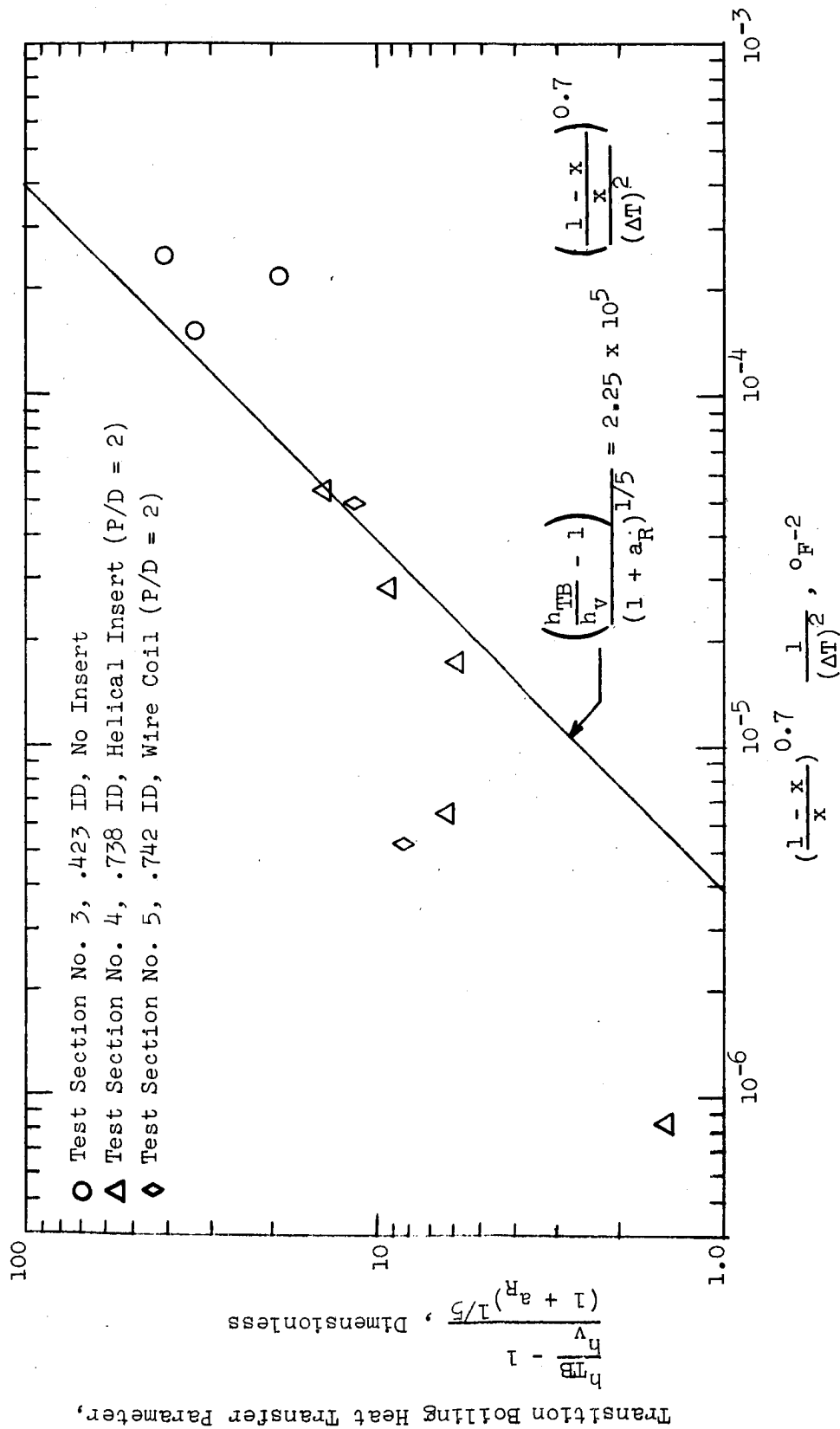
Figure 57. Transition Boiling Heat Transfer Coefficient Data And Empirical Correlation

-179-
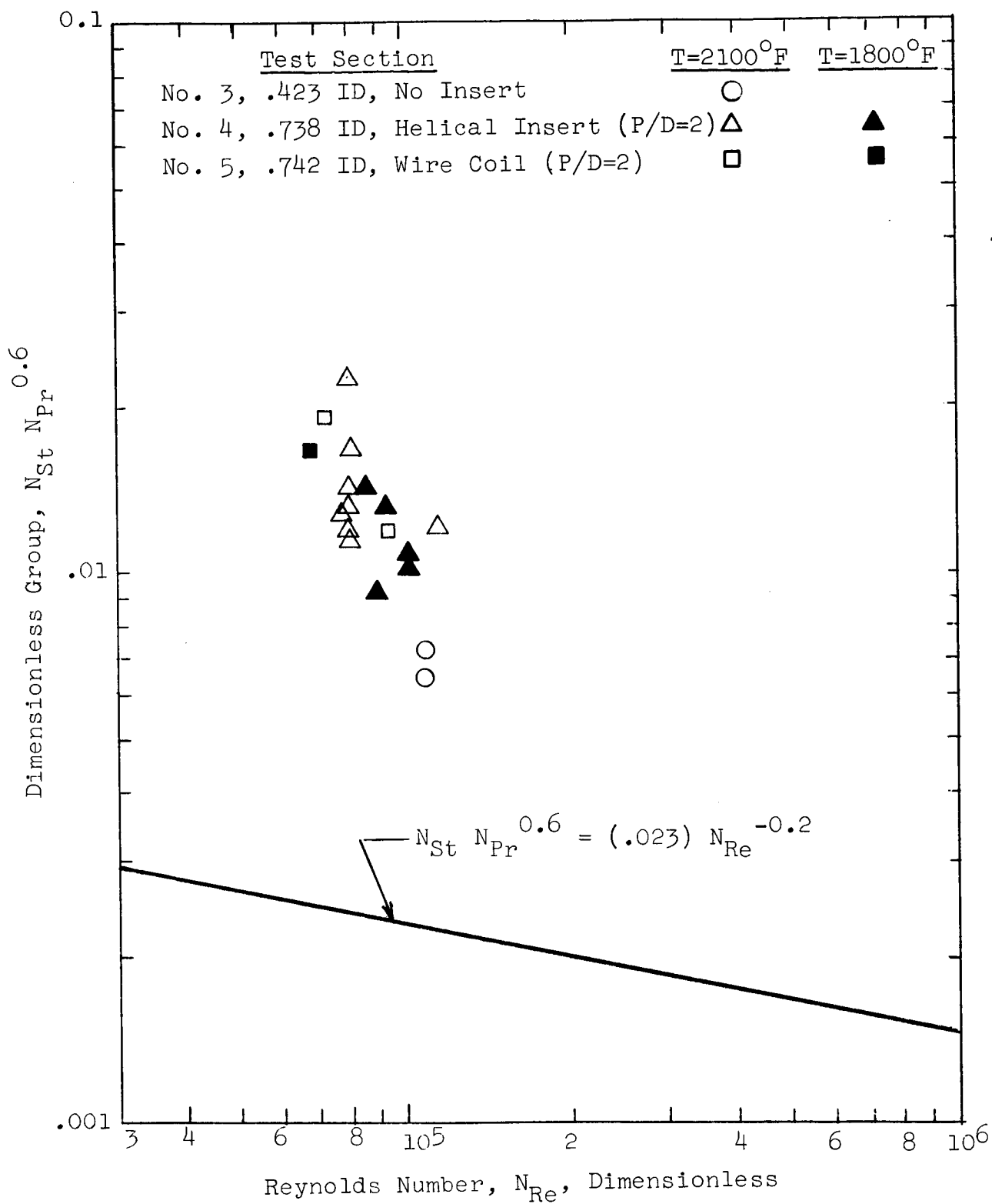
Figure 58. Film Boiling Results Calculated Assuming
Axial Flow (Equation 28)

Figure 59.   Film Boiling Results Calculated Assuming Helical
Flow (Equation 29)
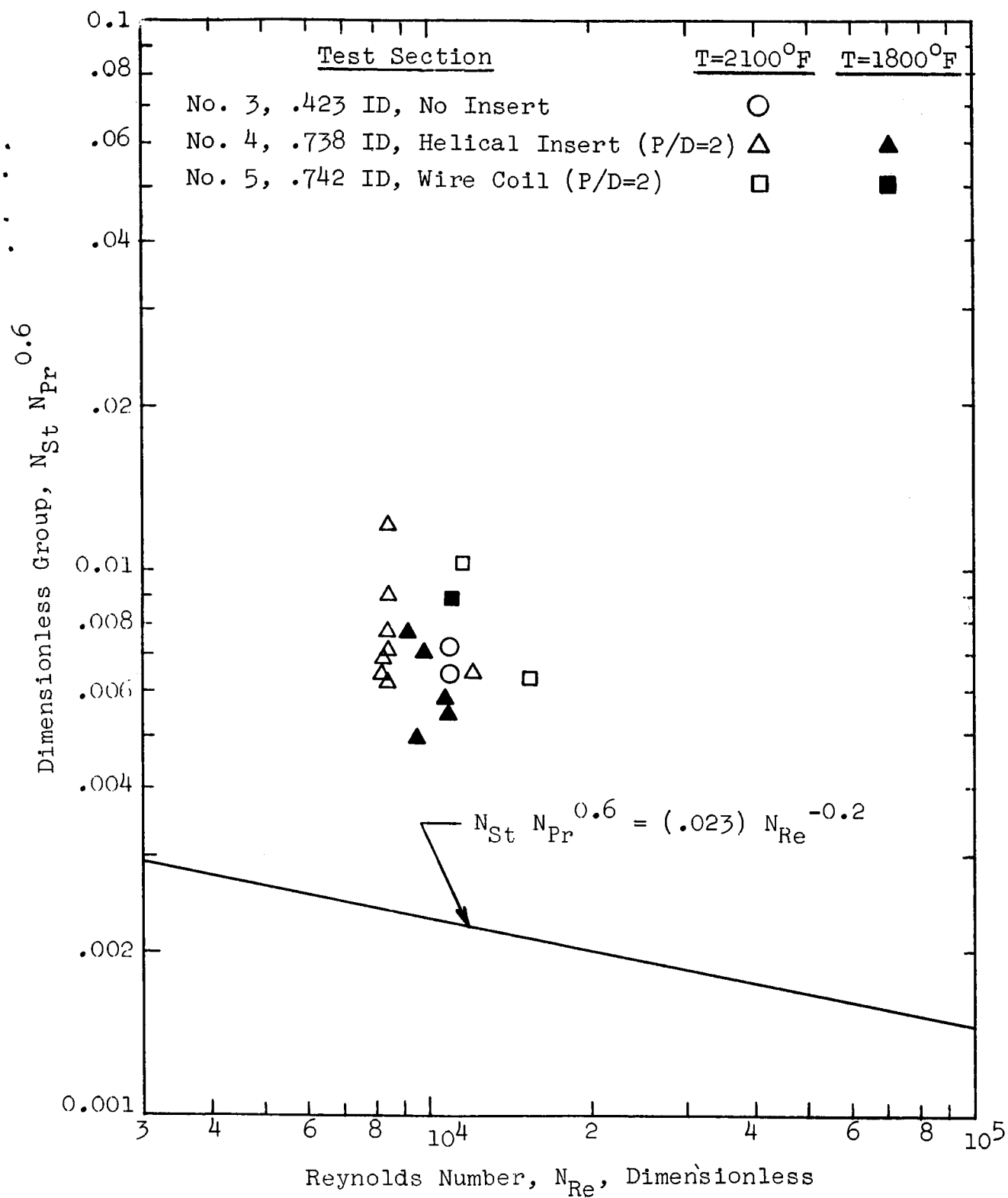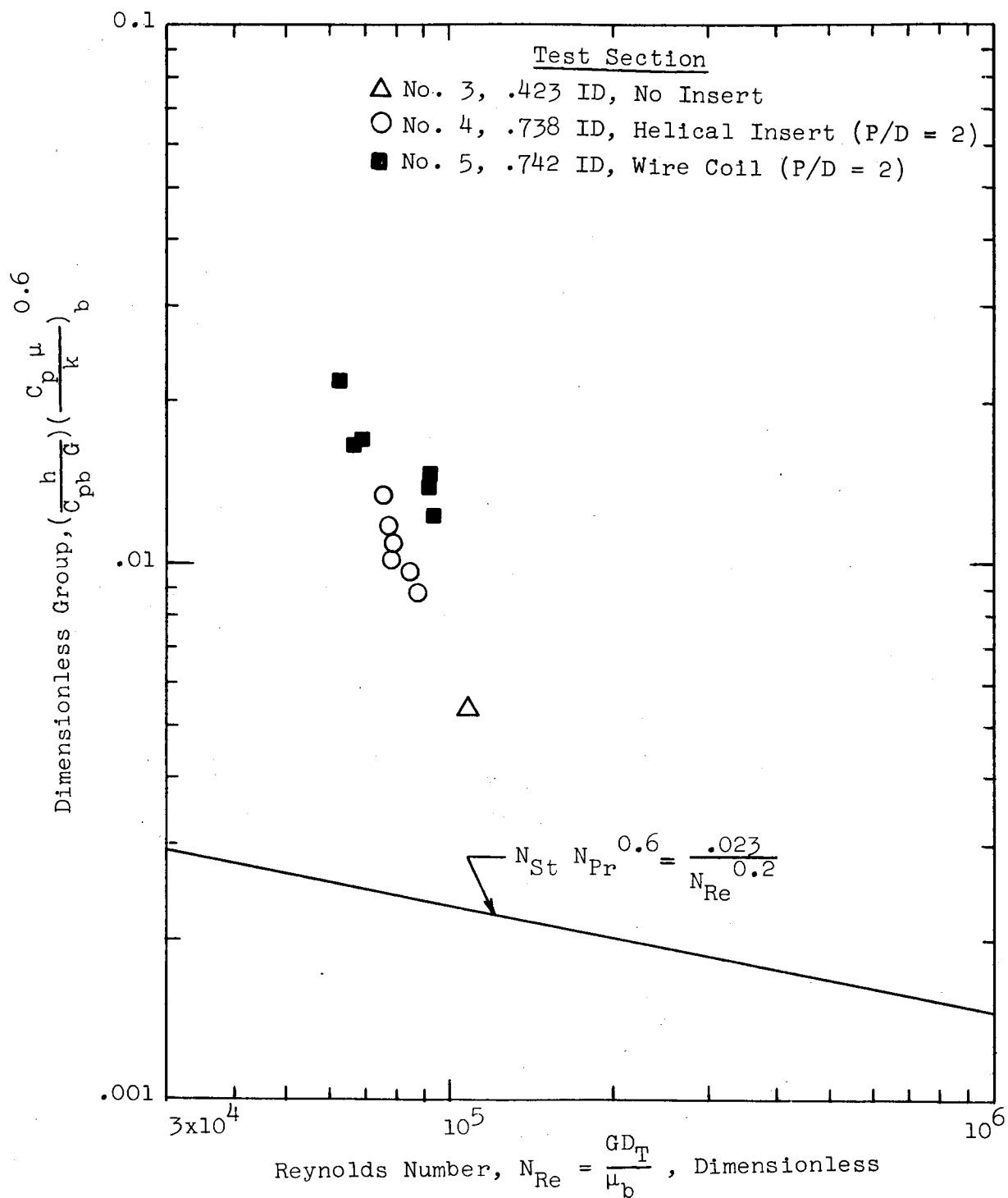
Figure 60 Uncorrected Superheated Vapor Results
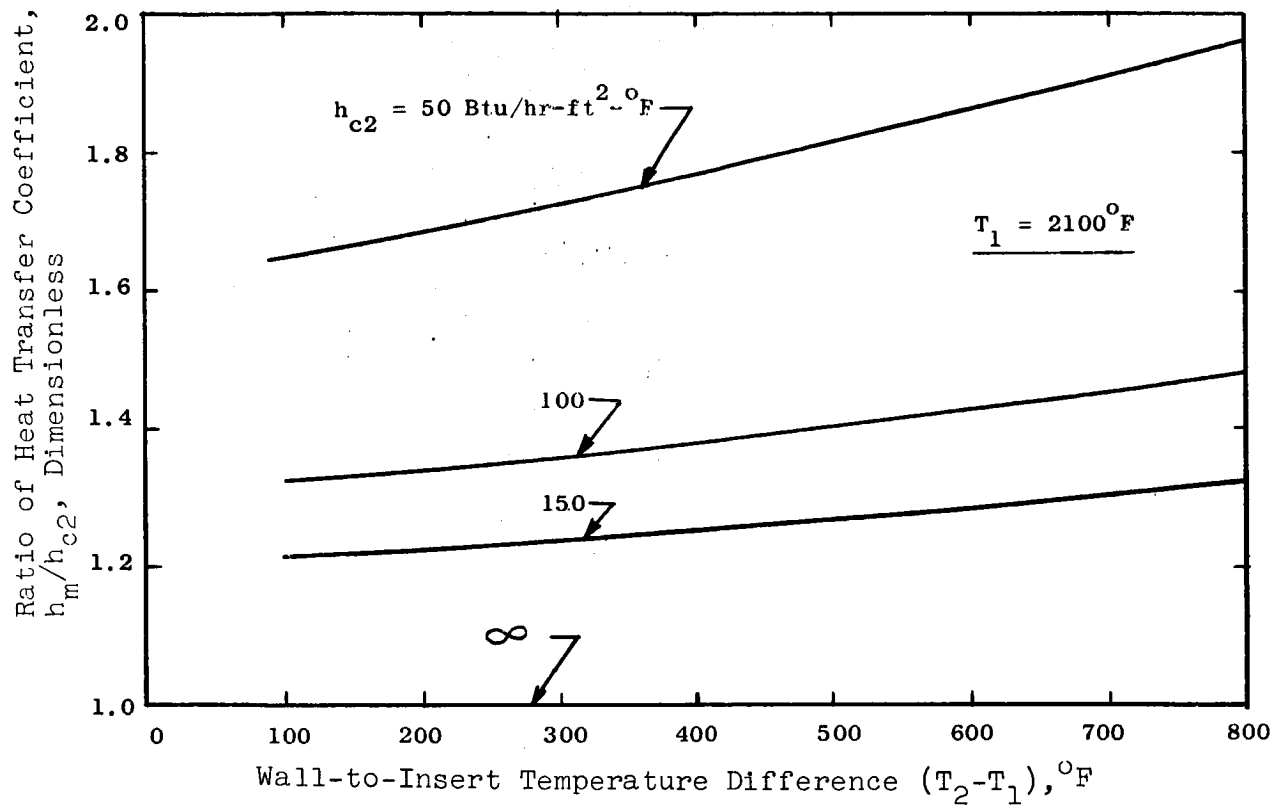
Figure 61. Predicted Effect of Radiation on the Measured Superheated Vapor Heat Transfer Coefficient For Test Section No. 4 (.738"ID with Annular Plug and Helix P/D = 2)
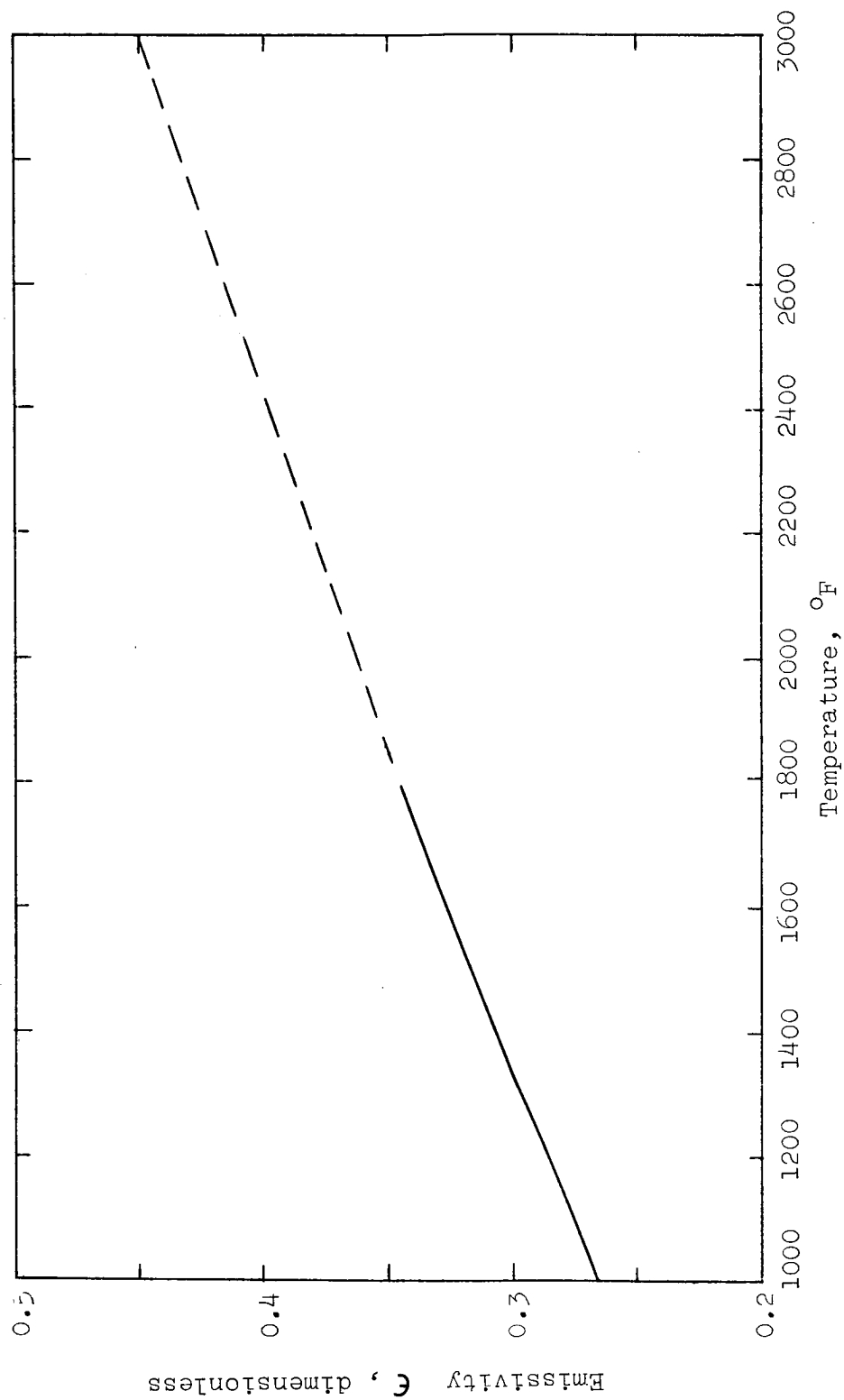
Figure 62. Total Hemispherical Emissivity of Cb-1%Zr from Reference 24
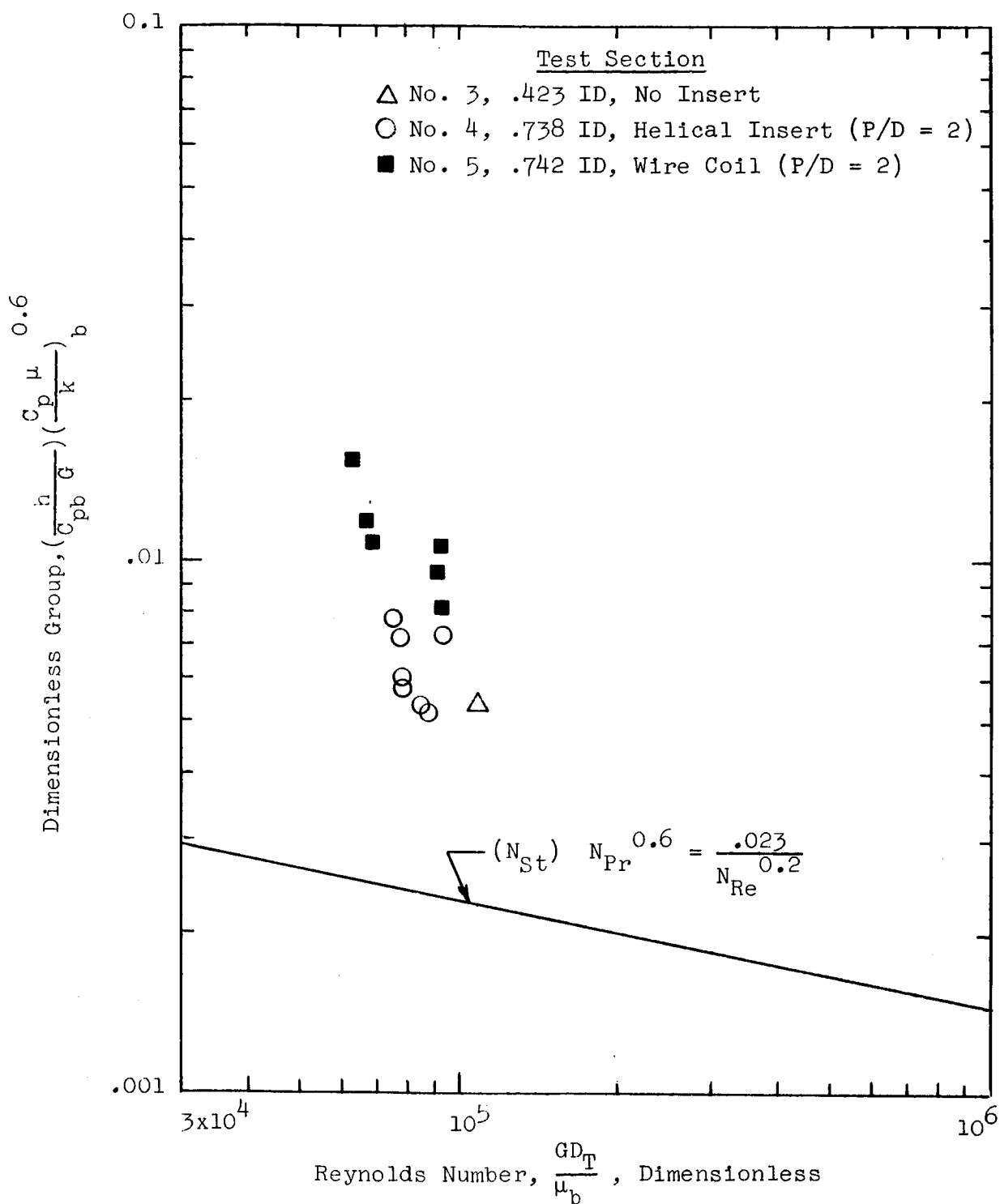
Figure 63. Superheated Vapor Results After Correction For Radiation Effects Using Equation (49)
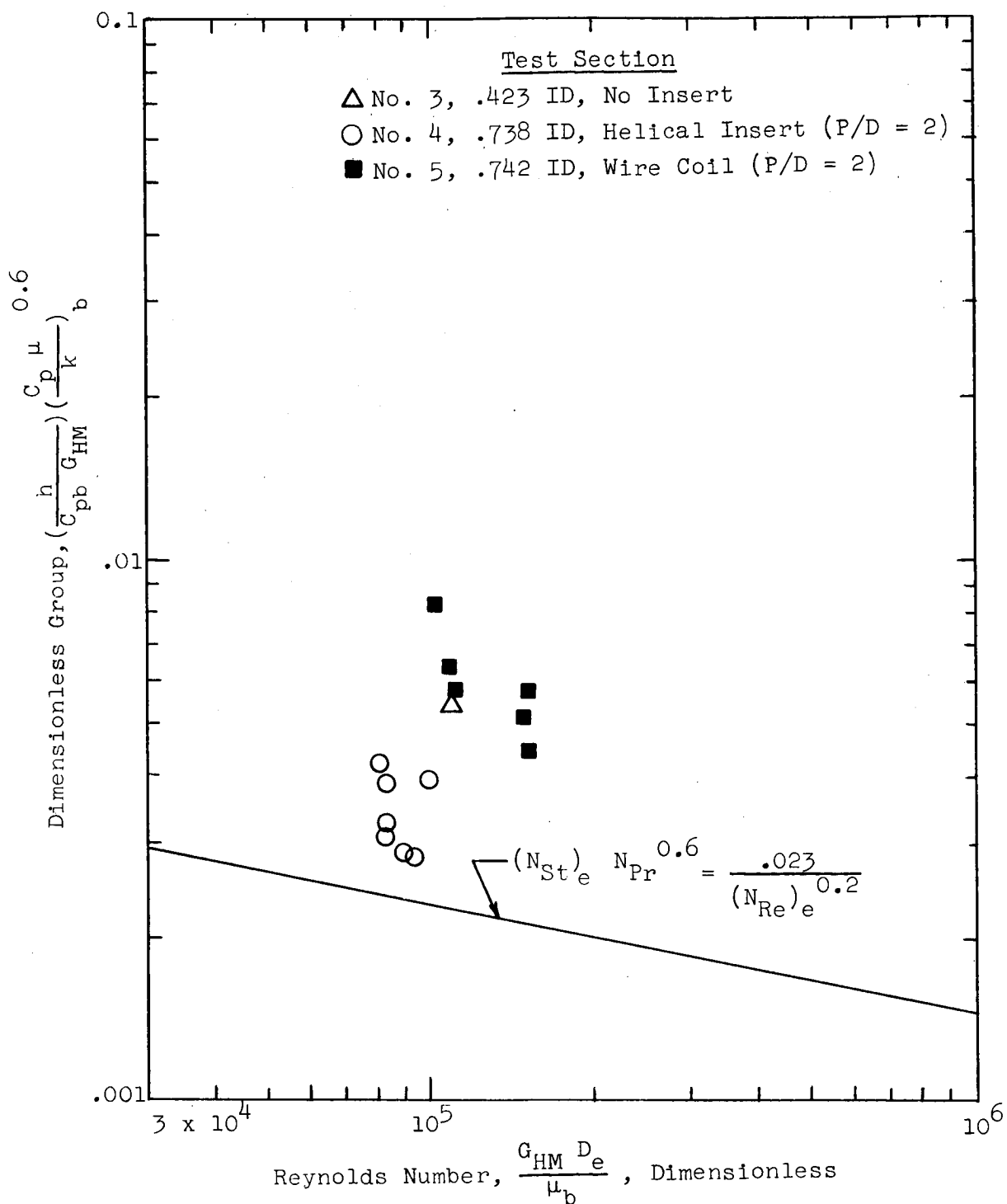
Figure 64a. Superheated Vapor Results After Correction For Radiation Effects Using Equation (49) And Assuming Helical Flow (Equations 50 and 51)
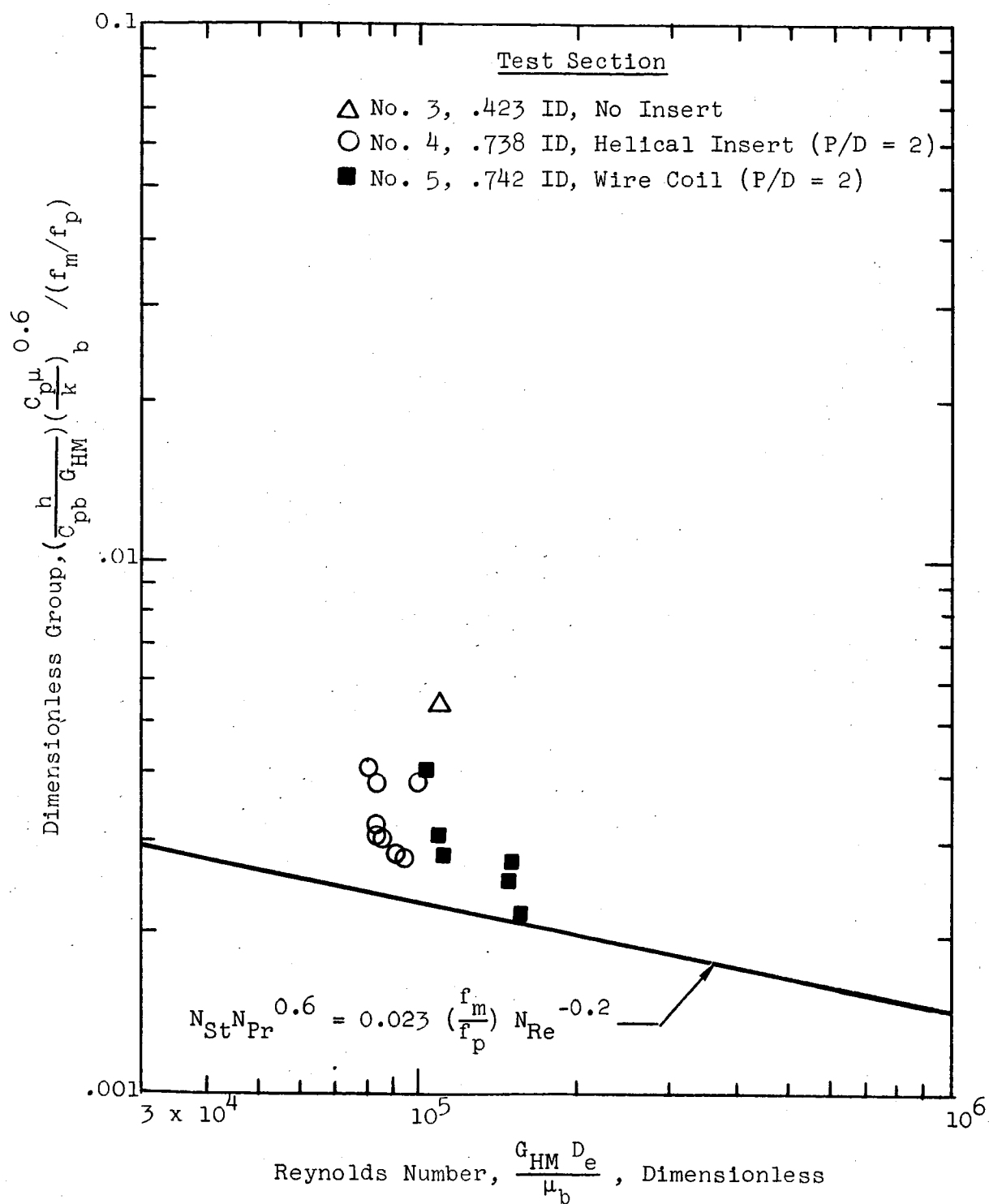
Figure 64b. Superheated Vapor Results After Correction For Effects Of Radiation (Equation 49), Helical Flow (Equations 50, 51) and Increased Friction (Equation 55)

-187-
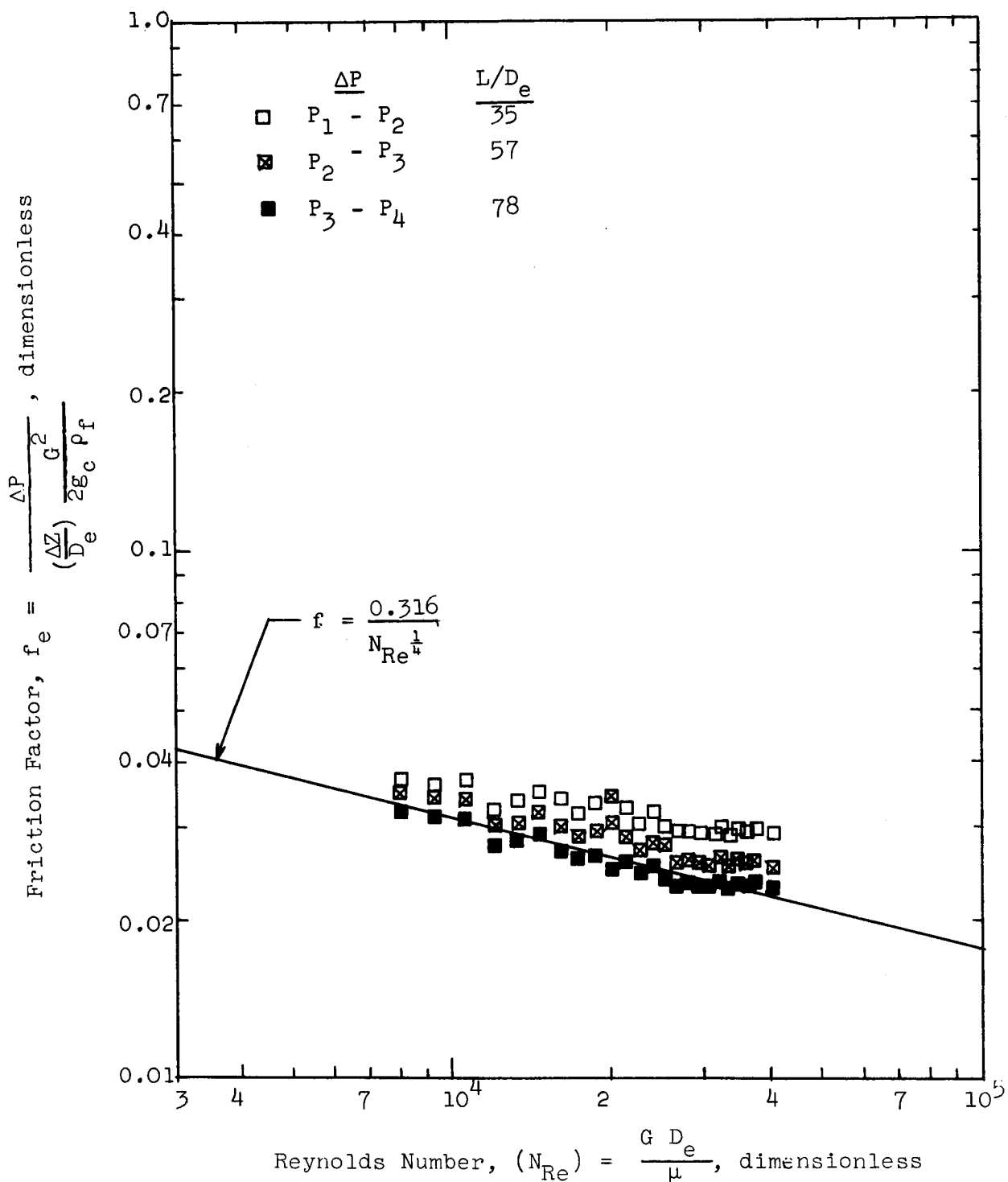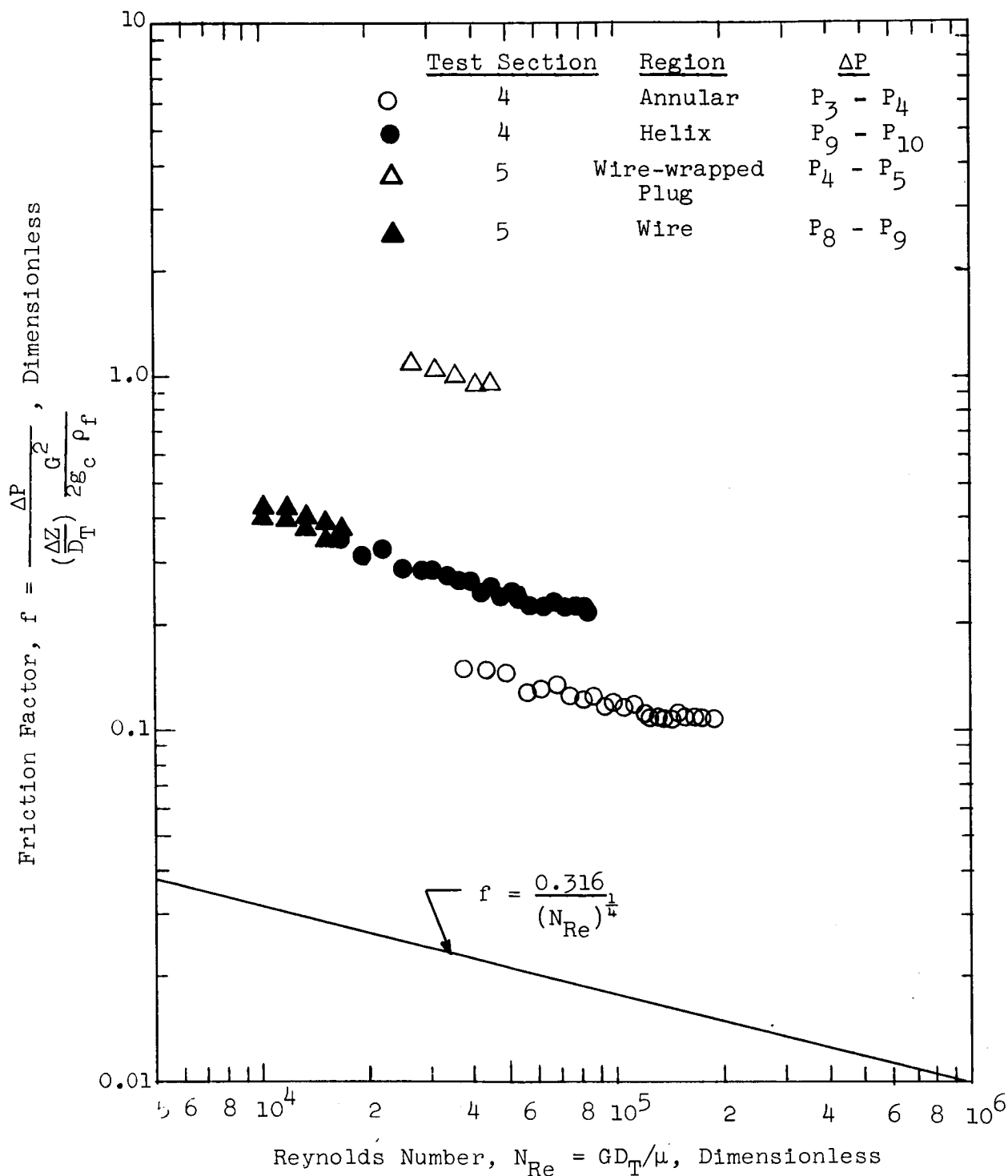
Figure 65. Single-Phase Water Friction Factors in the Annular Region of Test Section No. 4 (.738"ID with annular plug and helix (P/D = 2)
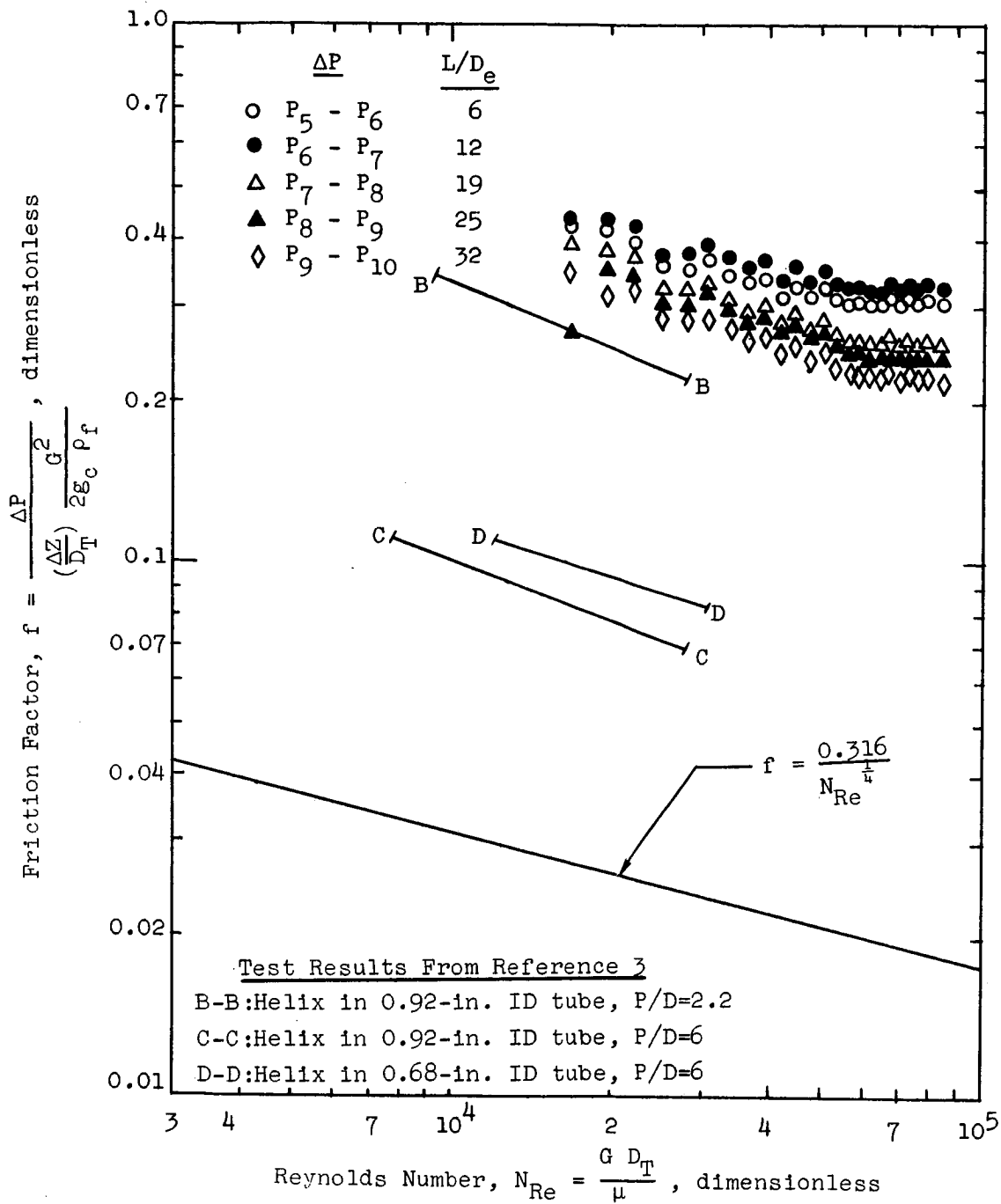
Figure 66. Single-phase Water Friction Factors in the Helix Region of Test Section No. 4 (.738"ID with annular plug and helix P/D = 2) Compared With Experimental Results from Reference 3, Evaluated Assuming Axial Flow
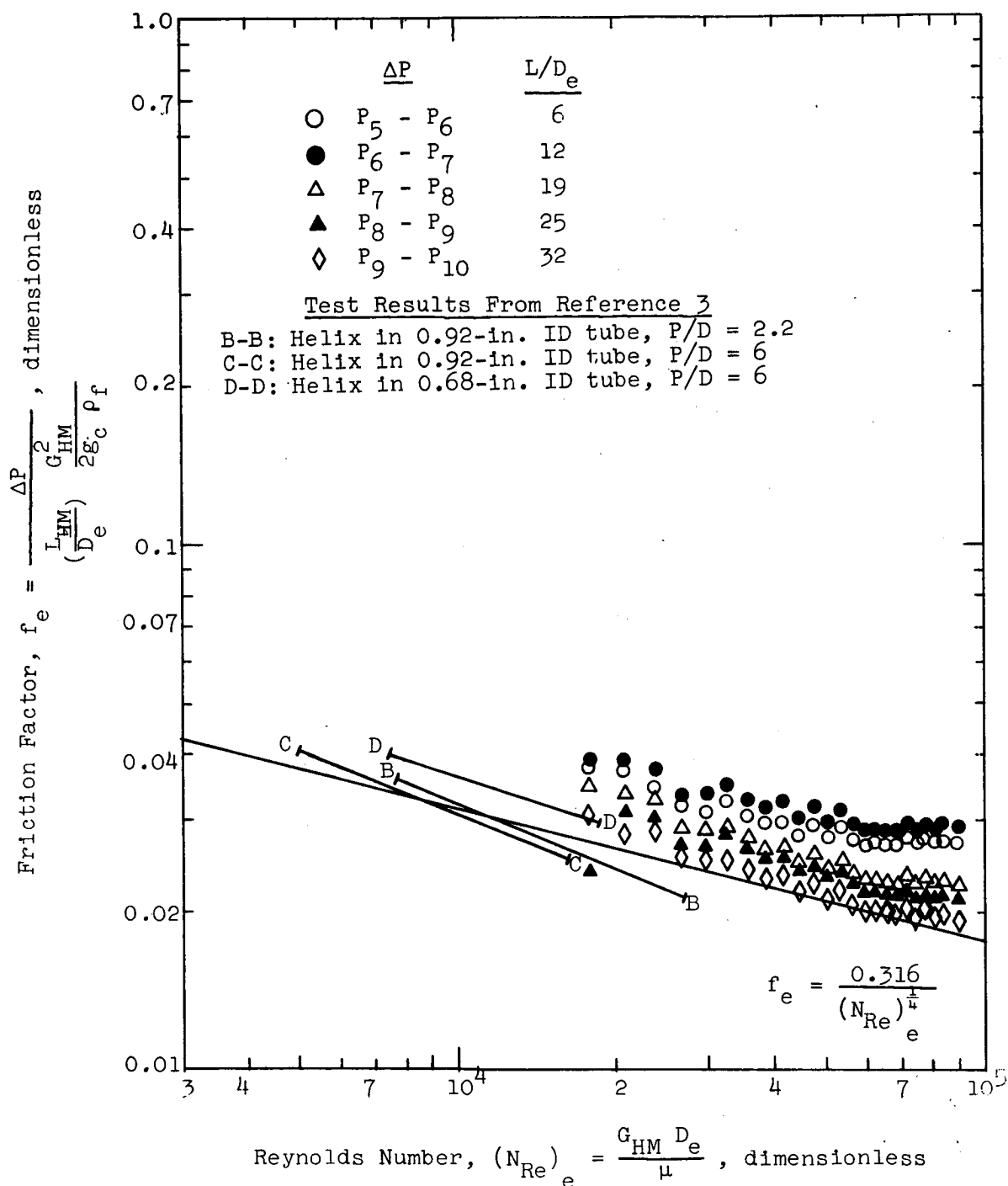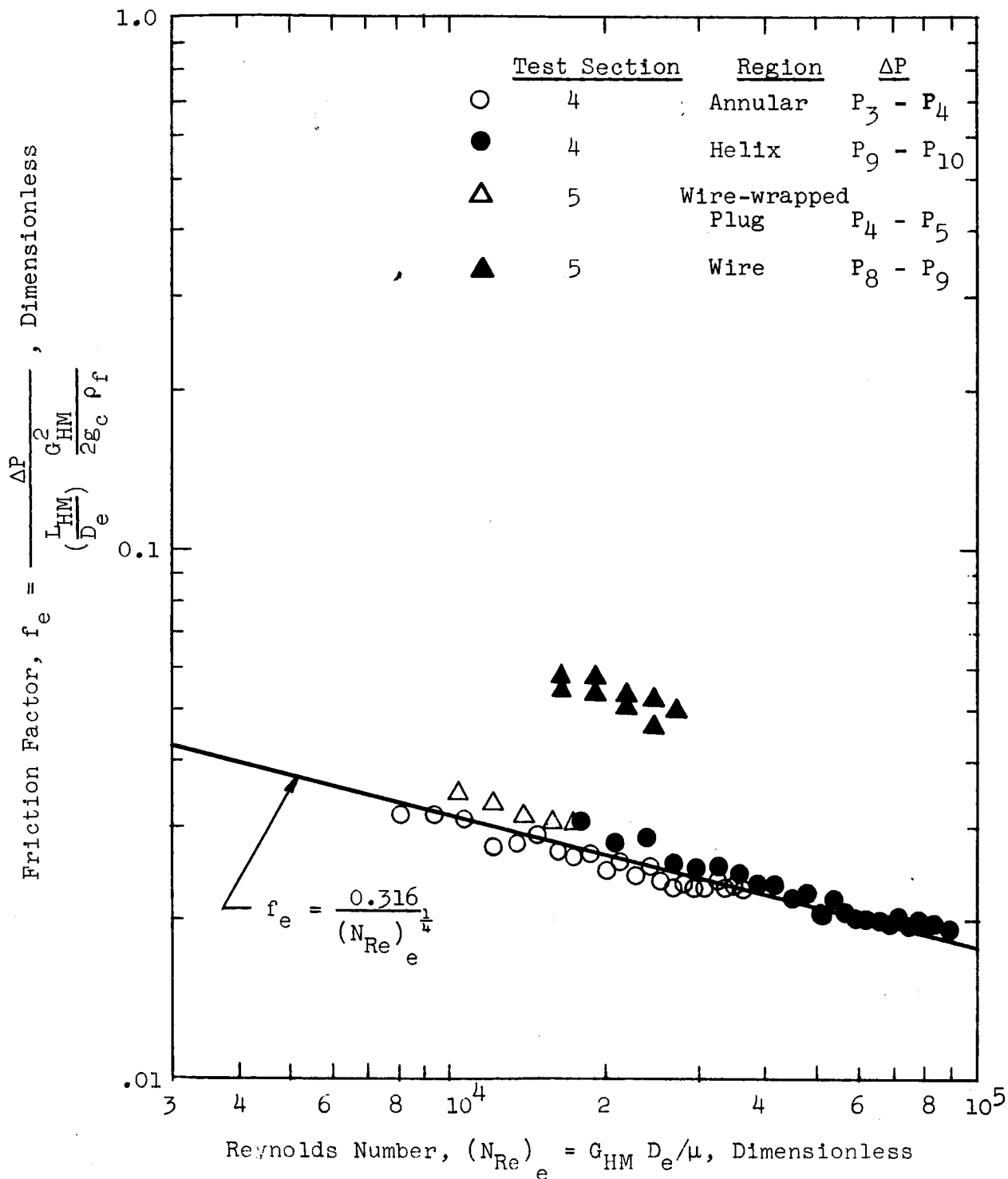
Figure 67. Equivalent Single-Phase Water Friction Factors in the Helix Region of Test Section No. 4 (.738"ID with Annular Plug and Helix P/D = 2) Evaluated Assuming Helical Flow

-190-
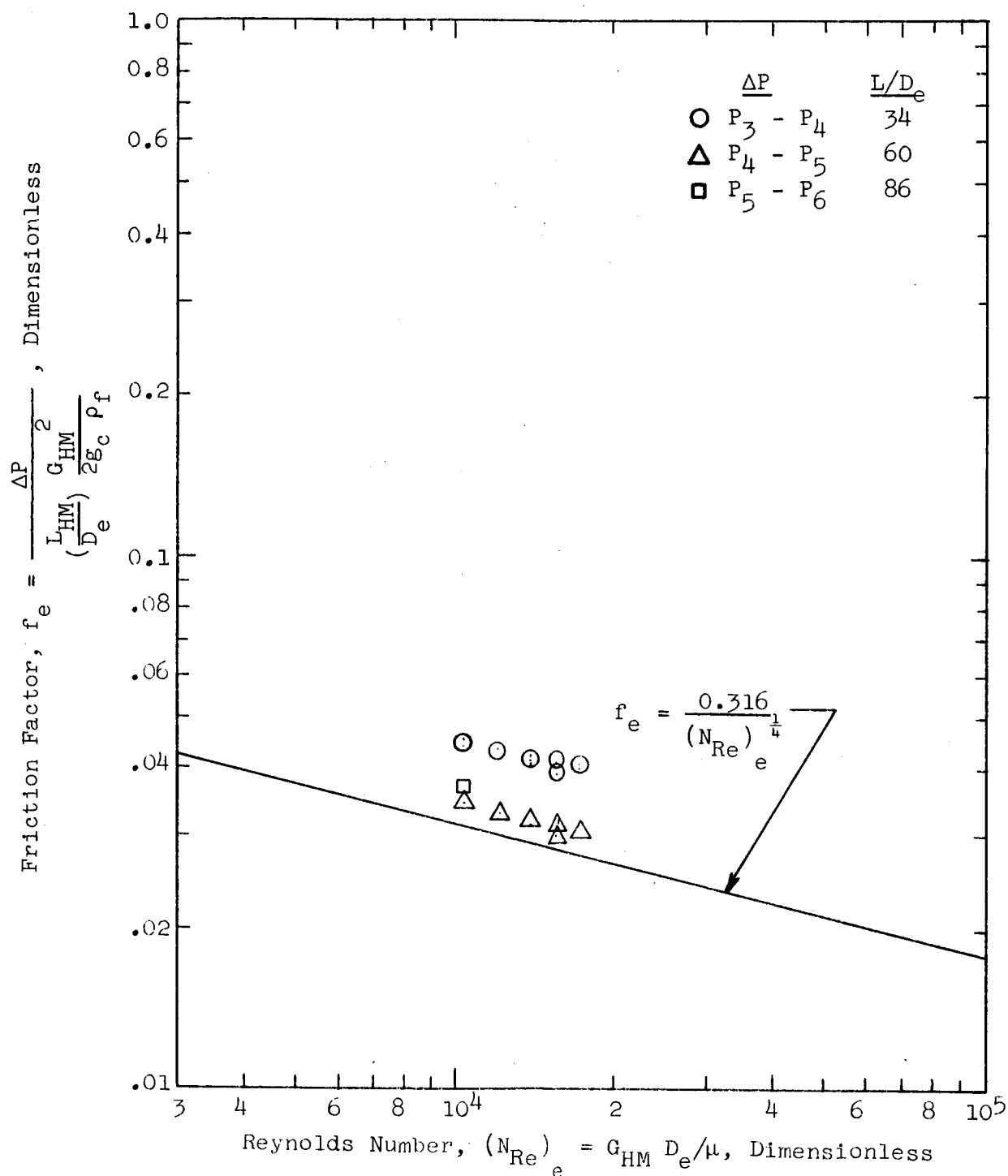
Figure 68. Equivalent Single-Phase Water Friction Factors in the Wire Wrapped Plug Region of Test Section No. 5 (.742"ID with wire-wrapped plug and wire coil P/D = 2) Evaluated Assuming Helical Flow

-191-

The plot shows Friction Factor, $f = \dfrac{\Delta P}{\left(\dfrac{\Delta Z}{D_T}\right) \dfrac{G^2}{2g_c \, \rho_f}}$, Dimensionless on the vertical axis versus Reynolds Number, $N_{Re} = G \, D_T/\mu$, Dimensionless on the horizontal axis.

$$\Delta P = P_8 - P_9$$

$$f = \frac{0.316}{(N_{Re})^{\frac{1}{4}}}$$
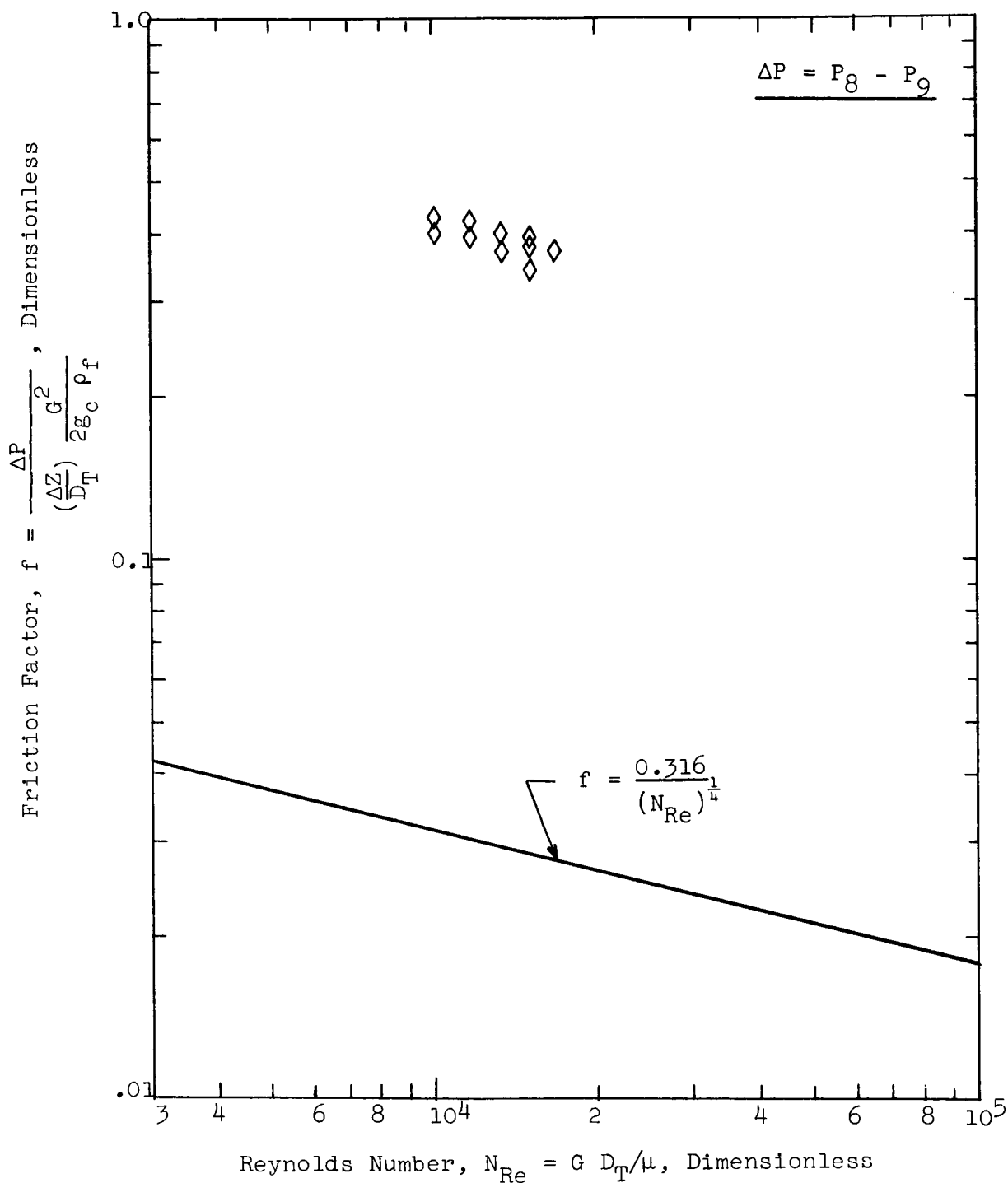
Figure 69. Single-Phase Water Friction Factors in the Wire Coil Region of Test Section No. 5 (.742"ID with wire-wrapped plug and wire coil P/D = 2), Evaluated Assuming Axial Flow

-192-
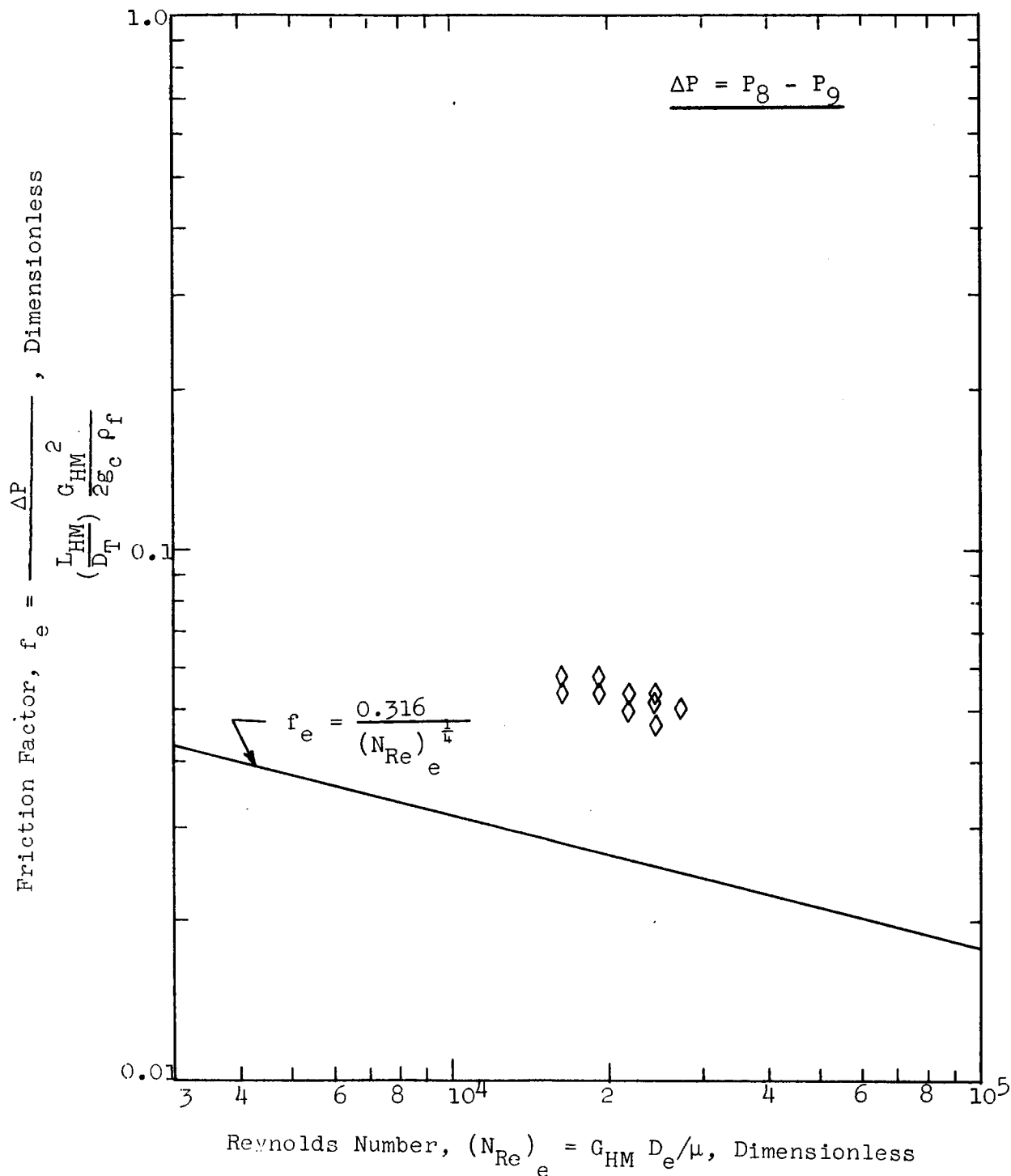
Figure 70. Equivalent Single-Phase Water Friction Factors in the Wire Coil Region of Test Section No. 5 (.742"ID with wire wrapped plug and wire coil P/D = 2), Evaluated Assuming Helical Flow

Figure 71. Comparison of Single-Phase Water Friction Factors in the Four Geometries of Test Sections No. 4 (.738"ID with annular plug and helix P/D = 2) and No. 5 (.742 ID with wire-wrapped plug and wire coil P/D = 2), Evaluated Assuming Axial Flow

-194-

Figure 72. Comparison of Equivalent Single-Phase Water Friction
Factors in Four Geometries of Test Sections No. 4
(.738" ID with annular plug and helix P/D = 2) and 5
(.742" ID with wire-wrapped plug and wire coil P/D = 2)
Evaluated Assuming Helical Flow

-195-
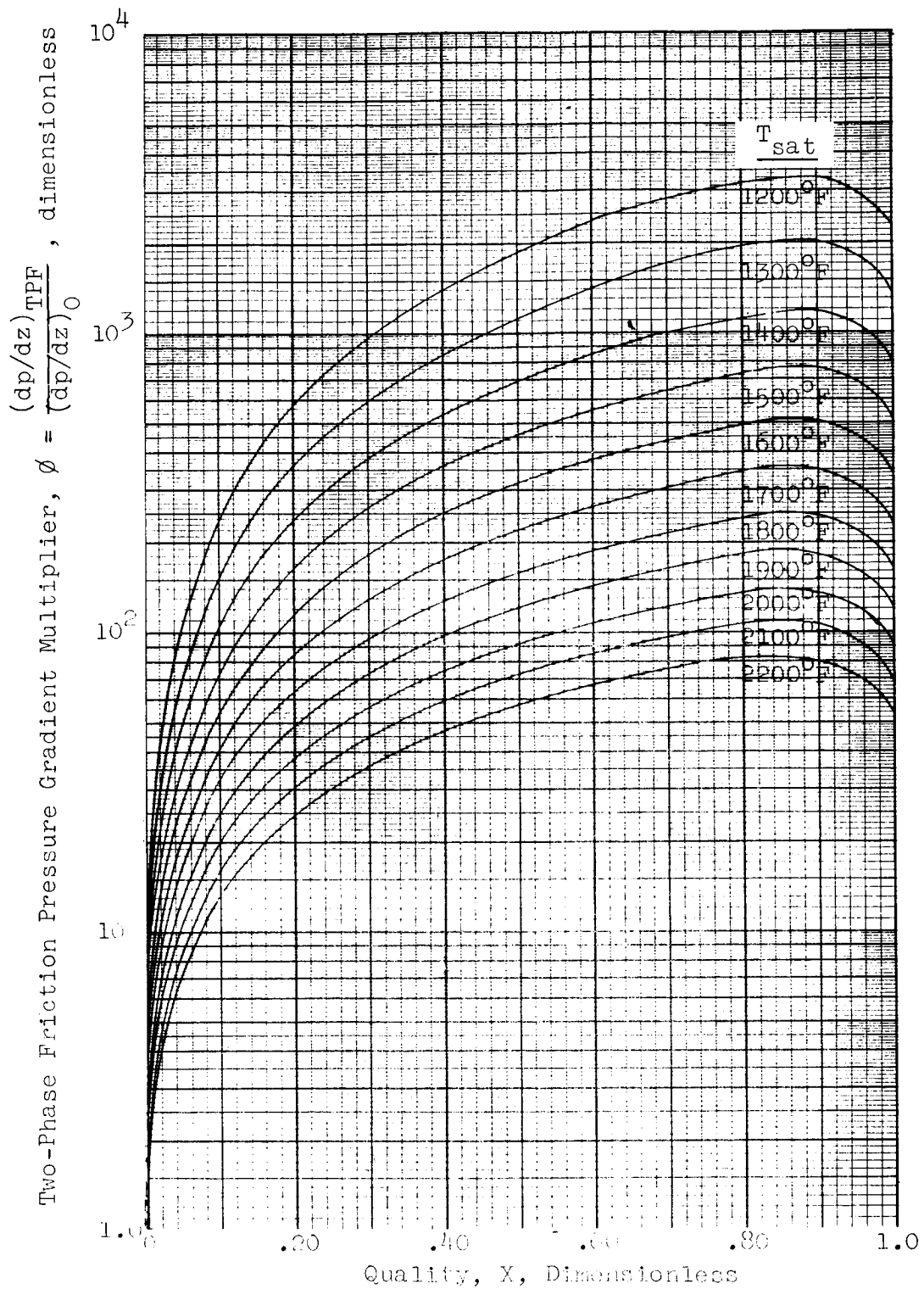
Figure 73. Two-Phase Friction Pressure Gradient Multipliers For Potassium From Modified Martinelli Model of Reference 10
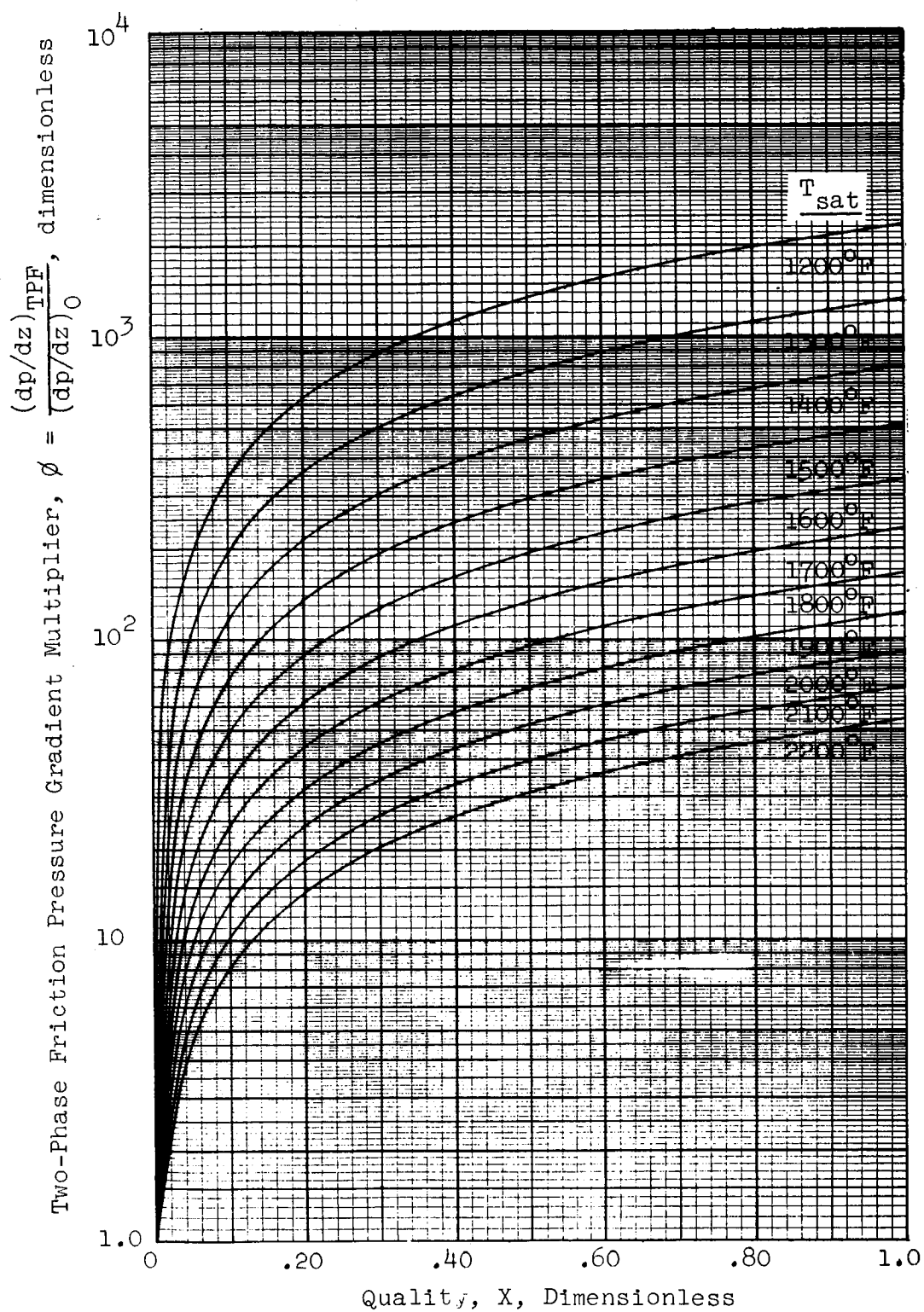
Figure 74. Two-Phase Friction Pressure Gradient Multipliers For Potassium From Homogeneous Model, Equation (69)
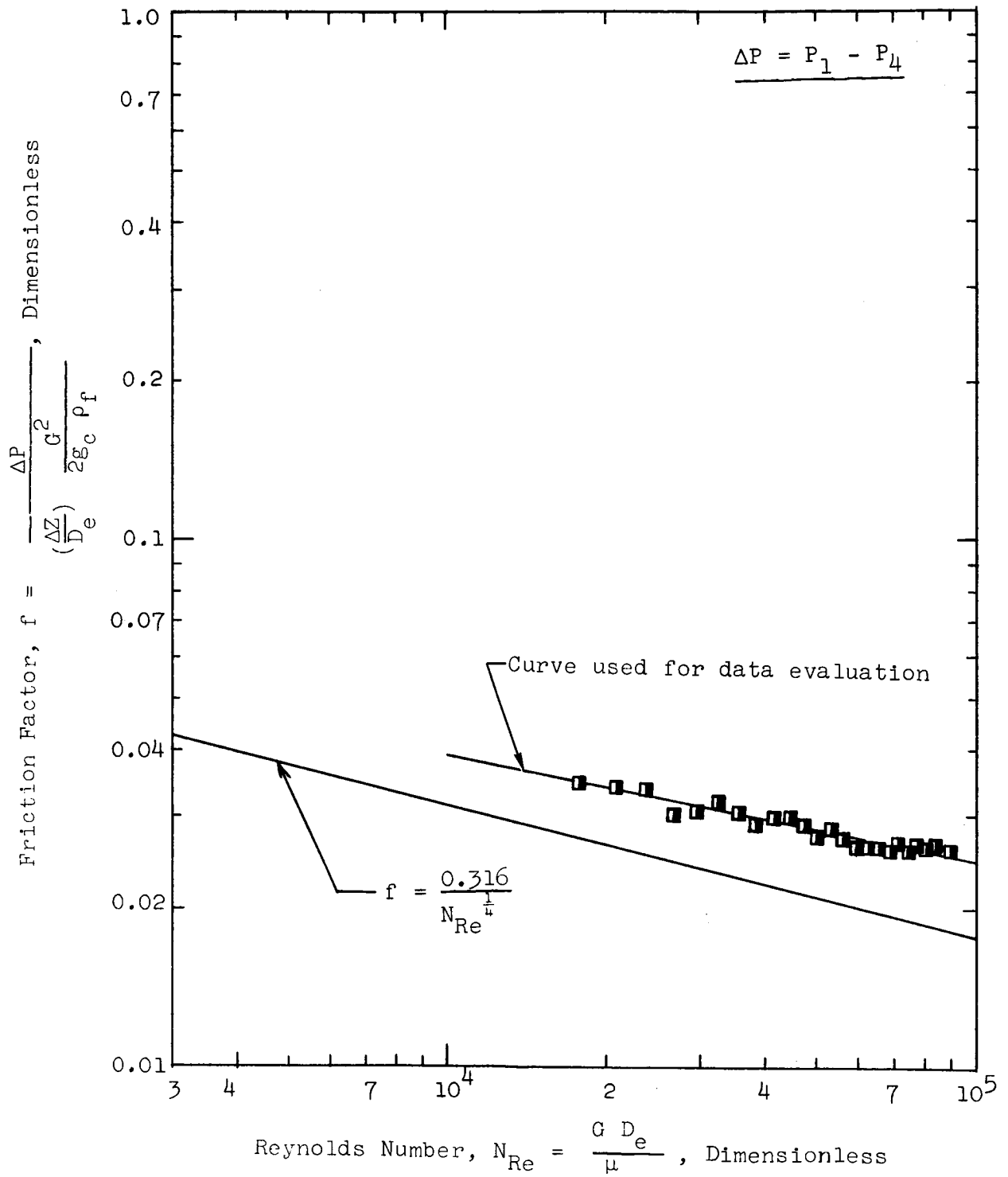
Figure 75. Liquid-Phase Friction Factors Used in Evaluating Two-Phase
Pressure Drop For Annulus Region of Test Section No. 4
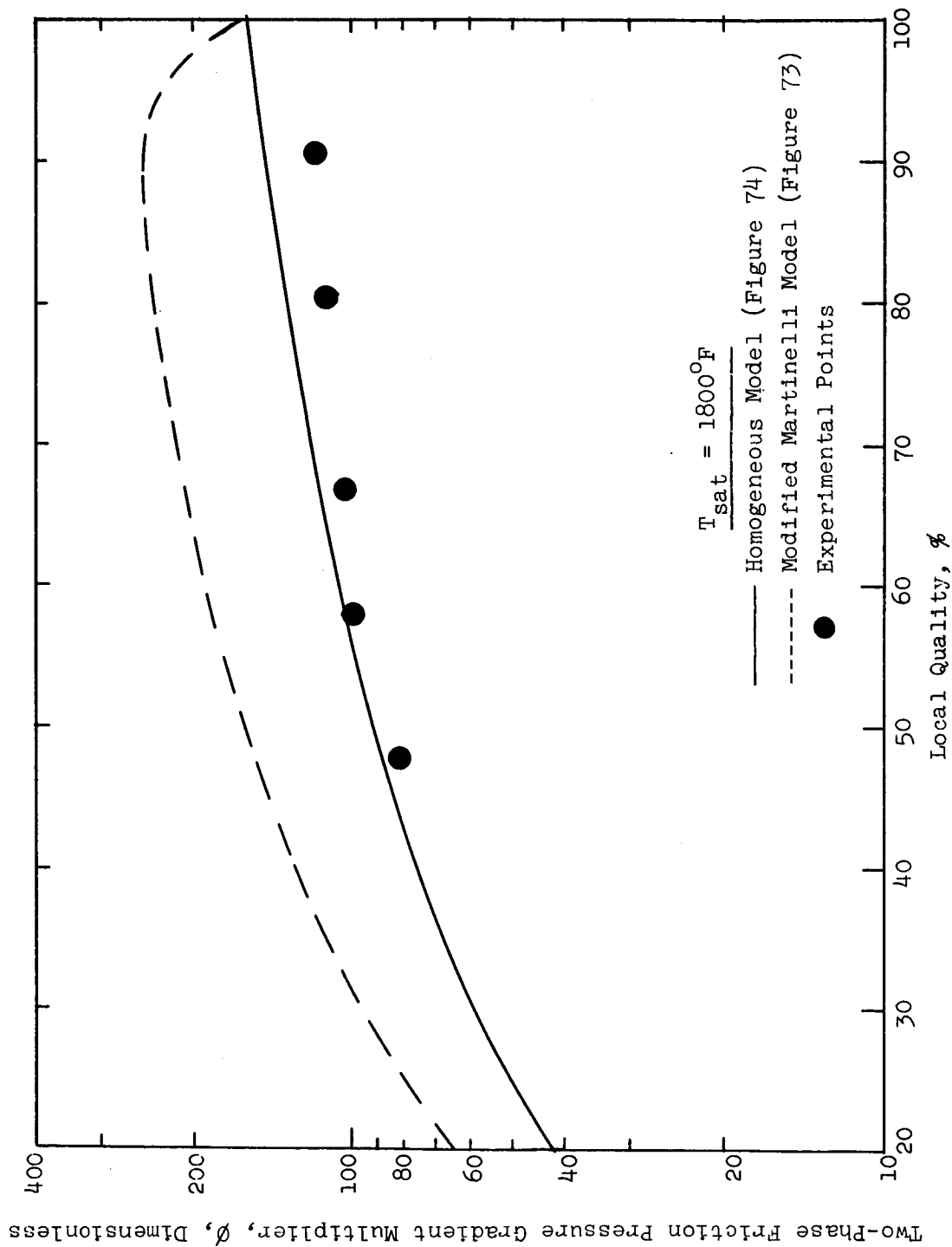(.738"ID with annular plug and helix P/D = 2)

-198-
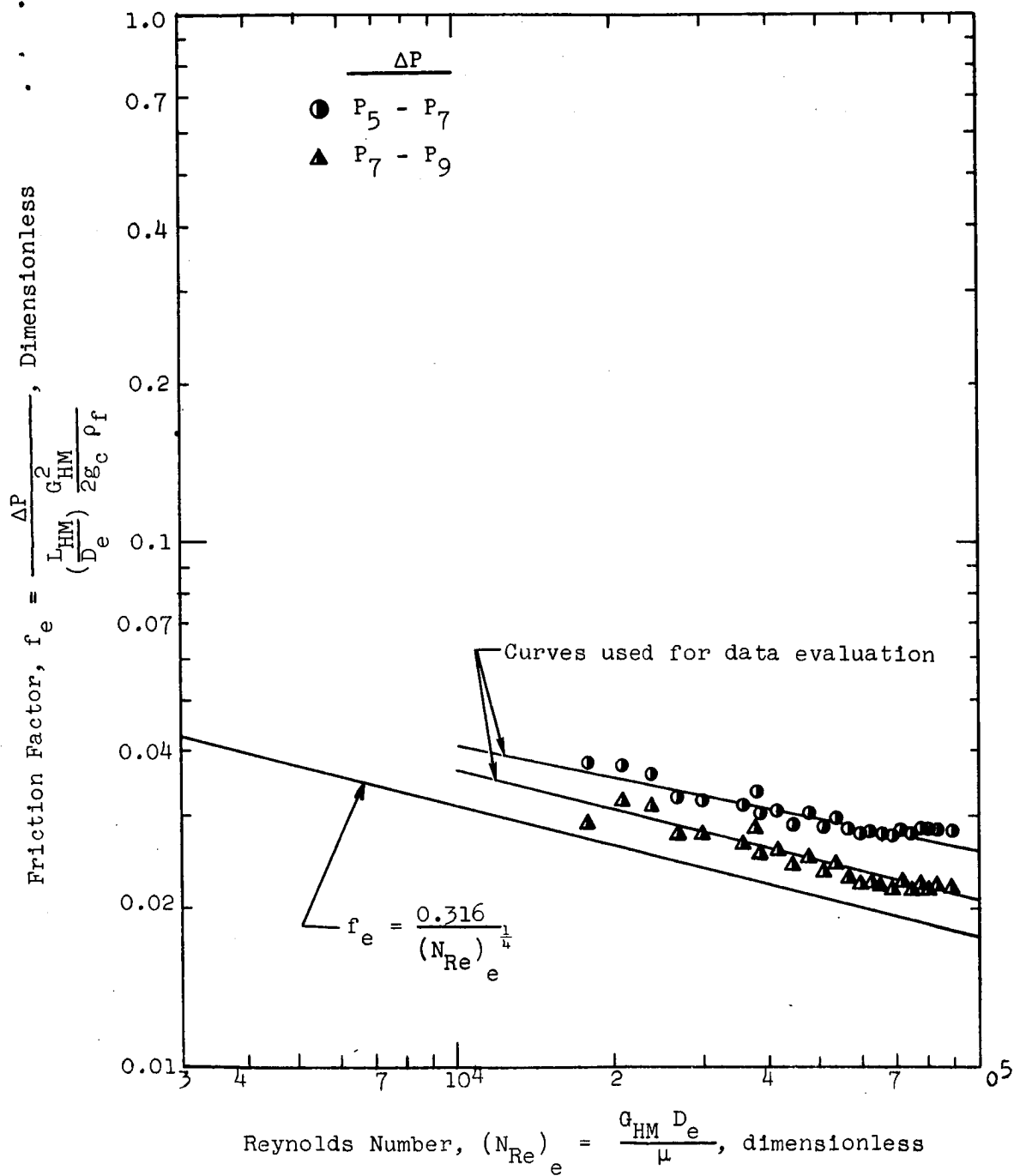
Figure 76. Liquid-Phase Friction Factors Used in Evaluating Two-Phase Pressure Drop For Helix Region of Test Section No. 4 (.738" ID with annular plug and helix P/D = 2)

Figure 77. Two-Phase Friction Pressure Drop Multipliers in the
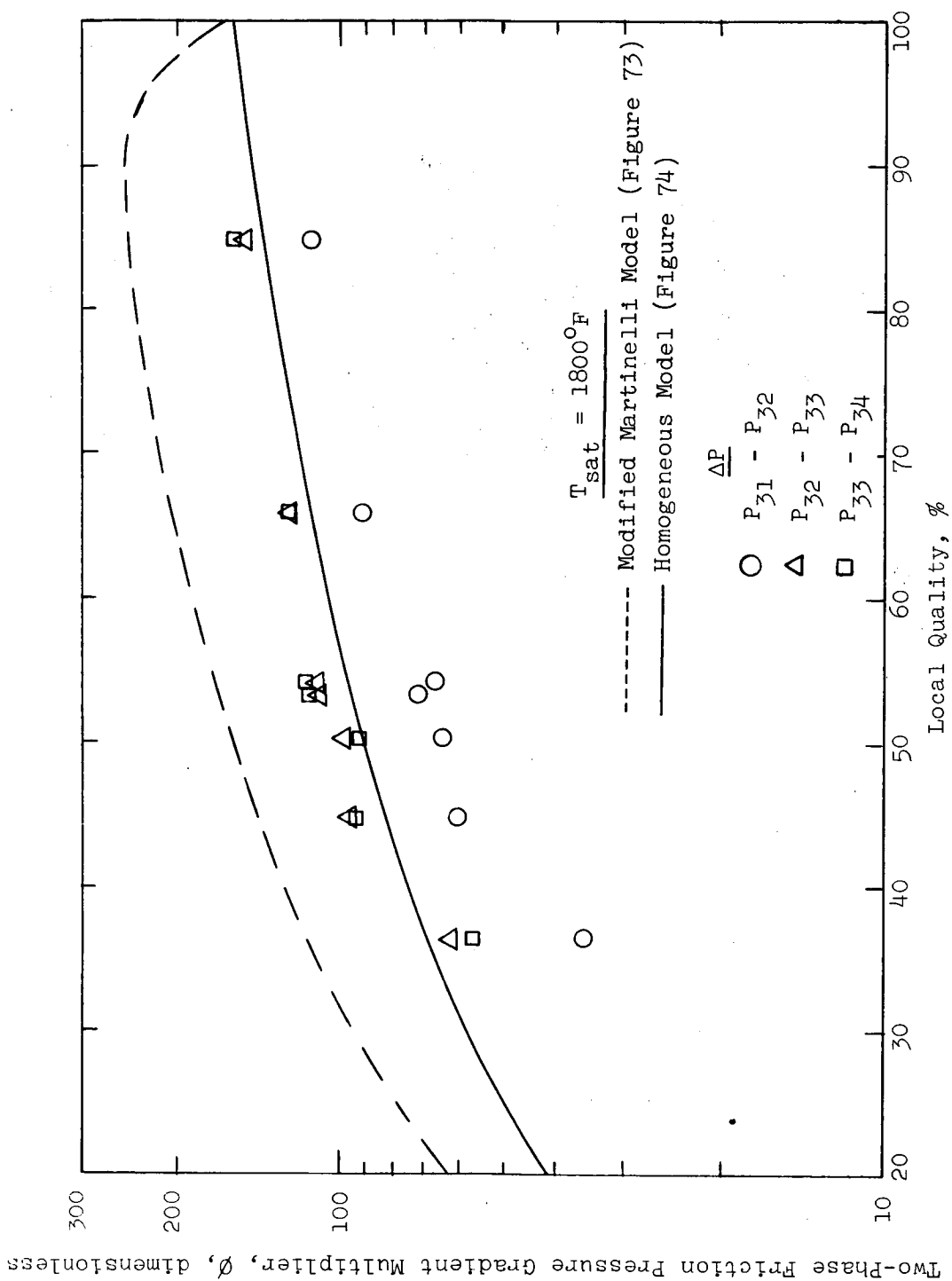Annular Region of Test Section No. 4 (.738"ID with
annular plug and helix P/D = 2)
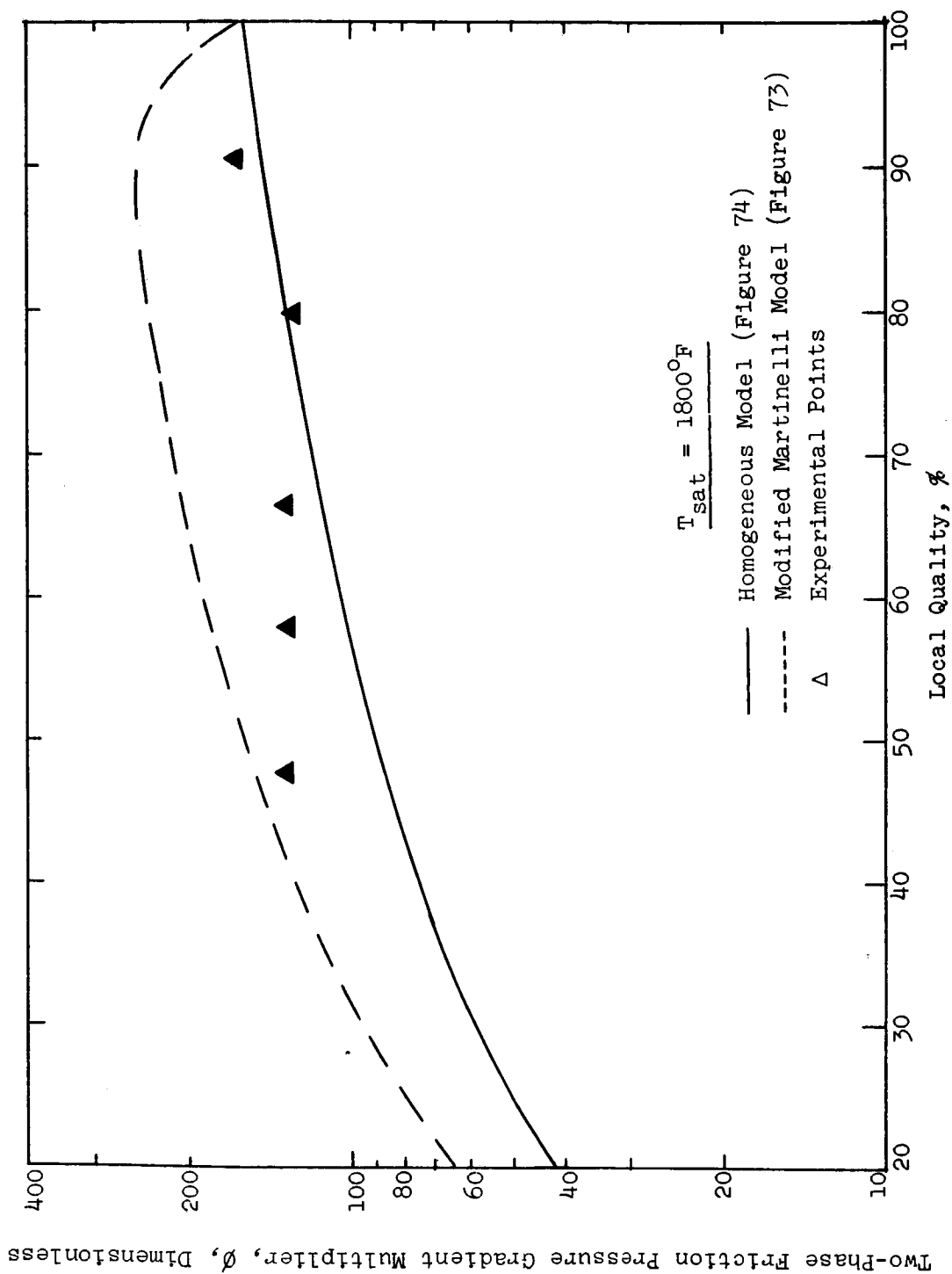
Figure 78. Two-Phase Friction Pressure Drop Multipliers in the Helix Region of Test Section No. 4 (.738 ID with annular plug and helix P/D = 2)

Figure 79. Two-Phase Friction Pressure Drop Multipliers in the Wire-Wrapped Plug Region of Test Section No. 5 (.742"ID with wire-wrapped plug and wire coil P/D = 2)
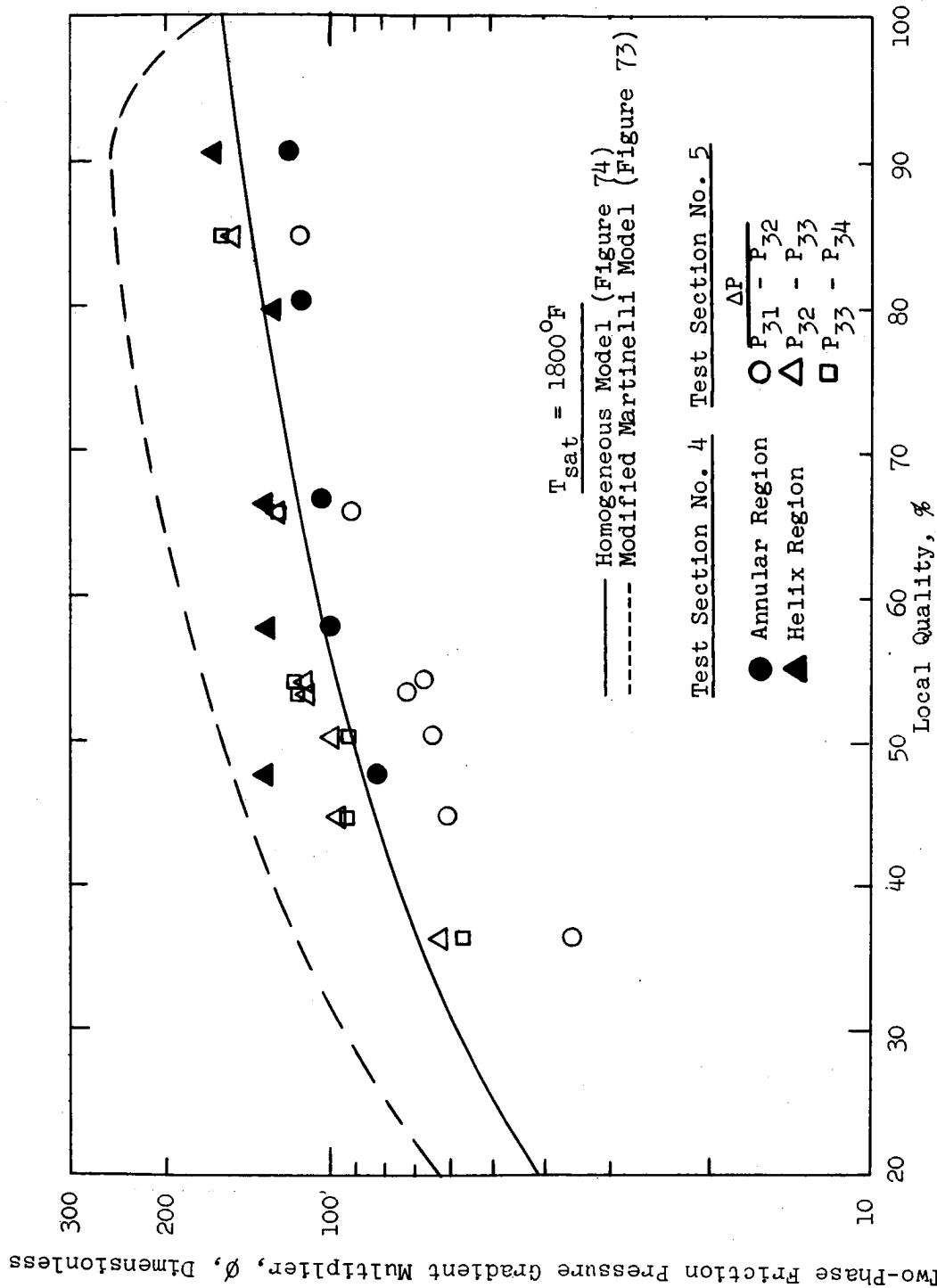
-202-

Figure 80. Comparison of Two-Phase Friction Pressure Drop Results
From Test Sections No. 4 (.738"ID with annular plug and
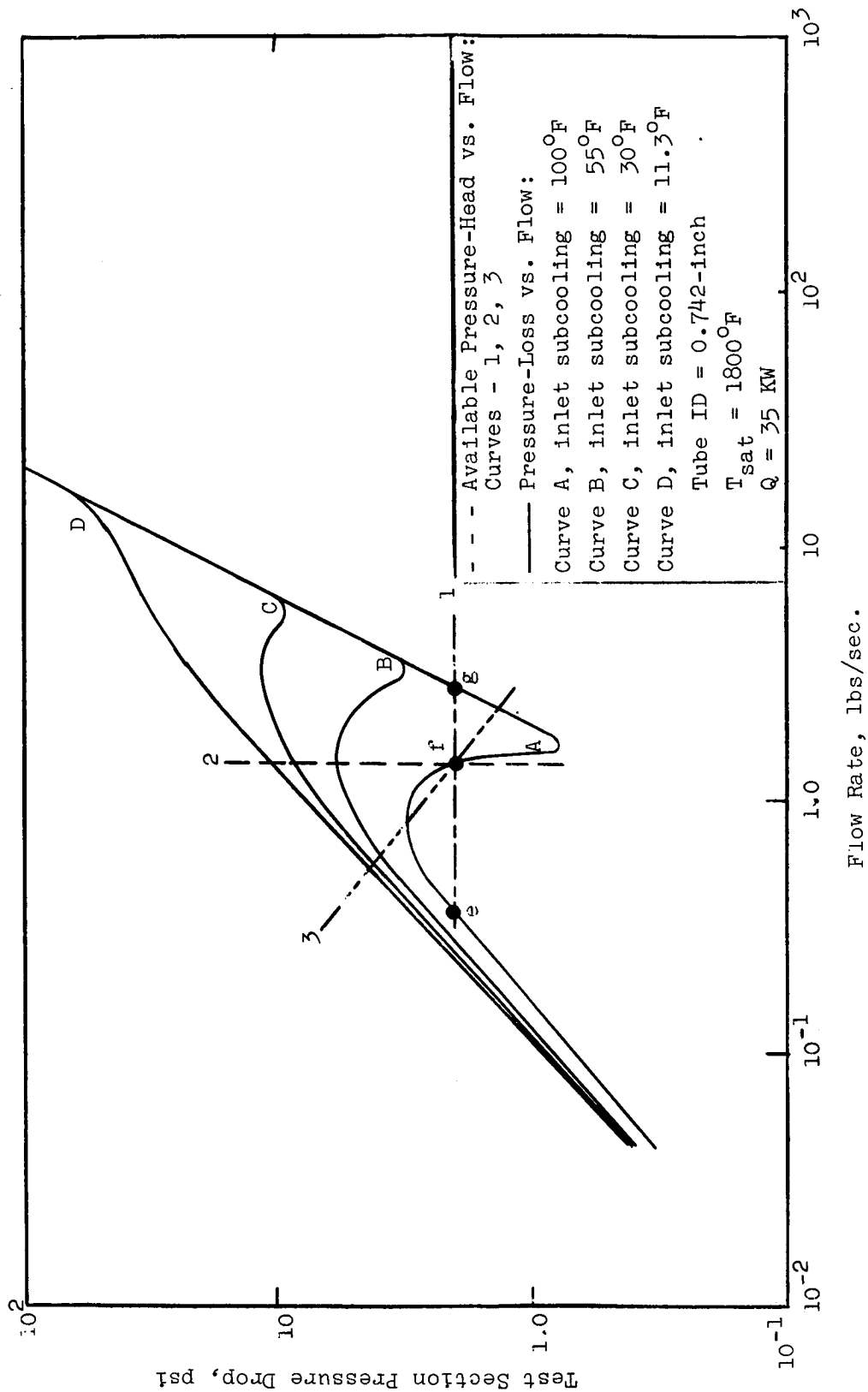helix P/D = 2) and 5 (.742"ID with wire-wrapped plug and
wire coil P/D = 2)

Figure 81. Calculated Pressure-Loss Characteristics Compared With
Different Available Pressure-Head Characteristics For
Test Section No. 1 (.767"ID, no insert) Showing Possible
Operating Points

The figure legend reads:

– – – Available Pressure-Head vs. Flow:
Curves – 1, 2, 3

——— Pressure-Loss vs. Flow:

Curve A, inlet subcooling = 100°F
Curve B, inlet subcooling = 55°F
Curve C, inlet subcooling = 30°F
Curve D, inlet subcooling = 11.3°F

Tube ID = 0.742-inch
T_{sat} = 1800°F
Q = 35 KW

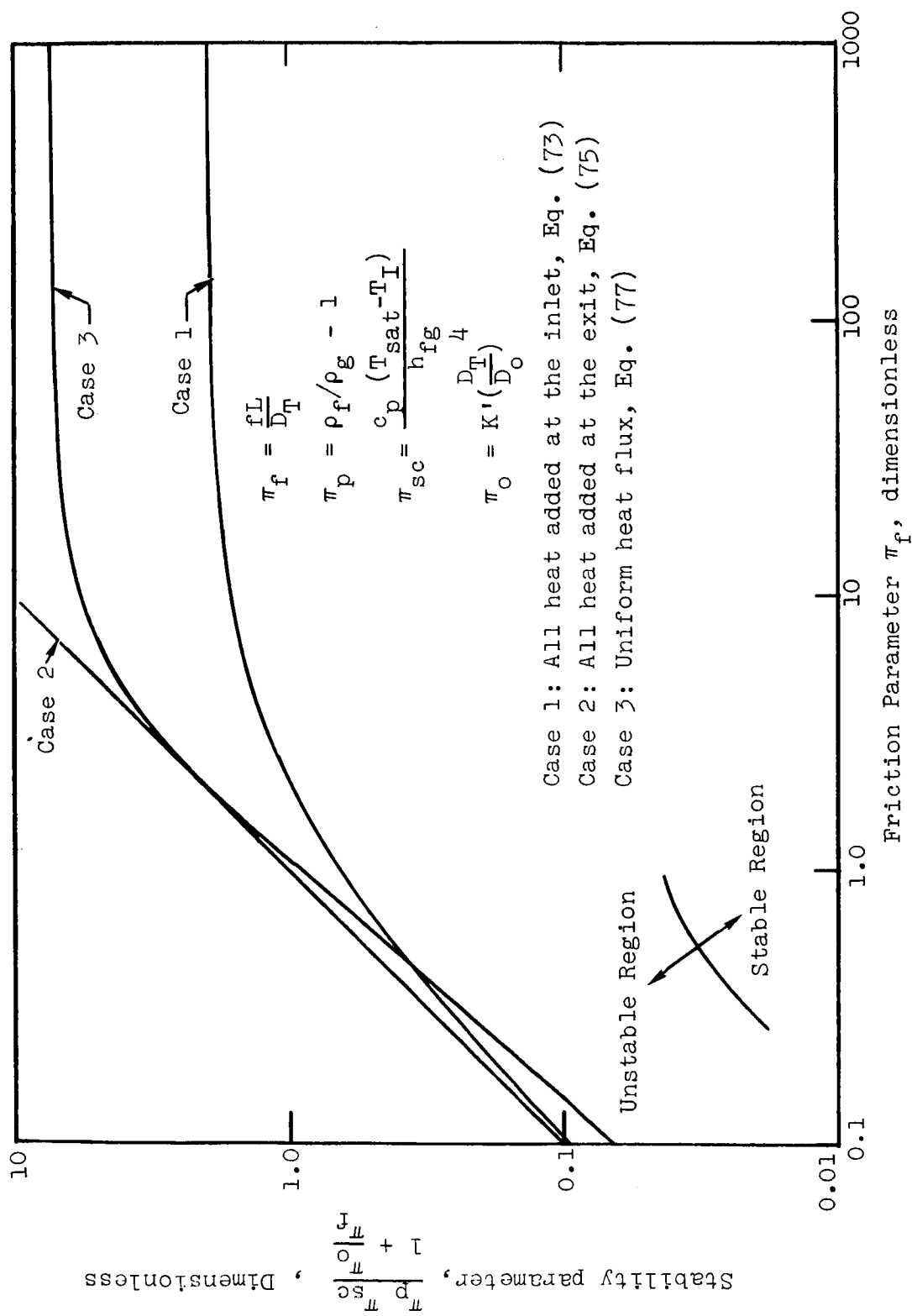Flow Rate, lbs/sec.

Test Section Pressure Drop, psi

Figure 82. Boundaries Between Stable and Unstable Operating Regions
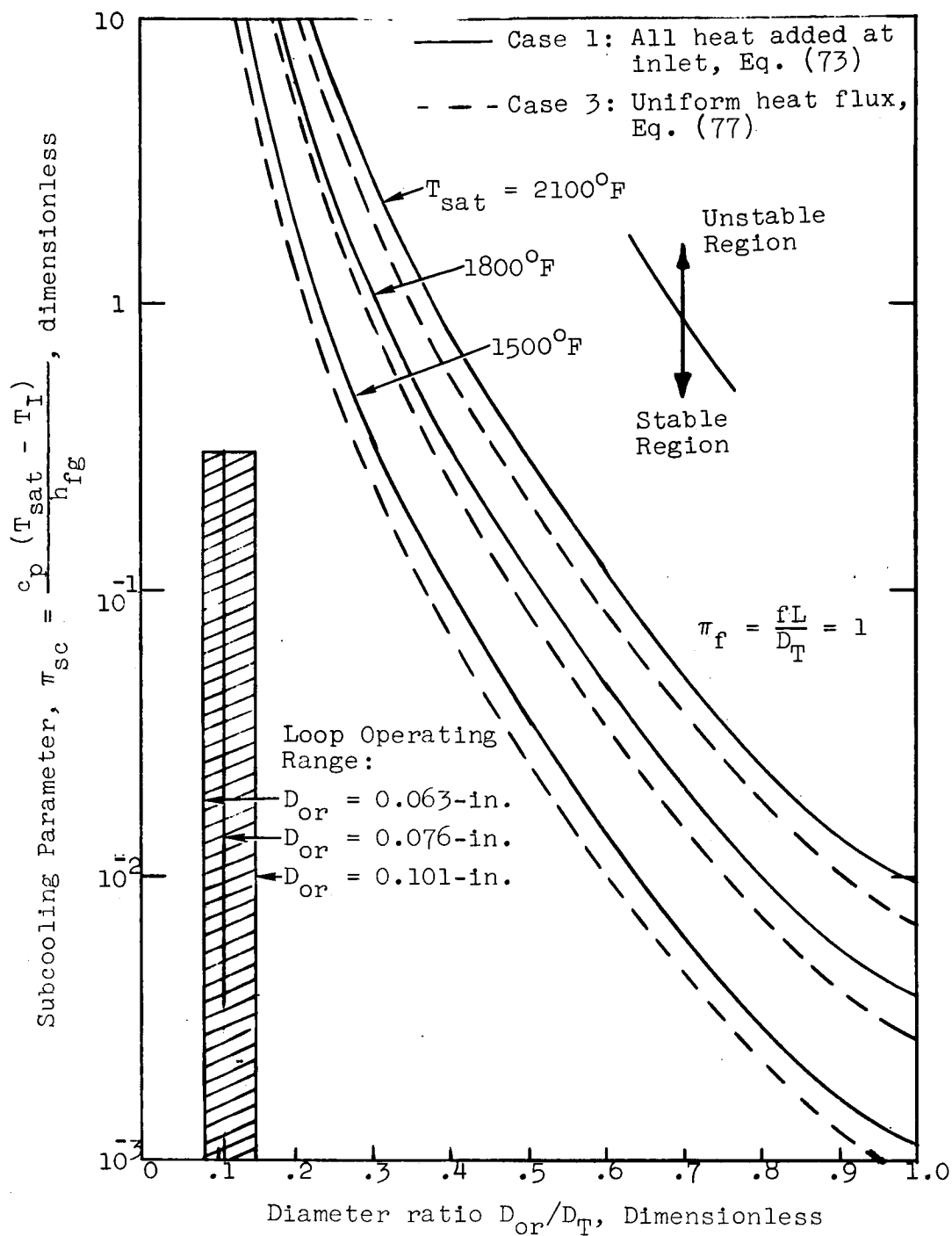Calculated Using the Ledinegg Stability Criterion

Figure 83. Effect of Temperature and Orifice Size On Boundaries Between Stable and Unstable Operating Regions For Cb-1%Zr Facility Calculated Using Ledinegg Stability Criterion
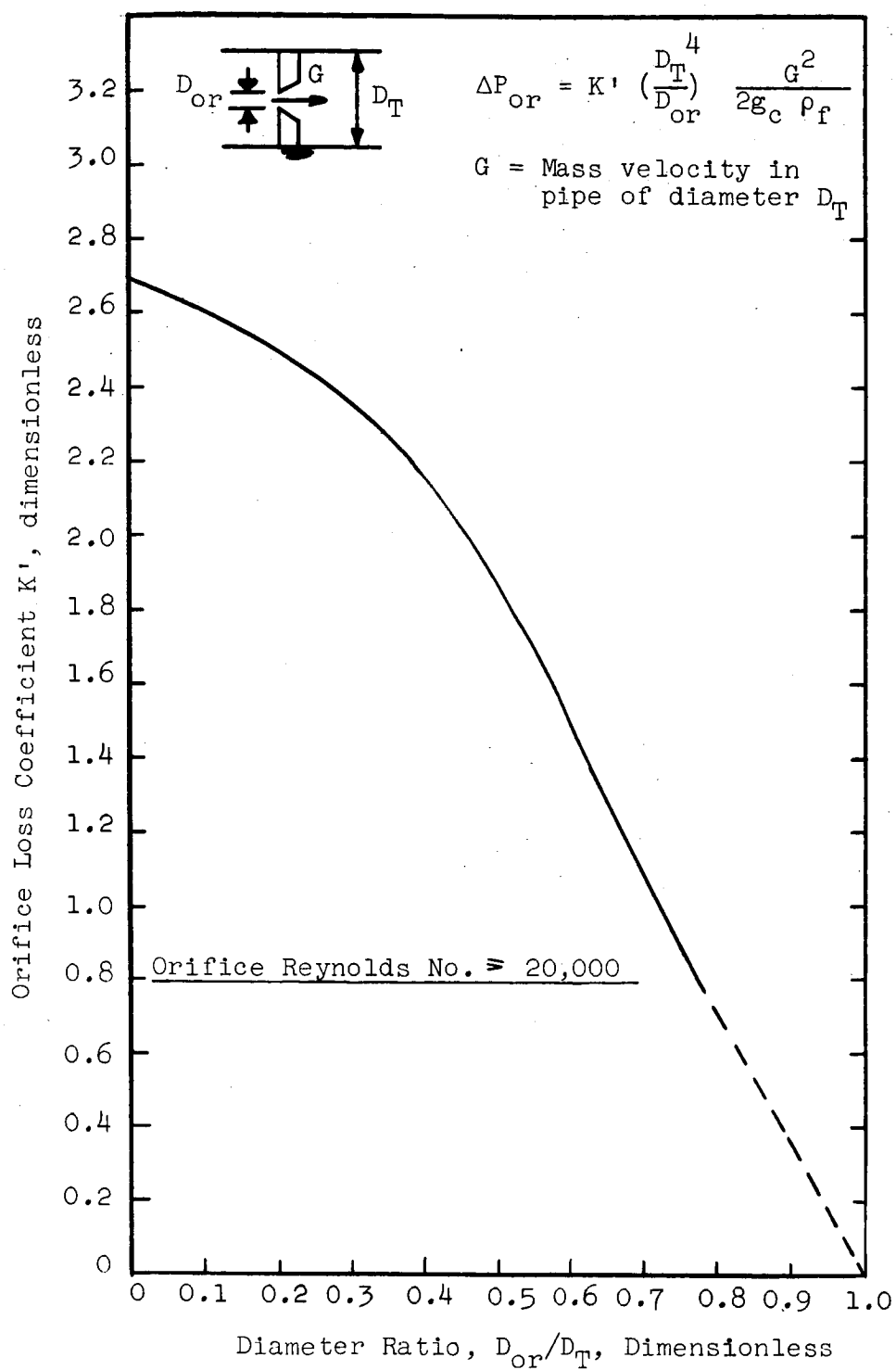
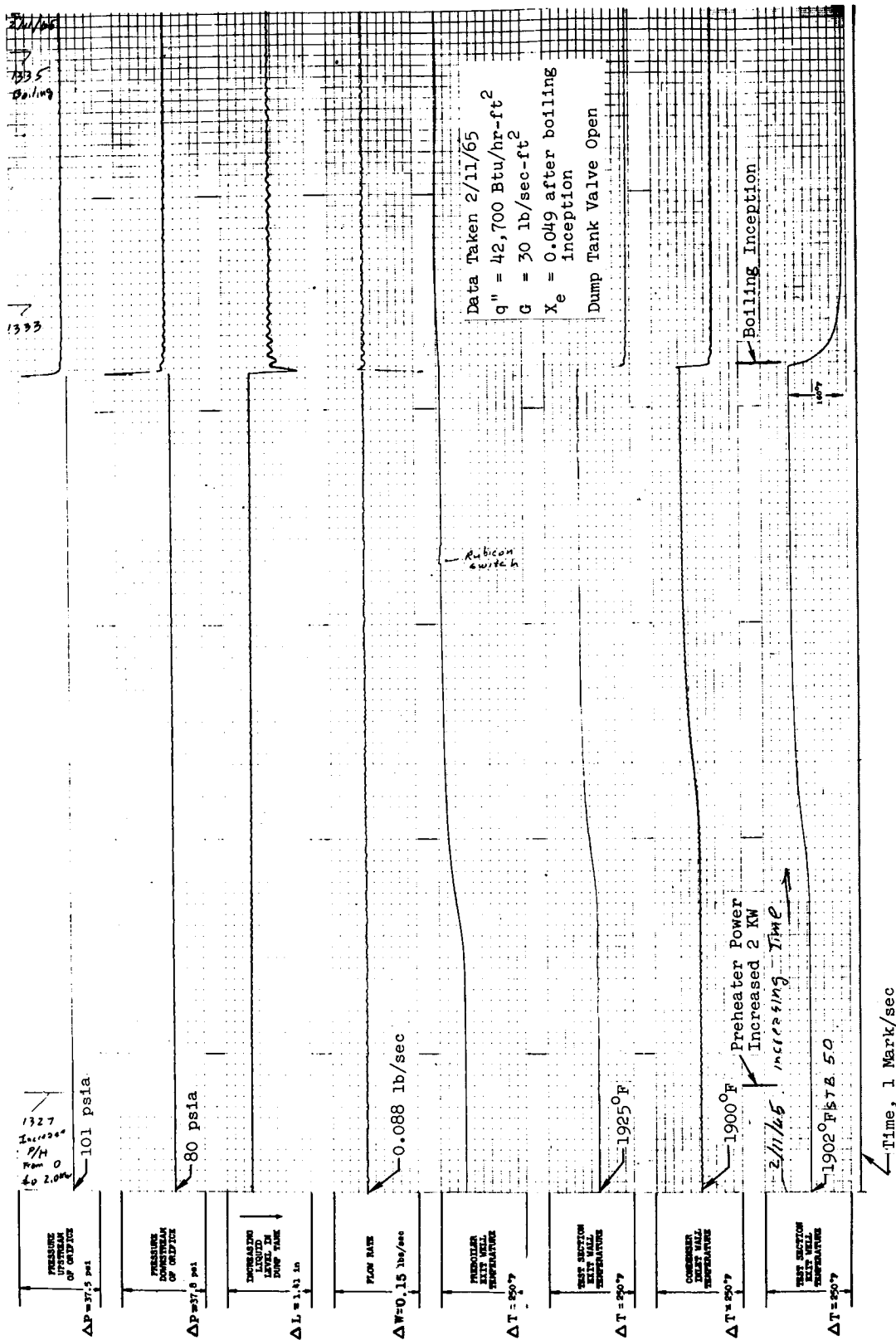Figure 84. Calculated Orifice Loss Coefficients From Reference 37

Figure 85. Recorder Chart Showing Boiling Inception at High Flow (G = 30 lb/sec-ft^2) with Test Section No. 2 (.74" ID with helical insert P/D = 6)
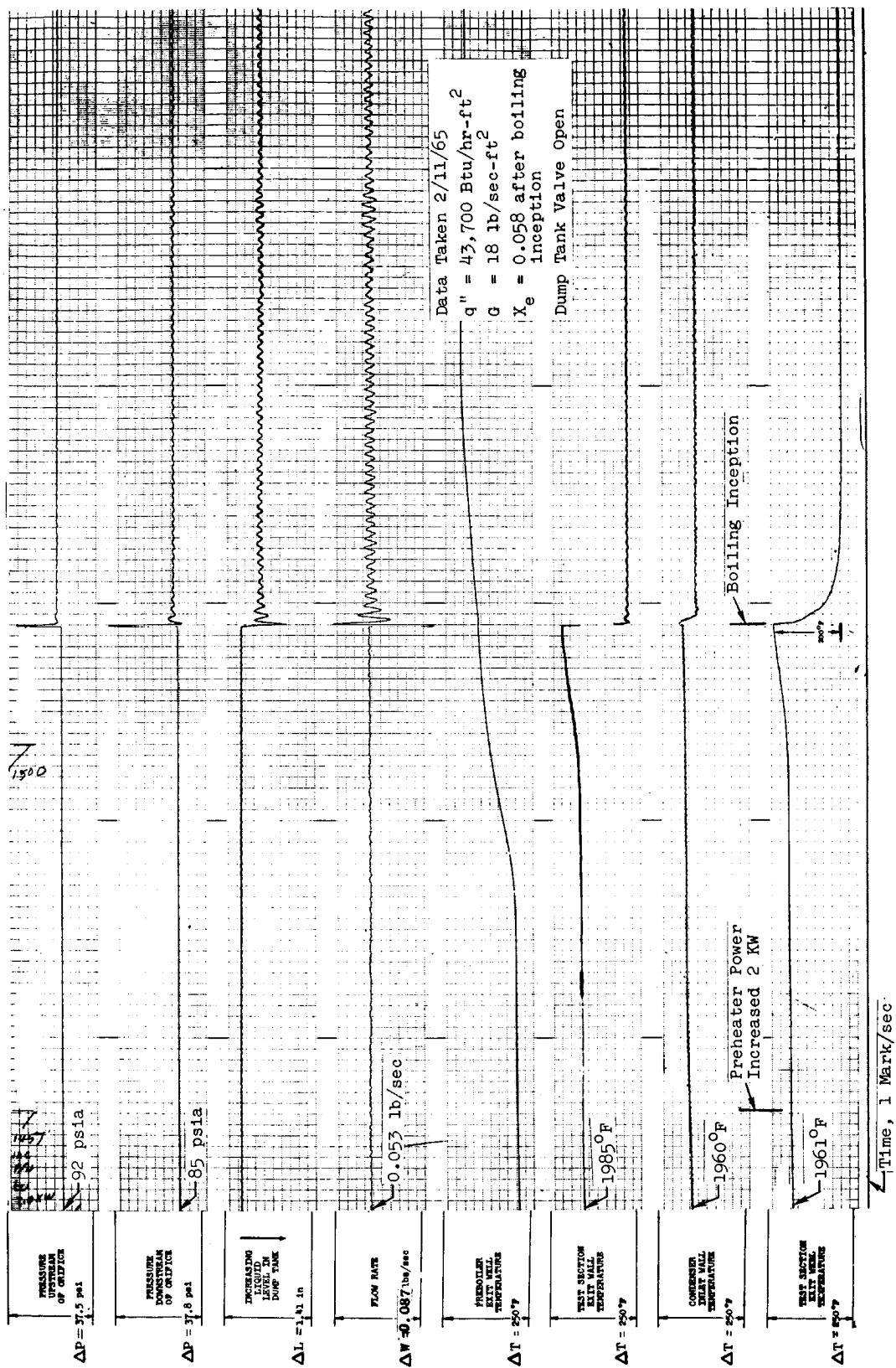
Figure 86. Recorder Chart Showing Boiling Inception at Low Flow (G = 18 lb/sec-ft2) with Test Section No. 2 (.74" ID with helical insert P/D = 6)
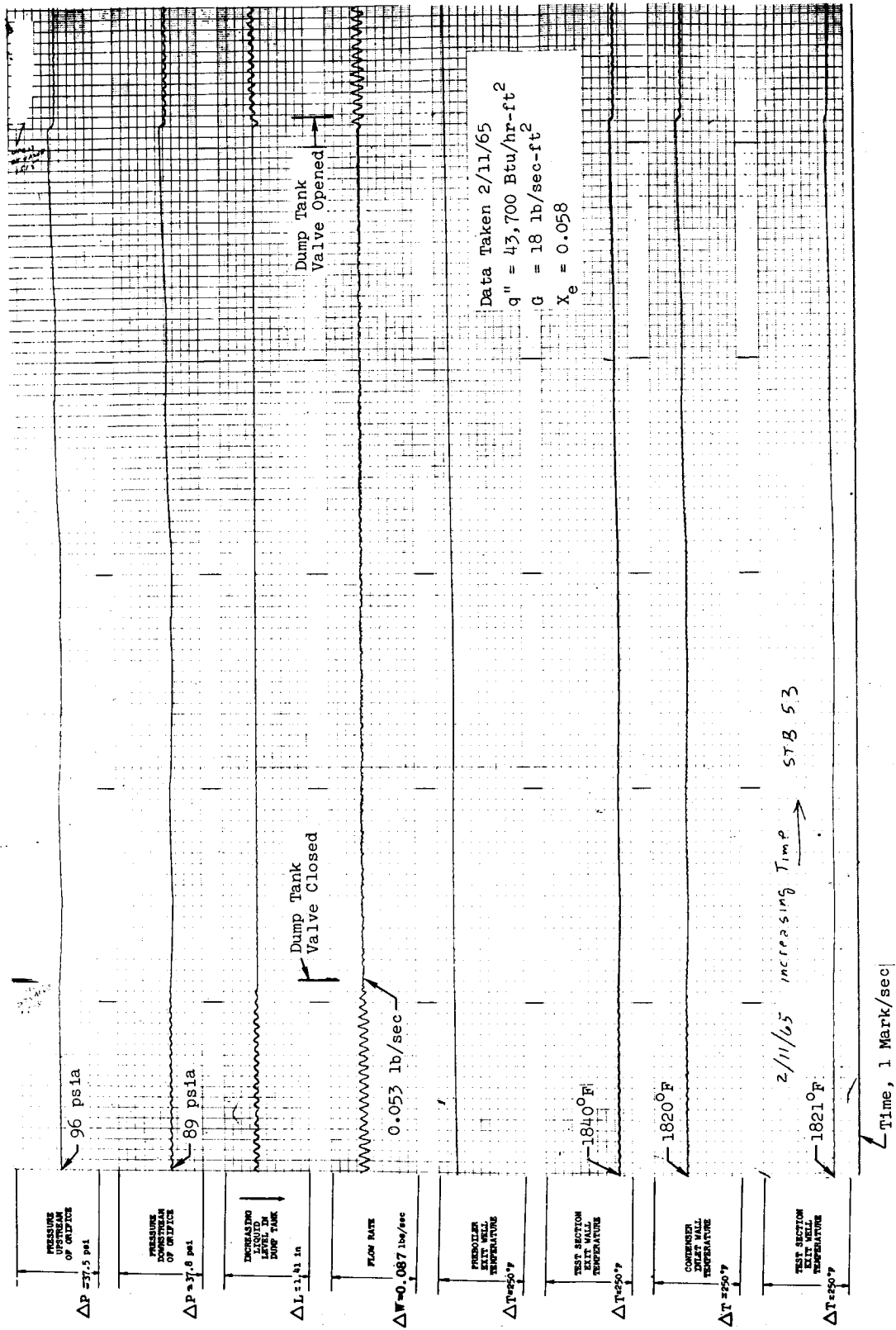
Figure 87. Recorder Chart Showing Effect of Dump Tank Valve Closure on Loop Stability After Boiling Inception at Low Flow (G = 18 lb/sec-ft²) with Test Section No. 2 (.74" ID with helical insert P/D = 6) (Continuation of run shown in Figure 86)

-210-
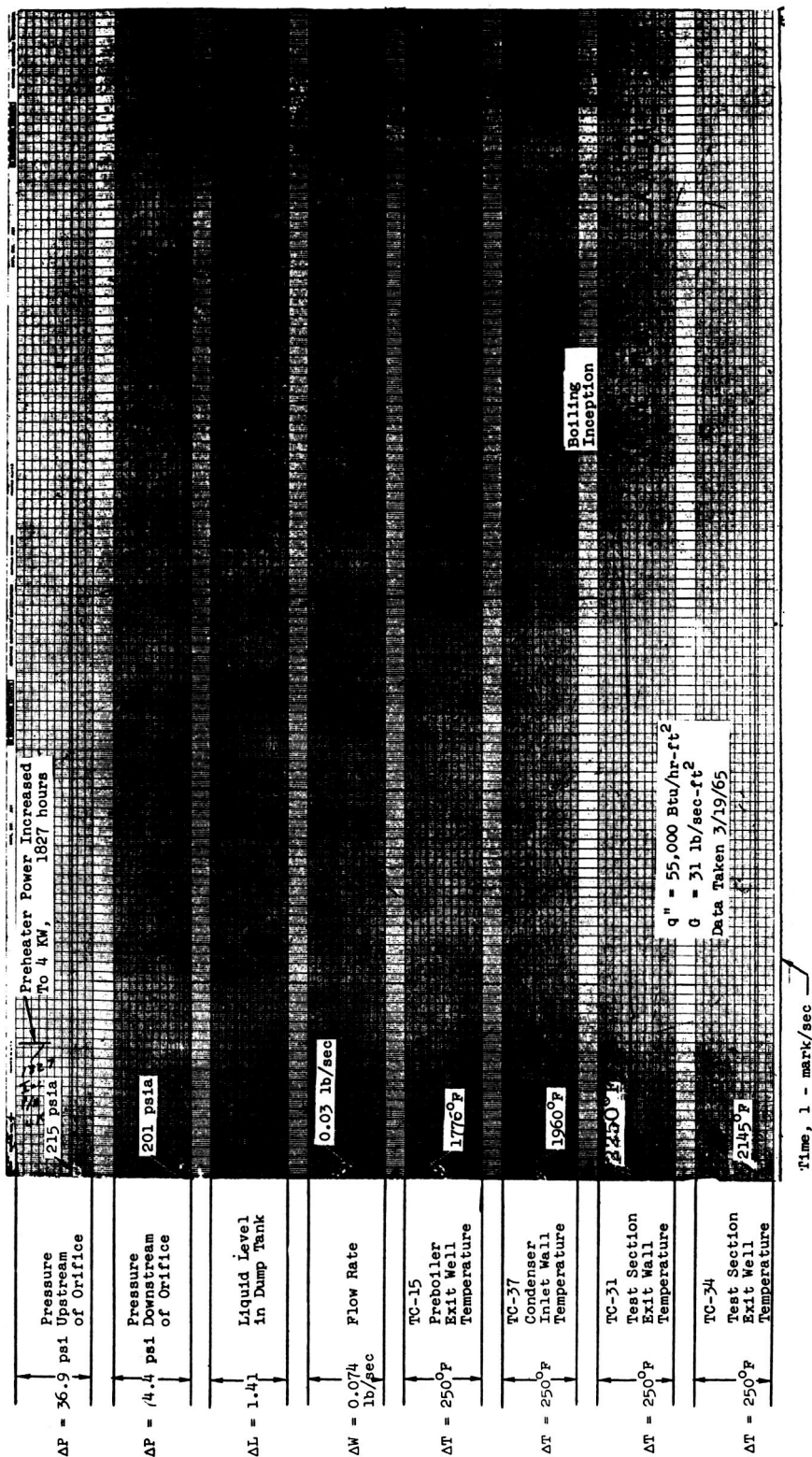
Figure 88. Recorder Chart Showing Boiling Inception at High-Pressure (201 psia, T_{sat} = 2100°F) with Test Section No. 3 (.423"ID, No Insert).
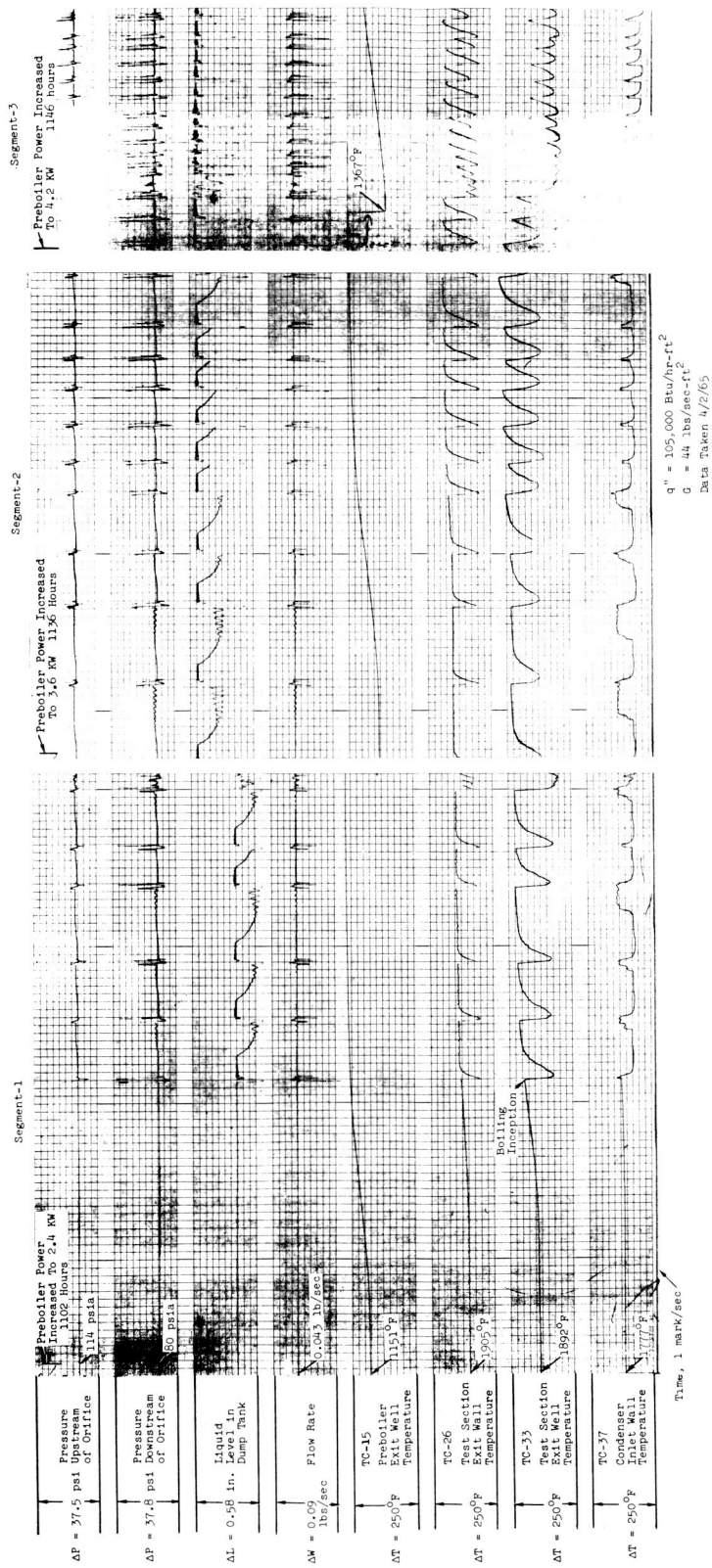
-211-

Figure 89a. Recorder Chart Showing Boiling Inception and Subsequent
Boiling Instability at Intermediate Pressure (80 psia,
T_{sat} = 1800°F) With Test Section No. 3 (.423"ID, no insert)

-212-

Figure 89b. Recorder Chart Showing Boiling Instability at Intermediate Pressure with Test Section No. 3 (.423"ID, no Insert) (Continuation of Figure 89a)

-213-

(a) Plot of High-Speed Digital Recorder Print-out Showing
Detail of Exit Fluid Temperature Behavior

(b) Oscillograph Recorder Chart Segment Showing Exit Wall
And Fluid Temperature Behavior

Figure 90. Behavior of Wall and Fluid Temperatures at Test Section
Exit During Boiling Instability at Intermediate Pressure
(80 psia) with Test Section No. 3 (.423" ID, No Insert)

Preboiler Power
Increased to 3.6 KW
1509 hours

Preboiler Power
Increased to 6 KW
1526 Hours

q" = 65,000 Btu/hr-ft²
G = 45 lb/sec-ft²

Data Taken 4/2/65

Boiling Inception
In Test Section

ΔP = 3.75 psi — Pressure Upstream of Orifice — 461 psia

ΔP = 37.8 psi — Pressure Downstream of Orifice — 427 psia

ΔL = 0.58 in. — Liquid Level in Dump Tank

ΔW = 0.085 lb/sec — Flow Rate — 0.045 lb/sec

ΔT = 250°F — TC-15 Preboiler Exit Well Temperature — 1411°F

ΔT = 250°F — TC-26 Test Section Exit Wall Temperature — 1812°F

ΔT = 250°F — TC-33 Test Section Exit Well Temperature — 1804°F
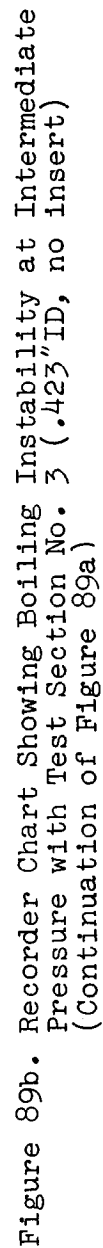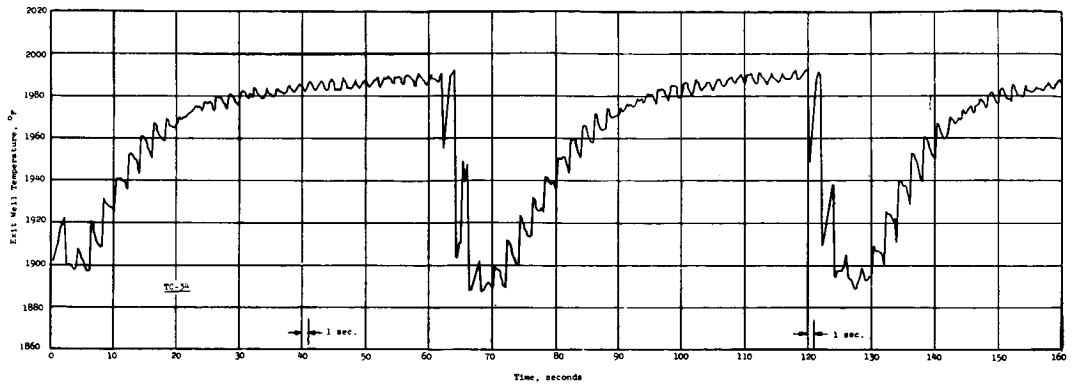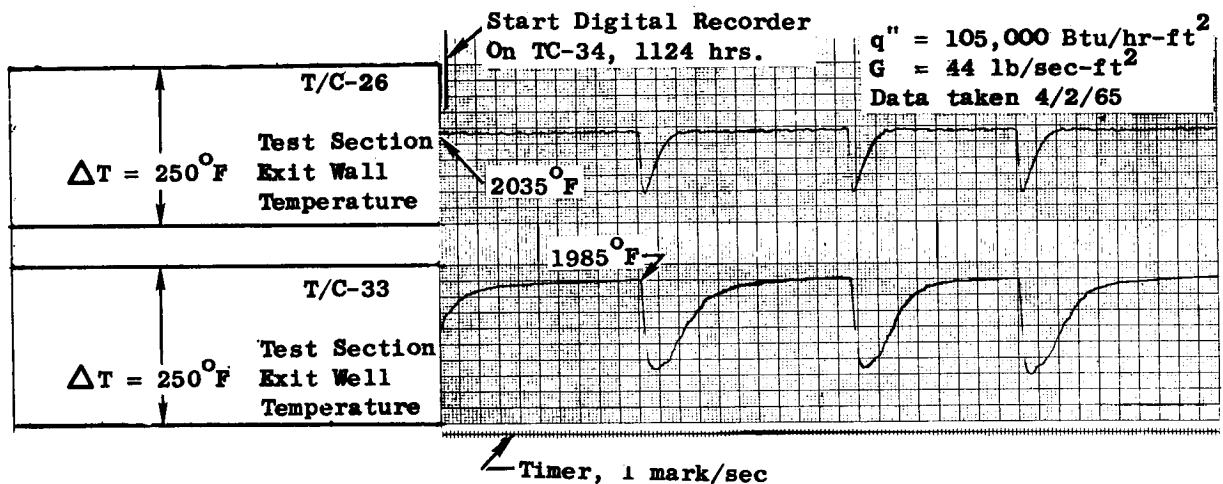
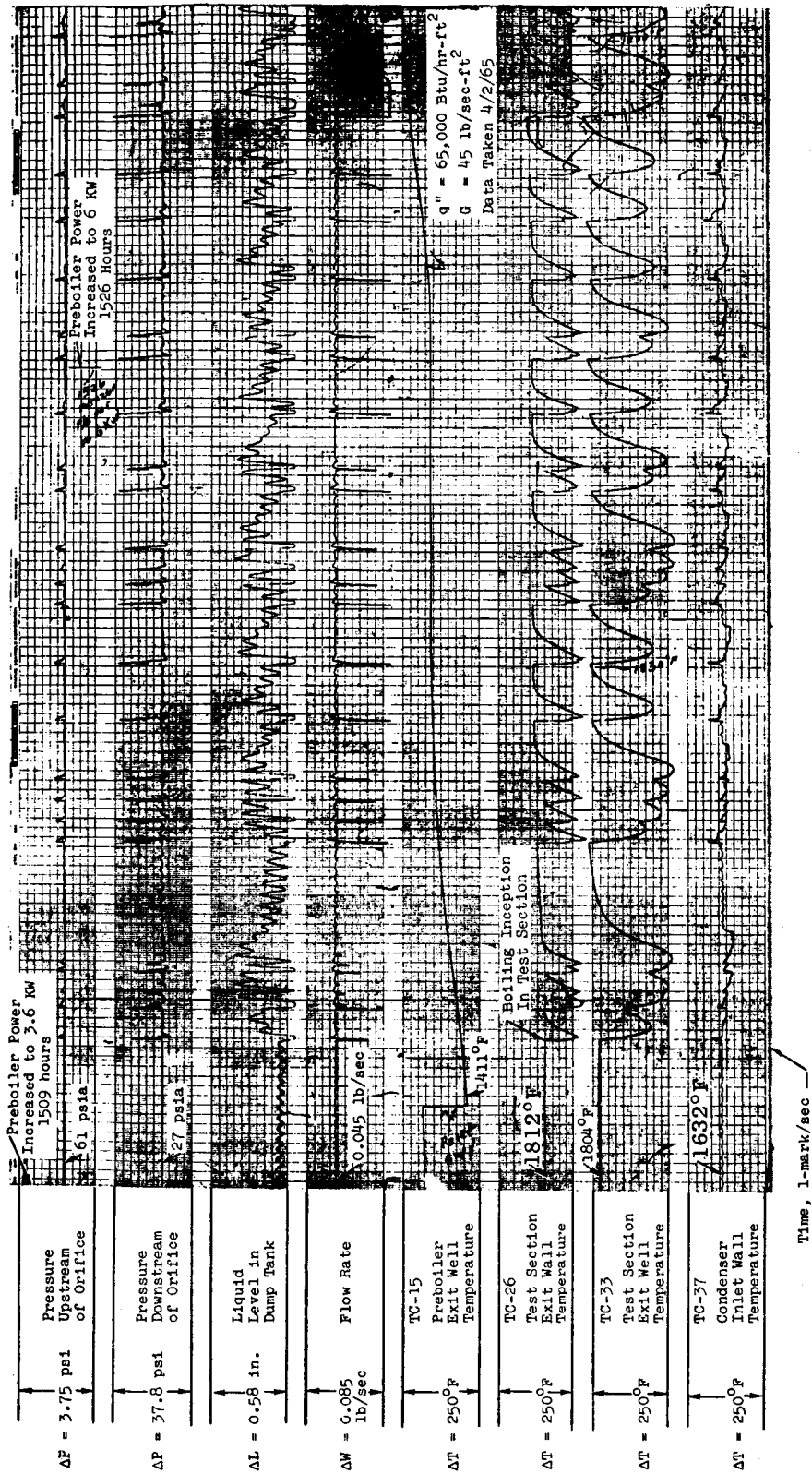ΔT = 250°F — TC-37 Condenser Inlet Wall Temperature — 1632°F

Time, 1-mark/sec

Figure 91.   Recorder Chart Showing Boiling Inception and Subsequent Boiling
Instability at Low Pressure (27 psia, T_{sat} = 1520°F) with Test
Section No. 3 (.423"ID, No Insert).

-215-

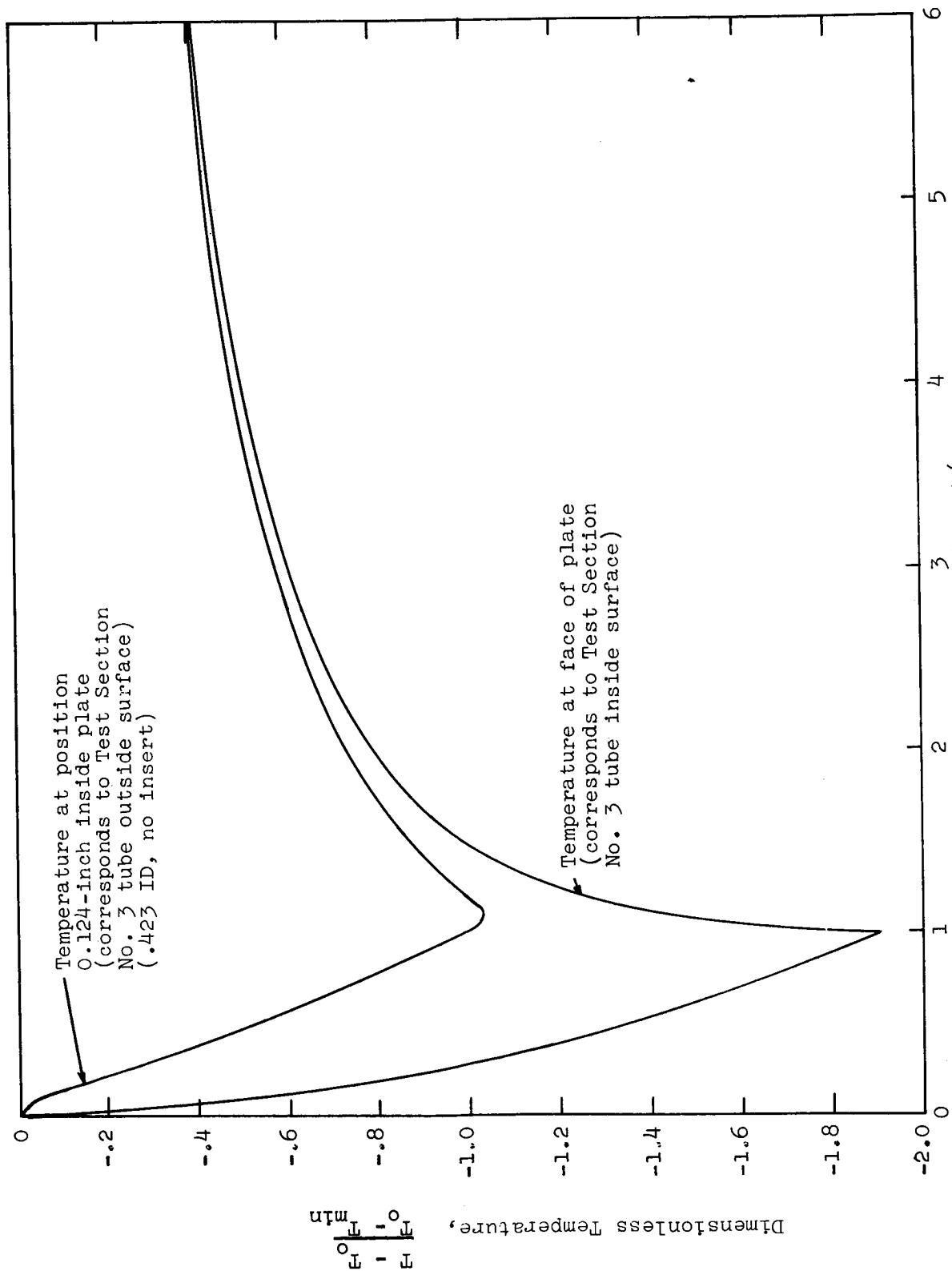Figure 92. Temperature Response of a Semi-infinite Flat Plate After A Step Change In Surface Heat Flux

-216-

The figure contains the following labels and annotations:

Lyon, Reference 9:

$$N_{Nu} = 7 + 0.025(N_{Pe})^{0.8}$$

Lubarsky and Kaufman, Reference 44:

$$N_{Nu} = 0.625(N_{Pe})^{0.4}$$

Nusselt Number, $N_{Nu} = \dfrac{h\, D_e}{k}$, Dimensionless

Peclet Number, $N_{Pe} = G\, D_e\, C_p/k$, dimensionless

Figure 93. Liquid Heat Transfer Results From The Wire-Wrapped Plug Region of Test Section No. 5 (.742" ID with wire-wrapped plug and wire coil P/D = 2), Evaluated Assuming Axial Flow

-217-
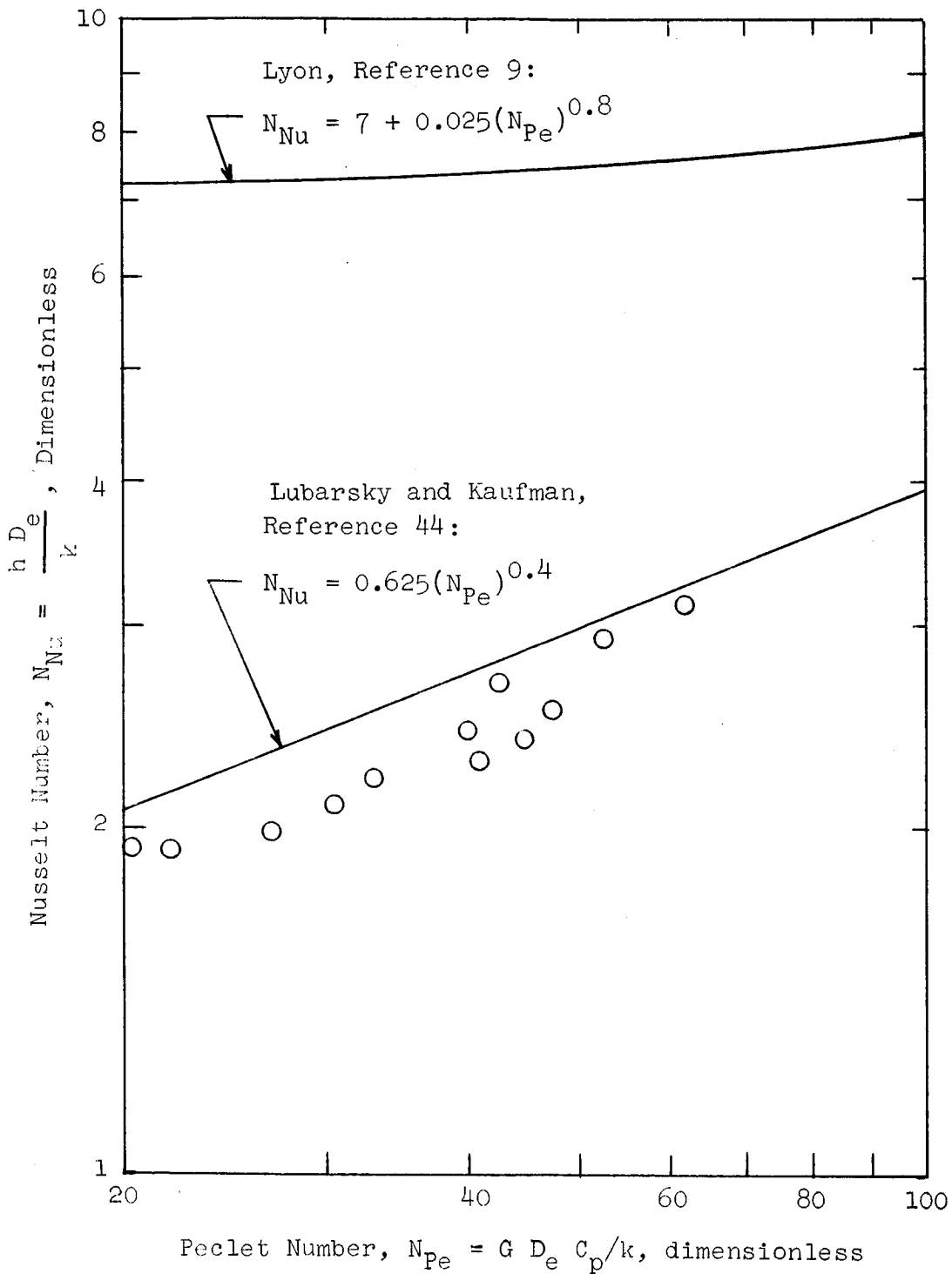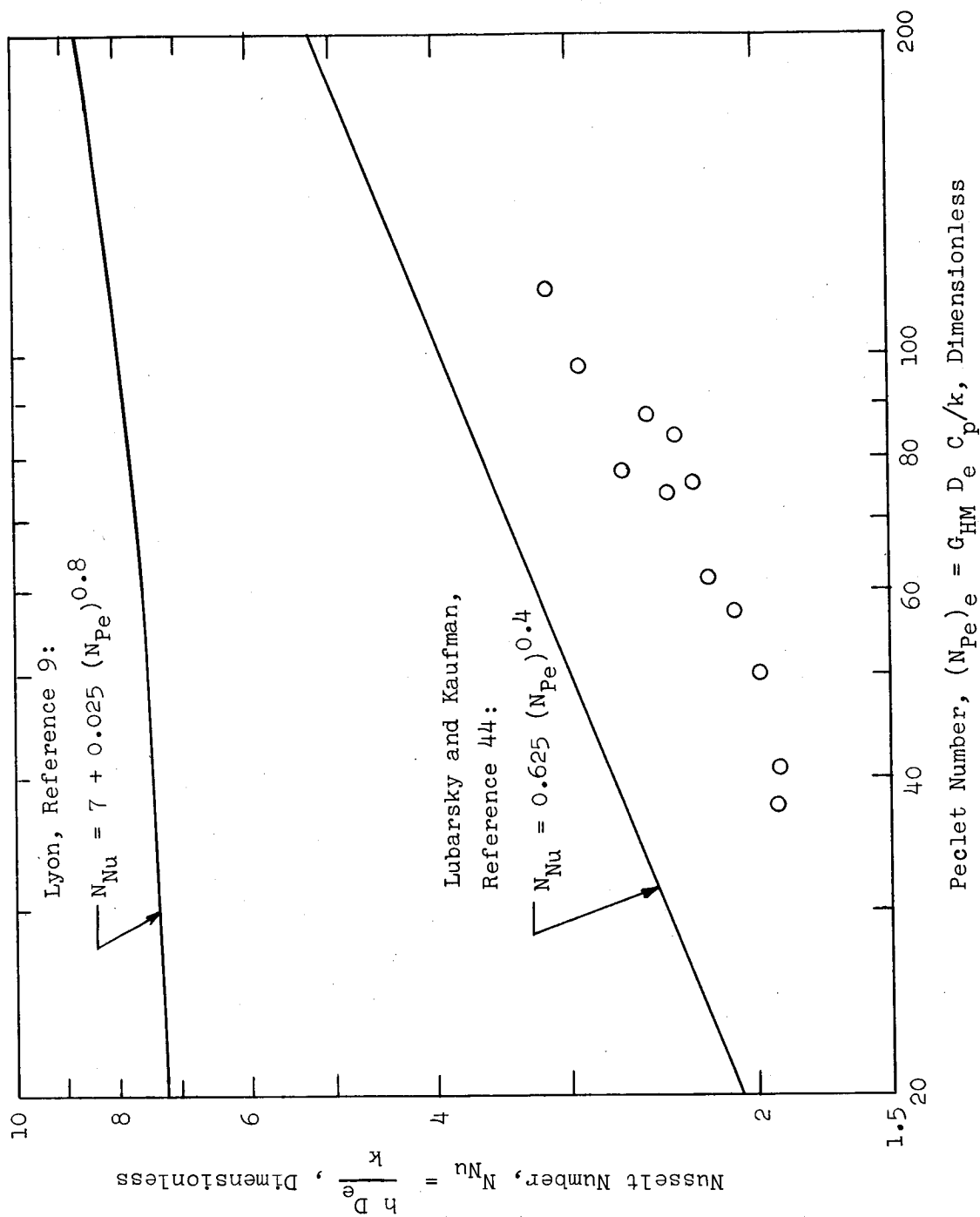
Figure 94. Liquid Heat Transfer Results From the Wire-Wrapped Plug Region of Test Section No. 5 (.742"ID with wire-wrapped plug and wire coil P/D = 2) Evaluated Assuming Helical Flow

IV CONCLUDING REMARKS

The results of this investigation include local forced-convection heat transfer data from boiling inception to superheated vapor conditions for potassium at saturation temperatures from 1800°F to 2100°F. The data are applicable to design of boilers for Rankine cycle space power systems employing potassium as the working fluid. These results supplement other boiling potassium data, such as that presented in Reference 3, by extending the range of available data to 2100°F and by providing more detailed information on local heat transfer performance. The principal conclusions resulting from this investigation are as follows:

1. For tubes without inserts in nucleate boiling, the following trends are indicated:

a. The heat transfer coefficients are in the order of 10,000 Btu/hr-ft^2-°F for heat fluxes greater than about 100,000 Btu/hr-ft^2 (Figures 43-45).

b. The heat transfer coefficients generally increase with increasing heat flux (Figures 43-45).

c. The heat transfer coefficient increases with quality at qualities less than about 20% (Figure 42) and is essentially independent of quality in the quality range above 20% up to the quality at critical heat flux onset (Figures 43-46).

d. No definite trends of the heat transfer coefficient with saturation temperature, mass velocity or tube diameter were found for the ranges tested, indicating that the actual trends with these variables are less than the scatter in the data (Figures 43-45).

e. Two analytical models of the vaporization process were developed,
    one based on a film evaporation hypothesis and the other based on
    a bubble formation hypothesis. An analytical procedure using these
    two models (Equations 6 and 11, respectively) was found to give
    reasonable estimates of the local nucleate boiling heat transfer
    coefficients in tubes without inserts.

2. For tubes containing vortex generator inserts in nucleate boiling,
the following trends are indicated.

a. An effect of vortex generator inserts is to reduce the nucleate
    boiling heat transfer coefficient below the corresponding value for
    tubes without inserts.

b. The general trends in the heat transfer coefficients with respect
    to heat flux and vapor quality appear to be similar to those found
    for tubes without inserts (items 1-b and 1-c above).

c. At constant radial acceleration and constant heat flux, the heat
    transfer coefficient increases in proportion to the insert pitch-to-
    diameter ratio for the inserts tested (Equation 23).

d. At constant heat flux for a given insert, the heat transfer coefficient
    increases approximately in proportion to the 0.16-power of the radial
    acceleration for the range of radial accelerations tested (Equation 23).

e. At constant radial acceleration for a given insert, the heat transfer
    coefficient increases about linearly with heat flux for the range of heat
    fluxes tested. (Equation 23).

3. Critical heat flux data were obtained in test sections with and without vortex generator inserts. These data, together with those from Reference 3, are correlated with vapor quality and radial acceleration by Equation 24 which predicts the following trends in the critical heat flux:

    a. The critical heat flux decreases with increasing vapor quality.

    b. At constant quality, the critical heat flux increases with increasing radial acceleration developed by the insert.

4. The transition boiling regime extends from the critical heat flux point to the establishment of stable film boiling. The following trends were observed for the transition boiling regime.

    a. The local test section wall temperature oscillates within an envelope whose upper temperature bound increases with increasing quality and whose lower bound remains approximately constant at the temperature corresponding to nucleate boiling (Figures 52 and 54).

    b. Vortex generator inserts have an effect of prolonging the transition boiling regime to higher vapor qualities (relative to values measured in tubes without inserts), prior to beginning of stable film boiling (Figure 55).

    c. The local transition boiling heat transfer coefficients, obtained from time-average values of the fluctuating local wall temperature are in reasonable agreement with Equation (26) which was developed empirically in Reference 3.

    d. The transition boiling heat transfer coefficient decreases with increasing quality (Equation 26).

e. The transition boiling heat transfer coefficient increases with increasing radial acceleration developed by the insert (Equation 26).

f. The transition boiling heat transfer coefficient decreases with increasing wall-to-fluid temperature difference (Equation 26).

5. The film boiling regime extends from the end of the transition boiling regime (where the wall temperature stabilizes) to the point at which the vapor quality is 100%. Comparison of the measured data with predictions based on the conventional Dittus-Boelter equation indicate that:

a. The film boiling coefficient may be in the order of two to five times the value predicted by the Dittus-Boelter equation (Equation 28).

b. If a vortex generator insert is used, then the helical flow values of the mass velocity and equivalent diameter should be used in the Dittus Boelter equation (Equation 29) to calculate film boiling coefficients.

6. Superheated potassium vapor heat transfer coefficient data were obtained in a plain tube with no insert, a tube containing a helical insert, and a tube with a wire coil insert. These data indicate that:

a. The Dittus-Boelter equation provides a low-side estimate of the heat transfer coefficient after corrections for helical flow (for helical inserts) and radiation effects are made (Equation 29).

b. In the case of a wire coil insert, an additional empirical correction to the data must be made to correlate the data with those taken in the plain tube and in the tube containing a helical insert (Equation 55).

7. Friction pressure drop data were obtained in single phase flow (with water) and in two-phase adiabatic flow (with high-temperature potassium). These data indicate that:

    a. Single-phase friction factors for the helical insert geometry can be calculated with good accuracy using the Blasius equation (Equation 57) when the helical flow values of the mass velocity and equivalent diameter are used (Figure 67).

    b. The single-phase friction factor data taken with the wire-coil geometry are about twice as high as those measured at the same conditions for the helical insert geometry at the same twist ratio (P/D = 2).

    c. The adiabatic two-phase friction pressure gradient multiplier can be predicted within about $\pm$ 30% using the homogeneous flow model given by Equation (69) (Figures 77-80).

8. Observations of boiling inception and instabilities encountered can be summarized as follows:

    a. Some of the instabilities experienced can be attributed to the high liquid superheats present at the point where boiling starts (Figures 85-91).

    b. In general, raising the system pressure (saturation temperature) or flow rate tends to alleviate the instabilities.

    c. Bulk liquid superheats as high as 300°F above saturation temperature were measured at the point of boiling inception at saturation temperatures of about 1500°F (Figure 91).

    d. The liquid superheats required for boiling inception tend to reduce as the boiling pressure is increased, resulting in bulk superheats in the order of about 100°F or less at the boiling inception point for saturation temperatures of about 2100°F (Figure 88).

9. Liquid potassium heat transfer coefficients measured in the wire-wrapped plug region of Test Section No. 5 (helical annulus) are in the range of 2,400 to 4,000 Btu/hr-ft^2-°F) and they are in fair agreement with the Lubarsky and Kaufman correlation (Reference 44) when evaluated using axial flow parameters (Figure 93).

Component Descriptions

ENVIRONMENTAL CHAMBER AND VACUUM SYSTEM

The vacuum environmental chamber, shown in Figure 95, is a cylindrical stainless steel tank consisting of two separate sections. The lower section is fixed and contains instrumentation, power feed-through and pumping ports. The upper section can be raised vertically to provide easy access to the loop piping and instrumentation. A high-vacuum seal between the upper and lower sections of the chamber is maintained with two butyl rubber "O" rings mounted concentrically in the main flange. Stainless steel tubing, welded to the outside of the chamber wall, serves as a channel for cooling water. During loop operation, the water cools the chamber walls, which provide a heat sink for the radiant condenser. Three synthetic sapphire windows are installed in the upper section of the chamber to provide viewports. The entire chamber is insulated with about four inches of fiberfrax insulation which is supported and protected by an outer sheet metal jacket. Calrod heaters, mounted between the chamber and the insulation, are provided for bakeout purposes during pumpdown.

Evacuation of the chamber is accomplished with a 10-inch oil diffusion pump backed by a main mechanical roughing pump (Figure 96). An auxiliary mechanical roughing pump evacuates the space between the "O" rings in the main flange and automatically assumes the function of the main roughing pump in the event of failure. The vacuum pumping system maintains chamber pressures in the 10^{-8} to 10^{-6} torr range during loop operation.

ELECTROMAGNETIC PUMP

The electromagnetic pump is a General Electric model KY414PB1 designed to pump sodium or potassium at temperatures up to 2200°F with a rating of 1.29 gpm at 100 psi developed pressure. The pump duct, shown in Figure 97, is constructed

from Cb-1%Zr. The fluid enters the duct and flows through a central tube, reverses direction at the opposite end and flows through a helical passage in which the pressure is developed by the interaction of the magnetic field and current which flows as a result of the voltage induced in the liquid metal contained in the pump duct. Further details of the pump can be found in Reference 1.

FLOWMETER

The total flow rate was measured with a permanent magnet type electromagnetic flowmeter. The flowmeter duct was a 3/8-inch Schedule 80 Cb-1%Zr pipe. The electrical connection to the pipe was made by resistance welding two Cb-1%Zr wires on diametrically opposite sides of the pipe perpendicular to the pipe centerline and to the lines of magnetic flux. The flowmeter duct was flame-sprayed with a 0.005-inch layer of alumina and was then thermally insulated from the magnet pole faces with about 25 layers of dimpled Cb-1%Zr foil.

CONDENSER

The radiant condenser consisted of approximately 60 ft of 3/4-inch Schedule 80 Cb-1%Zr pipe formed into a 20-inch diameter helix on a 3-inch pitch. Figure 98 is a view of the condenser piping during an early stage of the loop fabrication.
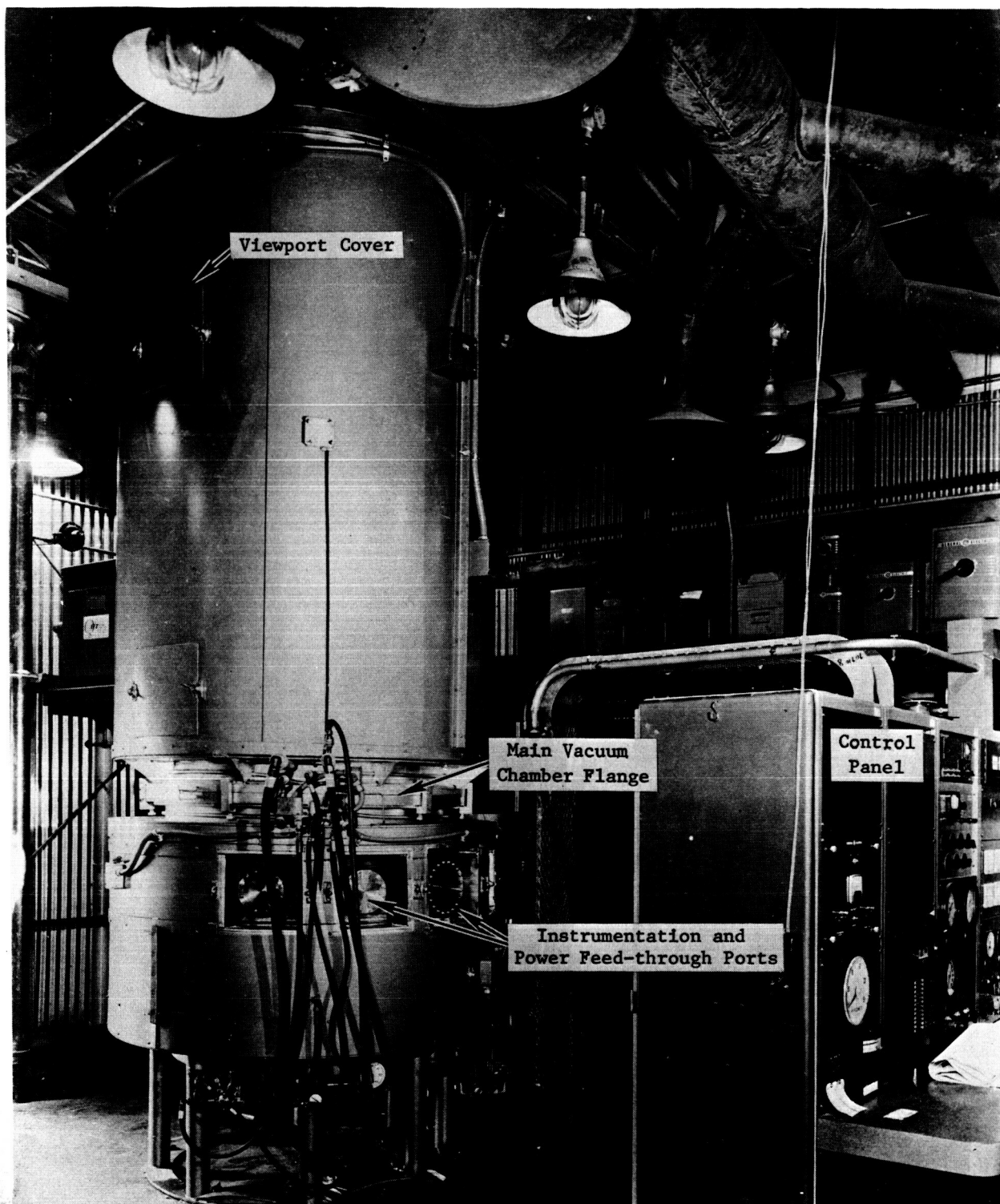
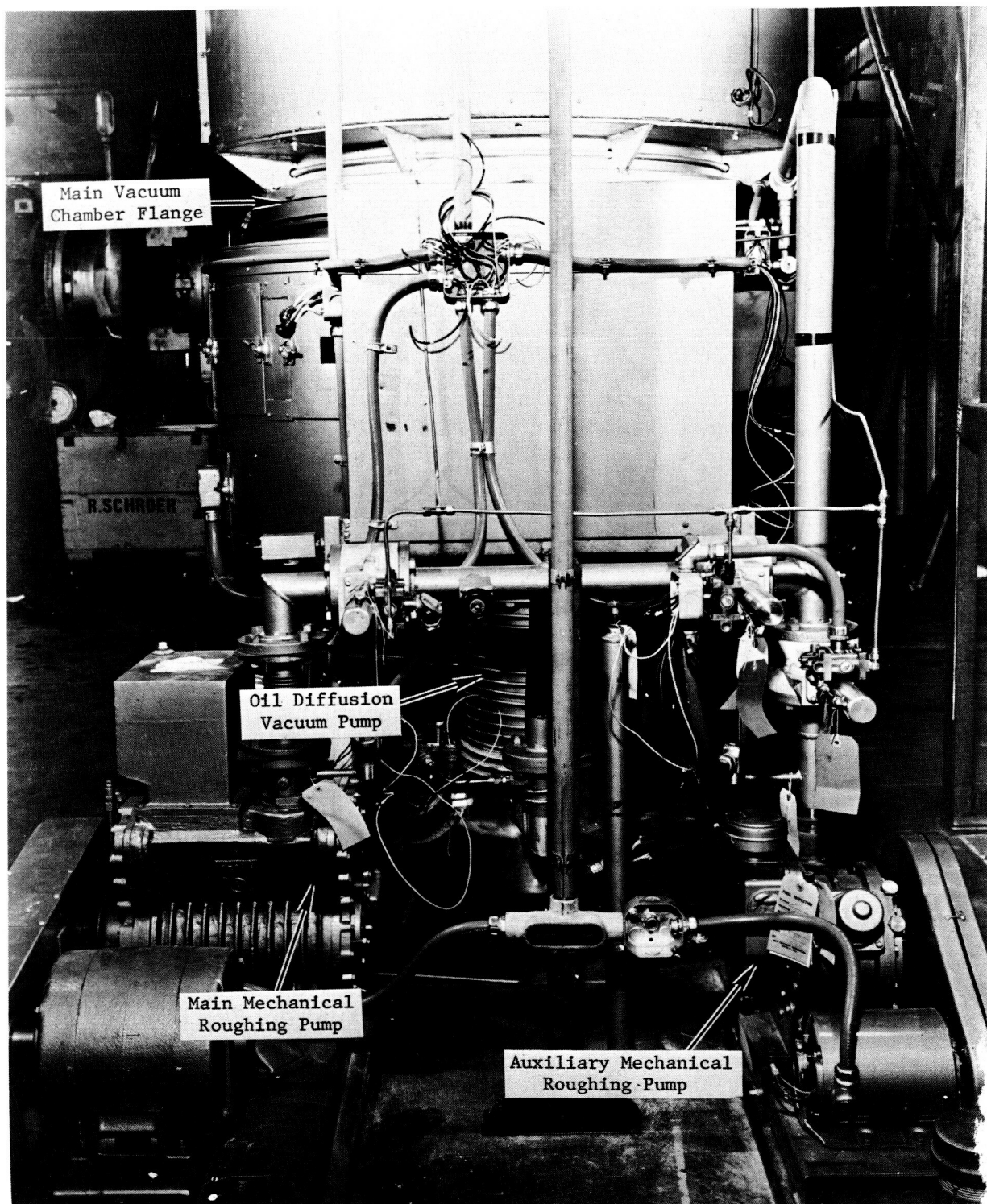Figure 95. Cb-1%Zr Facility Vacuum Chamber

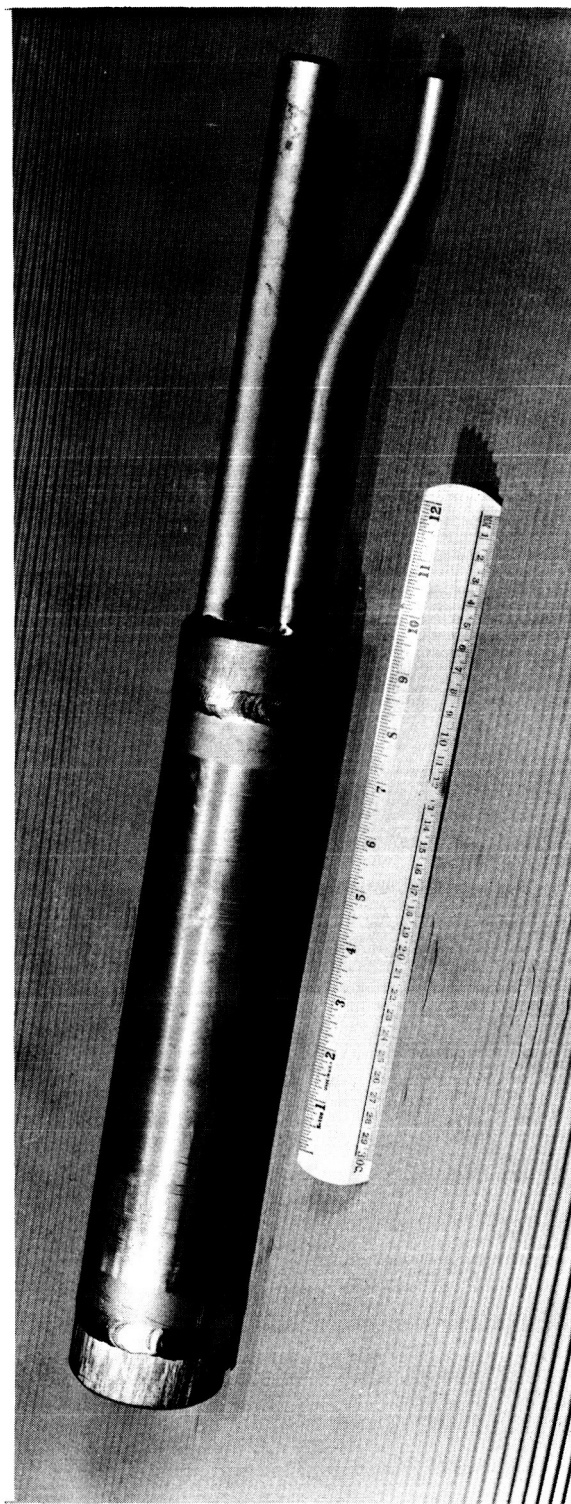Figure 96. Cb-1%Zr Facility Vacuum Pumps and Associated Piping

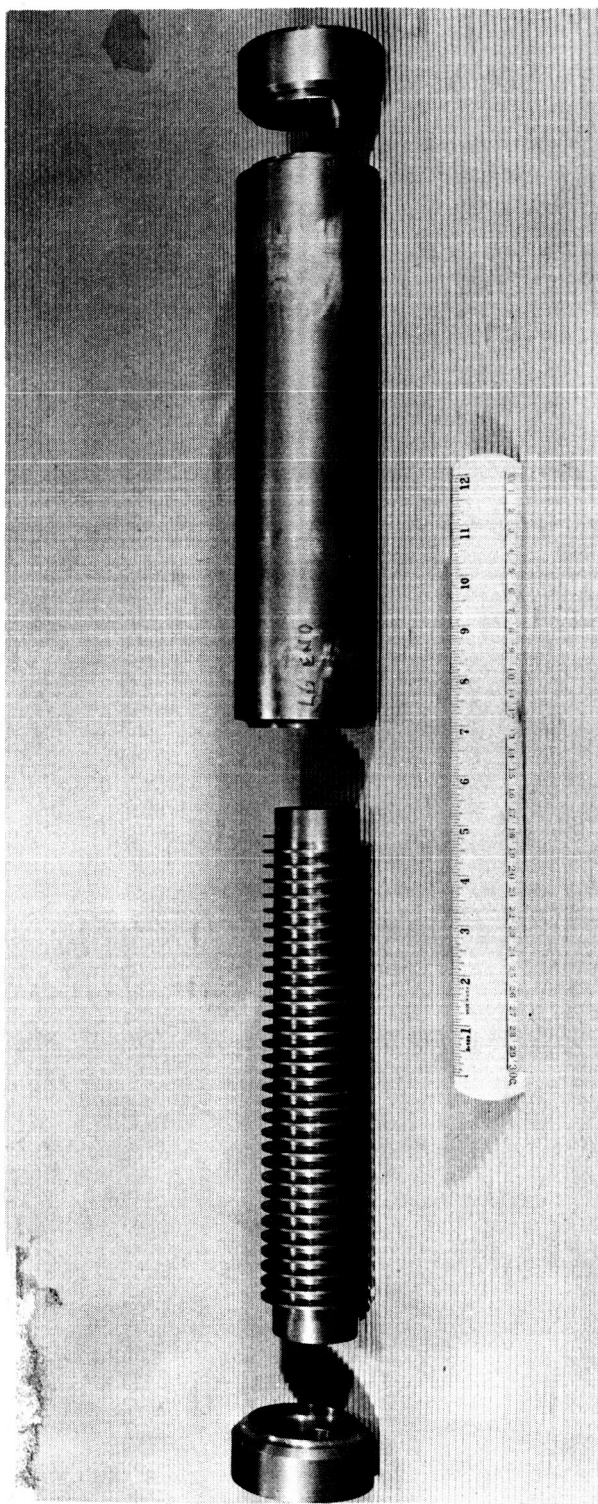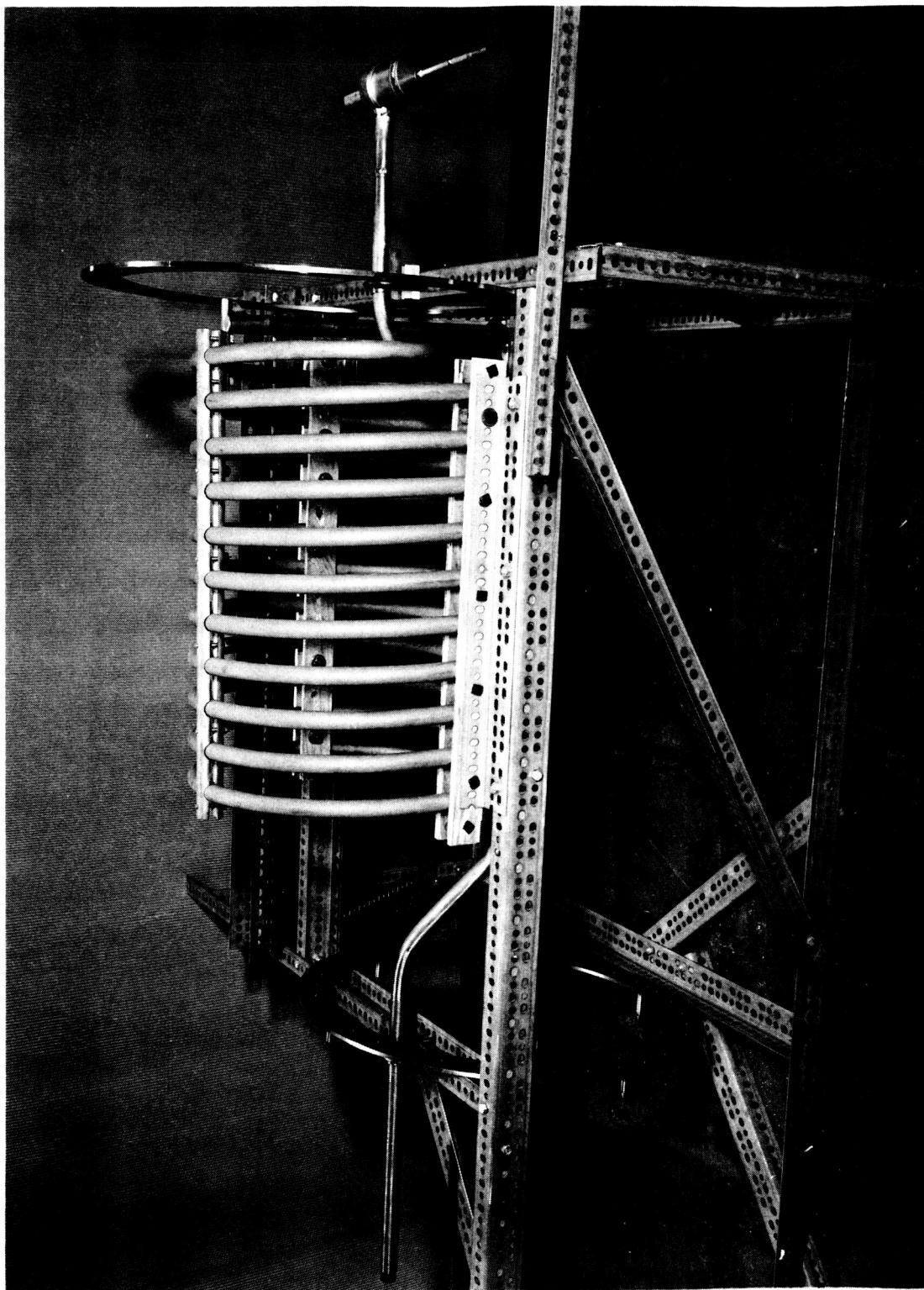Figure 97. Cb-1%Zr Facility Helical Flow Pump Duct Before and After Welding

Figure 98. Cb-1%Zr Facility Condenser Coil Before Final Assembly

APPENDIX B

Analysis of Fluid Radial Pressure and Temperature
Variations In Tubes Containing Helical Inserts

Consider the flow of a single component two-phase fluid in a tube containing a helical insert. In order to calculate the radial variations of pressure and temperature at any axial station a velocity distribution will be assumed and the pressure variations will be obtained from the Navier-Stokes equations. The temperature distribution will then be obtained by assuming that the vapor is saturated vapor at the calculated pressure.

The following assumptions will be used in the analysis:

1. Annular flow of a two-phase single component fluid (all the liquid flowing as a film on the tube wall and all the vapor flowing in the core).

2. Steady flow

3. Incompressible flow (Mach No. $\ll$ 1)

4. Rate of change of pressure in axial direction is small.

The velocity distribution is defined by the following assumption.

1. The radial velocity is zero (V_r = 0 at any r)

2. The axial component of velocity is independent of radius within each phase (i.e., $\bar{V}_z = V_z$ (z; phase))

3. The resultant velocity vector $\bar{V}$ always makes an angle θ (θ = helix angle) with the r - α plane, in cylindrical coordinates (sketch-A).

Z, tube axis

y

r

α
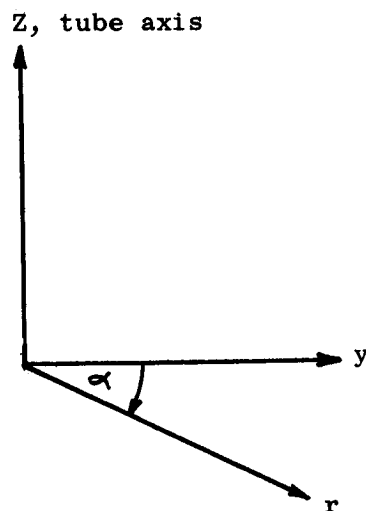
Cylindrical Coordinates

$\bar{V}$

V_z

θ

V_α
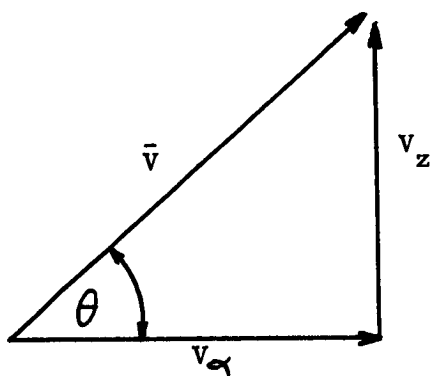
Velocity Components

$\sqrt{4\pi^2 r^2 + p^2}$

p

θ

$2\pi r$

Helix Angle, θ

Sketch-A

-232-

From sketch-A the following relationship is obtained.

$$\frac{V_\alpha}{V_z} = \frac{2\pi r}{p^2} \tag{B-1}$$

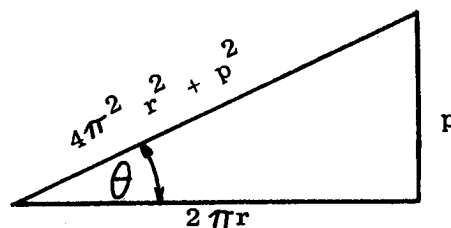From continuity considerations, the axial velocity in the vapor phase is

$$V_{zg} = \frac{XG}{\rho_g R_g} \tag{B-2}$$

Therefore, using Equation (B-2)

$$V_{\alpha g} = \left[\frac{2\pi r}{p}\right] \left[\frac{XG}{\rho_g R_g}\right] \tag{B-3}$$

Thus, since $V_\alpha = V_\theta$, the radial acceleration in the vapor phase $a_g = V_{\theta g}^2/r$ is, using Equation (B-3)

$$a_g = \frac{4\pi^2 x^2 G^2 r}{\rho_g^2 R_g^2 p^2} \tag{B-4}$$

Equations (B-3) and (B-4) indicate that both the tangential velocity $V_{\alpha g} = V_{\theta g}$ and the radial acceleration a_g are linear functions of radius in the vapor core.

In an analogous manner expressions for the axial velocity $V_{z\ell}$, the tangential velocity $V_{\alpha \ell}$ and the radial acceleration a_ℓ in the liquid film adjacent to the wall can be obtained, which are:

$$V_{z\ell} = \frac{(1-x)G}{\rho_f R_\ell} \tag{B-5}$$

$$V_{\alpha\ell} = \frac{2\pi r}{p} \frac{(1-x)G}{\rho_f R_\ell} \qquad (B-6)$$

$$a_\ell = \frac{4\pi^2 (1-x)^2 G^2 r}{p^2 \rho_f^2 R_\ell^2} \qquad (B-7)$$

From the Navier-Stokes equations (Reference 47) in the radial direction

$$\frac{\rho}{g_c} \frac{V_\alpha^2}{r} = \frac{\partial P}{\partial r} \qquad (B-8)$$

from which, using $a = V_\alpha^2/r$ and, for the helix, $V_\alpha = V_\theta$,

$$\frac{\partial P}{\partial r} = \rho a_r \qquad (B-9)$$

where a_r is the radial acceleration a normalized to standard gravitational acceleration g_c, so that

$$a_r = a/g_c \qquad (B-10)$$

Thus, substituting from (B-4) and (B-10) into (B-9) gives for the vapor core

$$\left(\frac{\partial P}{\partial r}\right)_g = \rho_g \left(\frac{2\pi r}{p}\right)^2 \left(\frac{x}{R_g}\right)^2 \left(\frac{G^2}{g_c r \rho_g^2}\right) \qquad (B-11)$$

Similarly, substituting from (B-7) and (B-10) into (B-9) gives for the liquid film

$$\left(\frac{\partial P}{\partial r}\right)_\ell = \rho_f \left(\frac{2\pi r}{p}\right)^2 \left(\frac{1-x}{R_\ell}\right)^2 \left[\frac{G^2}{g_c r \rho_f^2}\right] \qquad (B-12)$$

For the test sections with helical inserts, the total change in pressure

between the insert centerbody and the tube wall can be obtained by integrating Equation (B-11) and (B-12) and adding the results together to obtain

$$P_w - P_{cb} = \int_{r_{if}}^{R} \left(\frac{\partial P}{\partial r}\right)_\ell dr + \int_{r_{cb}}^{r_{if}} \left(\frac{\partial P}{\partial r}\right)_g dr \qquad (B-13)$$

Carrying out the integration of Equations (B-11) and (B-12), substituting the results into Equation (B-13) and introducing the phase velocity slip ratio $K = V_g/V_\ell$ and the helical insert pitch-to-diameter ratio (P/D) gives

$$\frac{P_w - P_{cb}}{\rho_f D_T/2} = \left(\frac{\pi}{P/D}\right)^2 \left(\frac{G^2}{g_c D_T \rho_f^2}\right)\left(\frac{1-x}{R_\ell}\right)^2 \left[1 + \left(\frac{D_{if}}{D_T}\right)^2\left(\frac{\rho_g}{\rho_f} K^2 - 1\right) - \left(\frac{D_{cb}}{D_T}\right)^2 \frac{\rho_g}{\rho_f} K^2\right] \qquad (B-14)$$

Substituting Equation (B-7) into (B-10) and evaluating the results at the wall, where $a_{r\ell} = a_R$ gives

$$a_R = 2 \left(\frac{\pi}{P/D}\right)^2 \left(\frac{1-x}{R_\ell}\right)^2 \left(\frac{G^2}{g_c \rho_f^2 D_T}\right) \qquad (B-15)$$

Combining Equation (B-15) into (B-14) results in

$$\frac{P_w - P_{cb}}{\rho_f D_T/2} = \frac{a_R}{2} \left[1 + \left(\frac{D_{if}}{D_T}\right)^2 \frac{\rho_g}{\rho_f} K^2 - 1) - \left(\frac{D_{cb}}{D_T}\right)^2 \frac{\rho_g}{\rho_f} K^2\right] \qquad (B-16)$$

Following Fauske's suggestion (Reference 48) and as discussed further in Reference 10, it will be assumed for the rest of the analysis that the slip ratio $K = \sqrt{\rho_f/\rho_g}$. With this assumption, for all of the liquid flowing in the liquid film on the wall, Equation (B-16) reduces to

$$\frac{P_w - P_{cb}}{\rho_f D_T/2} = \frac{a_R}{2} \left[1 - (\frac{D_{cb}}{D_T})^2 \right] \qquad (B-17)$$

Assuming that the fluid is in thermodynamic equilibrium and that the pressure differences are sufficiently small that the change in fluid thermodynamic properties along the radius are negligible, the Clausius equation (Reference 49),

$$\frac{dT}{dP} = \frac{Tv_{fg}}{Jh_{fg}} \qquad (B-18)$$

can be used to relate the radial pressure difference with the corresponding change in saturation temperature. Thus, integrating equation (B-18) and combining the result with Equation (B-17) gives for the change in saturation temperature between the insert centerbody and the tube-wall.

$$T_{sat-w} - T_{sat-cb} = \frac{a_R}{2} (\frac{\rho_f D_T}{2}) (\frac{Tv_{fg}}{Jh_{fg}}) \left[1 - (\frac{D_{cb}}{D_T})^2 \right] \qquad (B-19)$$

Equation (B-19) was used to correct the measured wall-to-fluid temperature differences for the evaluations of the nucleate boiling data taken with vortex generator inserts, as discussed in Section III-A.

REFERENCES

1. Brooks, R.D., (Editor), "Alkali Metals Boiling and Condensing Investigations, Vol. I - Experimental Program", Final Report Covering the Period January 1, 1961 to June 30, 1962, Contract NAS 5-681, SPPS, RSD, General Electric Company, June 1, 1964.

2. Semmel, J.W., Jr., Young, W.R. and Kearns, W.H., "Alkali Metals Boiling and Condensing Investigations, Vol. II - Materials Support", Final Report, Contract NAS 5-681, SPPS, RSD, General Electric Company, January 14, 1963.

3. Peterson, J.R., "High Performance "Once-Through" Boiling of Potassium In Single Tubes", 300 KW Boiling Project Topical Report, NASA 3-2528, SPPS, RSD, General Electric Company, June 1966.

4. Affel, R.G., Burger, G.H. and Pearce, C.L., "Calibration and Testing of 2- and $3\frac{1}{2}$-inch Magnetic Flowmeters for High-Temperature NaK Service", Oak Ridge National Laboratory, ORNL-2793, (No Date).

5. Stone, J.P., Ewing, C.T., Spann, J.R., Stienkuller, E.W., Williams, D.D., and Miller, R.R., "High Temperature Properties of Sodium, Potassium, and Cesium", NRL Report 6128, August 1964.

6. Tippets, F.E. and Converse, G.L., (Editors), "Alkali Metals Boiling and Condensing Investigations", Quarterly Report No. 10, Contract NAS 3-2528, SPPS, RSD, General Electric Company, January 20, 1965.

7. Levy, S., "Steam Slip-Theoretical Prediction from Momentum Model", Journal of Heat Transfer, Vol. 82, p. 113, May 1960.

8. Kutateladze, S.S., Fundamentals of Heat Transfer, Academic Press, Inc., New York, 1963.

9. Lyon, R.N. "Liquid-Metal Heat Transfer Coefficient", Chem. Eng. Progress, 47: 75-79, 1951.

10. Tippets, F.E., (Editor), "Alkali Metals Boiling and Condensing Investigations", Quarterly Report No. 8, NASA-CR-54138, Contract NAS 3-2528, SPPS, MSD, General Electric Company, July 20, 1964.

11. Bonilla, C.F., Wiener, M.M., Bilfinger, H., "Pool Boiling of Potassium", Oak Ridge National Laboratory, September 5, 1963.

12. Bergles, A.E., Rohsenow, W.M., "The Determination of Forced Convection Surface Boiling", ASME Paper 63-HT-22.

13. Griffith, P., and Wallis, J.D., "The Role of Surface Conditions in Nucleate Boiling", Chem. Eng. Progr. Symposium Series, No. 30, Vol. 56, 1960.

14. Rohsenow, W.M., Editor, "Developments in Heat Transfer", MIT Press, 1964

15. Gouse, S.Q., Jr., Coumou, K.G., "Heat Transfer and Fluid Flow Inside a Horizontal Tube Evaporator", Report DSR 9649-1, Engineering Project Laboratory, Department of Mechanical Engineering, MIT, June 1964.

16. Staub, F.W., and Zuber, N., "A Program of Two-Phase Flow Investigation", Second Quarterly Report, July-September 1963, EURAEC 866.

17. Merte, J., Jr. and J.A. Clark, "Study of Pool Boiling in an Accelerating System," ASME Paper 60-HT-22.

18. Westwater, J.W., "Things We Don't Know About Boiling Heat Transfer", Article in Fundamental Research In Heat Transfer - J.A. Clark, Pergamon Press, 1963, p. 61.

19. Greene, N.D. (Convair Aircraft), "Confined-Vortex-Flow Heat Transfer", cited as private communication to W.R. Gambill and R.D. Bundy in "An Evaluation of the Present Status of Swirl-Flow Heat Transfer", Oak Ridge Report Central Files Number 61-4-61, April 1961.

20. Ewing, C.T., Stone, J.P., Spann, J.R., Steinkuller, E.W., Williams, D.D. and Miller, R.R., "High-Temperature Properties of Potassium", U.S. Naval Research Laboratory, NRL Report 6233, September 24, 1965.

21. Weatherford, W.D., Jr., Tyler, J.C., and Ku, P.M., "Properties of Inorganic Energy Conversion and Heat Transfer Fluid for Space Applications", WADD Technical Report 61-96, November, 1961.

22. McAdams, W.H., Heat Transmission, 3rd ed., New York, McGraw Hill Book Company, Inc.

23. Sutherland, W.A., "Heat Transfer to Superheated Steam", General Electric Company, GEAP-4258, May 1963.

24. McElroy, D.L., and Kollie, T.G., "The Total Hemispherical Emittance of Platinum, Columbium-1% Zirconium, and Polished and Oxidized Inor-8 in the Range of 100° to 1200°C, From NASA-SP-31, Symposium on the Measurement of Thermal Radiation Properties of Solids, Held at Dayton, Ohio (September 1962).

25. Sams, E.W., "Heat Transfer and Pressure-Drop Characteristics of Wire-Coil Type Turbulence Promoters", Reactor Heat Transfer Conference Sponsored by U.S. Atomic Energy Commission, November 1 and 2, 1956.

26. Lockhart, R.W., and Martinelli, R.C., "Proposed Correlation of Data For Isothermal Two-Phase, Two-Component Flow in Pipes", Chem. Eng. Prog., Vol. 45, P. 39, 1949.

27. Martinelli, R.C., Boelter, L.M.K., Taylor, T.H.M., Thompsen, E.G., and Morrin, E.H., "Isothermal Pressure Drop for Two-Phase, Two-Component Flow in a Horizontal Pipe", Trans. ASME, Vol. 66, p. 139, 1944.

28. Martinelli, R.C., Putnam, J.A., and Lockhard, R.W., "Two-Phase Two Component Flow in the Viscous Region", Trans. AIChE, Vol. 42, p. 681, 1946

29. Martinelli, R.C., and Nelson, D.B., "Prediction of Pressure Drop During Forced-Circulation Boiling of Water", Trans. ASME, Vol. 70.

30. Blasius, H., Forschungsarbeiten auf dem Gebiete des Ingenieurwesens, 131, 1913.

31. Gambill, W.R. , Bundy, R.D., and Wansbrough, R.W., "Heat Transfer, Burnout, and Pressure Drop For Water in Swirl Flow Through Tubes With Internal Twisted Tapes", Oak Ridge National Laboratory, ORNL-2911, April 11, 1960.

32. Knudsen, J.G., and Katz, D.L., Fluid Dynamics and Heat Transfer, New York, McGraw-Hill Book Company, 1958.

33. Ledinegg, M. Unstabilitat der Stromung bei naturlidhem und Zwangumlauf, Die Warme, 891-898 (1938)

34. Chilton, H. "A Theoretical Study of Stability in Water Flow through Heated Passages," J. Nuclear Energy, 5, (1957)

35. Anderson, R.P., Lottes, P.A., "Boiling Stability Reactor Technology," J. Nuclear Energy, B.2, No. 3, 28, 1962.

36. Tippets, F.E., and Converse, G.L., (Editors), "Alkali Metals Boiling and Condensing Investigations", Quarterly Report No. 11, Contract NAS 3-2528, SPPS, RSD, General Electric Company, April 23, 1965.

37. McCabe, W.L., and Smith, J.C., Unit Operations of Chemical Engineering, P. 108, McGraw-Hill Book Company, Inc., 1956.

38. Ferguson, D.R. and Tippets, F.E. (Editors), "Alkali Metals Boiling and Condensing Investigations", Quarterly Report No. 13, Contract NAS 3-2528, NASA-CR-54890, RSD, SPPS, General Electric Company, October 29, 1965.

39. Marto, P.J., and Rohsenow, W.H., "The Effect of Surface Conditions on Nucleate Pool Boiling Heat Transfer to Sodium," Report No. 5219-33, Department of Mechanical Engineering, Massachusetts Institute of Technology, Contract No. AT(30-1)3357, AEC Codi. Report MIT-3357-1, January, 1965.

40. Hoffman, H.W., and Krakoviak, A.I., "Convective Boiling with Liquid Potassium," Heat Transfer and Fluid Mechanics Institute, Stanford, Cal. (1964).

41. Converse, G.L., and Tippets, F.E., "Alkali Metals Boiling and Condensing Investigation," Quarterly Report No. 12, NASA-CR-54739, Contract NAS 3-2528, SPPS, MSD, General Electric Company, July 23, 1965.

42. Carslaw, H.S. and Jaeger, J.C., Conduction of Heat In Solids, 2nd Edition, Oxford, 1959, pg. 76

43. Hoffman, E.E., "Boiling Potassium Stability Studies," Metals and Ceramics Division Annual Progress Report for Period Ending May 31, 1963, ORNL-3470, November 11, 1963, p. 114-118.

44. Lubarsky, B., and Kaufman, S.J., "Review of Experimental Investigations of Liquid-Metal Heat Transfer", NASA Report No. 1270, 1956.

45. Frank, R.G., "Materials For Potassium Lubricated Journal Bearings", Quarterly Report No. 11, Contract NAS 3-2534, SPPS, RSD, General Electric Company.

46. Tippets, F.E., "Alkali Metals Boiling and Condensing Investigation", Quarterly Report No. 7, NASA-CR-54038, Contract NAS 3-2528, SPPS, MSD, General Electric Company, April 20, 1964.

47. Schlicting, H., "Boundary Layer Theory", Pergammon Press (1955).

48. Fauske, H.F., "Contribution To The Theory Of Two-Phase, One-Component Critical Flow", ANL-6633, October 1962.

49. Keenan, J.H., "Thermodynamics", McGraw-Hill.